Intermediate report for the project
"Analysis of airborne- and surface measurements of the actinic flux":

Actinic fluxes during ATOP96

Arve Kylling

November 2, 2000

1 Objectives

During June 1996 the joint ATOP/PAUR (Experimental Study of the altitude dependence of the tropospheric ozone photolysis frequency J($O(^1D)$) between 0 and 12 km height)/Photochemical Activity and solar Ultraviolet Radiation) measurement campaign took place in the Aegean Ocean. Airplane measurements were made of the actinic flux at selected altitudes. In addition surface based measurements of the UV irradiance, ozone column and aerosol properties were made.

The objective of this report is to use these measurements together with a state of the art radiative transfer model to investigate the altitude dependence of the actinic flux under clear sky conditions.

All measured and simulated data presented and the software needed to perform the simulations and the subsequent analysis are available on the CD accompanying this report.

2 Results

The instrumentation used for to measure the actinic flux are described by (Hofzumahaus et al., 1999) and (Hofzumahaus et al., 2001). Below the model simulations and subsequent data analysis are described.

2.1 Simulation of the ATOP96 measurements

The UVSPEC radiative transfer model was used to simulate the measured spectra. UVSPEC is part of the libRadtran package available from http://www.libradtran.org. The UVSPEC model includes various methods for solving the radiative transfer equation. Here the discrete ordinate radiative transfer equation solver of (Stamnes et al., 1988) is used in 16–streams mode. A relatively large number of streams is needed since the actinic flux is calculated from the radiances output by the solver and the angular response of the instrument accounted for. Often the ideal actinic flux is calculated with 2-streams approximation in order to save computer time. (Kylling et al., 1995) showed that 2-stream approximations under certain conditions may give errors of 20% compared to 16–stream calculations. The 4-stream approximation is however sufficient for most calculations of the ideal actinic flux. To simulate a measured up- or downwelling actinic flux spectrum, azimuthally averaged radiances were calculated at 1° polar angle steps from nadir to zenith at high, 0.05 nm, spectral resolution. The resulting spectral radiances were convolved with the instrument slit function and interpolated to the center wavelength of the measurements. Finally, the radiances were multiplied with the angular response of the up– and downlooking input optics and integrated over the appropriate polar angle intervals to yield the simulated spectrum.

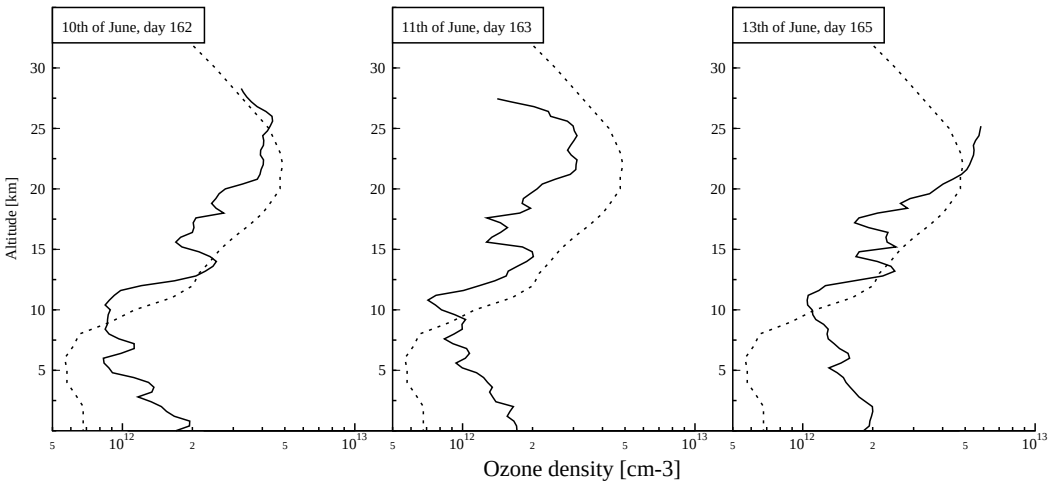

Figure 1: Ozone concentration (solid lines) measured by ozone sondes launched from Thessaloniki, Greece. The ozone profiles have been smoothed with a triangular function with a full width at half maximum (FWHM) of 400 m and interpolated to 400 m resolution using cubic splines. Included for reference is the U.S. standard profile (dashed lines, (Anderson et al., 1986)).

Changes in the solar zenith angle due to changes in aircraft location and time duration of a single scan, were accounted for. Temperature dependent ozone cross sections were taken from (Bass and Paur, 1985) and the Rayleigh scattering cross section was calculated from the formula given by (Nicolet, 1984). The Earth-Sun distance during the campaign was accounted for. UVSPEC has been thoroughly compared against surface irradiance measurements (Mayer et al., 1997); (Kylling et al., 1998); (van Weele et al., 2000).

Input to the radiative transfer model are ozone profiles, aerosol optical depth, single scattering albedo and phase function profiles, the surface albedo, and an extraterrestrial solar spectrum. The ozone column and aerosol optical depth column were deduced from the direct Sun spectra recorded by spectroradiometers located at the Tatoi airfield (38.112°N, 23.781°E, 255 m) outside Athens (Bentham DM 150) and on Agios Efstratios (39.57°N, 24.97°E, 49 m) (Brewer MK III). For more information on the instruments and the ozone and aerosol data see (Kylling et al., 1998).

Ozone profiles were taken from ozone sonde measurement made from the nearby airport of the city of Thessaloniki on June 10, 11, and 13, 1996 (Figure 1).

The aerosol optical depth profiles were taken from simultaneous lidar measurements made on the nearby island of Agios Efstratios as described by (Marenco et al., 1997). The aerosol profile was scaled to the total aerosol optical depth measured with the double Brewer spectroradiometer located on Agios Efstratios for the flights on dyas 162, 163 and 165, while data from the Bentham spectroradiometer was used for the flight over Athens, day 166, (Kylling et al., 1998). The aerosol single scattering albedo and phase function profiles and the surface albedo were taken as the values that provided the best agreement between model and surface based irradiance measurements by the Brewer spectroradiometer (days 162, 163 and 165) and the Bentham Spectroradiometer (day 166) made simultaneously to the flight (Kylling et al., 1998).

The extraterrestrial spectrum was adopted from several sources. Between 280 and 407.8 nm the Atlas 3 spectrum shifted to air wavelengths (M. E. VanHoosier, personal communication, 1996) was used. Atlas 2 (Woods et al., 1996) was used between 407.8 and 419.9 nm. Above 419.9 nm the solar spectrum in the Modtran 3.5 radiation model was used (Anderson et al., 1993).

The vertical distribution of the aerosol optical depth was measured by an aerosol lidar on the

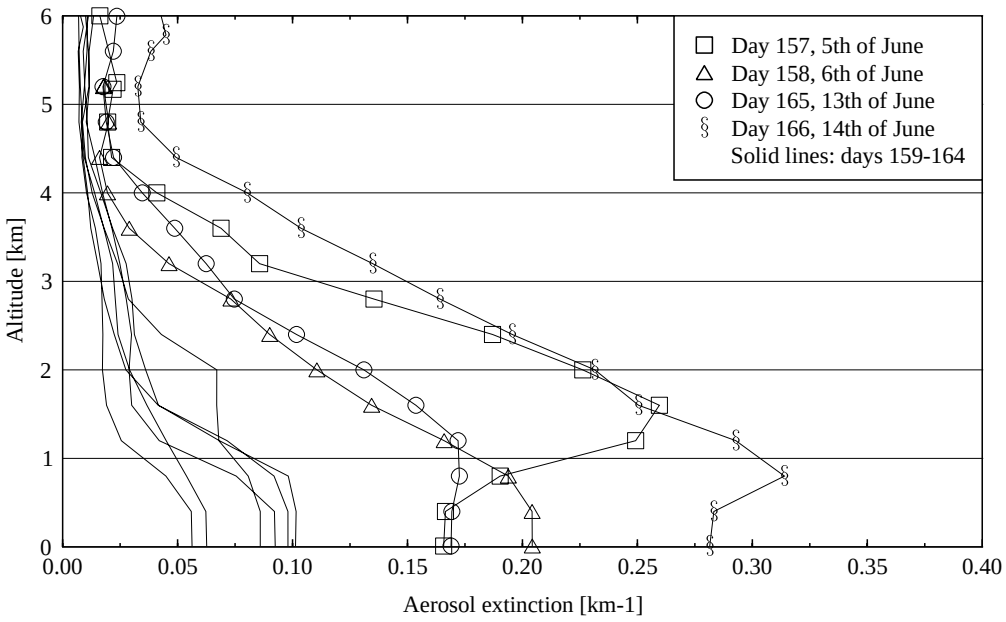

Figure 2: Smoothed and daily averaged aerosol optical depth profiles as measured by the lidar on Agios Efstratios at 355 nm. The aerosol profiles have been smoothed with a triangular function with a FWHM of 400 m and interpolated to 400 m resolution using cubic splines.

island of Agios Efstratios between June 5 and 14 (Marenco et al., 1997). The aerosol optical profile was measured at 355 and 532 nm. Since interest here is in the UV, only the shortest wavelength is used. Both lidar wavelengths may be used to calculate altitude dependent Ångström coefficients. However, because of considerable noise in the lidar measurements the Ångström coefficients estimated from the spectroradiometer measurements were used. The aerosol optical depth was measured in the altitude range 600–6000 m depending on conditions. The aerosol loading in the stratosphere was negligible during the PAUR campaign (Marenco et al., 1997).

Both the aerosol profile and the ozone profile were smoothed with a triangular function with a FWHM of 400 m and interpolated to 400 m resolution using cubic splines. The aerosol optical depth profile was assumed constant below 600 m. Above 6000 m the aerosol optical depth was set to zero. Daily averaged aerosol optical depth profiles are shown in Figure 2. For the ozone profile a constant mixing ratio was assumed above the balloon burst altitude.

For a specific radiative transfer simulation of a measurement the aerosol optical depth and ozone profiles closest in time were chosen. The aerosol optical depth and ozone profiles were scaled to the aerosol optical depth and ozone column measured by the spectroradiometers. Both the Brewer and the Bentham ozone retrieval algorithms utilize the ozone cross sections from (Bass and Paur, 1985). The same ozone cross sections were used for the model simulations.

The main input parameters used to simulate each measured spectrum are summarized in Tables 2–5, Appendix A. All model input parameters are from or based on analysis of independent measurements. Thus, the model/measurement comparison is an acid test of the correctness of the radiative transfer model, and hence for our understanding of the vertical variation of the actinic flux.

2.2 Comparison between measurements and model simulations

Flights were performed on four days in June 1996 under varying atmospheric conditions. During the flights over the Aegean Sea the sky was cloud free, whereas during the flight over land a few scattered clouds were present. The first flight was made around noon with solar zenith angles varying between $16.2 - 24.5°$. The aerosol load was relatively low with $\tau(355\,\mathrm{nm}) = 0.28$. The second flight was made for solar zenith angles between $32.1 - 60.0°$ with slightly lower aerosol concentrations, $\tau(355\,\mathrm{nm}) = 0.21$. During the third flight the aerosol load had increased, $\tau(355\,\mathrm{nm}) = 0.67$, the solar zenith angle was similar as on the first day, $16.1 - 22.4°$. The last flight was made over land near Athens for solar zenith angles between $16.1 - 29.8°$ and $\tau(355\,\mathrm{nm}) = 0.8$.

In Figures 10-128 is shown simulated and measured upwelling, downwelling and total actinic flux spectra for all flights, see Appendix C for description of the figures.

The measured and simulated spectra agree very well with respect to their wavelength scales. This is not surprising as the measured spectra were calibrated versus the Fraunhofer line pattern in the ATLAS-3 spectrum which also served as input to the model. The good agreement therefore only demonstrates that the wavelength calibration of the experimental spectra has been performed properly. The absolute accuracy can be estimated from the comparison vs. measurements of the mercury emission lines that have yielded agreement within ± 0.05 nm (see experimental section, and (Hofzumahaus et al., 1999)).

In general the absolute agreement between the simulations and the measurements are better for the downwelling actinic flux (red line, middle right panels) than for the upwelling actinic flux (red line, upper right panels). The measured upwelling spectra at the airport deviates significantly from the simulations (Figures 10, 11, 39, 40, 41, 42, 73, 74, 75, 105, 106, 107). This is mosl likely caused by a combination of factors including effects due to levelling of the input optics; uncertainties in how the model accounts for the angular response; and inhomogeneous surroundings not accounted for by the one-dimensional model. For the lowest flight levels (Figures 16-19, 51-55, 83-86) the upwelling actinic flux is systematically underestimated by the model by approximately 30%. The downwelling actinic flux is underestimated by 5-10%.

For the other flight levels the agreement between the simulated and measured upwelling and downwelling spectra are generally good. As the downwelling actinic flux contributes 70-90% to the total actinic flux the simulations and measurements shows general good agreement at all altitudes for the total actinic flux (red line, lower right panels) For wavelengths larger than 310 nm the differences between the model simulations and the measurements are within ±5 %, except for the lowest flight level where the model is about 12 % systematically lower than the measurements. For wavelengths shorter than 310 nm the model/measurement ratio increases somewhat, reaching values of ~ 1.1 at 300 nm for 3–12 km altitude. Increasing the ozone column by about 1 %, which is well within the experimental uncertainties of the ozone determination, removes this trend. Except for the lowest altitude, the differences are within the overall spectroradiometer error of ±6%.

Some of the spectra measured over Athens are affected by changing altitude and possibly surface albedo variations (Figures 108-109). The downwelling actinic flux spectra in Figures 112, 114 and 115 appears to be affected by scattered clouds. Possibly the upwelling actinic flux is also affected by underlying clouds backscattering radiation as the model is higher than the measurements for most upwelling actinic flux spectra recorded over Athens. These measured and simulated spectra show how a model may be used to identify spectra meausured under stable atmospheric conditions.

The model-measurement discrepancy of 12 % at the lowest flight level is not large, but significant with respect to the measurement uncertainty. One possible reason could be uncertainties in the model input-data for the aerosols which were located below 3 km. Since the flights were not performed directly above the island of Agios Efstratios which was the site which provided the measurements for the model input parameters, there might be inaccuracies in the aerosol optical depth due to horizontal inhomogeneity. Decreasing the aerosol optical depth $\tau(355\,\mathrm{nm})$ by 30 % from 0.267 to 0.176 reduced the discrepancy only slightly from 12% to 9-10%. (Balis et al., 2001) used an optical depth of 0.2 and an aerosol single scattering albedo of 0.96 for their simulations of the ATOP/PAUR actinic flux measurements. Repeating the simulations for the lowest layer with these input parameters left the model 7-8% lower than the measurements, similar to the results

reported by (Balis et al., 2001), their Figure 1. Completely ignoring aerosols, which is unrealistic for the conditions during the campaign, left a 4-5% systematic difference between the model simulations and the measurements with the model being too low. Thus changing the aerosol optical properties could not bring the model results at the lowest altitude into an agreement with the measurement similar to the agreement found at higher altitudes.

The observed deviations between measurements and simulations in this work are similar to those reported by (Mayer et al., 1997) for clear-sky UV-irradiances at ground. They used the same radiative transfer model as in this work and compared the simulations with 1200 spectra measured in Garmisch-Partenkirchen, Germany. The systematic differences were between -11 and 2% for wavelengths between 295 and 400 nm.

At longer wavelengths our results can be compared with studies of the NO_2 photolysis frequency by (Kelley et al., 1995) and (Volz-Thomas et al., 1996). Both groups found good agreement within their experimental uncertainties of 6 % between observed and modeled $J(NO_2)$ values under clear sky up to $\sim$ 7.5 km altitude when they used multi-stream models for their simulations. Their results are consistent with our comparison at wavelengths around 370 nm, where the spectral distribution of the NO_2 photolysis frequency has its median.

The direct solar beam contribution to the actinic flux is shown in the lower left panel of Figures 10-128. It increases with increasing altitude and have a minimum around 310–330 nm. The increase below 310 nm is due to increased absorption of diffuse radiation by ozone. The increase above 330 nm is due to less diffuse radiation due to the decrease of the Rayleigh scattering cross section with increasing wavelength.

The altitude variations of the actinic fluxes received by the downlooking (upwelling radiation) and uplooking (downwelling radiation) sensors are shown in Figures 6-9. The measured actinic fluxes (solid lines) have been normalised to their value at the lowest flight level. The modelled actinic fluxes (dashed lines) have been similarily normalised after adjusting for the difference between the model and measurement at the lowest flight level, see Figures 10-128. Hence, the modelled $F(z)/F(z_0)$, where z_0 is the altitude of the lowest flight level, is different from one for the modelled data.

The downwelling actinic flux exhibits little variation with altitude for the longer wavelengths. For the shorter wavelengths, e.g. 298 nm at 12,000 m, the downwelling actinic flux is approximately a factor of 3 larger than at the surface. The decrease with decreasing altitude is due to Rayleigh scattering and ozone absorption. The upwelling actinic flux above the lowest level is larger for all altitudes and wavelengths due to backscattered radiation from the underlying atmosphere. The relative decrease for short wavelengths above 9,000 m is due to absorption by ozone.

The results shown in Figures 6, 8 and 9 were made for similar solar zenith angles (see tables 2-5). They thus exhibit similar altitude behaviour, albeit the flight over Athens, Figure 9, is a little more noisy at the lowest flight levels. The rather different altitude behaviour seen in for the flight on 11 June, Figure 7, is due to the larger solar zenith angles encountered during this flight (table 3).

The model simulations in Figures 6-9 generally show the same behaviour as the measurements. The agreement between model and measurement is within ± 5 %, except for wavelengths where ozone absorbs for which differences are up to 10 %. However, these differences may be explained by the uncertainties in the ozone measurements as discussed earlier.

The measured downwelling flux is 3–5 times larger than the upwelling flux for all wavelengths and altitudes, except the shortest wavelength and the lowest altitude, bottom panels of Figures 6-9.

2.3 Angular distribution

Ideally an actinic flux instrument should have an angular response that is the same for all incoming angles. In practice the input optics will differ somewhat from the ideal response. In order to assess the error made by an imperfect angular response the angular distribution of the radiation is needed in addition to the angular response of the instrument. For the actinic fluc instrumentation used during ATOP the angular response has been presented by (Hofzumahaus et al., 2001). The angular distribution of the diffuse radiation for various wavelengths and altitudes for typical condtions

encountered during ATOP are presented in Figure 3. For all wavelengths the diffuse radiation field is more isotropic close to the surface than at 12 km. At the lowest altitudes most of the diffuse radiation is evenly distributed over the upper hemisphere. However, at high altitudes (e.g., 6.1 km and 12.1 km) the largest contribution to the diffuse radiation field is from the horizon where also the angular response deviates most from a true 4π response. We also note that due to the wavelength dependence of Rayleigh scattering, the radiation field is more isotropic at shorter wavelengths.

In order to assess the error made by the imperfect angular response, additional model runs have been performed for an ideal isotropic angular response. The ratio of the simulated to the ideal actinic flux is given by the black solid lines in the right column of Figures 10-128, Appendix C. The upper right plot is for the downpointing detector, the middle right plot for the uppointing detector, while the lower right plot is for the total actinic flux.

For the upwelling actinic flux the deviations vary significantly with altitude. For the surface measurements and the lowest flight level (about 120-130 m.a.s.l.) the simulated actinic flux may be up to factors of 1.9 and 1.4 respectively larger than the ideal actinic flux. The deviations are wavelength dependent with a maximum around 320-330 nm. The surface measurements of the upwelling actinic flux are influenced by the levelling of the input optics that were oriented with a slight tilt to compensate for the nick angle of the aircraft. At the lowest flight level the largest contributions to the upwelling actinic flux are from around the horizon where the angular response is the worst, see Figure 3. Hence, the larger deviations compared with the higher flight levels where a relatively larger amounts of the radiation comes from other directions. At the higher flight levels the simulated over actinic flux varies from 1.04 at 3000 m.a.s.l. to 0.98 at 12.000 m.a.s.l.

For the downwelling actinic flux the deviations vary only slowly with wavelength and varies between 0.96 at the surface to 1.06 at the highest flight level.

The downwelling actinic flux contributes between 70-90% to the the total actinic flux. Hence, the deviations for the total actinic flux behaves similar to that for the downwelling actinic flux. They range from 0.99 at the surface to 1.04 at the highest flight level. The increasing deviations with altitude can be understood by the overlap of the angular response characteristics of the instrument with the angular distribution of the diffuse radiance (Figure 3).

The relative contribution of direct radiation to the total acinic flux increases with height between 0.1 km and 12 km: from 55 % to 85 % at 300 nm, from 55 % to 70 % at 330 nm, and from 70 % to 77 % at 400 nm. Thus a significant portion of the measured signal is direct radiation, which for the solar zenith angles encountered during these flights was minimally affected by the instrumental angular response. This explains the relative small differences between the simulated radiation and the ideal actinic flux. It may thus be concluded that for the conditions during these flights the measured actinic fluxes are at maximum 4 % too high due to the non–ideal 4π response of the input optics.

2.4 Effect of Rayleigh scattering, ozone absorption and aerosol extinction

Various factors effect the actinic flux at different altitudes and wavelengths. To investigate the magnitude of the contributions from Rayleigh scattering, ozone absorption and aerosol extinction on the actinic flux spectra recorded during ATOP various sensitivity calculations were made. The base line calculation was taken to be the conditions encountered during flight 162 for the scan starting at 1023. For this scan the solar zenith angle was approximately 17°, which is representative for many of the scans made during the flights on days 162, 165 and 166. The ozone column was 342.85 DU. Further information on the input data is provided in Table 2, Appendix A.

An overview of the various sensitivity cases is given in Table 1. The cases will be described in detail as the results are discussed below.

The absolute values of the actinic flux for the various cases are shown in Figure 4 for selected wavelengths and the integrated UV-A (315-400 nm) and UV-B (280-315 nm) doserates. The relative changes for cases 2-6 versus case 1 are shown in Figure 5.

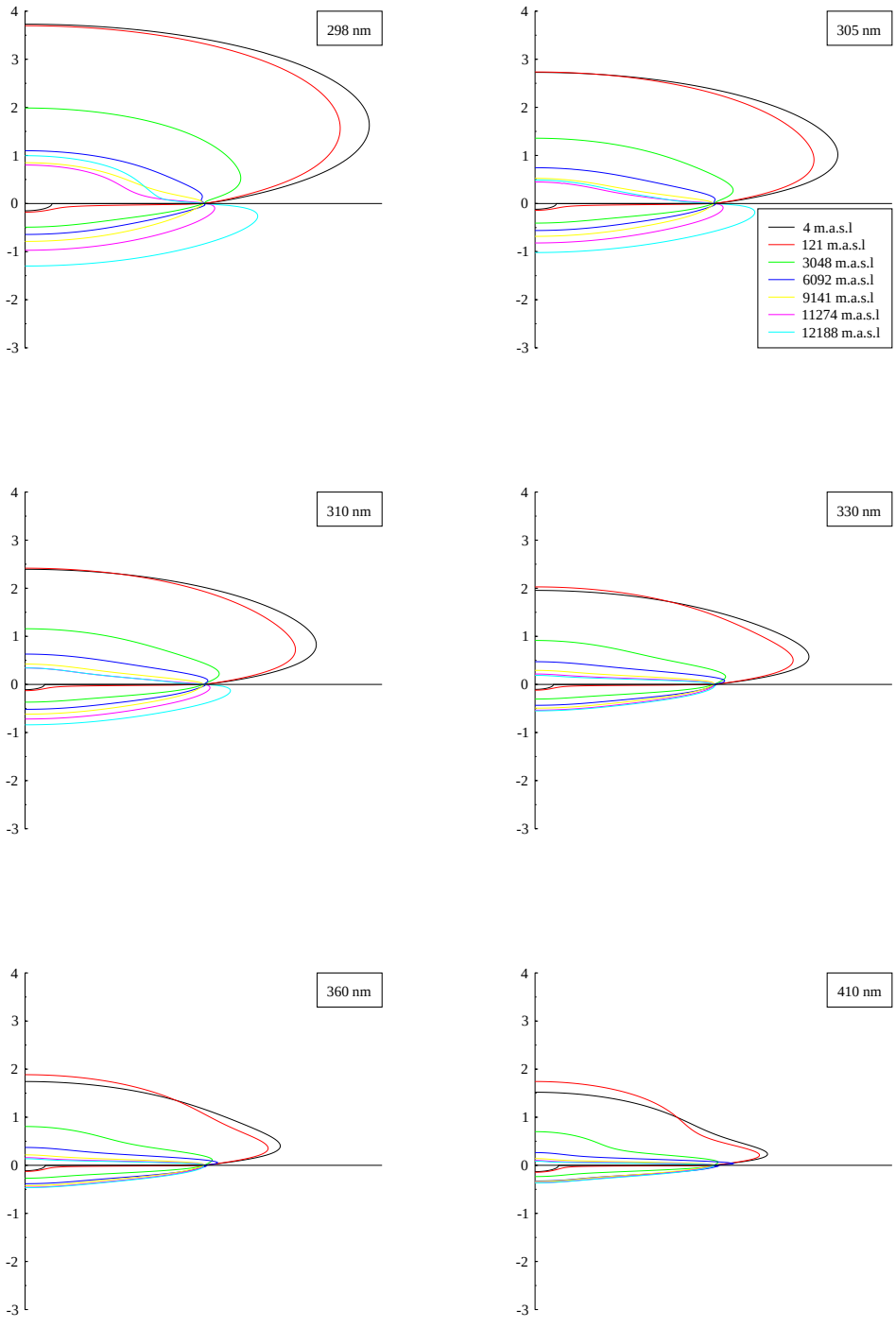
298 nm
305 nm
310 nm
330 nm
360 nm
410 nm
4 m.a.s.l
121 m.a.s.l
3048 m.a.s.l
6092 m.a.s.l
9141 m.a.s.l
11274 m.a.s.l
12188 m.a.s.l

Figure 3: .

Case	Ozone	Rayleigh	Aerosol	Comments
1	y	y	y	
2	y	y	y	Similar to case 1, but US standard atmosphere used.
3	y	y	n	
4	n	y	n	
5	y	y	n	Similar to case 3, but no ozone in the troposphere
6	n	n	n	

Table 1: Description of the different cases used for the sensitivity analysis. A 'y' ('n') indicates that the parameter was (not) included.

Case 1 is the base line calculation. Case 2 is similar to case 1 except that the U.S. standard atmosphere of (Anderson et al., 1986) was used instead of the ozone profile measured by the ozone sonde launched from the airport of Thessaloniki. These two profiles are shown in Figure 1. The U.S. standard atmosphere has relatively less ozone in the troposphere and more in the stratosphere. Furthermore it exhibits no vertical stratification in the stratosphere. Shifting ozone from the troposphere to the stratosphere gives more absorption due to ozone in the stratosphere and hence less radiation available in the upper troposphere. However, in the lower troposphere, less ozone gives more radiation due to less absorption of Rayleigh scattered photons. The effect of changing the ozone profile is obviously only seen for wavelengths where ozone absorbs appreciably (298, 305, 310 nm and UV-B in Figures 4-5)

In case 3 all aerosols have been omitted. Hence, only Rayleigh scattering and ozone absorption affect the actinic flux. The green line in Figure 5 shows that neglecting the aerosols increases the actinic flux by up to 7-8% at the surfaces. The effect decreases with increasing altitude and above the aerosol layer the effect on the actinic flux is negligible. The effect shows little variation with wavelength (note that the yellow line is on top of the green line for wavelengths 360 and 410 nm).

Case 4 is similar to case 3 but absorption by ozone is in addition neglected. Hence, only Rayleigh scattering has any effect on the actinic flux. The effect of neglecting ozone absorption is dramatic for the shorter wavelengts (298, 305 and 310 nm, Figure 4) resulting in a large increase in the actinic flux. The increase gets smaller for larger wavelengths and becomes negligible for wavelengths where ozone absorption is minimal.

In case 5 all ozone in the troposphere (0-18 km) has been removed. The total column is kept constant though. Thus effectively this is a shift of ozone from the troposphere to the stratosphere and thus shows the interaction of Rayleigh scattering and ozone absorption. Due to the magnitude of the Rayleigh scattering cross section and the altitude variation of the neutral atmosphere Rayleigh scattering is most effective in the lower part of the troposphere. Hence, the photon pathlength is longer in troposphere than in the stratosphere. Due to this increased pathlength there is for equal ozone amounts a higher likelihood that a photon is absorbed in the troposphere than in the stratosphere. The actinic flux is lower in the upper troposphere due to increased absorption by ozone in the stratosphere. However, in the lower troposphere lack of ozone and increasing Rayleigh scattering optical depth with decreasing altitude cause an increase in the actinic flux. Case 2 also resembles a shift of ozone from the troposphere to the stratosphere, but much smaller. However, the results of cases 2 (blue line Figure 5) and 5 (yellow line Figure 5) are quantitatively similar. Further information about the enhanced absorption of UV radiation due to multiple scattering is given in the paper by (Mayer et al., 1998).

Excluding ozone absorption, Rayleigh scattering and aerosol extinction, case 6 pink lines in Figures 4-5, lets the radiation travel without any interference through the atmosphere. Comparing case 4, including only Rayleigh scattering, and case 6 it is obvious that Rayleigh scattering increases the actinic flux, except for the very bottom of the atmosphere, compared with an atmosphere without any scattering properties.

References

Anderson, G., Clough, S., Kneizys, F., Chetwynd, J., and Shettle, E. (1986). AFGL atmospheric constituent profiles (0-120 km). *Tech. Rep. AFGL-TR-86-0110*, Air Force Geophys. Lab., Hanscom Air Force Base, Bedford, Mass.

Anderson, G. P., Chetwynd, J. H., Theriault, J.-M., Acharya, P. K., Berk, A., Robertson, D. C., Kneizys, F. X., Hoke, M. L., Abreu, L. W., and Shettle, E. P. (1993). MODTRAN2: Suitability for remote sensing. In Kohnle, A. and Miller, W. B., editors, *Atmospheric Propagation and Remote Sensing, SPIE Conf. Ser.,* vol. 1968, pages 514–525. Soc. of Photo–Optical–Instrum. Eng., Bellingham, Wash.

Balis, D. S., Zerefos, C. S., Lourtidis, K., Bais, A. F., Hofzumahaus, A., Kraus, A., Schmitt, R., Blumthaler, M., and Gobbi, G. P. (2001). Measurements and modeling of photolysis rates during the PAUR II campaign. *J. Geophys. Res.*, submitted.

Bass, A. M. and Paur, R. J. (1985). The ultraviolet cross–section of ozone, I, The measurements. In Zerefos, C. S. and Ghazi, A., editors, *Atmospheric Ozone: Proceedings of the Quadrennial Ozone Symposium*, pages 606–601. D. Reidel, Norwell, Mass.

Hofzumahaus, A., Kraus, A., Kylling, A., and Zerefos, C. (2001). Solar actinic radiation (280-420 nm) in the cloud-free troposphere between ground and 12 km altitude: Measurements and model results. *J. Geophys. Res.*, submitted.

Hofzumahaus, A., Kraus, A., and Müller, M. (1999). Solar actinic flux spectroradiometry: a technique for measuring photolysis frequencies in the atmosphere. *Appl. Opt.*, 38:4443–4460.

Kelley, P., Dickerson, R. R., Luke, W. T., and Kok, G. L. (1995). Rate of NO_2 photolysis from the surface to 7,6 km altitude in clear-sky and clouds. *Geophys. Res. Lett.*, 22:2621–2624.

Kylling, A., Bais, A. F., Blumthaler, M., Schreder, J., Zerefos, C. S., and Kosmidis, E. (1998). The effect of aerosols on solar UV irradiances during the Photochemical Activity and Solar Ultraviolet Radiation campaign. *J. Geophys. Res.*, 103:26,051–26,060.

Kylling, A., Stamnes, K., and Tsay, S.-C. (1995). A reliable and efficient two–stream algorithm for spherical radiative transfer: documentation of accuracy in realistic layered media . *J. of Atmospheric Chemistry*, 21:115–150.

Marenco, F., Santacesaria, V., Bais, A. F., Balis, D., di Sarra, A., Papayannis, A., and Zerefos, C. (1997). Optical properties of tropospheric aerosols determined by lidar and spectrophotometric measurements (Photochemical Activity and Solar Ultraviolet Radiation campaign). *Appl. Opt.*, 36:6875–6886.

Mayer, B., Kylling, A., Madronich, S., and Seckmeyer, G. (1998). Enhanced absorption of UV radiation due to multiple scattering in clouds: Experimental evidence and theoretical explanation. *J. Geophys. Res.*, 103:31,241–31,254.

Mayer, B., Seckmeyer, G., and Kylling, A. (1997). Systematic long–term comparison of spectral UV measurements and UVSPEC modeling results. *J. Geophys. Res.*, 102:8755–8767.

Nicolet, M. (1984). On the molecular scattering in the terrestrial atmosphere: An empirical formula for its calculation in the homosphere. *Planet. Space Sci.*, 32:1467–1468.

Stamnes, K., Tsay, S.-C., Wiscombe, W., and Jayaweera, K. (1988). Numerically stable algorithm for discrete–ordinate–method radiative transfer in multiple scattering and emitting layered media. *Appl. Opt.*, 27:2502–2509.

van Weele, M., Martin, T. J., Blumthaler, M., Brogniez, C., den Onter, P. N., Engelsen, O., Lenoble, J., Mayer, B., Pfister, G., Ruggaber, A., Walravens, B., Weihs, P., Gardiner, P. G., Gillotay, D., Haferl, D., Kylling, A., Seckmeyer, G., and Wauben, W. M. F. (2000). From model intercomparison towards benchmark UV spectra for six real atmospheric cases. *J. Geophys. Res.*, 105:4916–4925.

Volz-Thomas, A., Lerner, A., Pätz, H.-W., Schultz, M., McKenna, D. S., Schmitt, R., Madronich, S., and Röth, E. P. (1996). Airborne measurements of the photolysis frequency of NO_2. *J. Geophys. Res.*, 101:18,613–18,627.

Woods, T. N., Prinz, D. K., Rottmann, G. J., London, J., Crane, P. C., Cebula, R. P., Hilsenrath, E., Brueckner, G. E., Andrews, M. D., White, O. R., VanHoosier, M. E., Floyd, L. E., Herring, L. C., Knapp, B. G., Pankrantz, C. K., and Reiser, P. A. (1996). Validation of the UARS solar ultraviolet irradiances: Comparison with the Atlas 1 and 2 measurements. *J. Geophys. Res.*, 101:9541–9569.

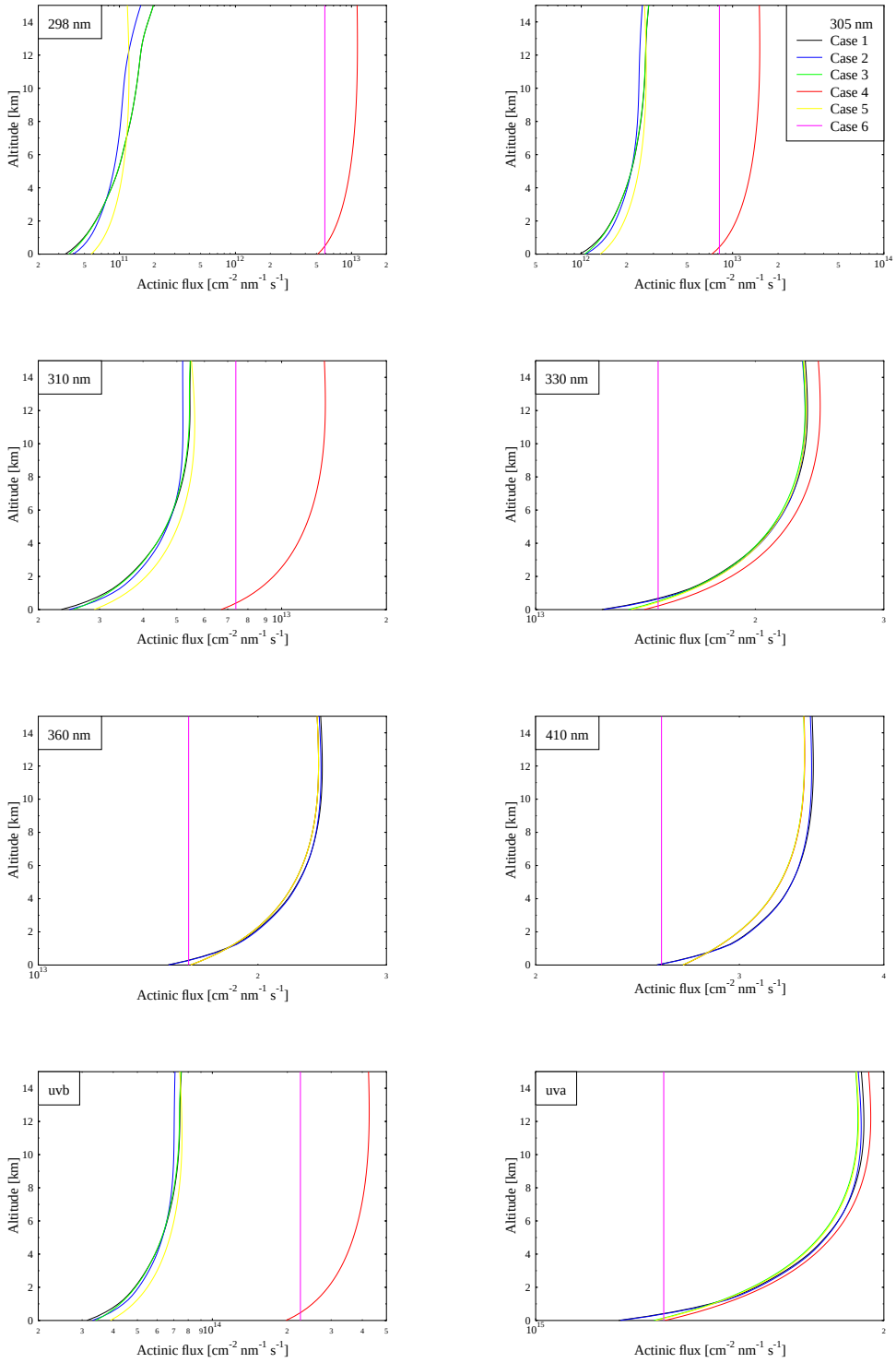

Figure 4: The total actinic flux for various wavelengths and the UV-A (315-400 nm) and UV-B (280-315 nm) doserates for various ozone, aerosol and Rayleigh scattering scenarios. See text for more information.

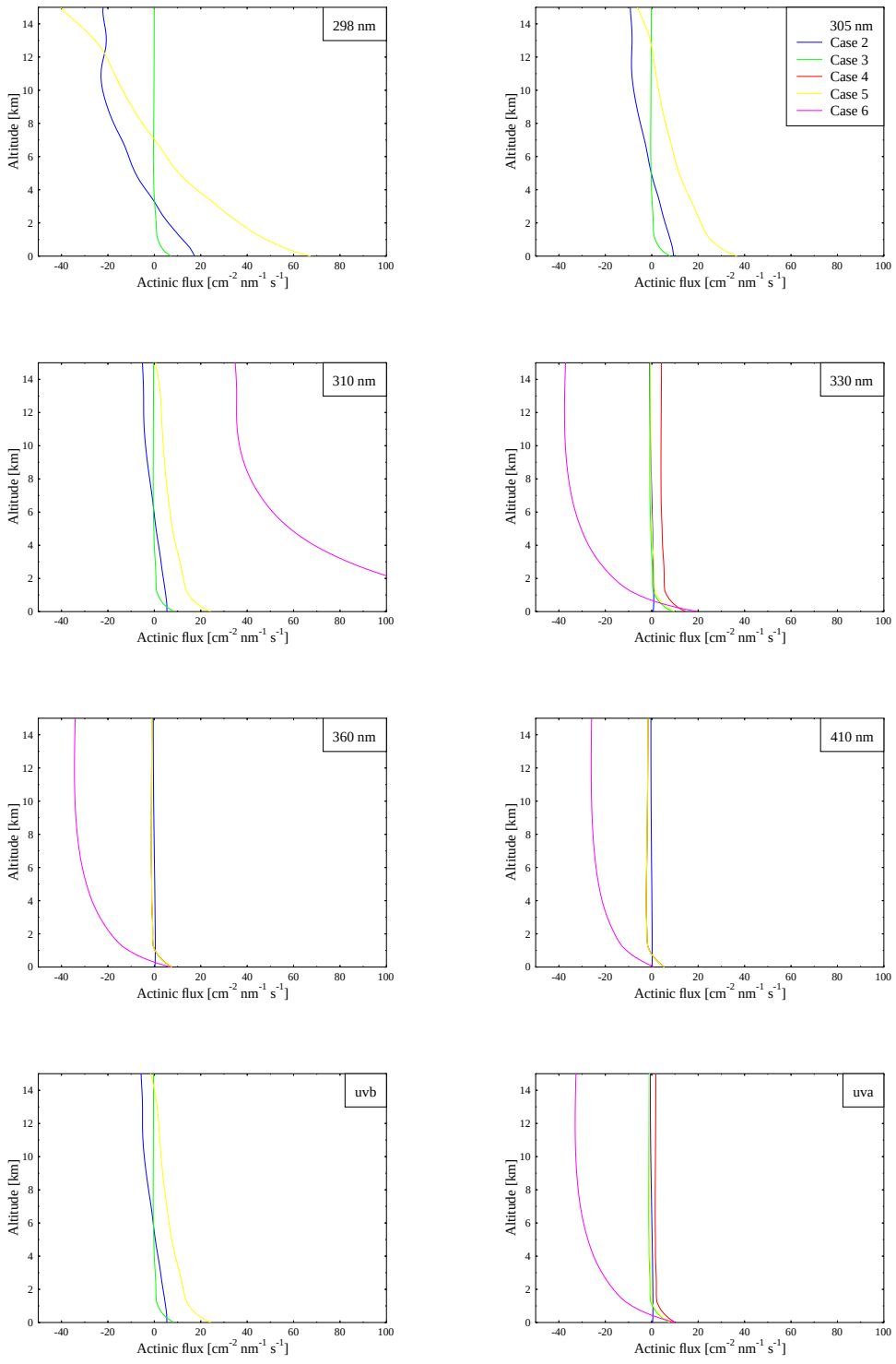

Figure 5: The absolute data for cases 2-6 in Figure 4 shown relative to case 1.

A Model input parameters

In Tables 2-5 on the following pages are listed the main input parameters used to simulate each measured spectrum. The time (column 1) gives the start and stop time for each spectrum. The corresponding solar zenith angle range and altitude range is provided in columns 2 and 3 respectively. The fourth column is the ozone column in Dobson units. Aerosol information is provided in columns 5-8 in terms of the aerosol optical depth (column 5), Ångströmβ and α coefficients (columns 6-7), and the aerosol single scattering albedo (column 8). Further information about the input parameters is provided in the data files. See the README files on the CD.

Time UTC (hh.dec)	Solar zenith angle	Altitude (m)	Ozone (DU)	τ_{355}	β	α	ω
8.9539- 8.9889	23.47-23.82	2.44- 4.27	342.60	0.275	0.070	1.320	0.900
8.9969- 9.0322	23.05-23.40	1.25- 3.35	342.60	0.275	0.070	1.320	0.900
9.7017- 9.7369	18.11-18.16	3045.68- 3051.46	342.60	0.264	0.090	1.040	0.900
9.7439- 9.7792	18.07-18.11	3045.38- 3047.19	342.60	0.264	0.090	1.040	0.900
9.7864- 9.8214	18.05-18.07	3045.67- 3047.19	342.60	0.264	0.090	1.040	0.900
9.8283- 9.8636	18.03-18.05	3046.28- 3047.80	342.60	0.264	0.090	1.040	0.900
9.9739-10.0092	17.06-17.33	112.16- 123.70	342.60	0.264	0.090	1.040	0.900
10.0164-10.0514	16.77-17.01	120.72- 124.34	342.60	0.264	0.090	1.040	0.900
10.0586-10.0936	16.49-16.72	120.39- 124.96	342.60	0.264	0.090	1.040	0.900
10.1042-10.1394	16.20-16.42	120.08- 124.35	342.60	0.264	0.090	1.040	0.900
10.2675-10.3028	16.35-16.48	6087.07- 6096.79	342.90	0.266	0.120	0.770	0.900
10.3097-10.3450	16.51-16.65	6091.34- 6095.59	342.90	0.266	0.120	0.770	0.900
10.3522-10.3875	16.68-16.83	6092.25- 6094.38	342.90	0.266	0.120	0.770	0.900
10.3944-10.4297	16.87-17.02	6091.94- 6097.43	342.90	0.266	0.120	0.770	0.900
10.5050-10.5403	16.90-16.97	6088.32- 6096.82	342.90	0.266	0.120	0.770	0.900
10.7742-10.8097	17.28-17.56	9139.44- 9142.49	344.70	0.278	0.120	0.810	0.900
10.8164-10.8517	17.60-17.88	9140.68- 9142.18	344.70	0.278	0.120	0.810	0.900
10.8586-10.8939	17.94-18.22	9140.66- 9141.87	344.70	0.278	0.120	0.810	0.900
10.9008-10.9364	18.28-18.56	9140.05- 9141.57	344.70	0.278	0.120	0.810	0.900
11.0594-11.0950	19.00-19.14	11274.42-11276.56	344.70	0.278	0.120	0.810	0.900
11.1033-11.1386	19.16-19.32	11273.52-11275.64	344.70	0.278	0.120	0.810	0.900
11.1458-11.1814	19.36-19.55	11272.92-11275.03	344.70	0.278	0.120	0.810	0.900
11.2889-11.3244	20.39-20.71	11272.29-11275.61	344.70	0.283	0.140	0.680	0.900
11.3353-11.3706	20.81-21.13	11273.51-11275.34	344.70	0.283	0.140	0.680	0.900
11.5092-11.5447	22.21-22.49	12188.48-12195.45	344.70	0.283	0.140	0.680	0.900
11.5519-11.5872	22.55-22.84	12188.15-12189.68	344.70	0.283	0.140	0.680	0.900
11.5942-11.6294	22.91-23.21	12187.85-12189.07	344.70	0.283	0.140	0.680	0.900
11.6369-11.6722	23.28-23.62	12187.85-12189.37	344.70	0.283	0.140	0.680	0.900
11.7697-11.8050	24.45-24.75	12187.67-12190.57	344.70	0.264	0.120	0.760	0.900

Table 2: Input data used for the 29 spectra recorded on day 162, 10 6 1996.

Time UTC (hh.dec)	Solar zenith angle	Altitude (m)	Ozone (DU)	τ_{355}	β	α	ω
11.7786-11.8139	22.96-23.31	0.00- 0.00	337.20	0.135	0.100	0.290	0.900
11.8247-11.8597	23.42-23.77	0.00- 0.00	337.20	0.135	0.100	0.290	0.900
11.8672-11.9025	23.84-24.20	0.00- 0.00	337.20	0.135	0.100	0.290	0.900
11.9097-11.9450	24.27-24.63	0.00- 0.00	337.20	0.135	0.100	0.290	0.900
12.6347-12.6700	32.15-32.74	6294.00- 6997.94	336.10	0.135	0.110	0.200	0.900
12.6811-12.7164	32.95-33.56	6993.00- 7002.00	337.80	0.116	0.040	1.030	0.900
12.8097-12.8453	34.96-35.47	4365.71- 5186.00	337.80	0.116	0.040	1.030	0.900
12.9542-12.9894	36.94-37.26	3035.00- 3038.97	337.80	0.116	0.040	1.030	0.900
13.0003-13.0358	37.36-37.67	3034.00- 3037.00	337.80	0.116	0.040	1.030	0.900
13.0428-13.0783	37.74-38.06	3033.82- 3036.00	337.80	0.116	0.040	1.030	0.900
13.1128-13.1481	38.50-38.97	3035.60- 3040.00	337.80	0.116	0.040	1.030	0.900
13.1553-13.1906	39.06-39.53	3035.00- 3037.00	337.80	0.116	0.040	1.030	0.900
13.2792-13.3144	40.61-40.95	141.00- 159.00	337.80	0.145	0.110	0.270	0.900
13.3231-13.3583	41.03-41.37	138.00- 142.98	337.80	0.145	0.110	0.270	0.900
13.3661-13.4014	41.43-41.77	137.12- 140.00	337.80	0.145	0.110	0.270	0.900
13.4089-13.4442	41.85-42.19	137.00- 142.00	337.80	0.145	0.110	0.270	0.900
13.4517-13.4869	42.26-42.60	137.00- 140.00	337.80	0.145	0.110	0.270	0.900
13.5983-13.6339	44.08-44.60	6067.14- 6081.00	337.80	0.145	0.110	0.270	0.900
13.6908-13.7261	45.29-45.58	6078.00- 6081.00	337.80	0.150	0.100	0.390	0.900
13.7903-13.8256	46.12-46.41	6078.00- 6081.00	337.80	0.150	0.100	0.390	0.900
13.8650-13.9003	46.94-47.43	6077.00- 6082.00	337.80	0.150	0.100	0.390	0.900
14.0325-14.0678	49.37-49.90	9120.21- 9131.92	337.80	0.150	0.100	0.390	0.900
14.1186-14.1542	50.59-50.86	9124.00- 9129.96	337.80	0.150	0.100	0.390	0.900
14.1611-14.1961	50.91-51.16	9129.00- 9130.00	337.80	0.150	0.100	0.390	0.900
14.2031-14.2386	51.22-51.48	9128.00- 9131.00	338.80	0.153	0.110	0.320	0.900
14.2456-14.2811	51.52-51.78	9129.00- 9131.00	338.80	0.153	0.110	0.320	0.900
14.4125-14.4478	53.41-53.96	11255.00-11261.00	338.80	0.153	0.110	0.320	0.900
14.4567-14.4919	54.11-54.66	11260.00-11263.00	338.80	0.153	0.110	0.320	0.900
14.4989-14.5344	54.77-55.33	11260.00-11262.99	338.80	0.153	0.110	0.320	0.900
14.6347-14.6703	56.26-56.50	11256.00-11259.93	338.80	0.153	0.110	0.320	0.900
14.7094-14.7450	56.77-57.04	12156.00-12175.97	340.40	0.155	0.150	0.030	0.900
14.8233-14.8586	58.10-58.65	12168.00-12173.92	340.40	0.155	0.150	0.030	0.900
14.8661-14.9014	58.77-59.32	12171.00-12174.00	340.40	0.155	0.150	0.030	0.900
14.9086-14.9439	59.43-59.99	12172.00-12174.95	340.40	0.155	0.150	0.030	0.900

Table 3: Input data used for the 34 spectra recorded on day 163, 11 6 1996.

Time UTC (hh.dec)	Solar zenith angle	Altitude (m)	Ozone (DU)	τ_{355}	β	α	ω
8.8656- 8.9008	24.33-24.69	24.06- 26.41	330.60	0.607	0.220	0.980	0.900
8.9083- 8.9433	23.90-24.25	24.61- 27.92	330.60	0.607	0.220	0.980	0.900
8.9506- 8.9858	23.47-23.82	24.74- 26.06	330.60	0.607	0.220	0.980	0.900
9.5208- 9.5561	18.94-19.03	3025.34- 3038.45	330.40	0.601	0.170	1.220	0.900
9.5647- 9.6000	18.85-18.92	3034.30- 3036.52	330.40	0.601	0.170	1.220	0.900
9.6136- 9.6489	18.77-18.83	3033.57- 3035.64	330.40	0.601	0.170	1.220	0.900
9.6569- 9.6919	18.71-18.75	3033.76- 3035.03	330.40	0.601	0.170	1.220	0.900
9.6992- 9.7342	18.66-18.70	3033.44- 3034.60	331.70	0.574	0.180	1.120	0.900
9.7961- 9.8314	18.01-18.36	3035.31- 3039.54	331.70	0.574	0.180	1.120	0.900
9.8381- 9.8733	17.63-17.95	3034.44- 3035.96	331.70	0.574	0.180	1.120	0.900
9.9647- 9.9997	16.59-16.85	135.06- 143.17	331.70	0.574	0.180	1.120	0.900
10.0069-10.0422	16.29-16.54	134.20- 137.89	331.70	0.574	0.180	1.120	0.900
10.0978-10.1331	16.07-16.13	135.25- 139.61	331.70	0.574	0.180	1.120	0.900
10.1400-10.1756	16.14-16.21	132.51- 137.74	331.70	0.574	0.180	1.120	0.900
10.2928-10.3283	16.54-16.68	6073.94- 6079.21	333.20	0.653	0.310	0.720	0.900
10.3814-10.4169	16.57-16.72	6072.70- 6079.26	333.20	0.653	0.310	0.720	0.900
10.4236-10.4592	16.42-16.54	6076.86- 6079.39	333.20	0.653	0.310	0.720	0.900
10.4661-10.5017	16.30-16.40	6077.87- 6080.01	333.20	0.653	0.310	0.720	0.900
10.5128-10.5483	16.21-16.28	6078.04- 6080.05	333.20	0.653	0.310	0.720	0.900
10.6797-10.7150	16.60-16.84	9171.24- 9179.00	334.60	0.674	0.310	0.750	0.900
10.7231-10.7583	16.90-17.15	9174.80- 9176.90	334.60	0.674	0.310	0.750	0.900
10.8256-10.8611	17.52-17.57	9159.29- 9163.24	334.60	0.674	0.310	0.750	0.900
10.8692-10.9044	17.57-17.64	9158.43- 9160.97	334.60	0.674	0.310	0.750	0.900
10.9114-10.9467	17.66-17.75	9158.04- 9160.20	334.60	0.674	0.310	0.750	0.900
11.0681-11.1036	18.44-18.74	10949.24-10955.52	334.60	0.674	0.310	0.750	0.900
11.1106-11.1458	18.80-19.11	10952.59-10955.59	334.60	0.674	0.310	0.750	0.900
11.1536-11.1889	19.17-19.48	10951.66-10954.67	334.60	0.674	0.310	0.750	0.900
11.2483-11.2836	19.88-20.04	10952.36-10957.12	333.10	0.642	0.250	0.910	0.900
11.3328-11.3683	20.37-20.64	12169.76-12178.16	333.10	0.642	0.250	0.910	0.900
11.4722-11.5075	21.54-21.85	12164.45-12169.96	333.10	0.642	0.250	0.910	0.900
11.5156-11.5508	21.92-22.22	12167.13-12170.76	333.10	0.642	0.250	0.910	0.900
11.5597-11.5950	22.29-22.60	12167.26-12169.96	333.10	0.642	0.250	0.910	0.900

Table 4: Input data used for the 32 spectra recorded on day 165, 13 6 1996.

Time UTC (hh.dec)	Solar zenith angle	Altitude (m)	Ozone (DU)	τ_{355}	β	α	ω
8.1236- 8.1589	32.59-60.78	0.00- 27.00	0.00	0.000	0.000	0.000	1.000
8.1656- 8.2008	31.91-32.30	27.00- 27.00	0.00	0.000	0.000	0.000	1.000
8.2150- 8.2503	31.34-31.75	27.00- 27.00	0.00	0.000	0.000	0.000	1.000
8.3914- 8.4269	29.43-29.80	323.20- 391.41	340.90	0.787	0.340	0.810	1.000
8.4339- 8.4692	28.94-29.35	418.00- 2243.03	340.90	0.787	0.340	0.810	1.000
8.4992- 8.5344	28.16-28.58	3031.00- 3036.92	340.90	0.787	0.340	0.810	1.000
8.5414- 8.5767	27.68-28.08	3034.07- 3039.00	340.90	0.787	0.340	0.810	1.000
8.5839- 8.6192	27.20-27.60	3037.00- 3039.00	340.90	0.787	0.340	0.810	1.000
8.6261- 8.6617	26.73-27.13	3038.00- 3039.00	340.90	0.787	0.340	0.810	1.000
8.7253- 8.7606	25.80-26.16	3037.02- 3039.00	340.90	0.787	0.340	0.810	1.000
8.8639- 8.8992	24.34-24.72	3030.09- 3878.93	340.90	0.787	0.340	0.810	1.000
9.0047- 9.0400	22.88-23.20	6075.00- 6084.96	340.90	0.787	0.340	0.810	1.000
9.0478- 9.0833	22.53-22.82	6080.00- 6082.00	340.90	0.787	0.340	0.810	1.000
9.1611- 9.1967	21.53-21.89	6080.10- 6084.00	340.90	0.787	0.340	0.810	1.000
9.2033- 9.2389	21.09-21.45	6081.00- 6084.00	340.90	0.787	0.340	0.810	1.000
9.2456- 9.2811	20.66-21.02	6082.00- 6084.00	340.90	0.787	0.340	0.810	1.000
9.3981- 9.4336	19.40-19.58	9124.00- 9131.00	341.30	0.884	0.390	0.790	1.000
9.4406- 9.4761	19.20-19.36	9127.00- 9132.00	341.30	0.884	0.390	0.790	1.000
9.5306- 9.5656	18.59-18.93	9131.00- 9133.00	341.30	0.884	0.390	0.790	1.000
9.5725- 9.6081	18.17-18.52	9127.07- 9132.00	341.30	0.884	0.390	0.790	1.000
9.8153- 9.8506	16.76-16.78	12177.00-12183.00	338.30	0.833	0.360	0.810	1.000
9.8575- 9.8928	16.76-16.78	12175.05-12178.93	338.30	0.833	0.360	0.810	1.000
9.9456- 9.9811	16.32-16.65	12174.00-12176.00	339.40	0.865	0.370	0.820	1.000
9.9881-10.0233	15.92-16.25	12173.00-12177.96	339.40	0.865	0.370	0.820	1.000

Table 5: Input data used for the 24 spectra recorded on day 166, 14 6 1996.

B Actinic flux ratio profiles

The change of the downwelling and upwelling actinic flux relative to the values at the lowest flight level are presented in Figures 6-9 for all flight days. Both measured and simulated profiles are shown for various wavelengths and integrated UV-B and UV-A. The ratio of the downwelling to the upwelling actinic flux is shown as well.

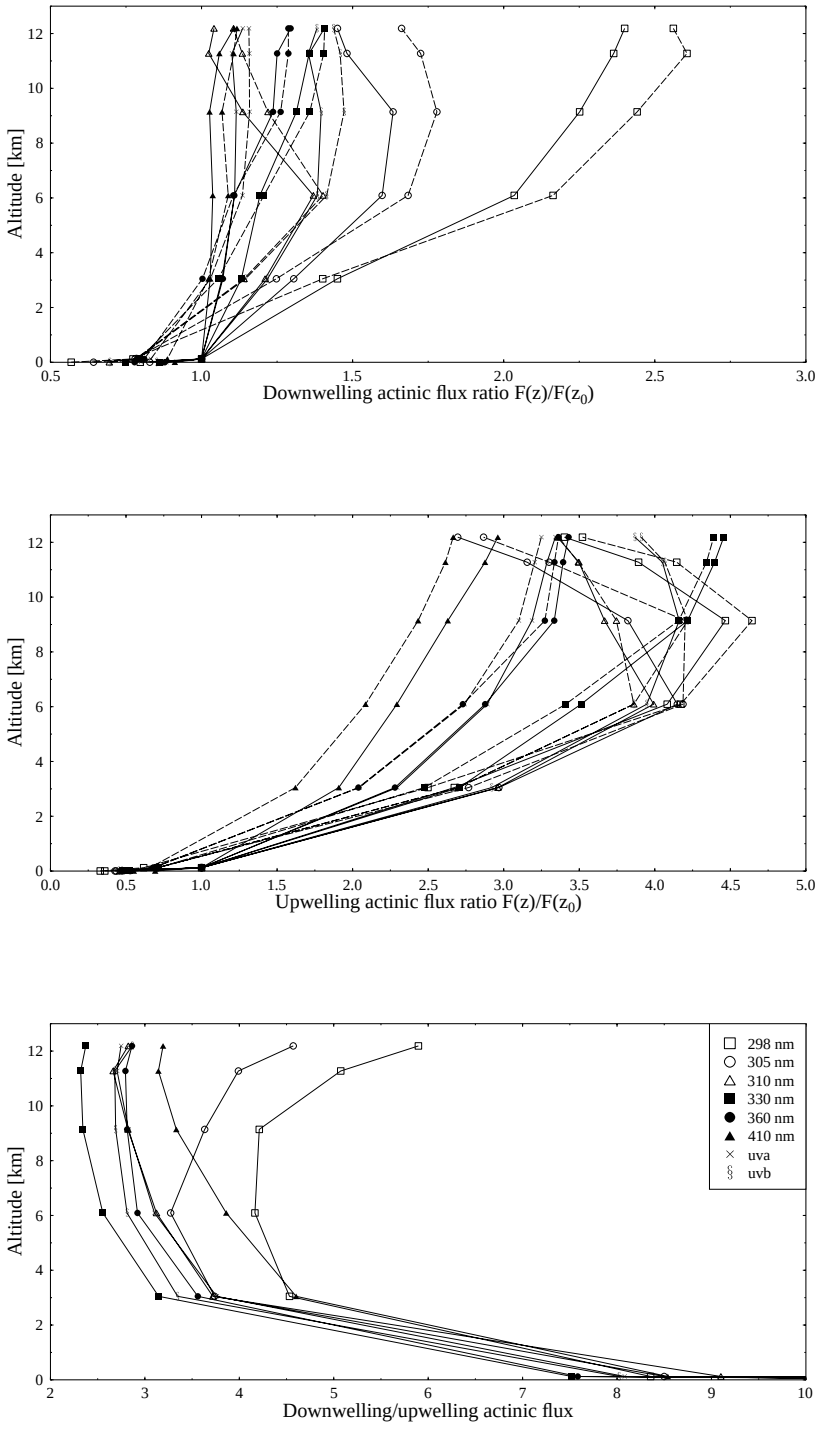

Figure 6: The measured (solid lines) and modelled (dashed) lines up– and downwelling actinic fluxes normalized to their value at the second lowest flight level. In the bottom panel is shown the ratio of the measured downwelling to the upwelling flux. Data from 10 June 1996.

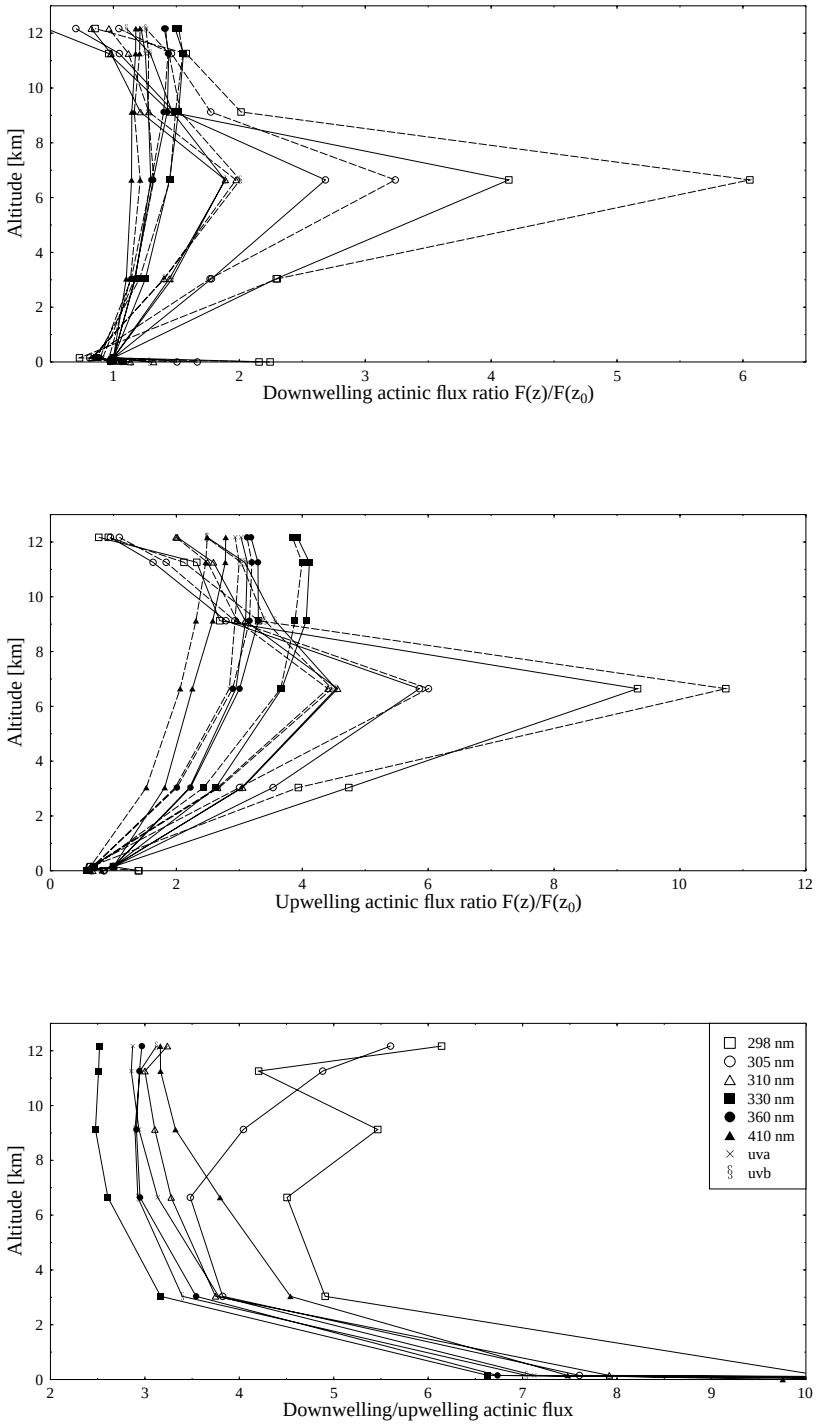

Figure 7: Same as Figure 6, but for 11 June 1996.

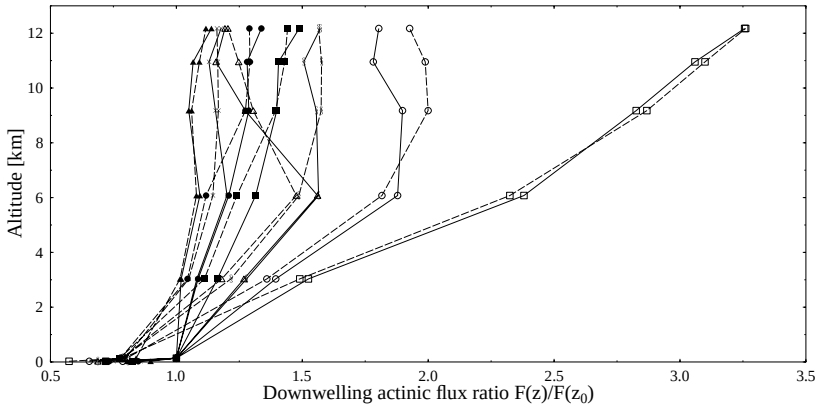

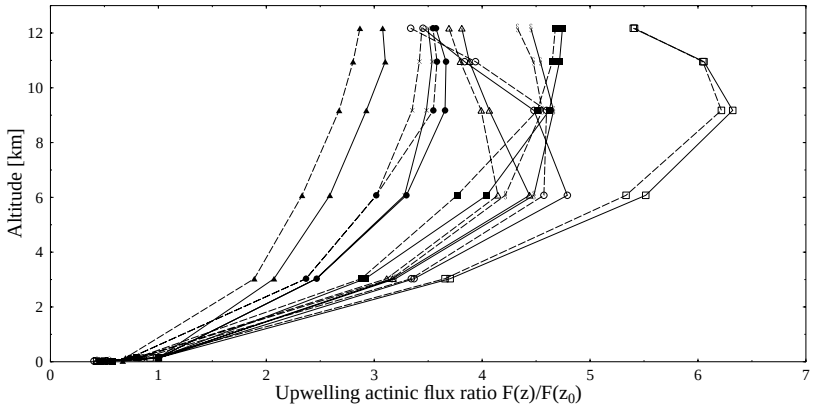

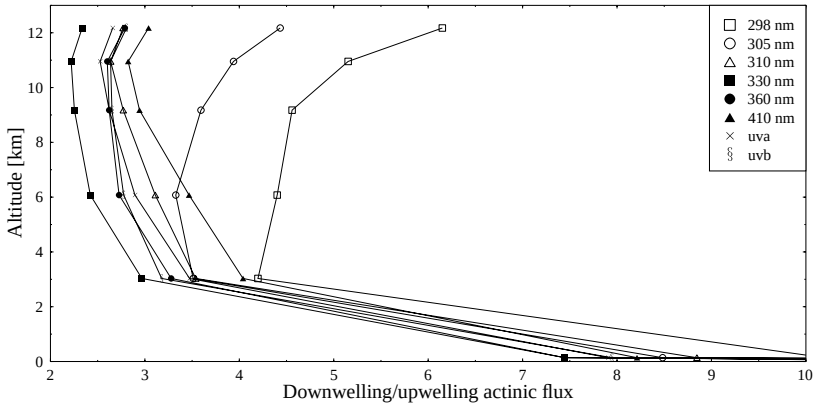

Figure 8: Same as Figure 6, but for 13 June 1996.

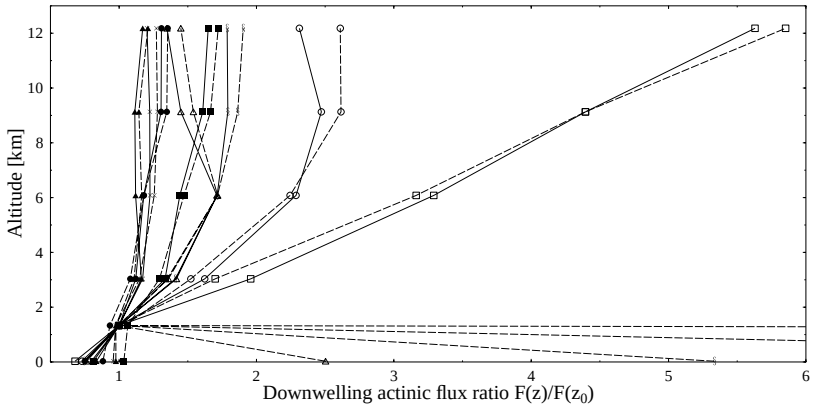

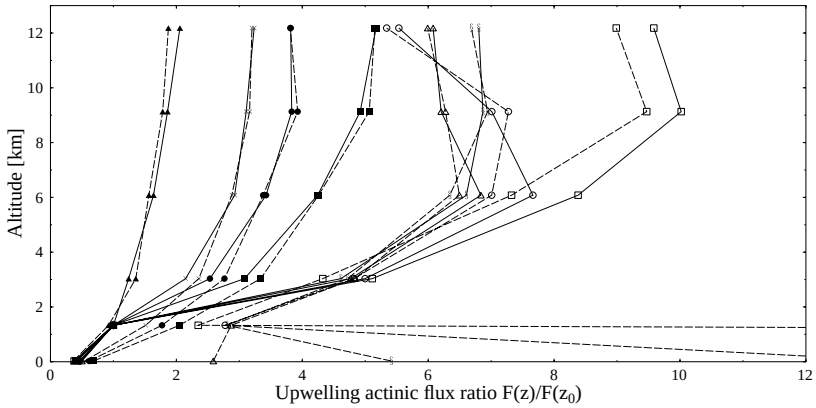

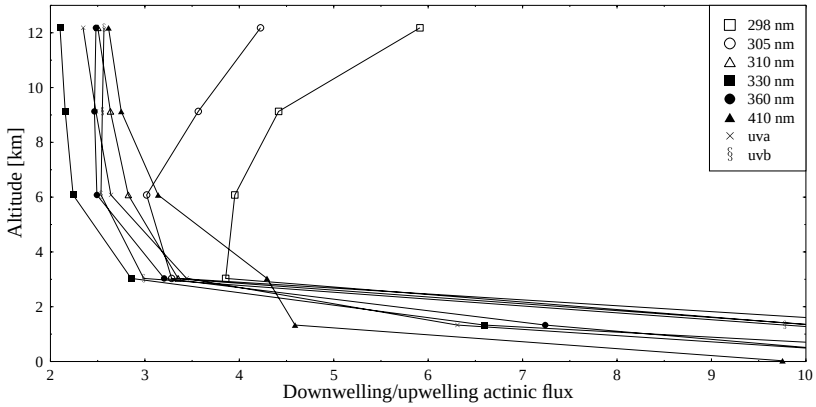

Figure 9: Same as Figure 6, but for 14 June 1996.

C ATOP96 simulation results

Each measured upwelling and downwelling actinic flux spectra has been simulated. On the following pages are shown plots of the measured and simulated spectra and ratios between them. The plot on each page corresponds to a set of simultaneously measured upwelling and downwelling spectra in addition to the total actinic flux formed by adding the two. The upper left panel shows the measured (black line) and simulated (red line) spectra. In addition the ratio of the upwelling to the total actinic flux is shown both as derived from the measurements (blue line) and from the model simulations (green line). Some of the main characteristics of the atmospheric conditions during the flight are given in the box. The middle left panel is similar to the upper left panel, but shows the downwelling actinic flux. The lower left panel shows the total measured (black line) and simulated (red line) actinic flux spectra. In addition the simulated direct to total actinic flux ratio is shown in green.

In the right column is shown various ratios of the measured and simulated spectra. The upper right panel shows the ratio of the simulated to the measured upwelling actinic flux (red line). Also shown is the ratio of the simulated actinic flux using the instrument angular response to the ideal (isotropic response) simulated actinic flux (black line). The middle and lower right panels are similar to the upper right panel, but for the downwelling and total actinic fluxes respectively.

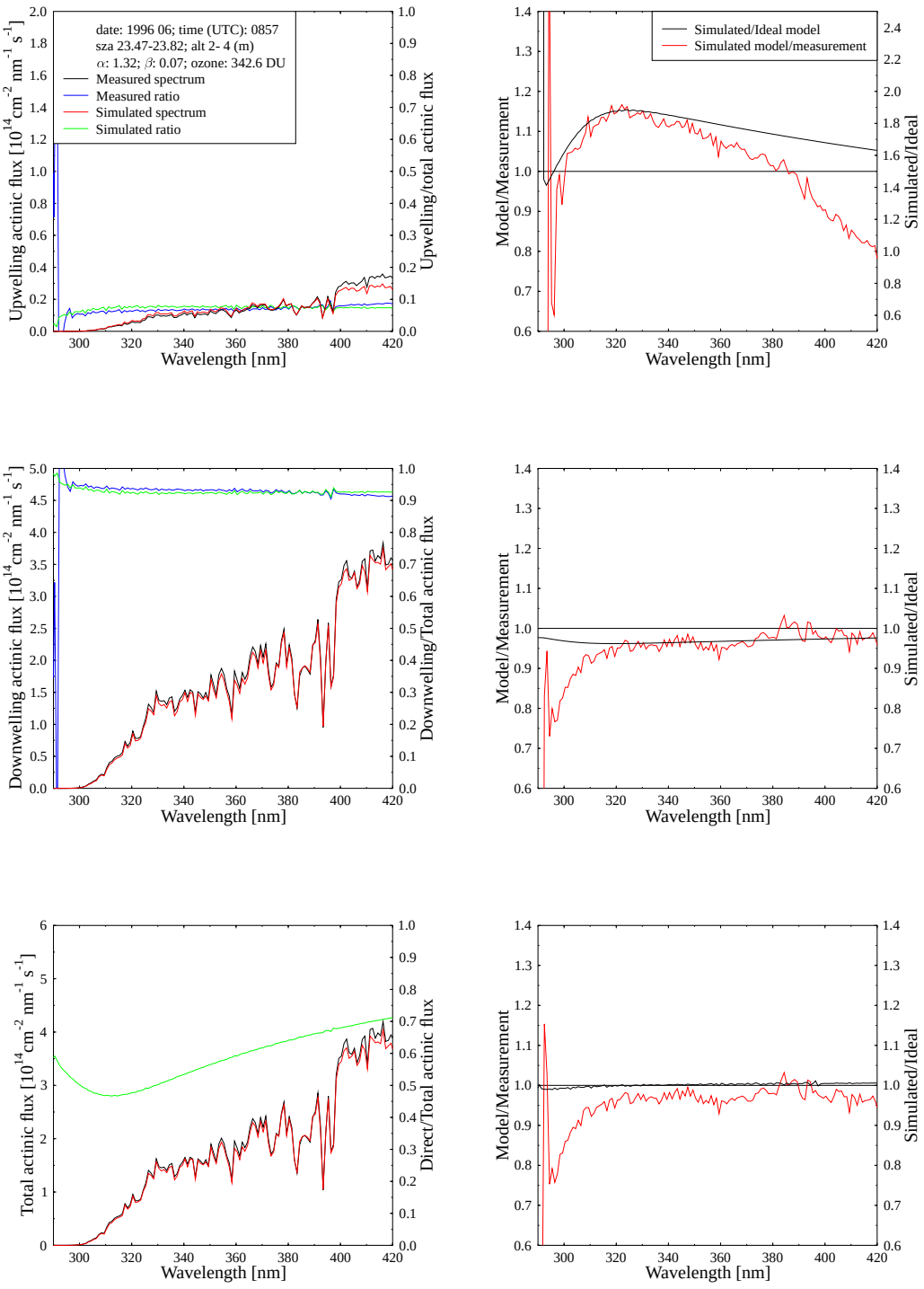

Figure 10: The measured and simulated upwelling, downwelling and simulated actinic flux spectra and various ratios of them. Spectra measured 0857 UTC on 10 June 1996 at an altitude of 2.44 m.a.s.l.

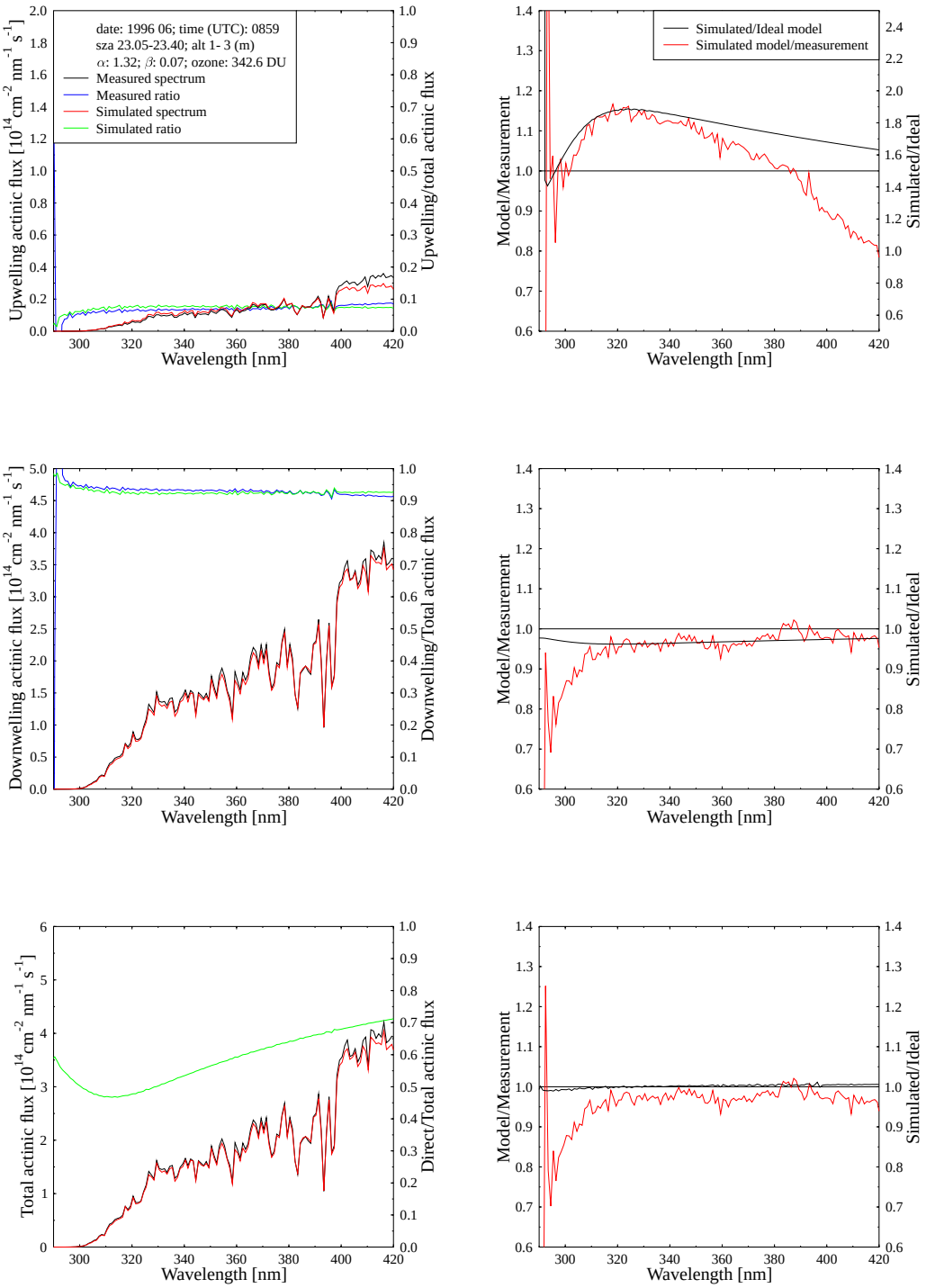

Figure 11: Same as Figure 10, except for 0859 UTC, 10 June 1996, and altitude 3.35 m.a.s.l.

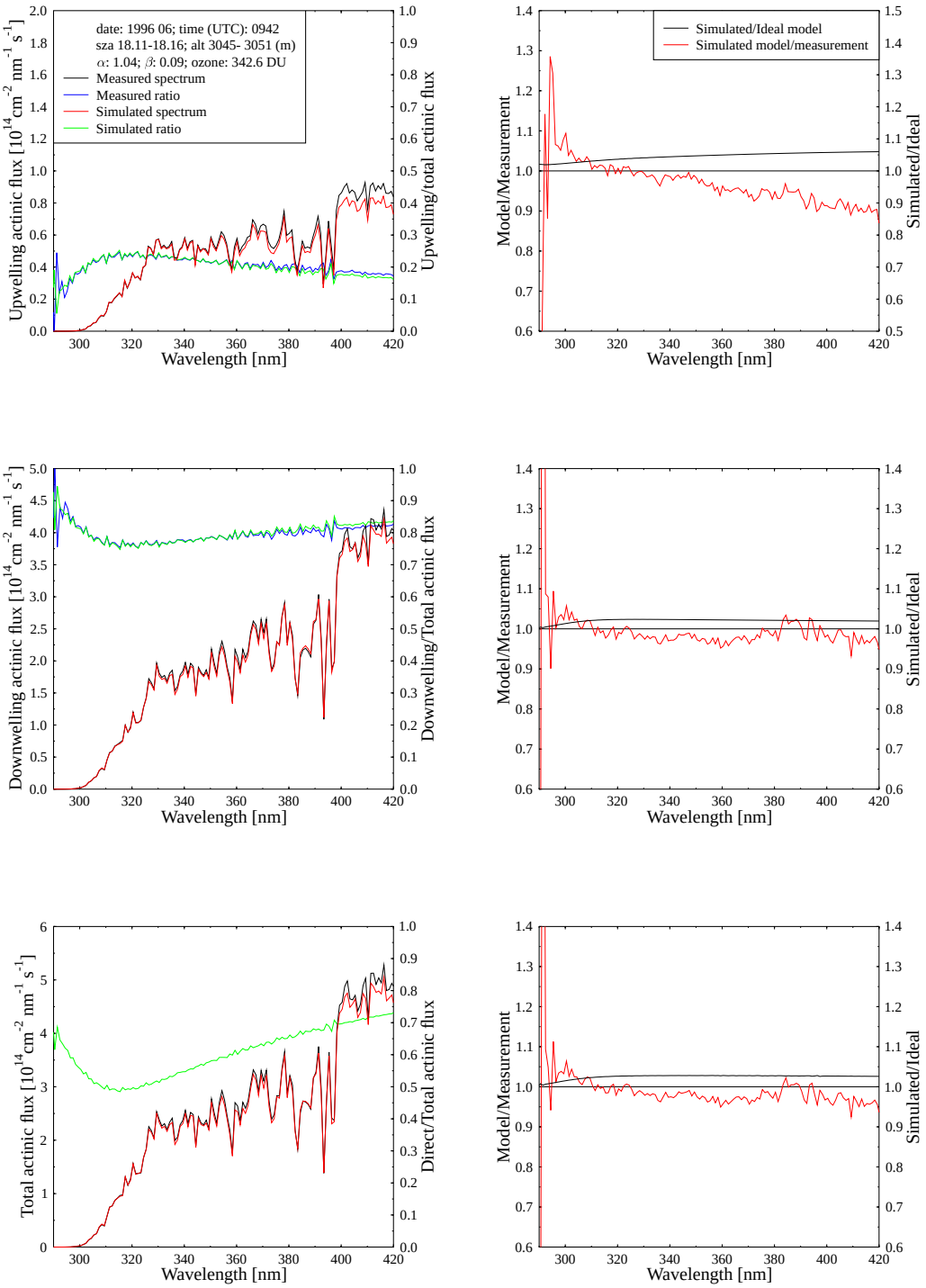

Figure 12: Same as Figure 10, except for 0942 UTC, 10 June 1996, and altitude 3050.66 m.a.s.l.

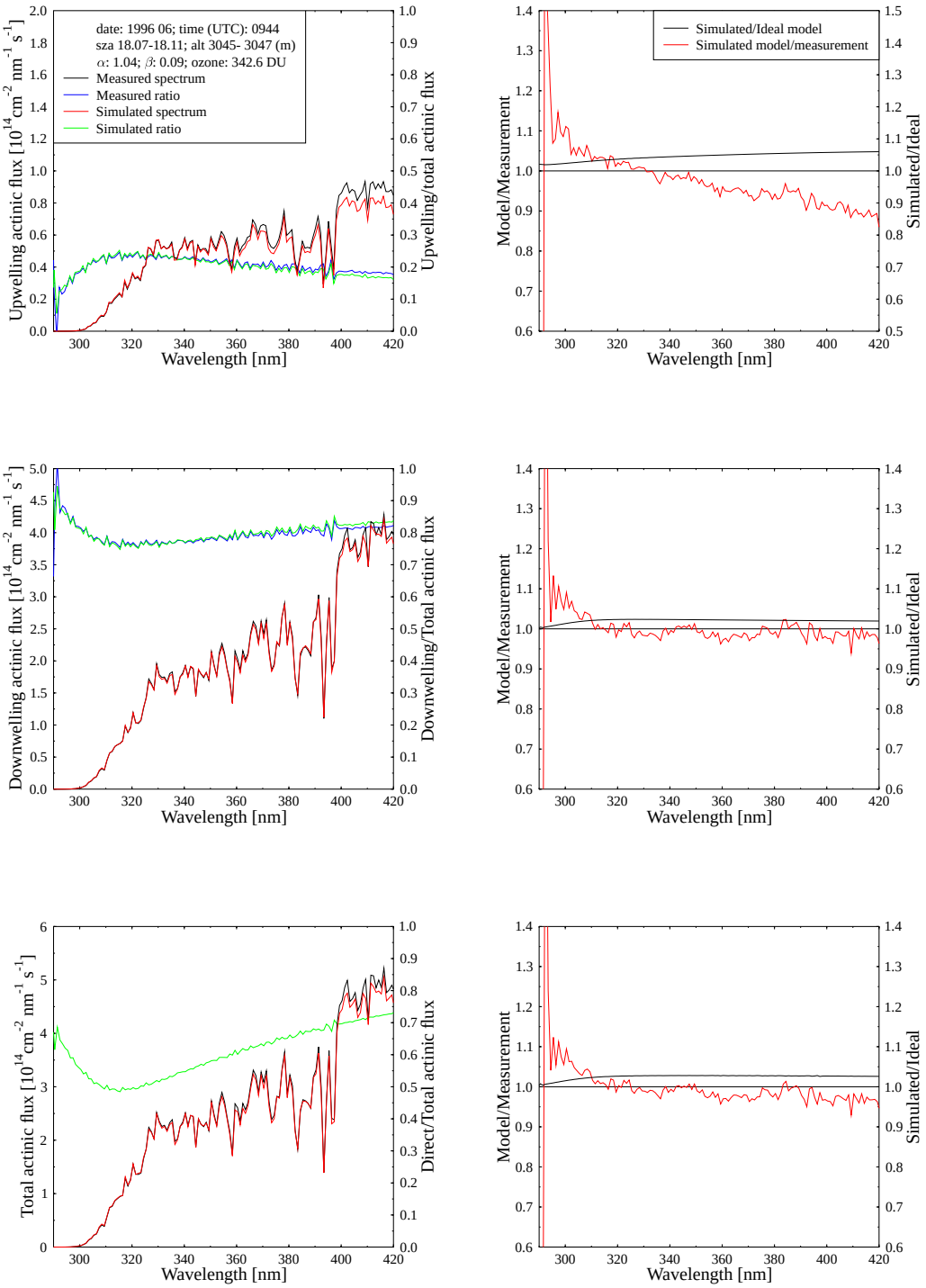

Figure 13: Same as Figure 10, except for 0944 UTC, 10 June 1996, and altitude 3045.97 m.a.s.l.

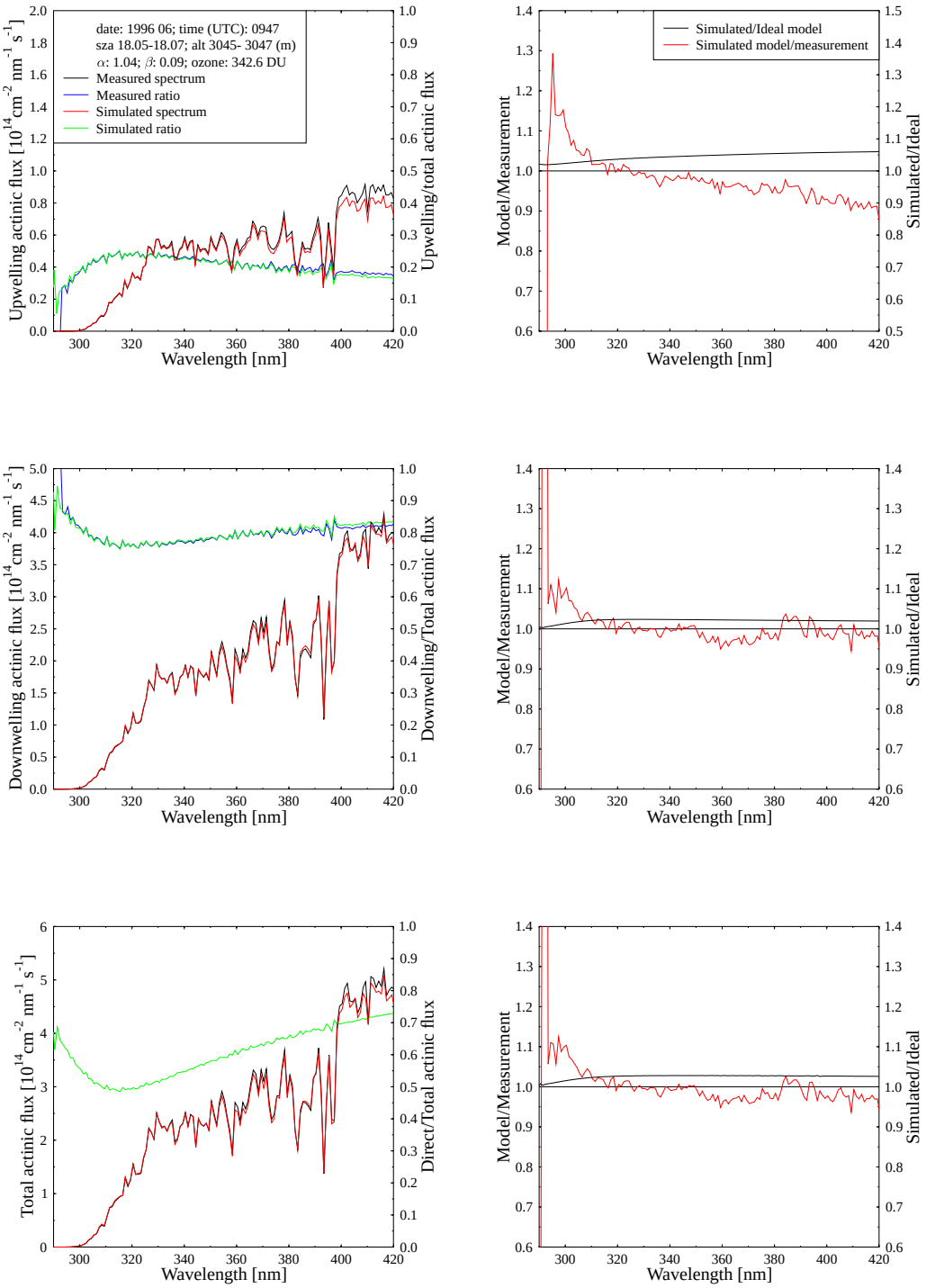

Figure 14: Same as Figure 10, except for 0947 UTC, 10 June 1996, and altitude 3047.19 m.a.s.l.

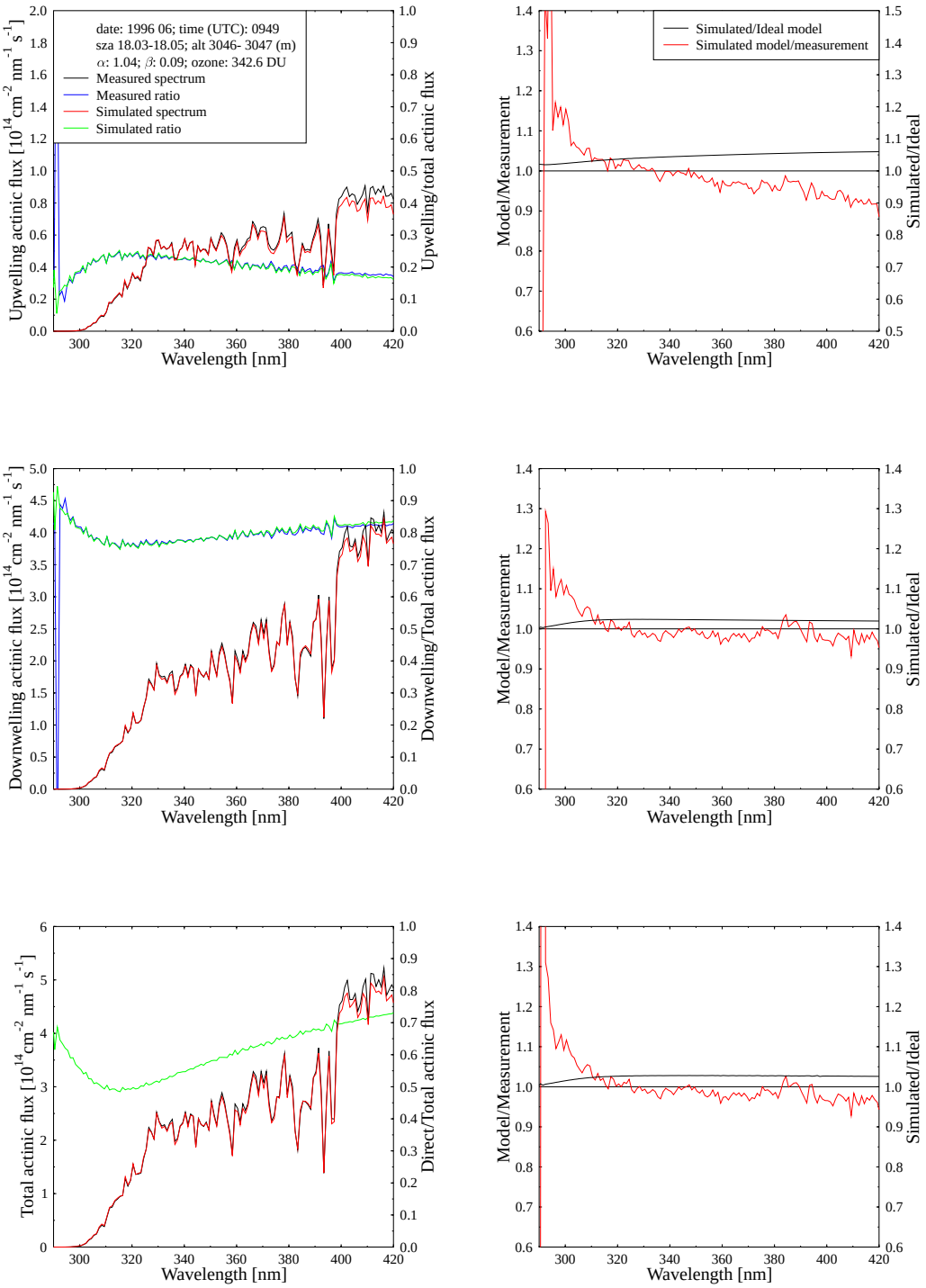

Figure 15: Same as Figure 10, except for 0949 UTC, 10 June 1996, and altitude 3046.89 m.a.s.l.

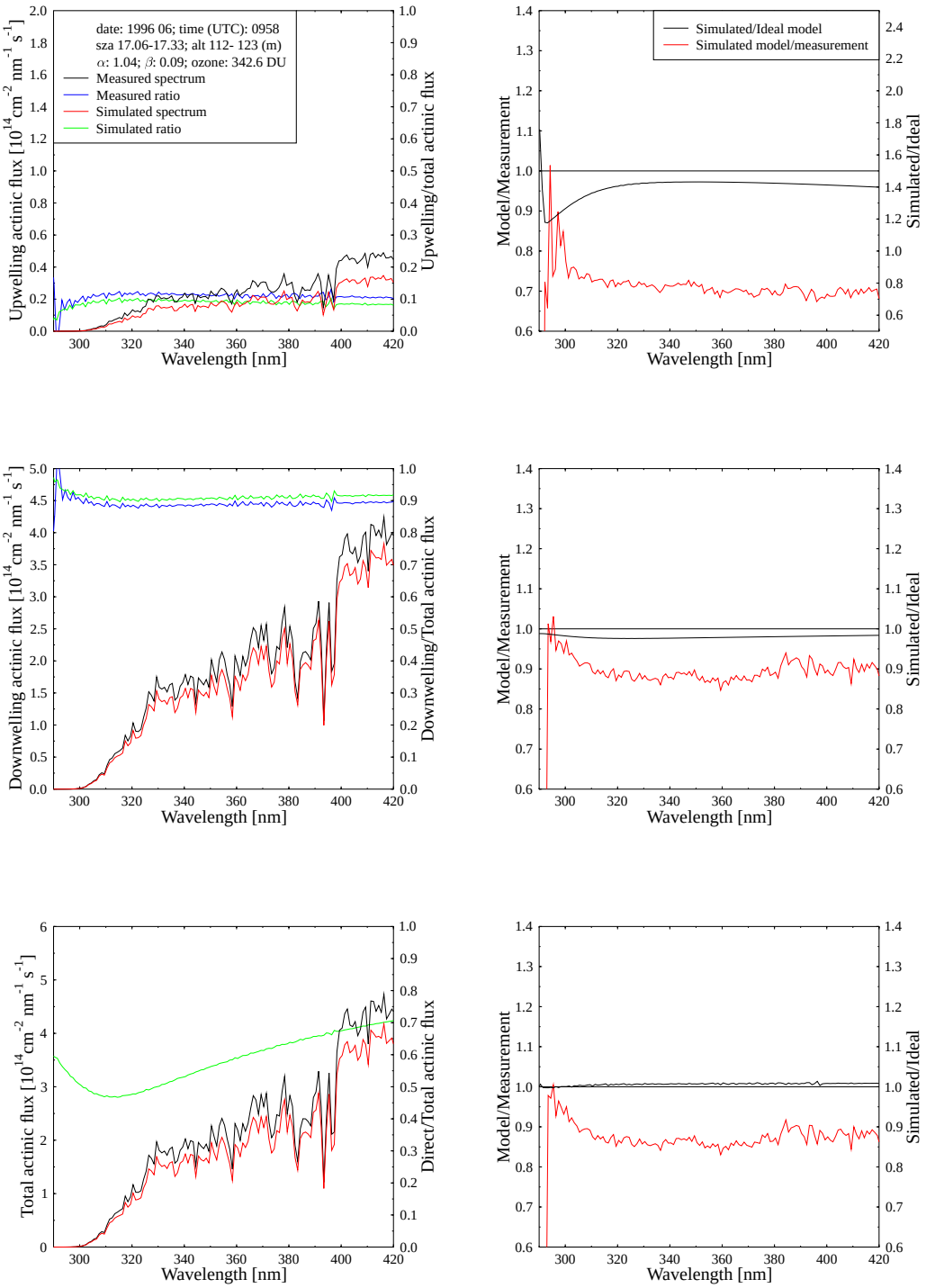

Figure 16: Same as Figure 10, except for 0958 UTC, 10 June 1996, and altitude 112.16 m.a.s.l.

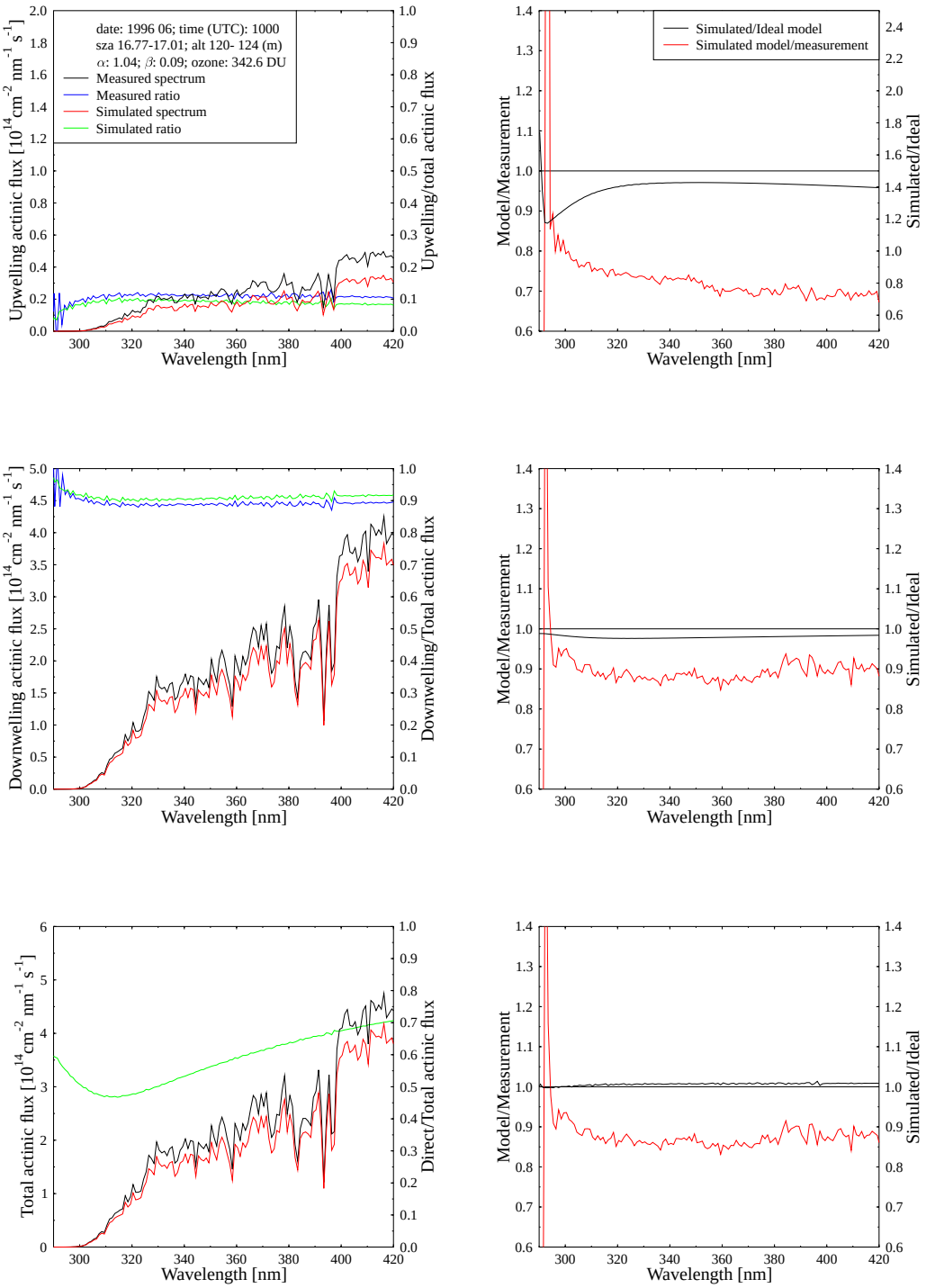

Figure 17: Same as Figure 10, except for 1000 UTC, 10 June 1996, and altitude 123.13 m.a.s.l.

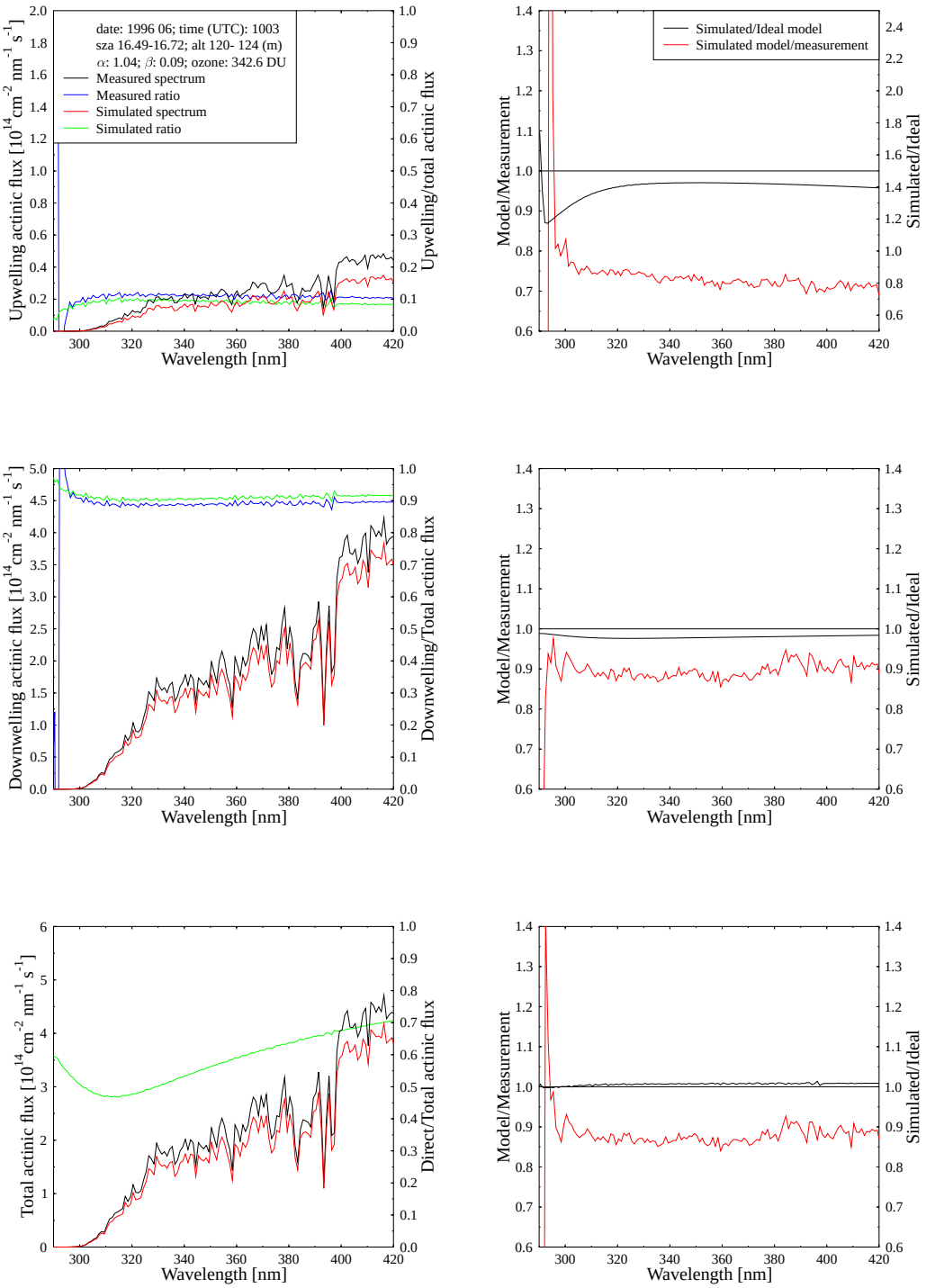

Figure 18: Same as Figure 10, except for 1003 UTC, 10 June 1996, and altitude 122.52 m.a.s.l.

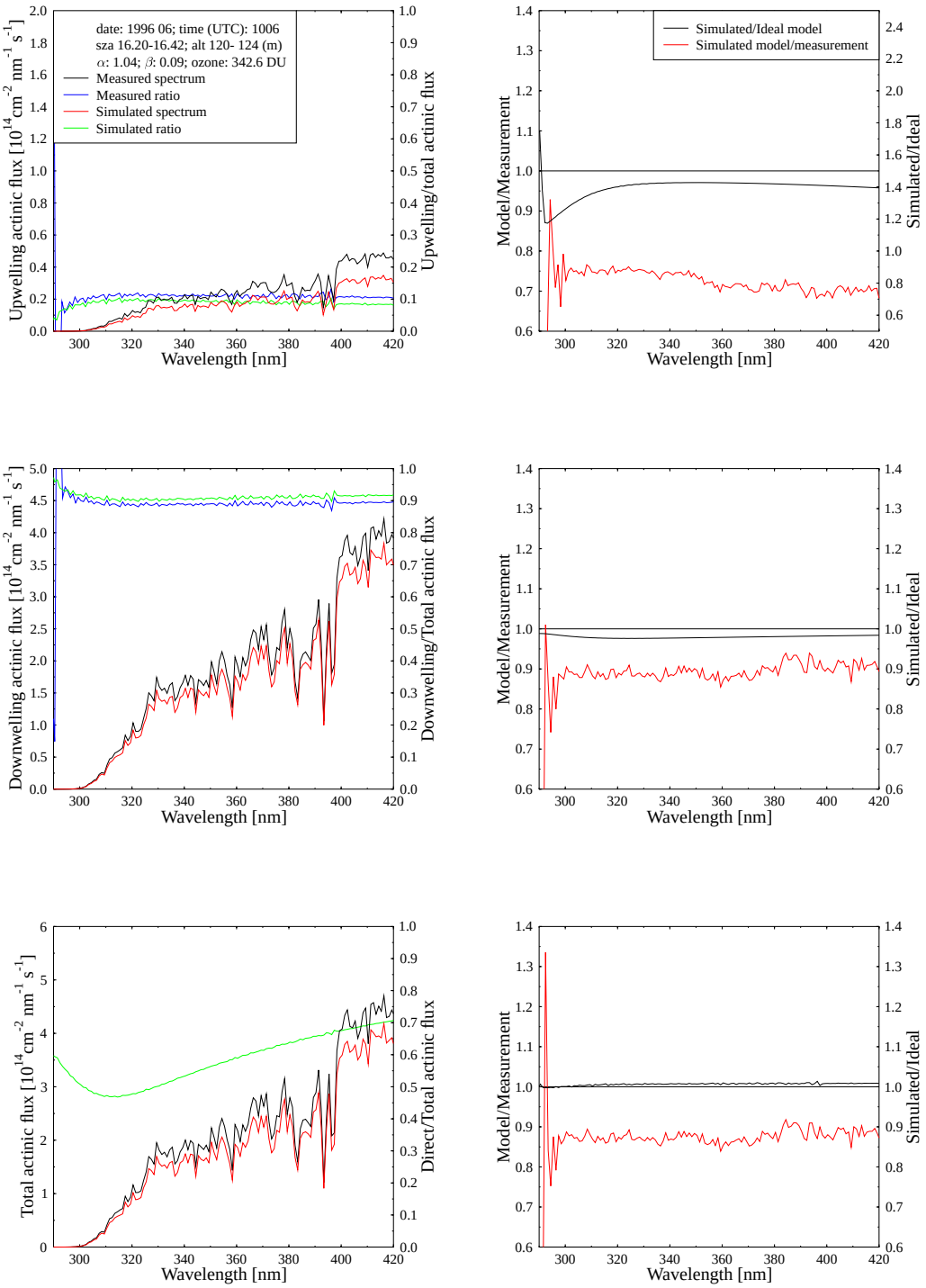

Figure 19: Same as Figure 10, except for 1006 UTC, 10 June 1996, and altitude 123.74 m.a.s.l.

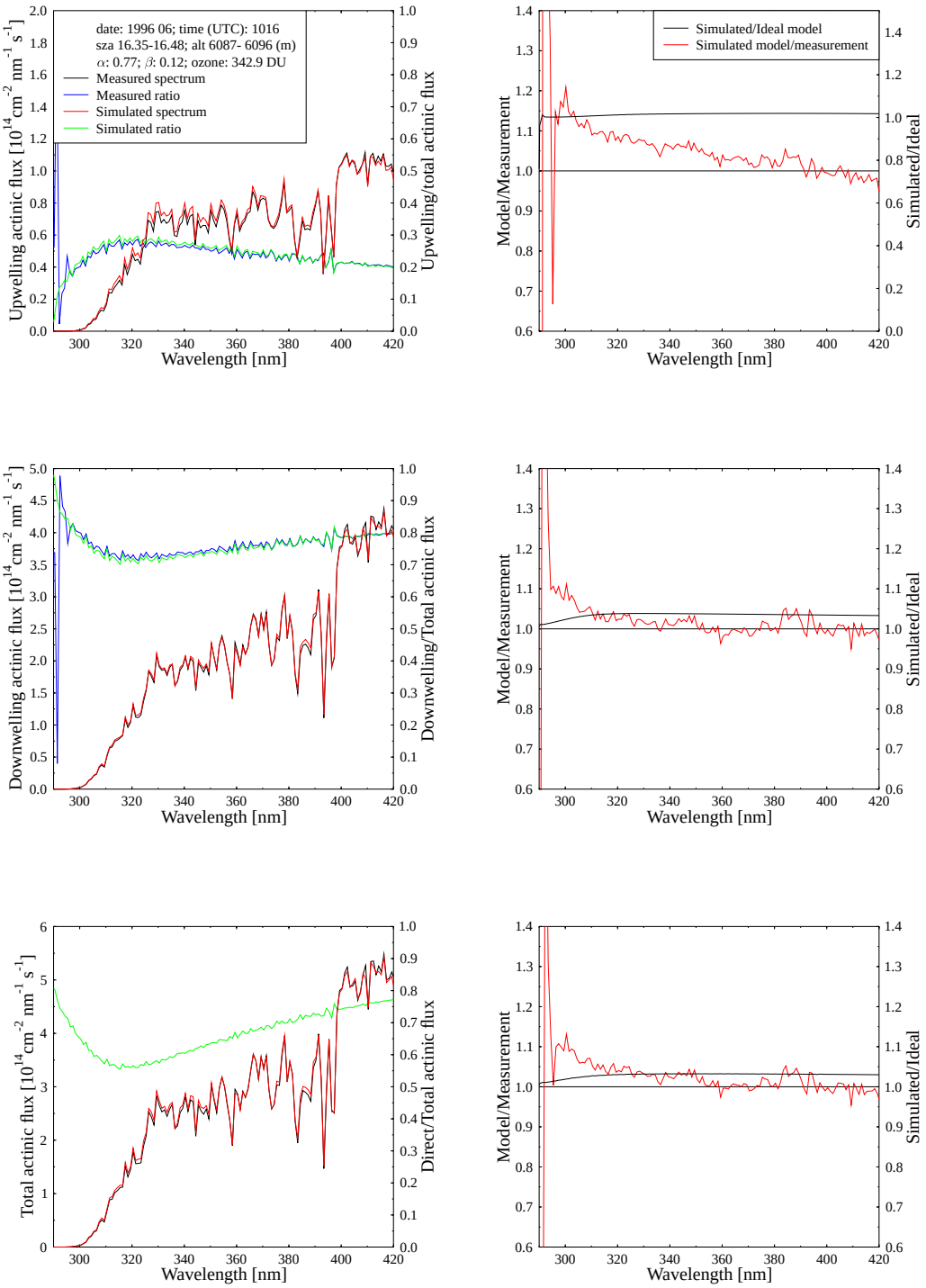

Figure 20: Same as Figure 10, except for 1016 UTC, 10 June 1996, and altitude 6089.2 m.a.s.l.

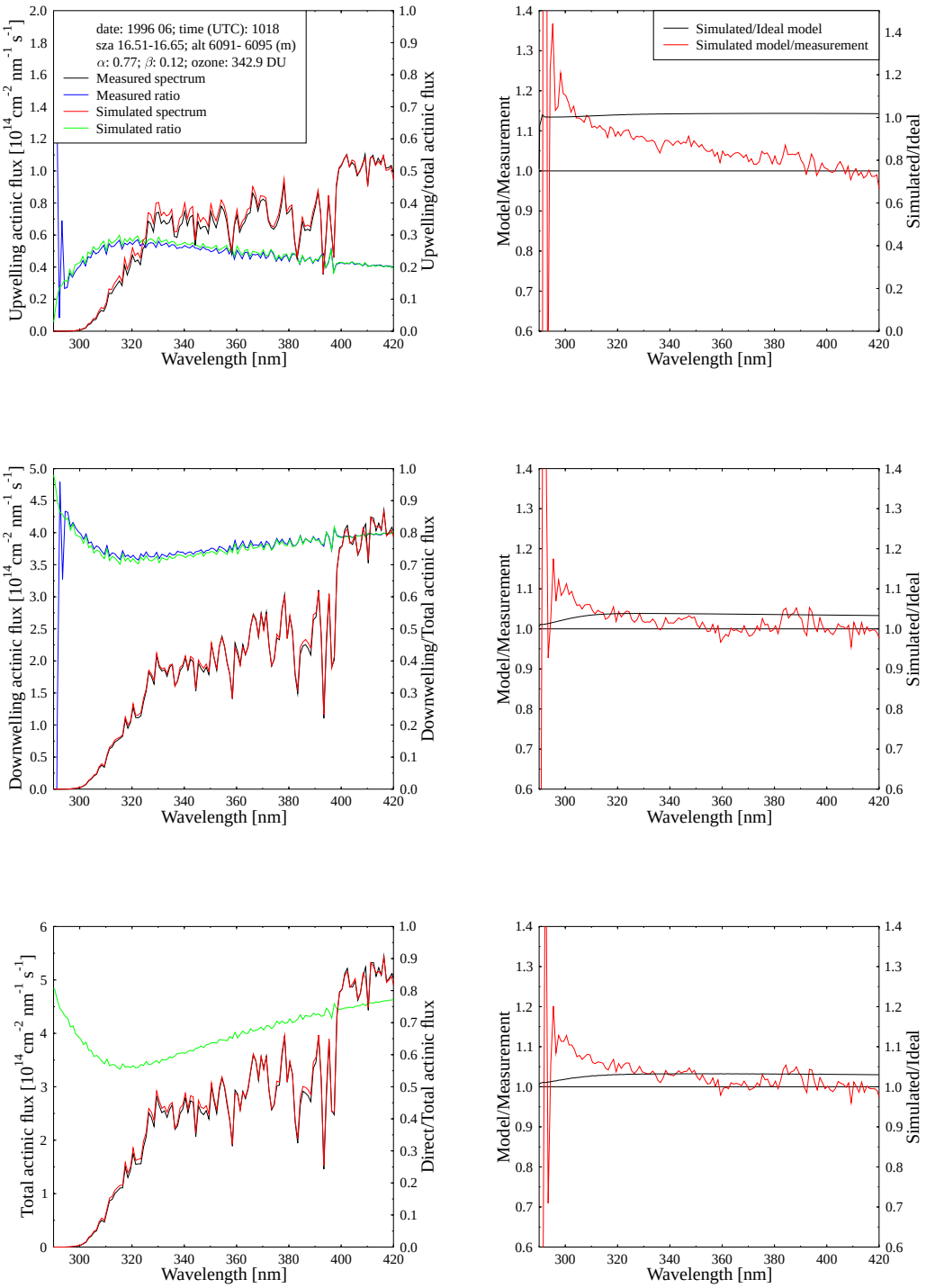

Figure 21: Same as Figure 10, except for 1018 UTC, 10 June 1996, and altitude 6095.59 m.a.s.l.

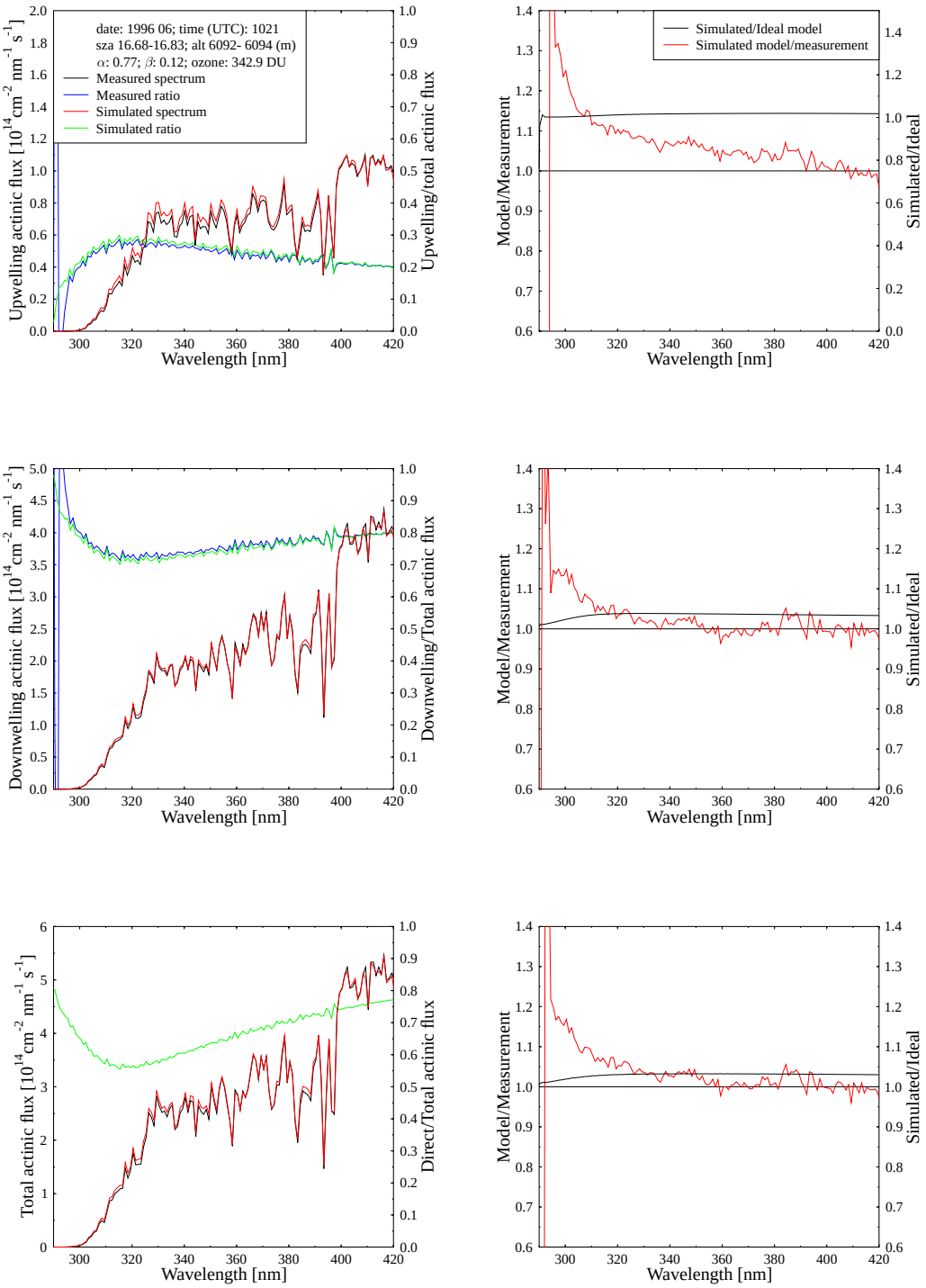

Figure 22: Same as Figure 10, except for 1021 UTC, 10 June 1996, and altitude 6093.16 m.a.s.l.

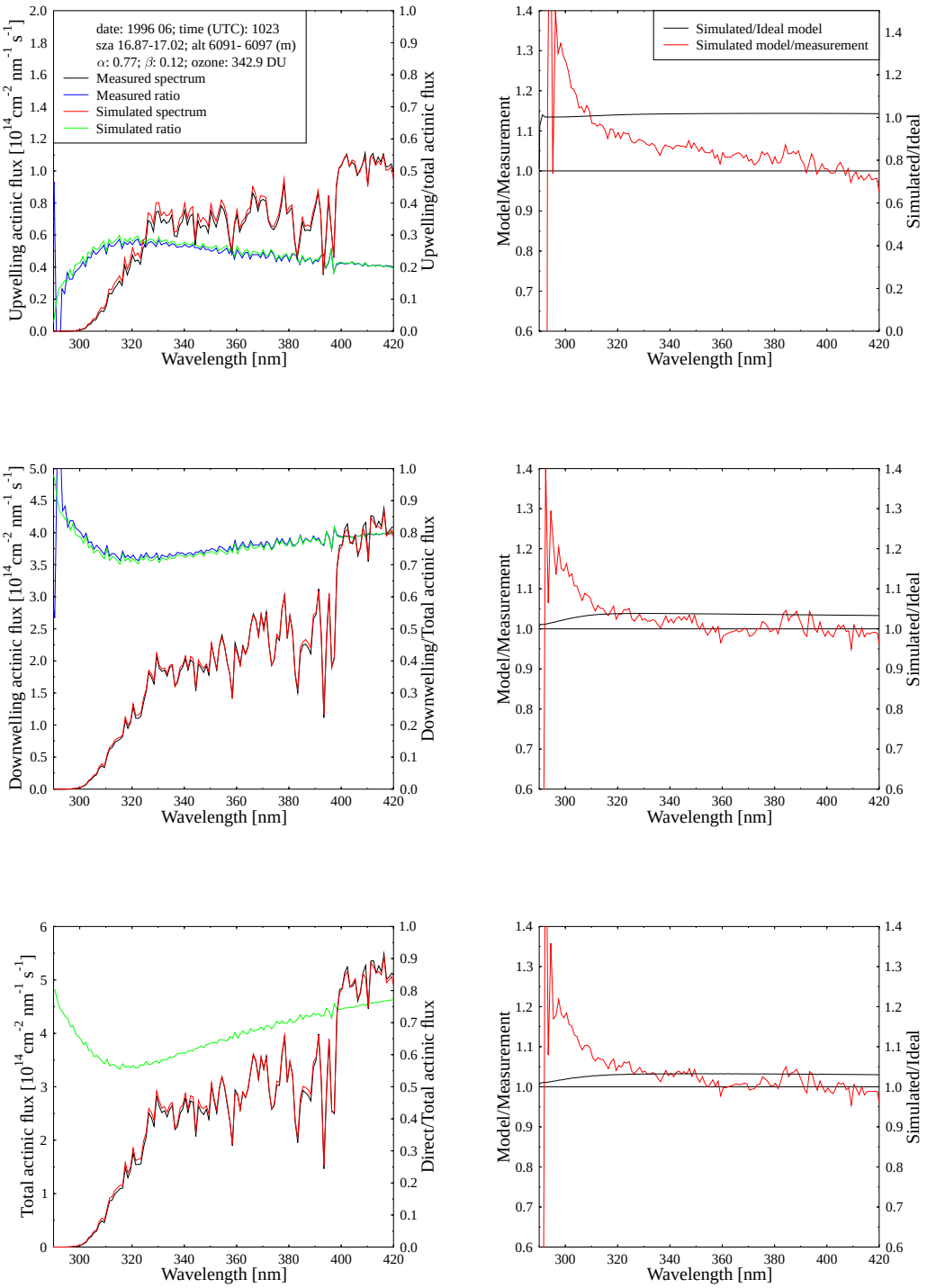

Figure 23: Same as Figure 10, except for 1023 UTC, 10 June 1996, and altitude 6094.07 m.a.s.l.

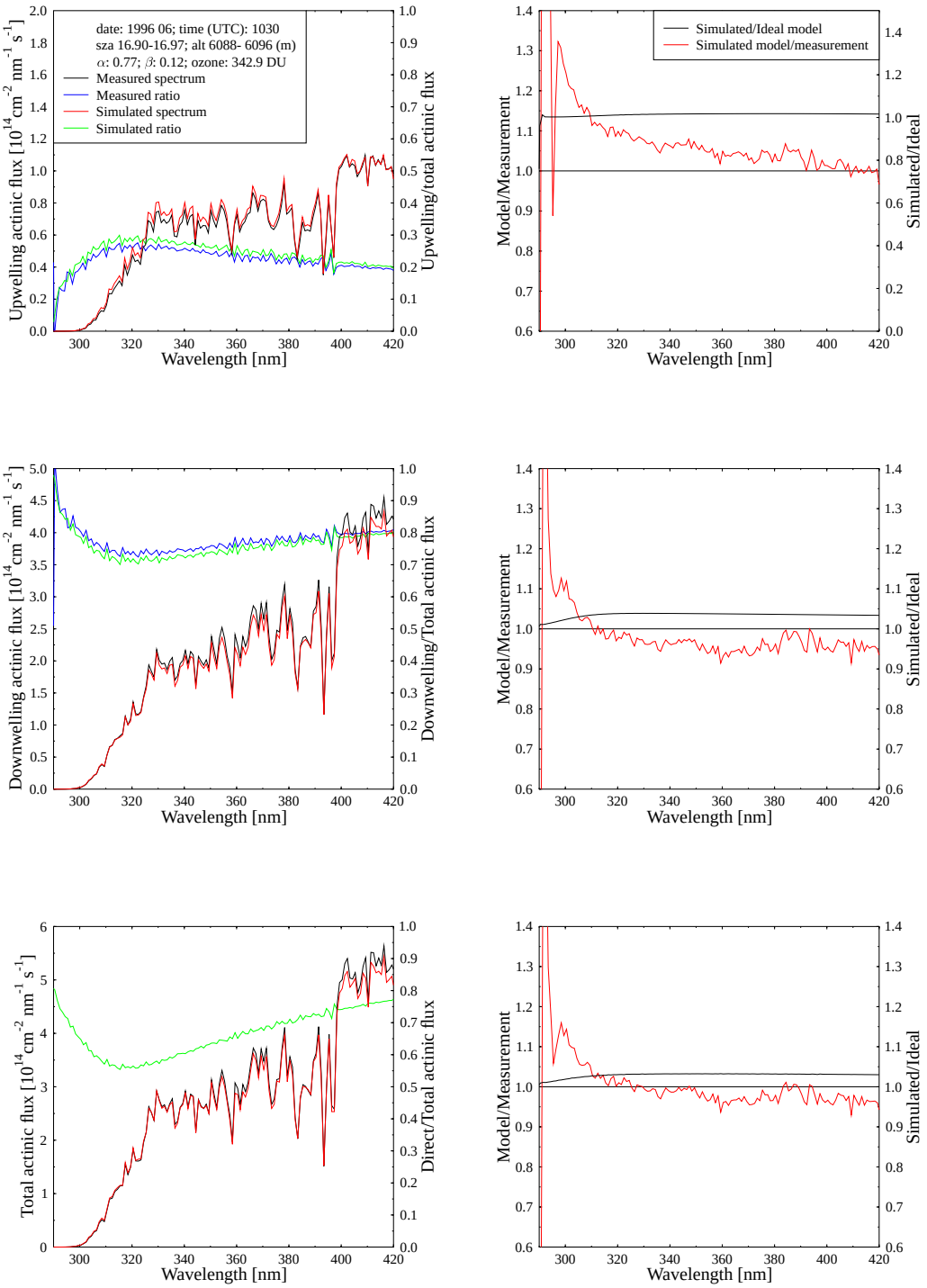

Figure 24: Same as Figure 10, except for 1030 UTC, 10 June 1996, and altitude 6096.82 m.a.s.l.

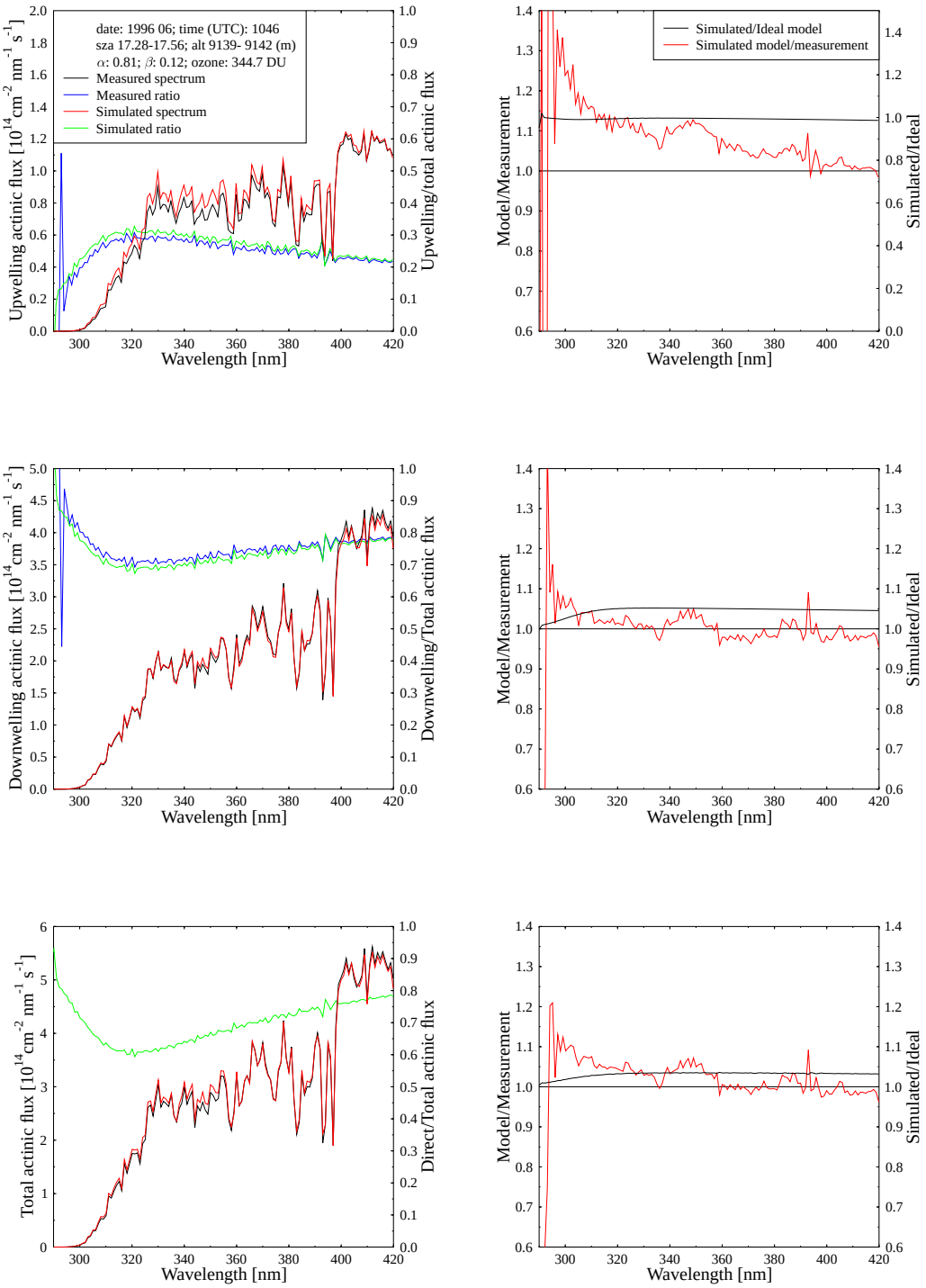

Figure 25: Same as Figure 10, except for 1046 UTC, 10 June 1996, and altitude 9139.44 m.a.s.l.

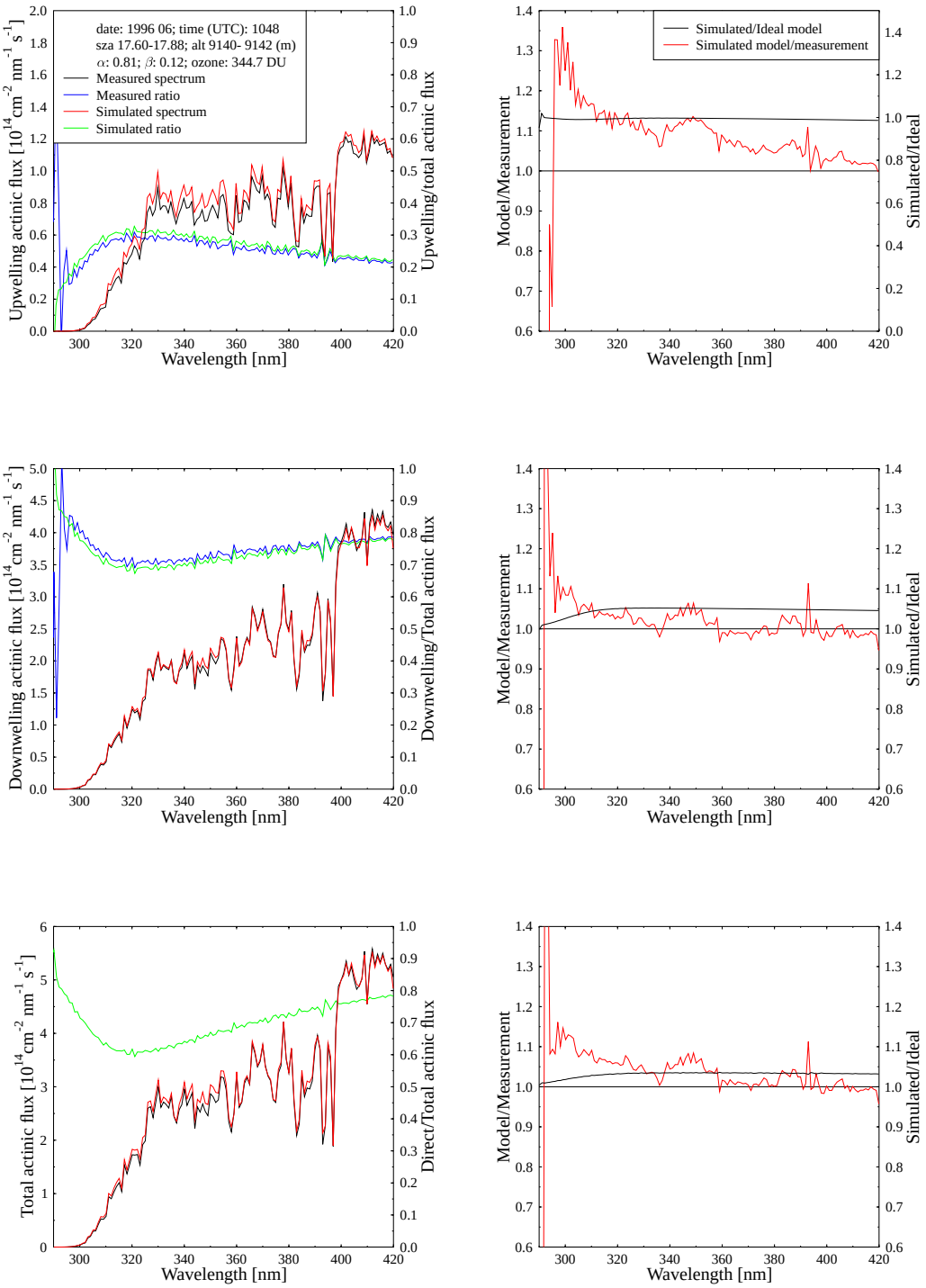

Figure 26: Same as Figure 10, except for 1048 UTC, 10 June 1996, and altitude 9141.88 m.a.s.l.

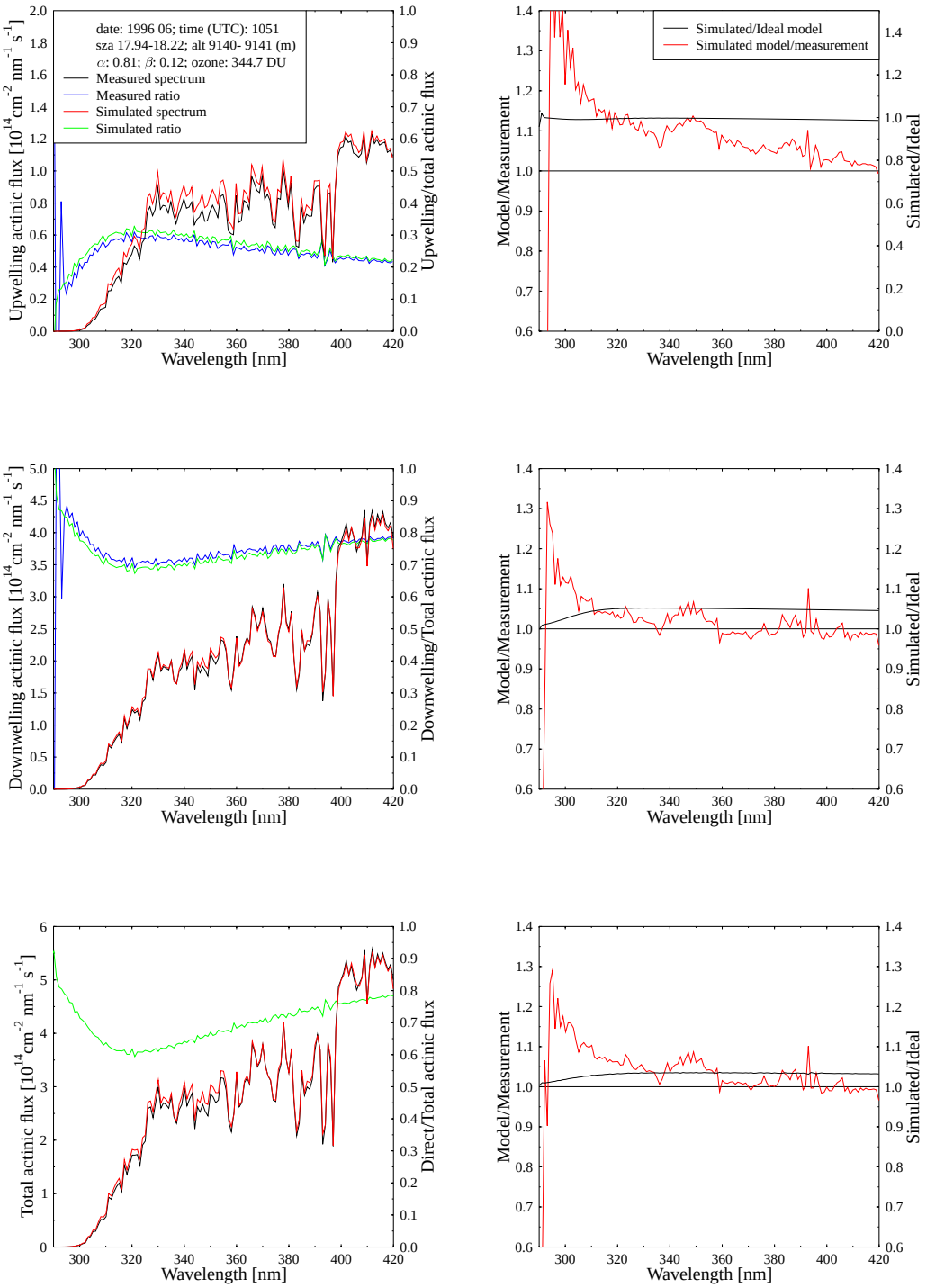

Figure 27: Same as Figure 10, except for 1051 UTC, 10 June 1996, and altitude 9141.57 m.a.s.l.

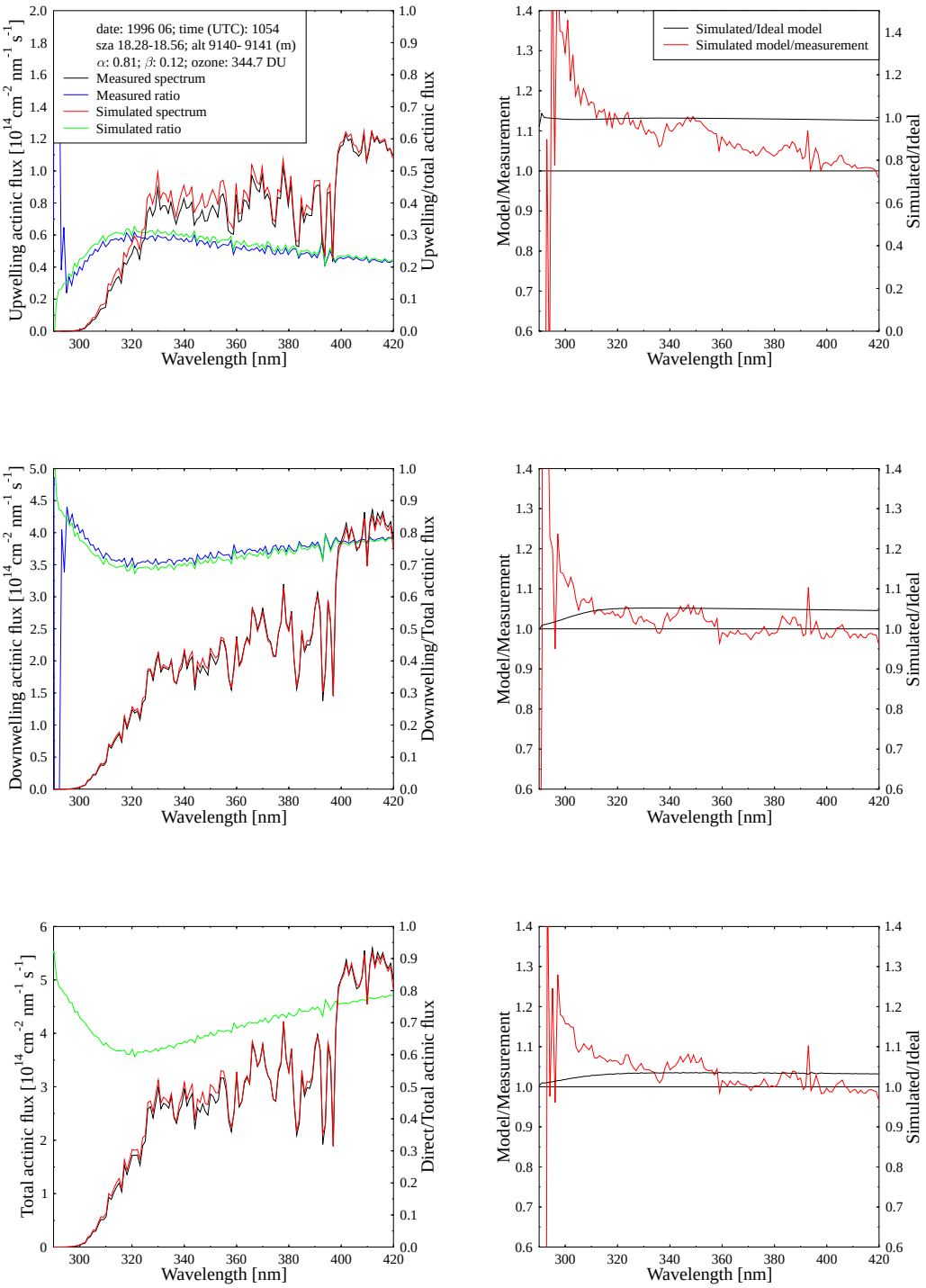

Figure 28: Same as Figure 10, except for 1054 UTC, 10 June 1996, and altitude 9140.96 m.a.s.l.

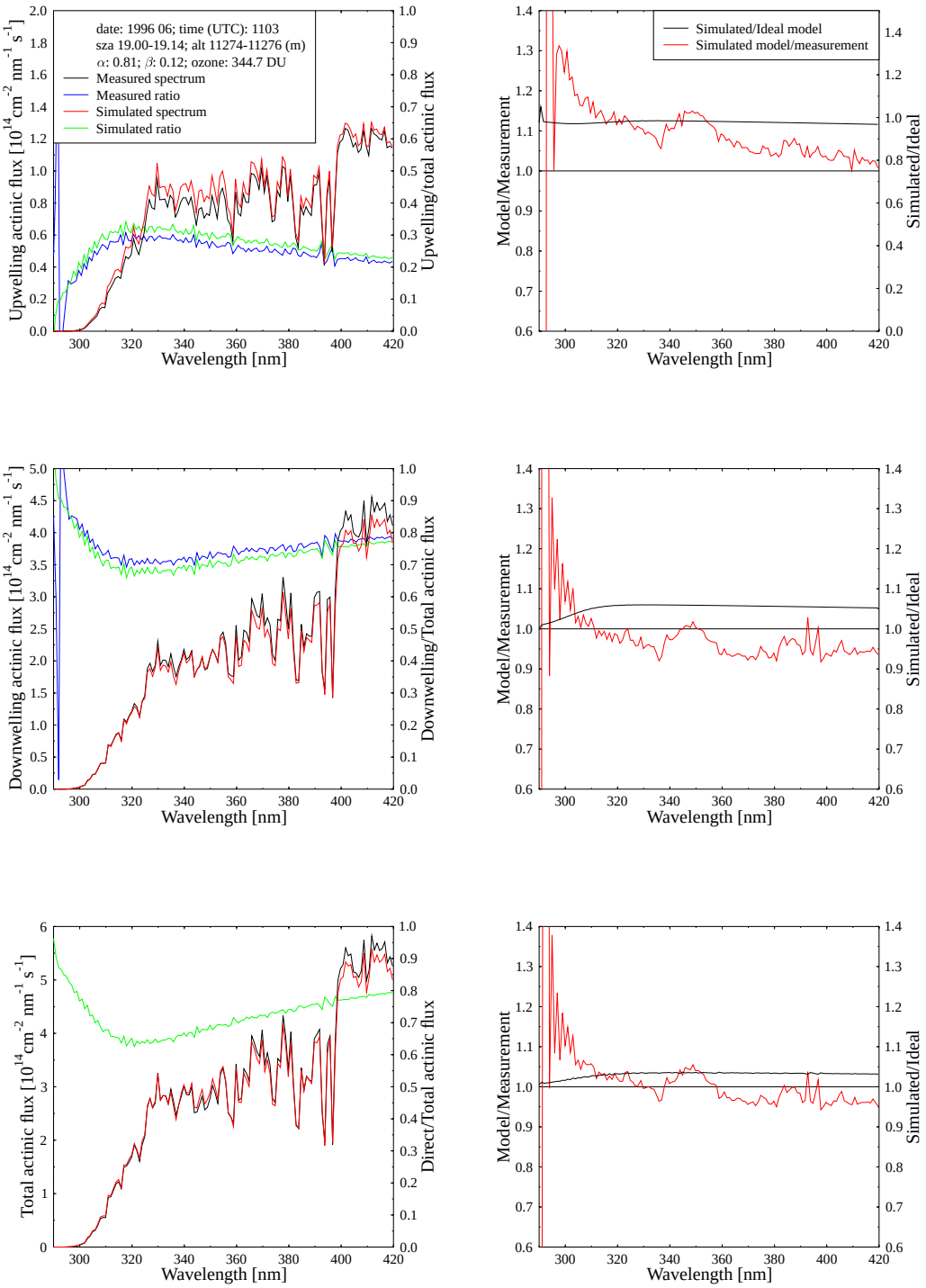

Figure 29: Same as Figure 10, except for 1103 UTC, 10 June 1996, and altitude 11275.95 m.a.s.l.

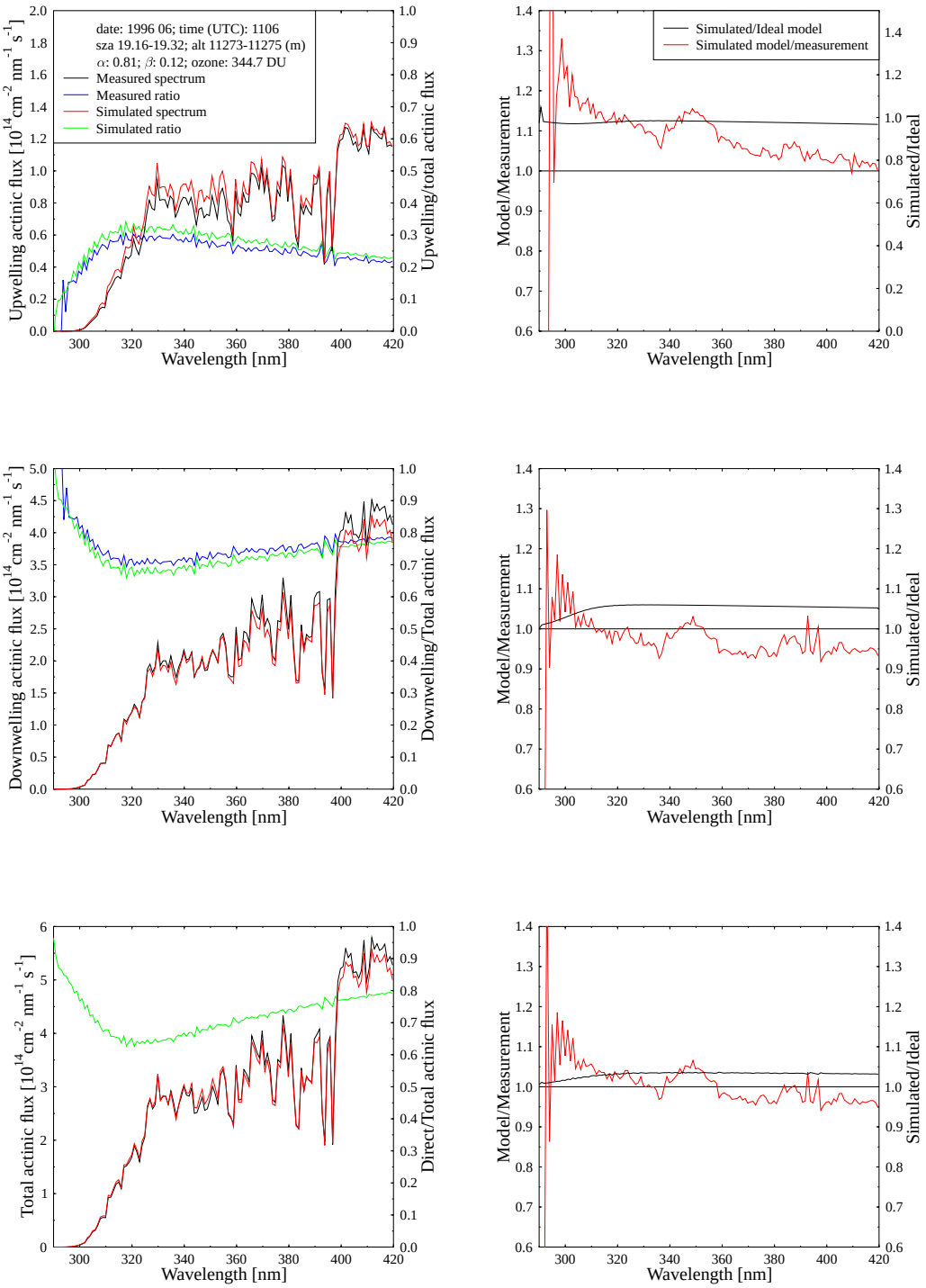

Figure 30: Same as Figure 10, except for 1106 UTC, 10 June 1996, and altitude 11275.64 m.a.s.l.

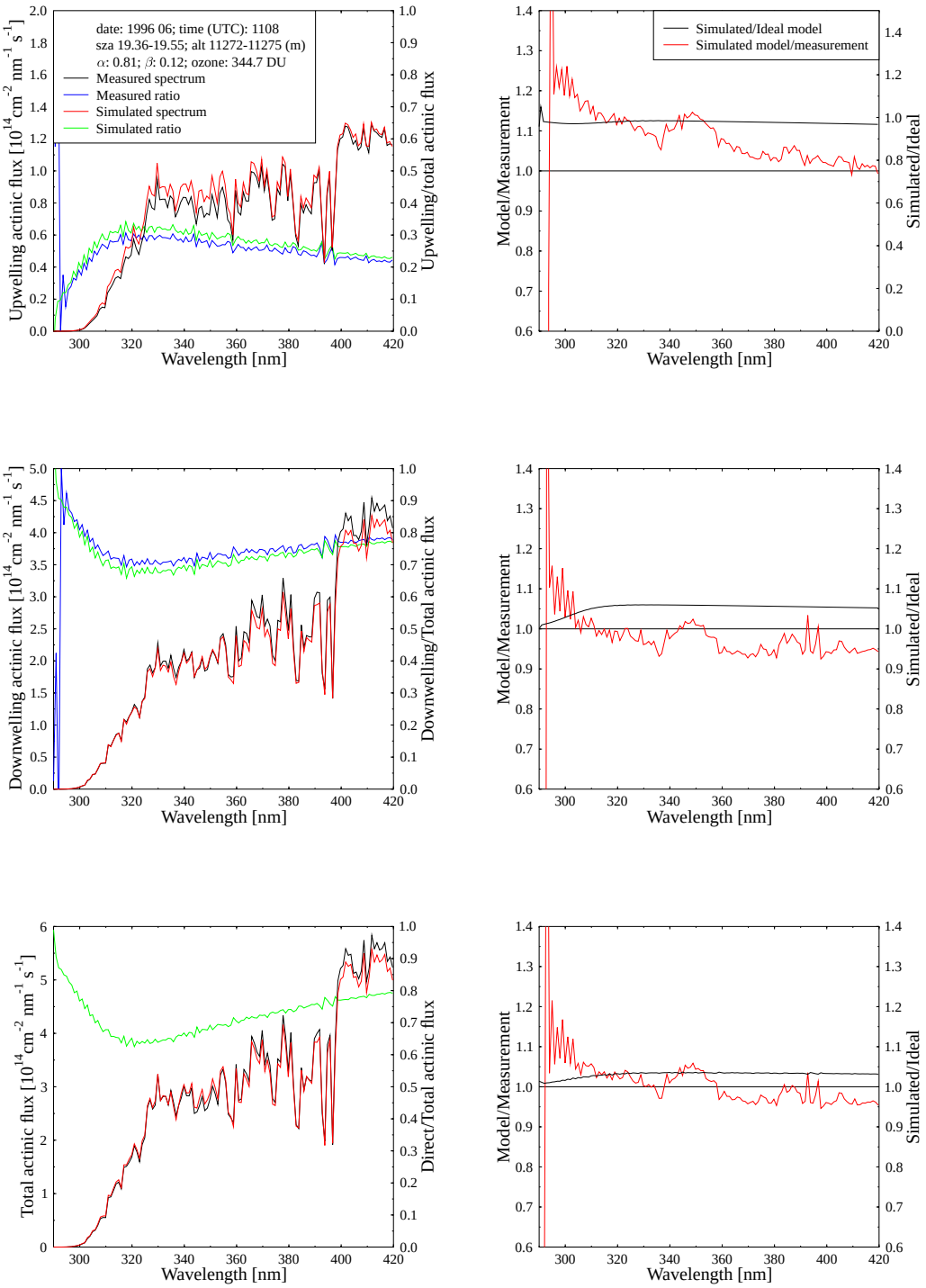

Figure 31: Same as Figure 10, except for 1108 UTC, 10 June 1996, and altitude 11273.82 m.a.s.l.

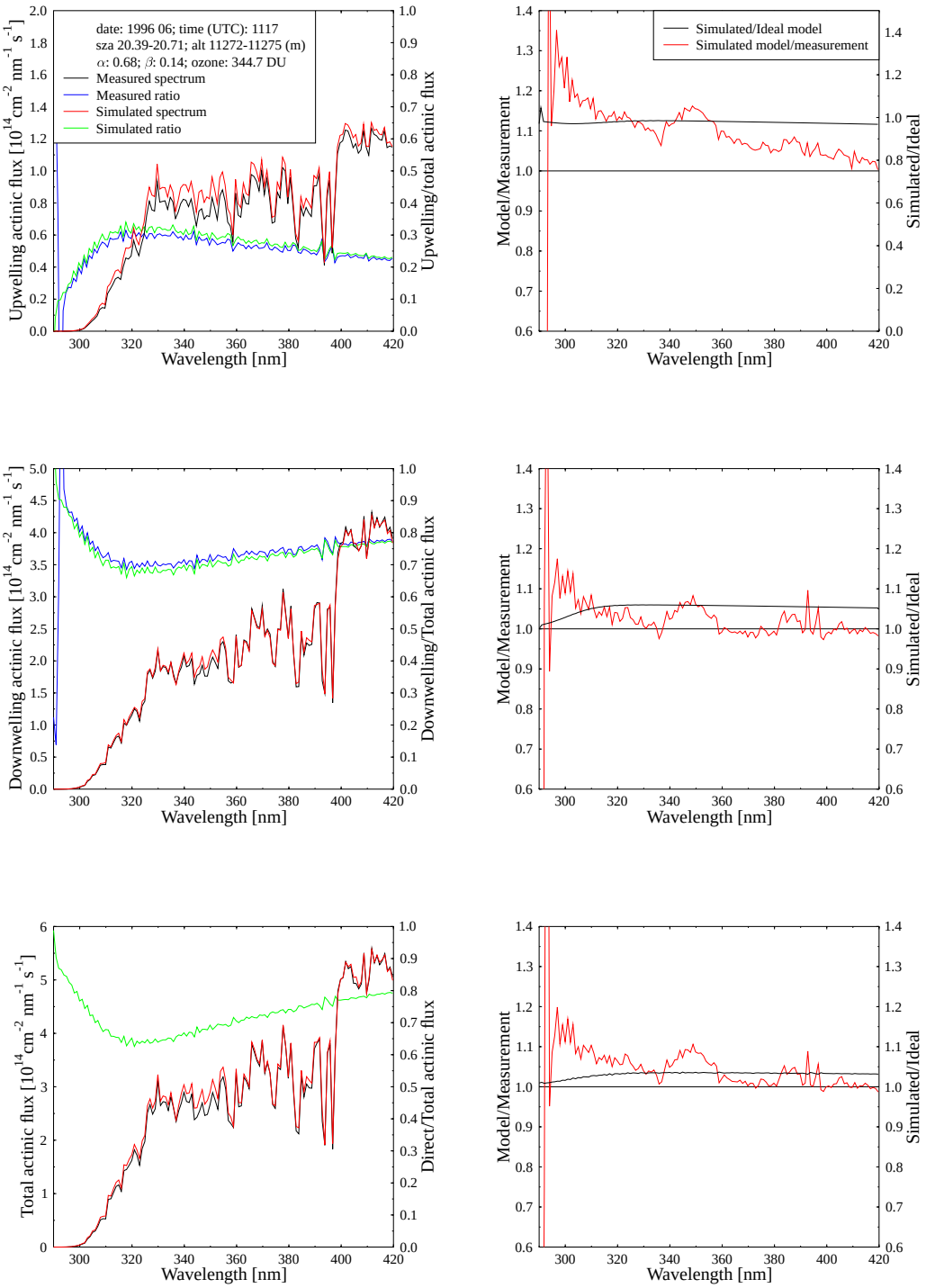

Figure 32: Same as Figure 10, except for 1117 UTC, 10 June 1996, and altitude 11272.29 m.a.s.l.

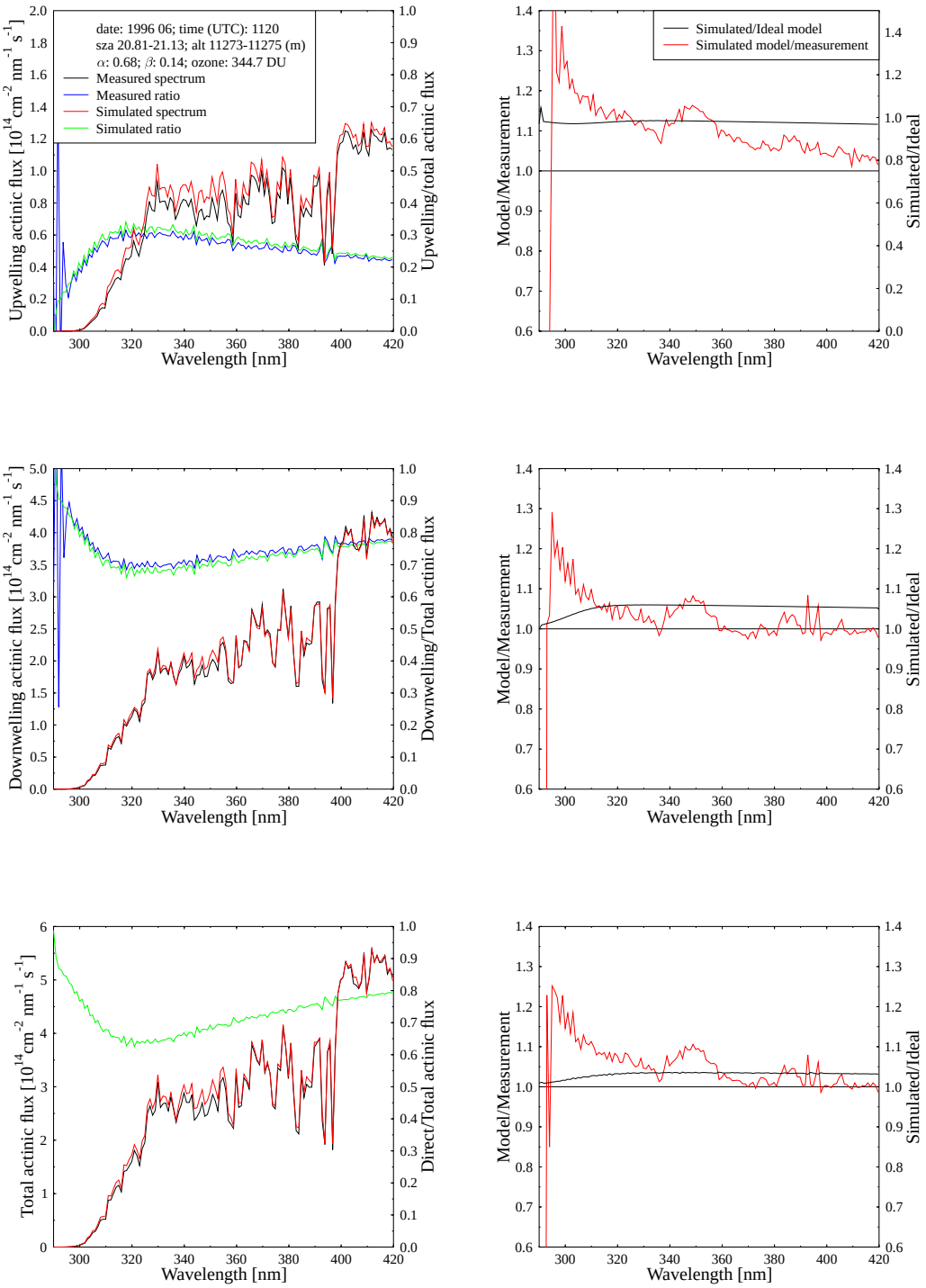

Figure 33: Same as Figure 10, except for 1120 UTC, 10 June 1996, and altitude 11274.73 m.a.s.l.

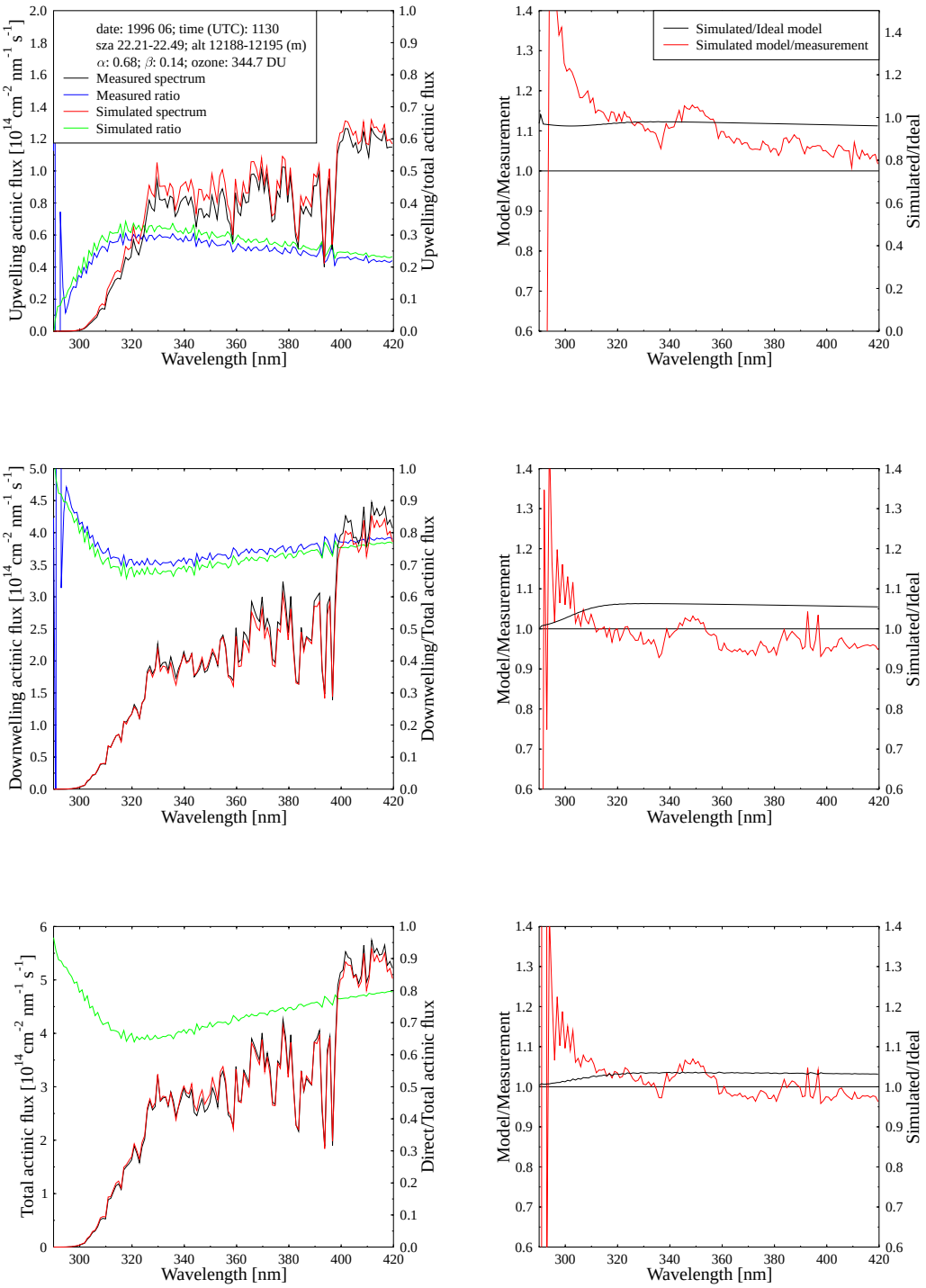

Figure 34: Same as Figure 10, except for 1130 UTC, 10 June 1996, and altitude 12194.25 m.a.s.l.

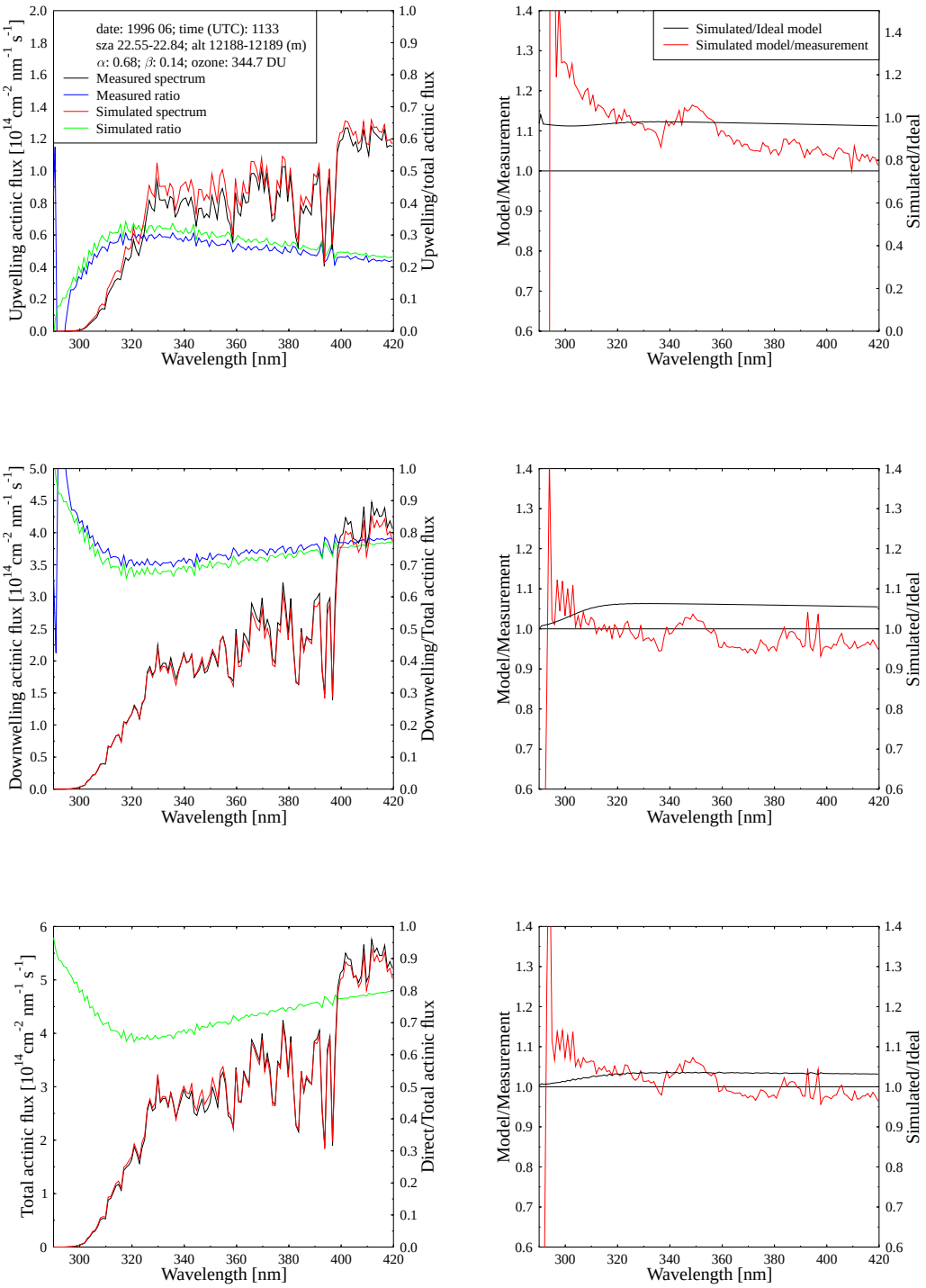

Figure 35: Same as Figure 10, except for 1133 UTC, 10 June 1996, and altitude 12189.37 m.a.s.l.

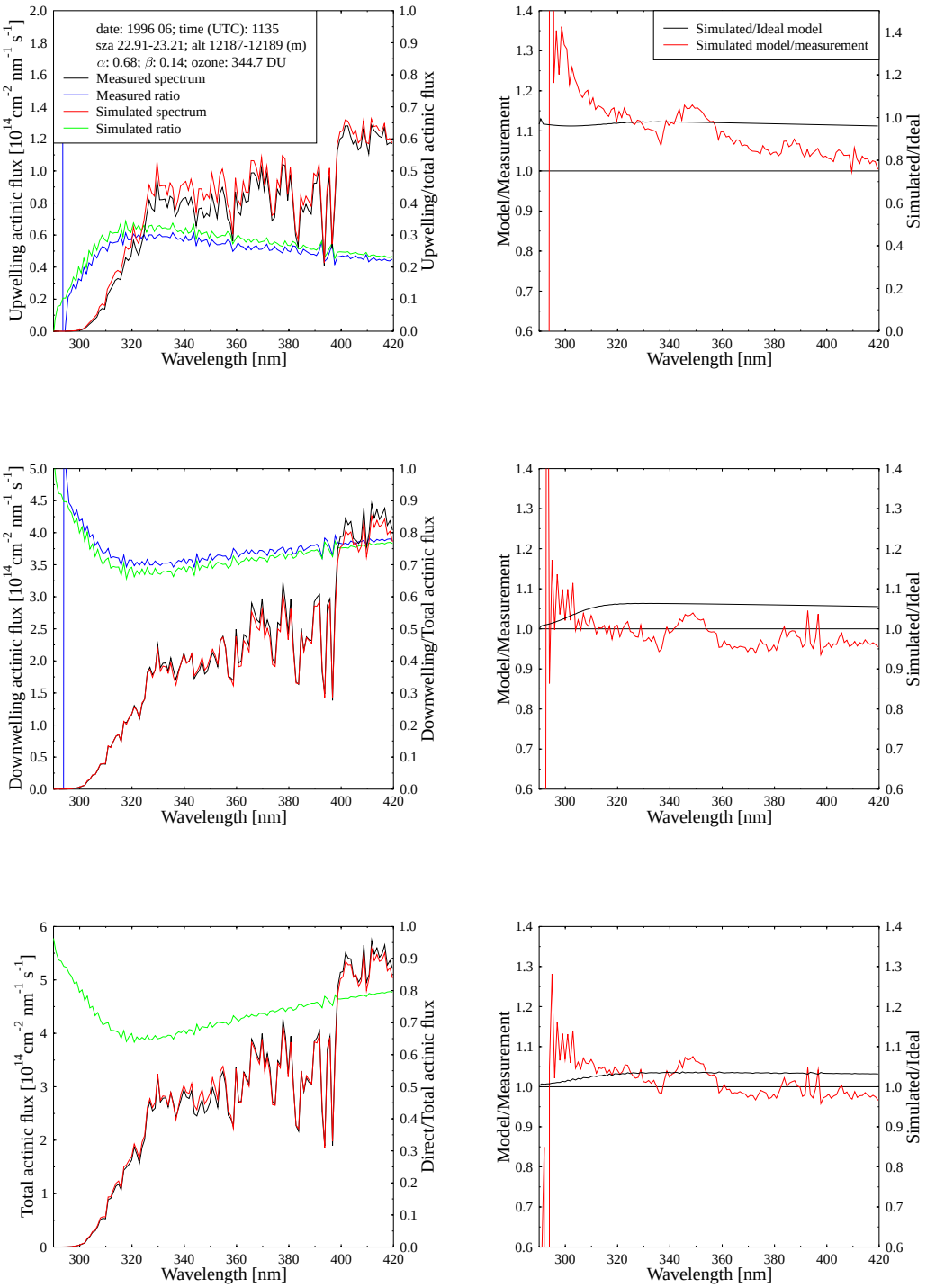

Figure 36: Same as Figure 10, except for 1135 UTC, 10 June 1996, and altitude 12188.46 m.a.s.l.

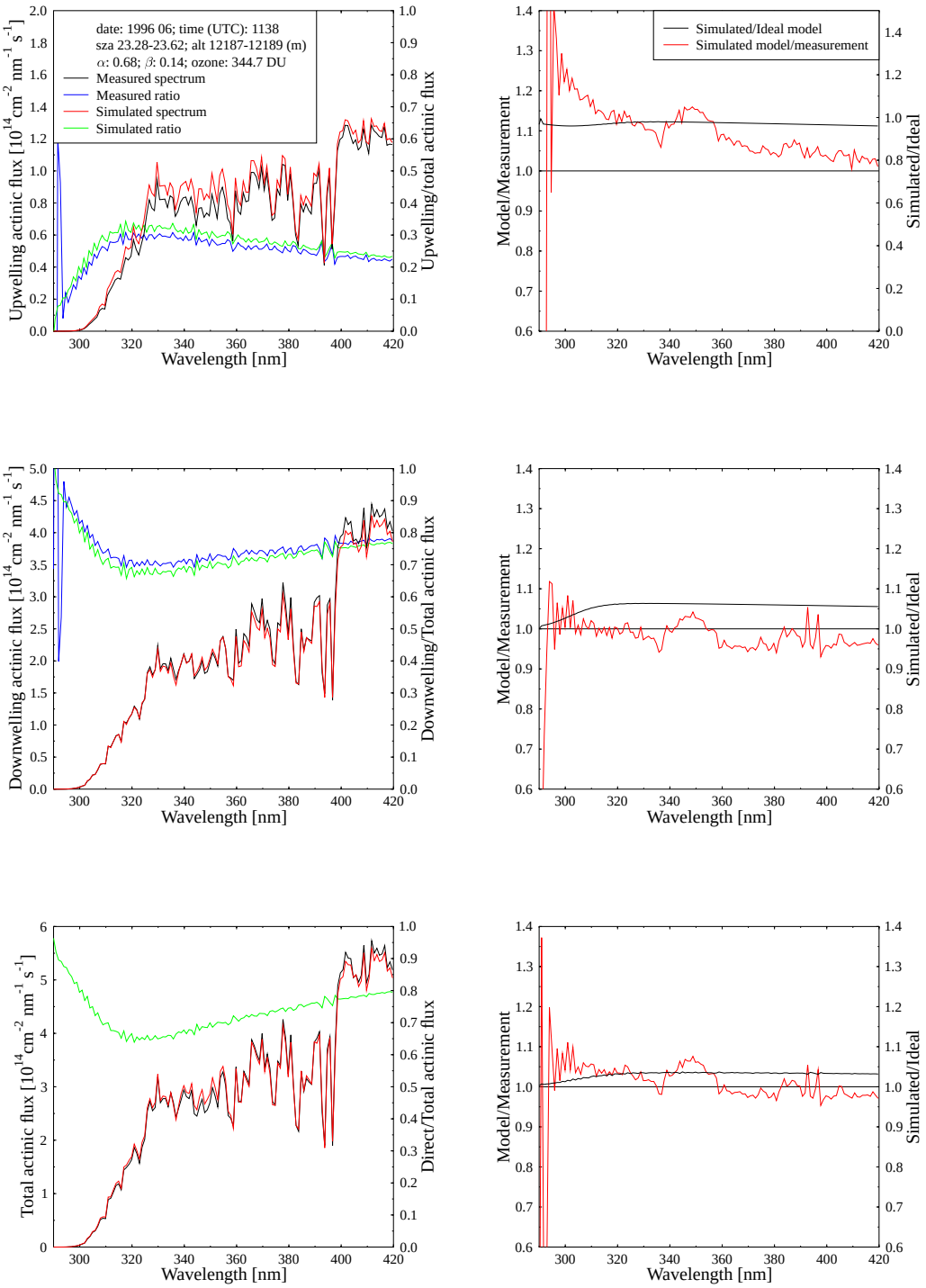

Figure 37: Same as Figure 10, except for 1138 UTC, 10 June 1996, and altitude 12188.15 m.a.s.l.

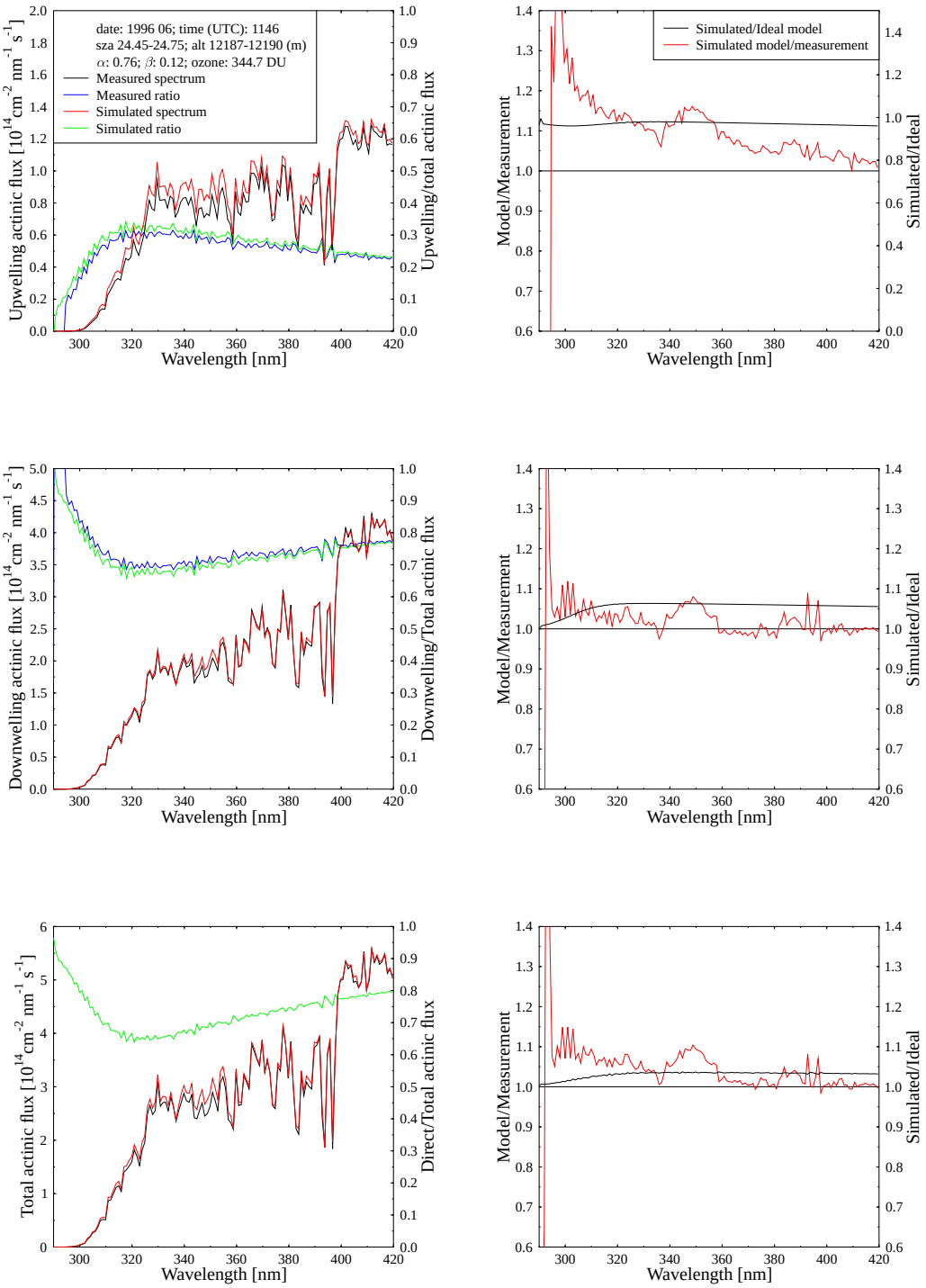

Figure 38: Same as Figure 10, except for 1146 UTC, 10 June 1996, and altitude 12189.37 m.a.s.l.

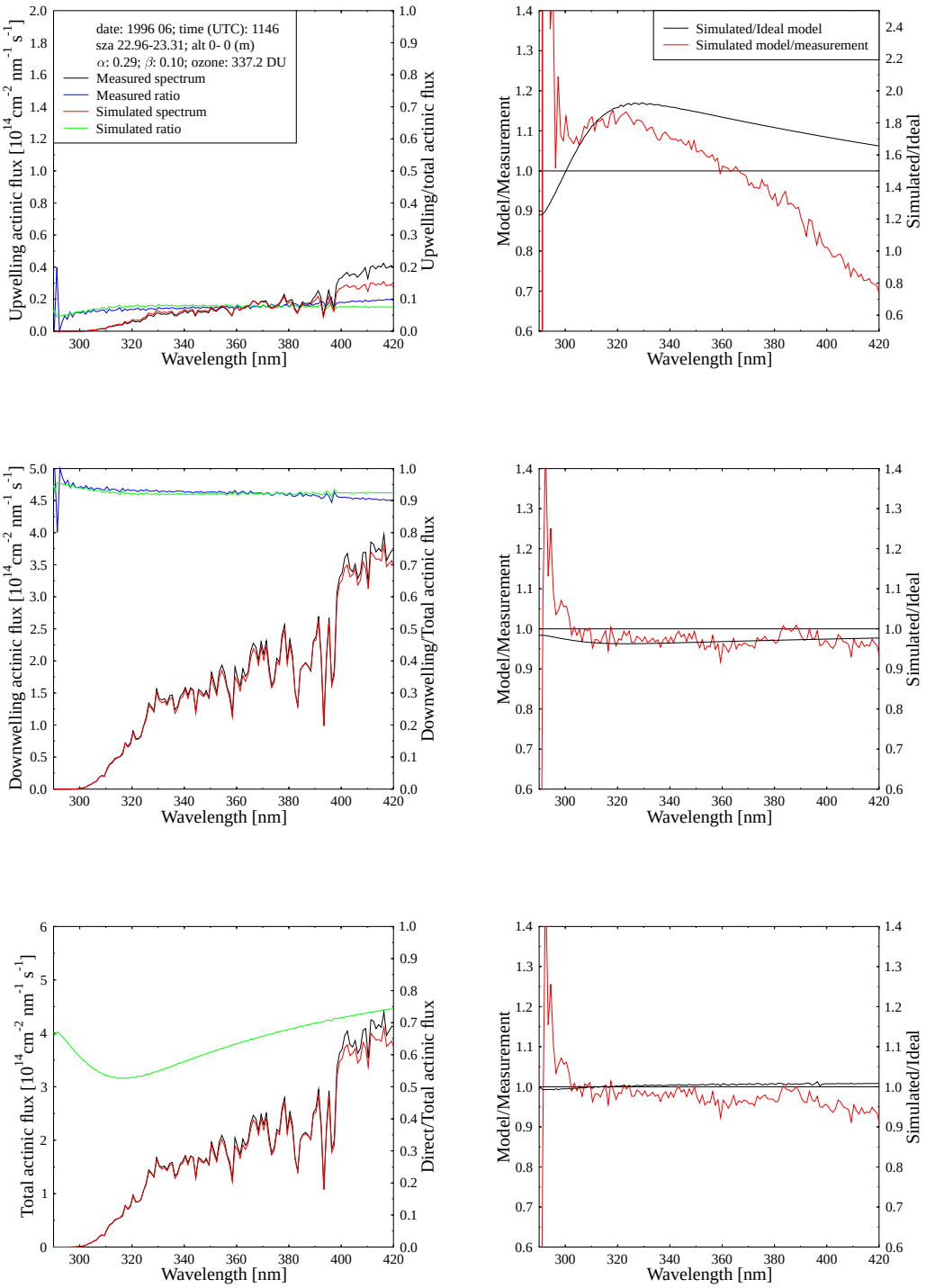

Figure 39: Same as Figure 10, except for 1146 UTC, 11 June 1996, and altitude 0 m.a.s.l.

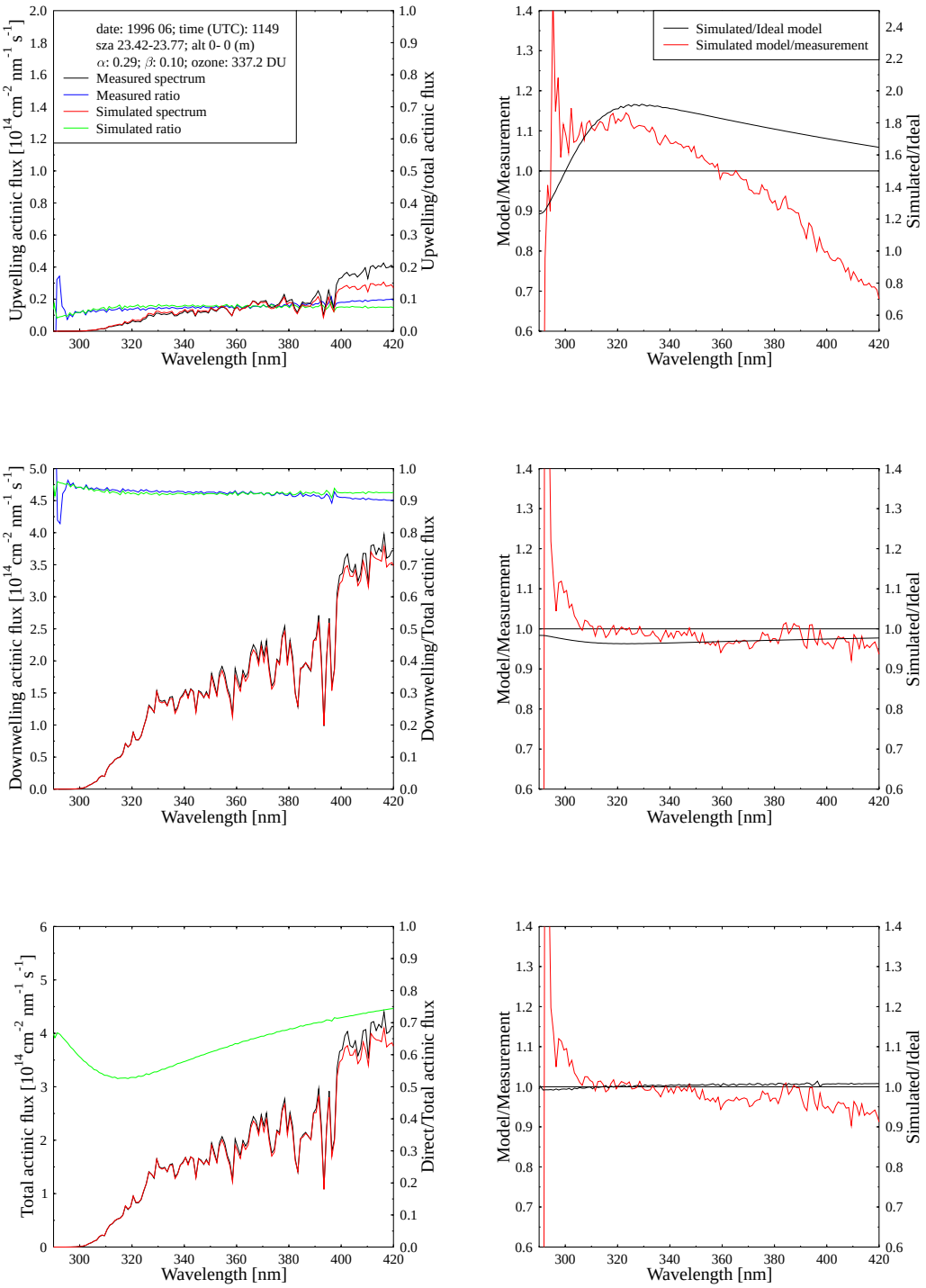

Figure 40: Same as Figure 10, except for 1149 UTC, 11 June 1996, and altitude 0 m.a.s.l.

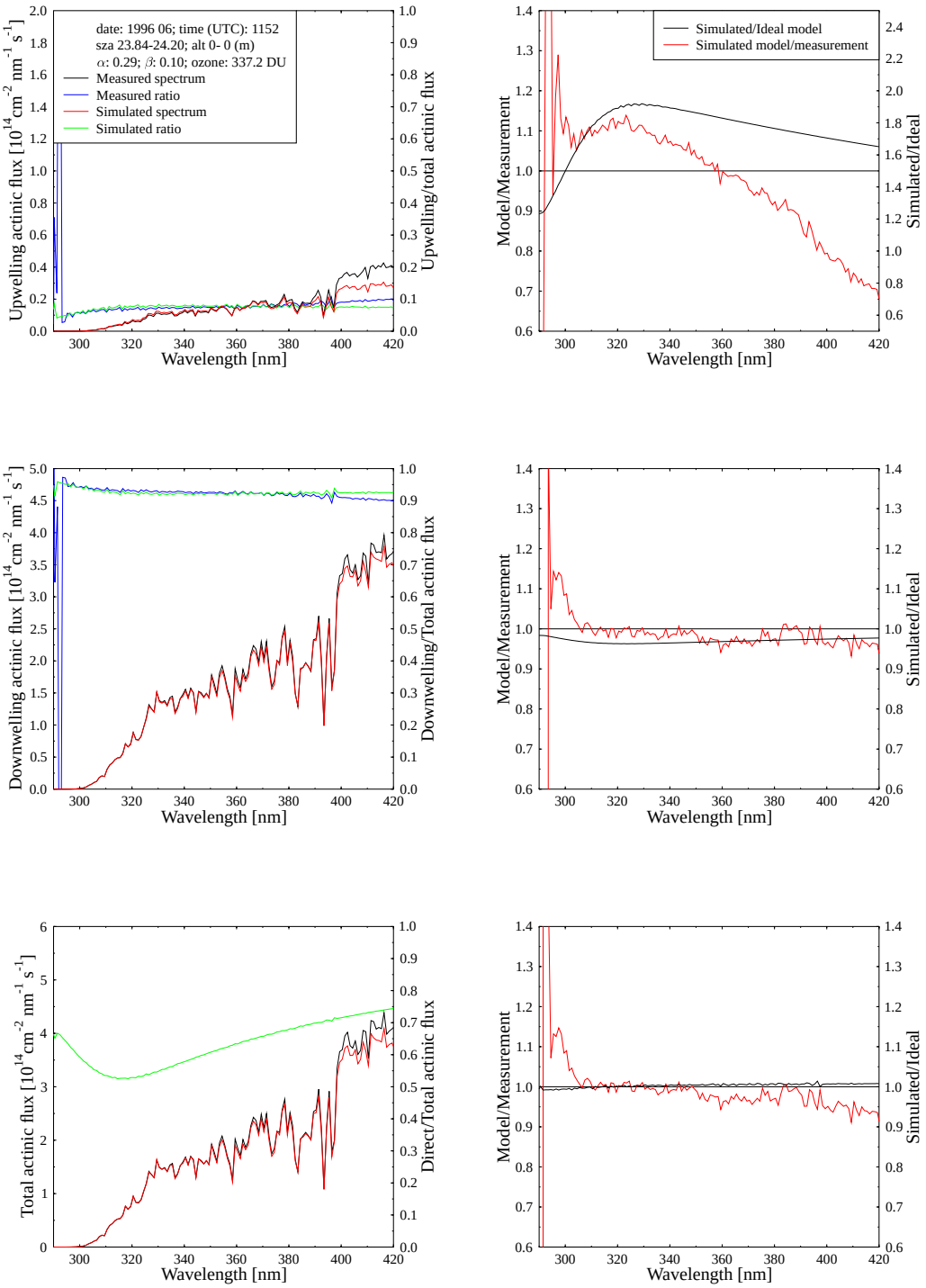

Figure 41: Same as Figure 10, except for 1152 UTC, 11 June 1996, and altitude 0 m.a.s.l.

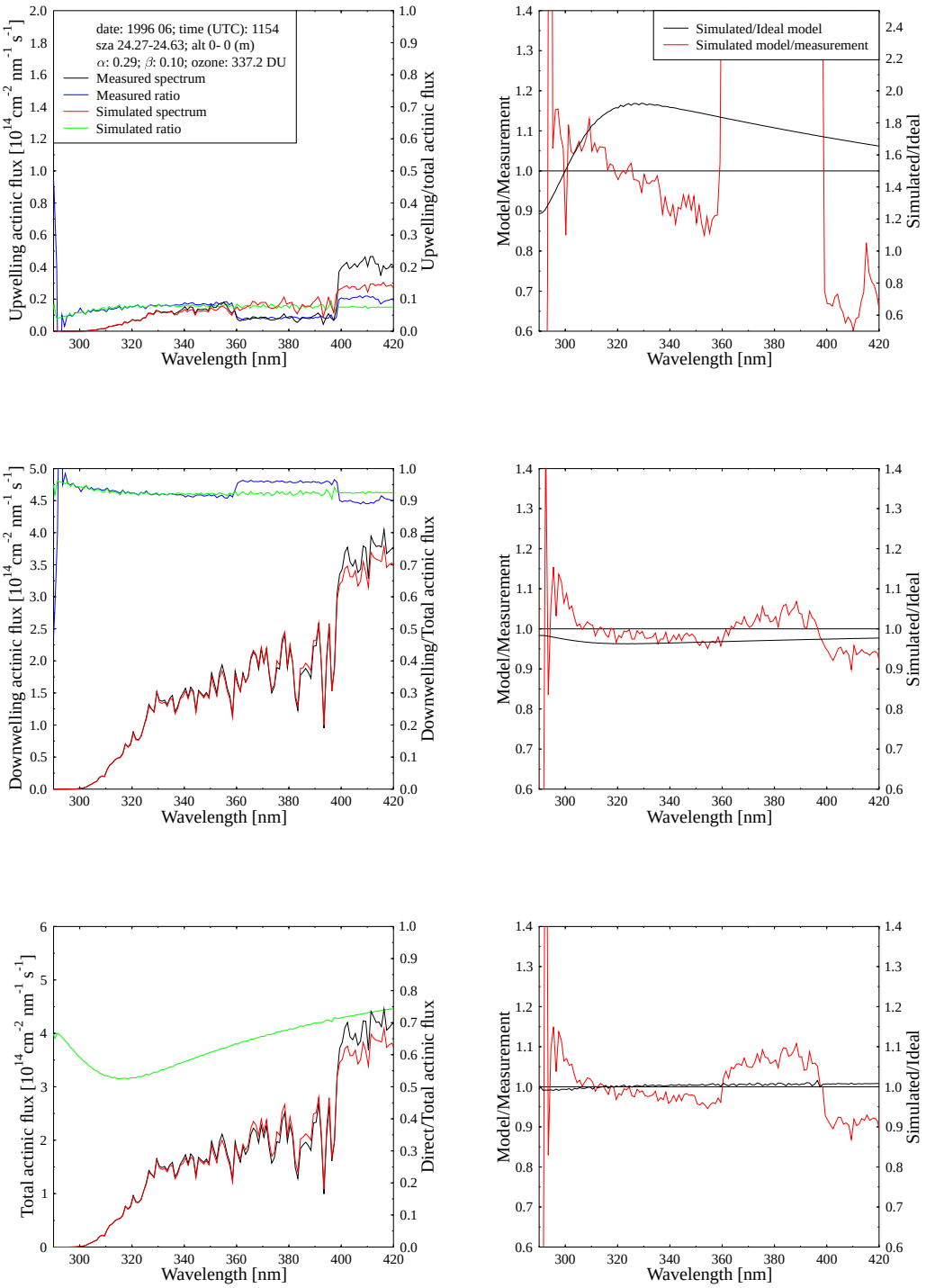

Figure 42: Same as Figure 10, except for 1154 UTC, 11 June 1996, and altitude 0 m.a.s.l.

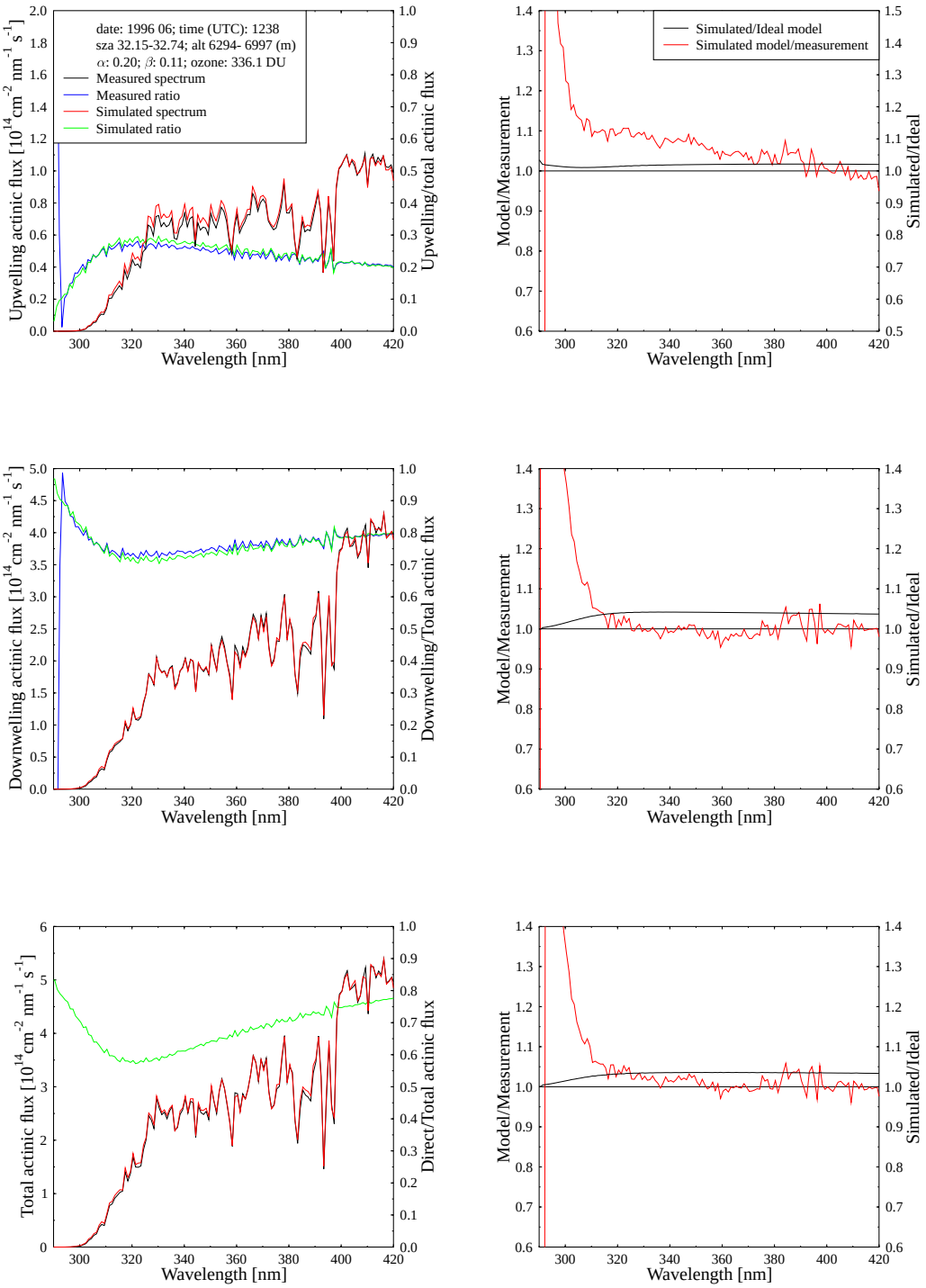

Figure 43: Same as Figure 10, except for 1238 UTC, 11 June 1996, and altitude 6294 m.a.s.l.

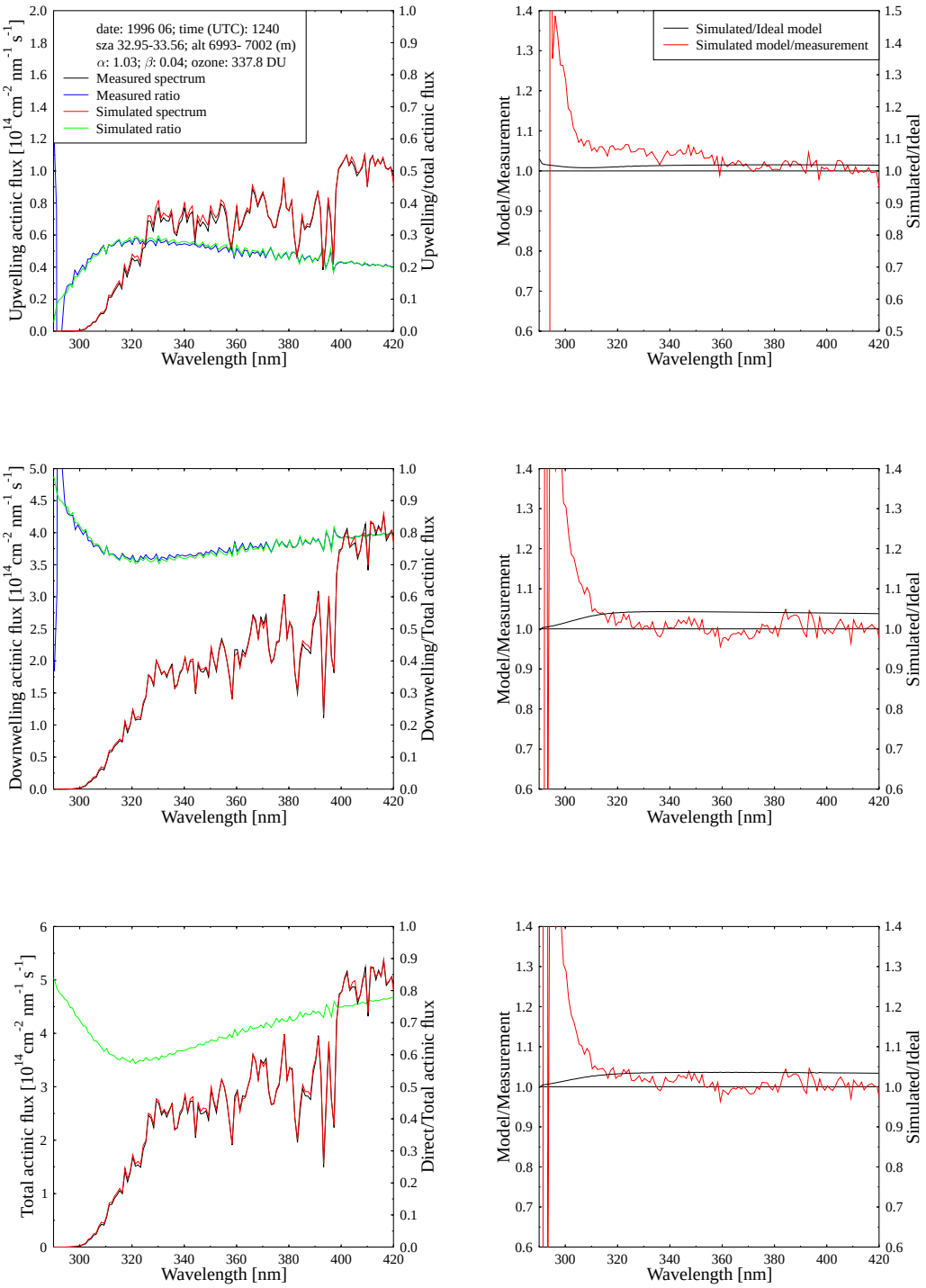

Figure 44: Same as Figure 10, except for 1240 UTC, 11 June 1996, and altitude 6995 m.a.s.l.

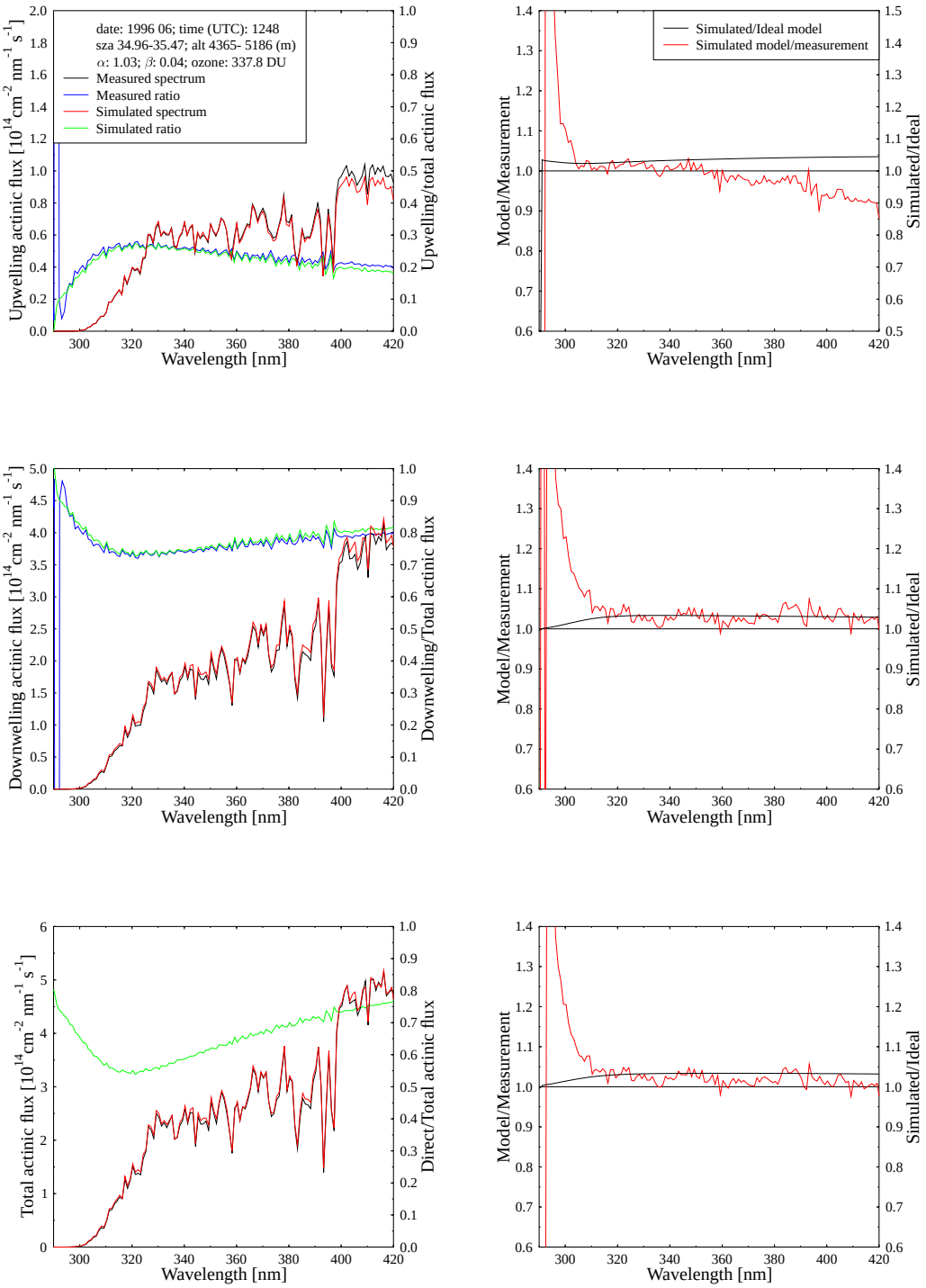

Figure 45: Same as Figure 10, except for 1248 UTC, 11 June 1996, and altitude 5186 m.a.s.l.

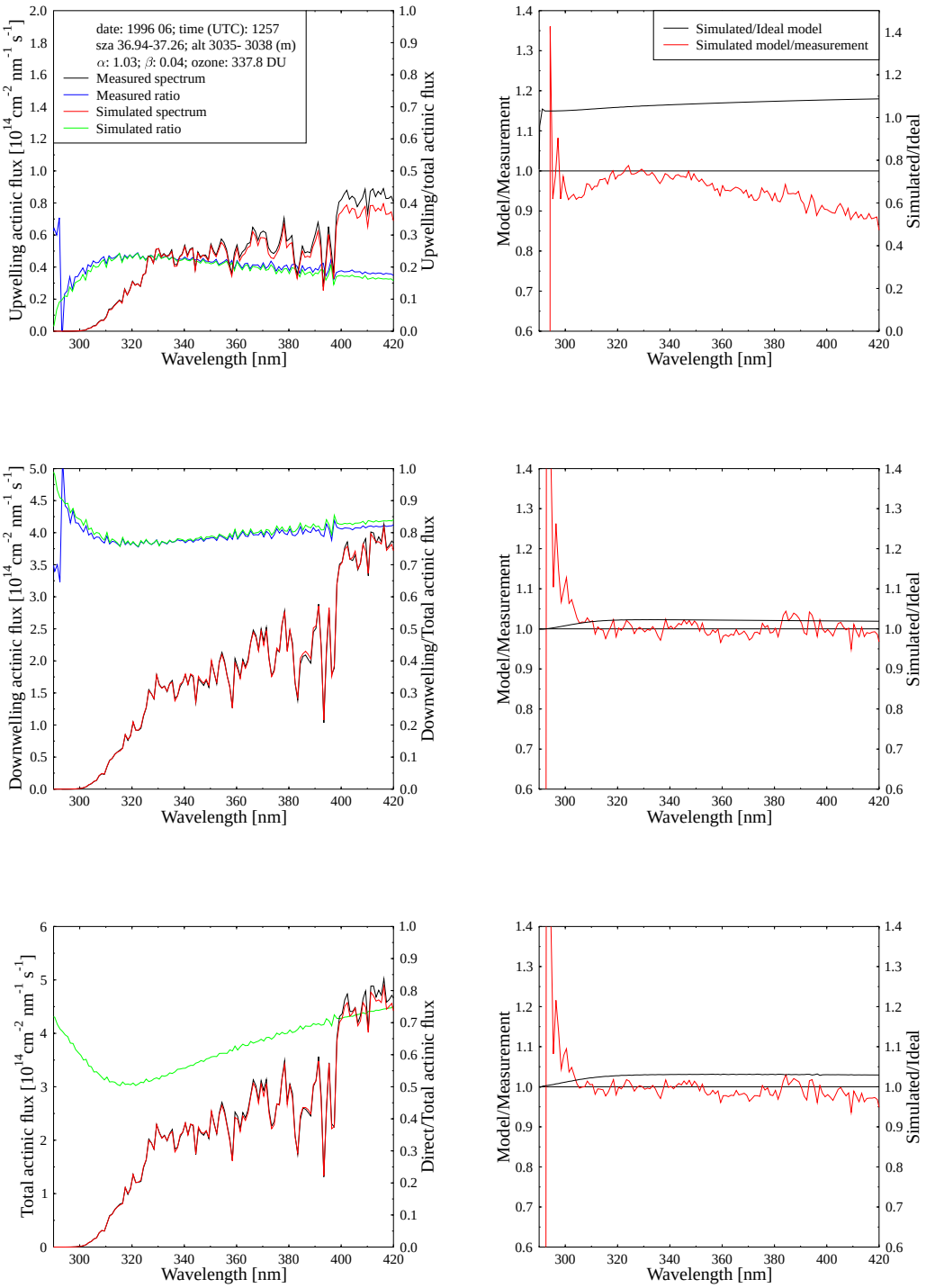

Figure 46: Same as Figure 10, except for 1257 UTC, 11 June 1996, and altitude 3036 m.a.s.l.

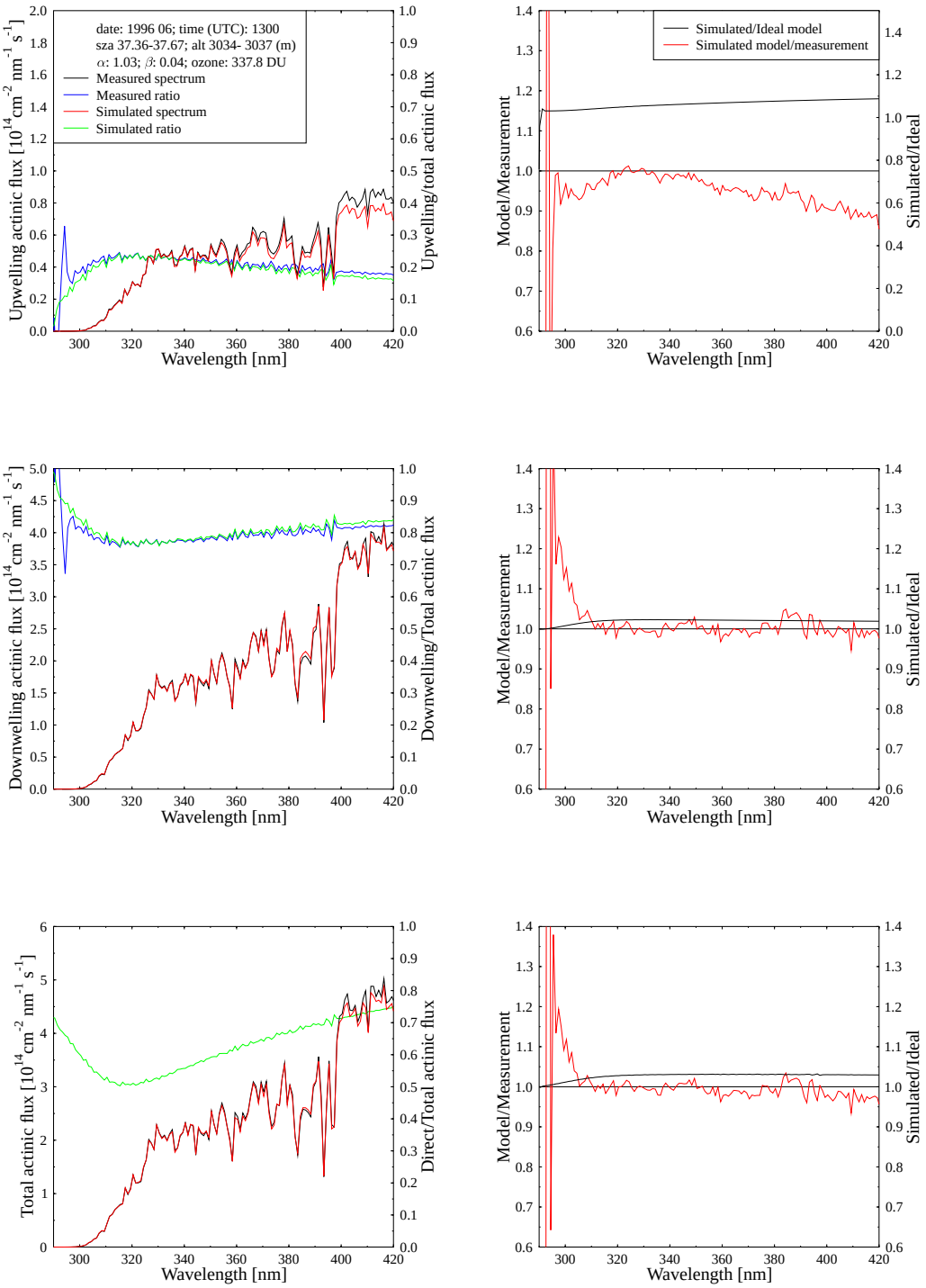

Figure 47: Same as Figure 10, except for 1300 UTC, 11 June 1996, and altitude 3035 m.a.s.l.

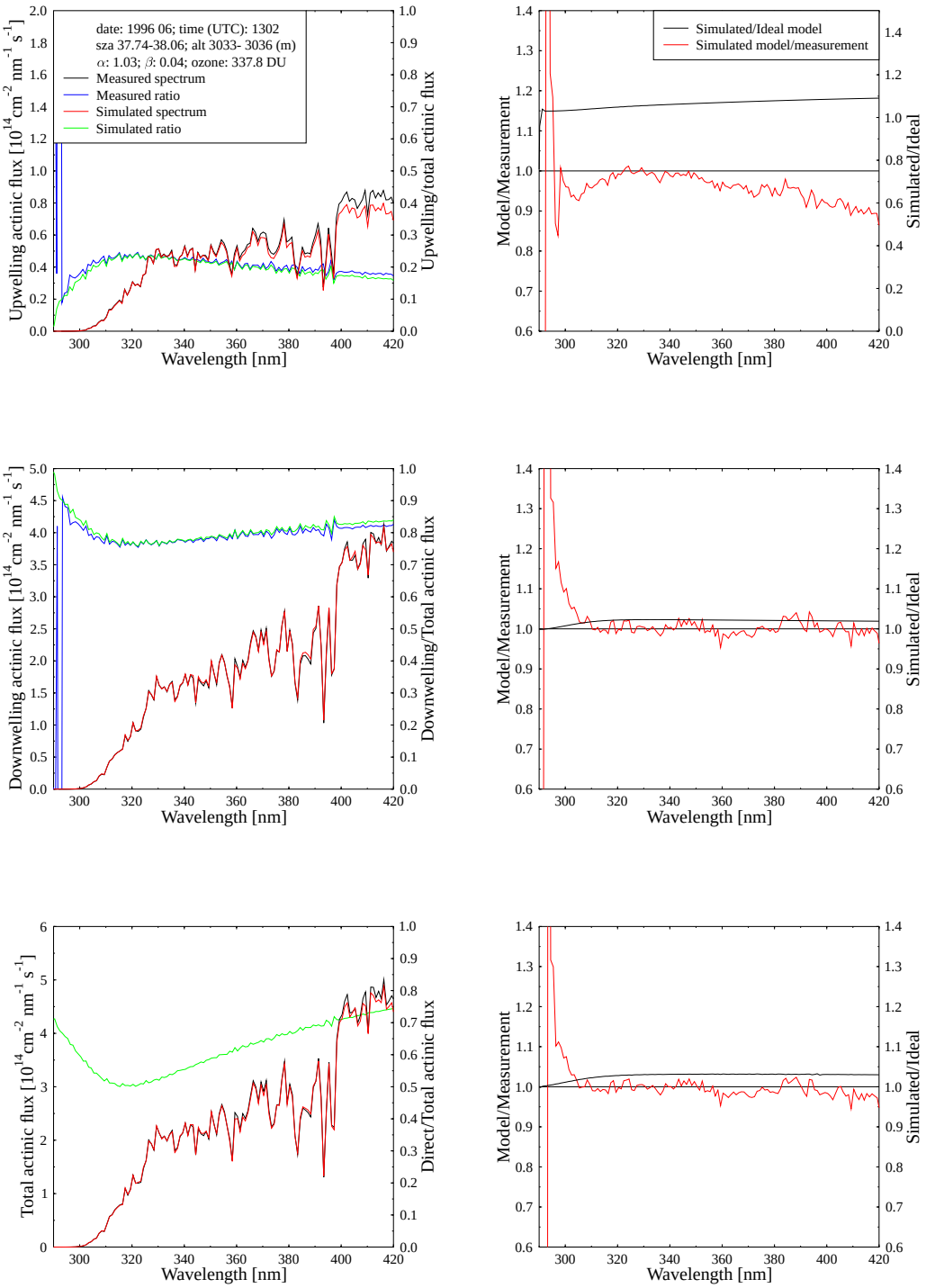

Figure 48: Same as Figure 10, except for 1302 UTC, 11 June 1996, and altitude 3034 m.a.s.l.

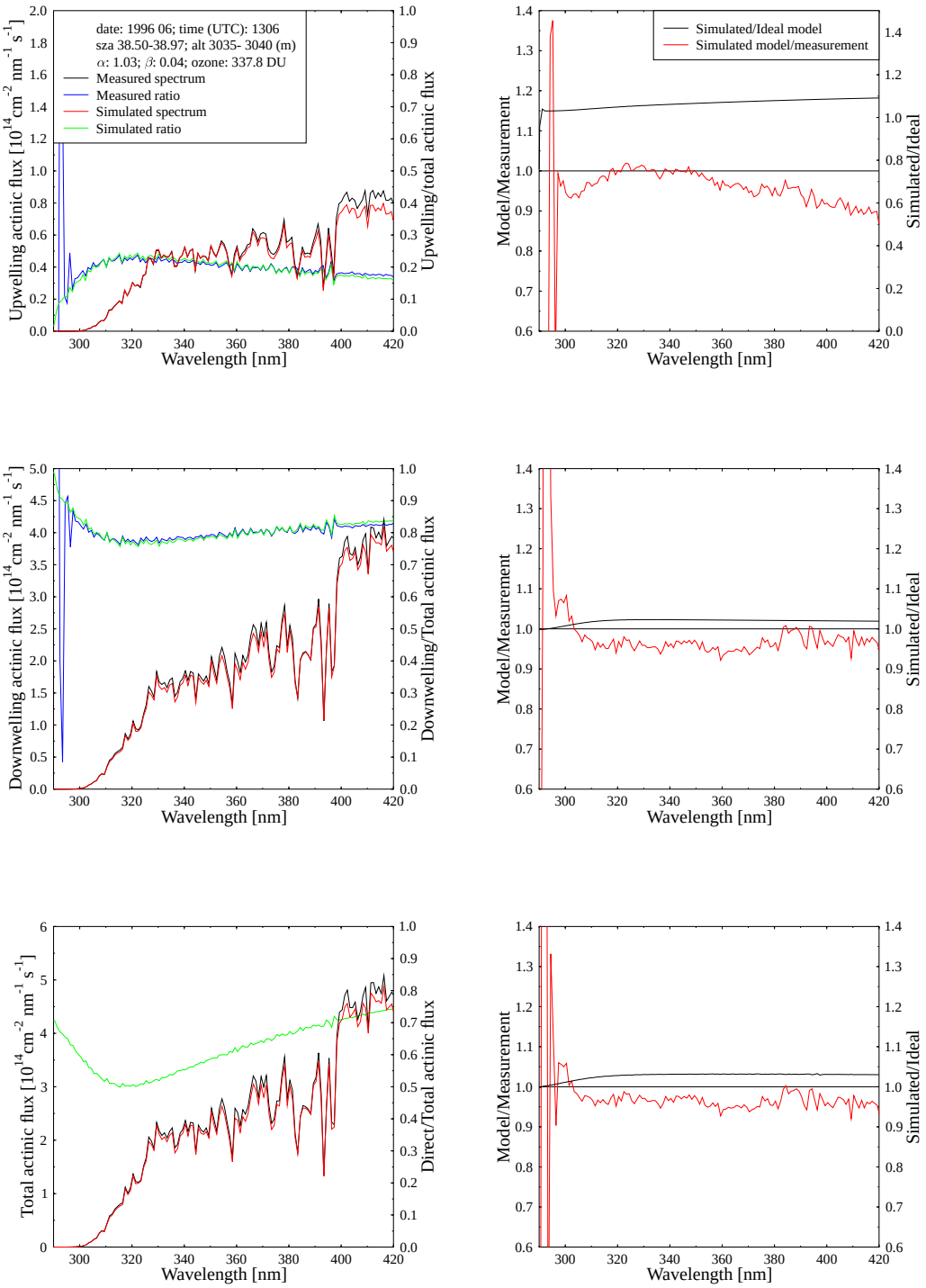

Figure 49: Same as Figure 10, except for 1306 UTC, 11 June 1996, and altitude 3038 m.a.s.l.

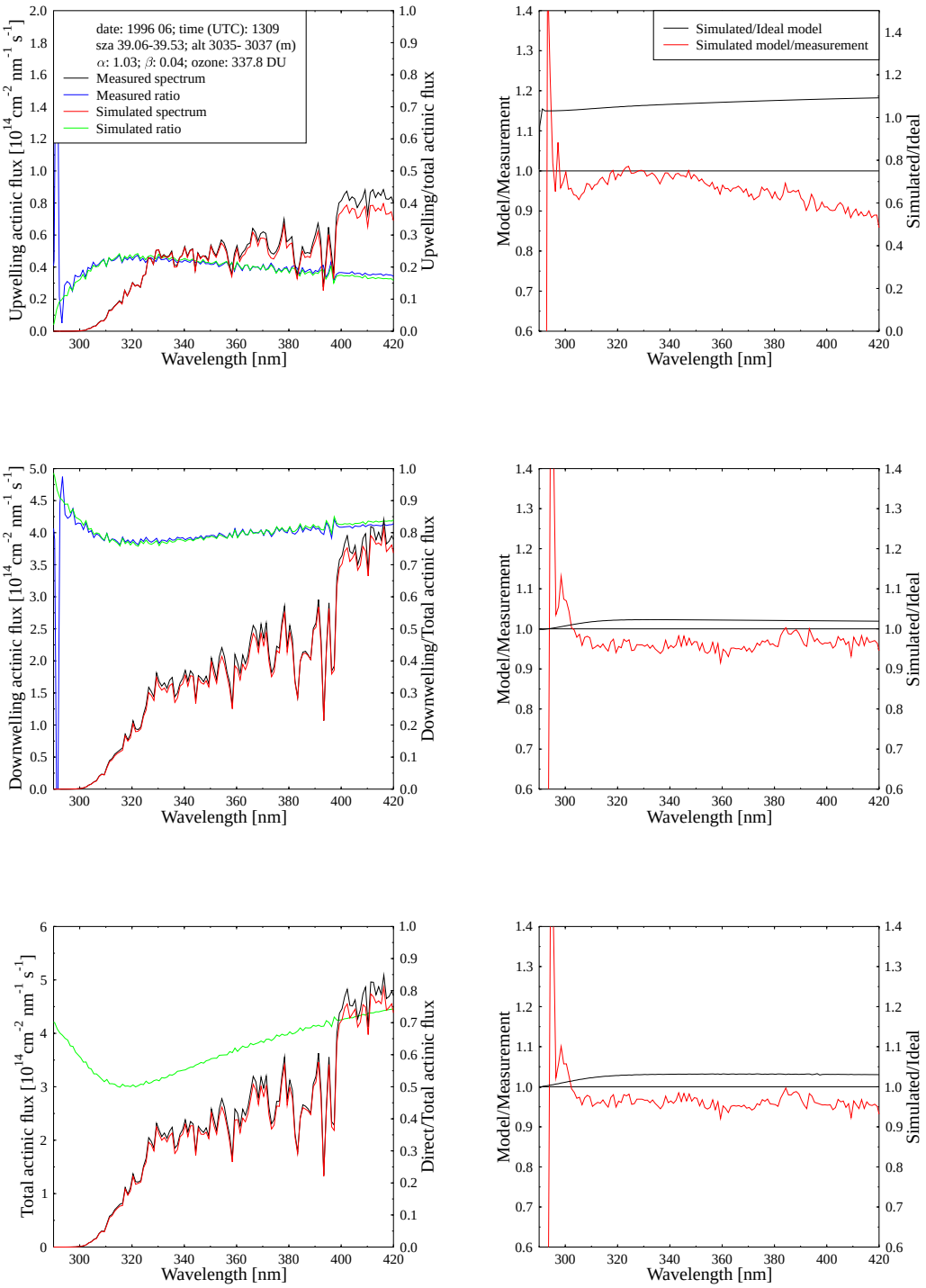

Figure 50: Same as Figure 10, except for 1309 UTC, 11 June 1996, and altitude 3035 m.a.s.l.

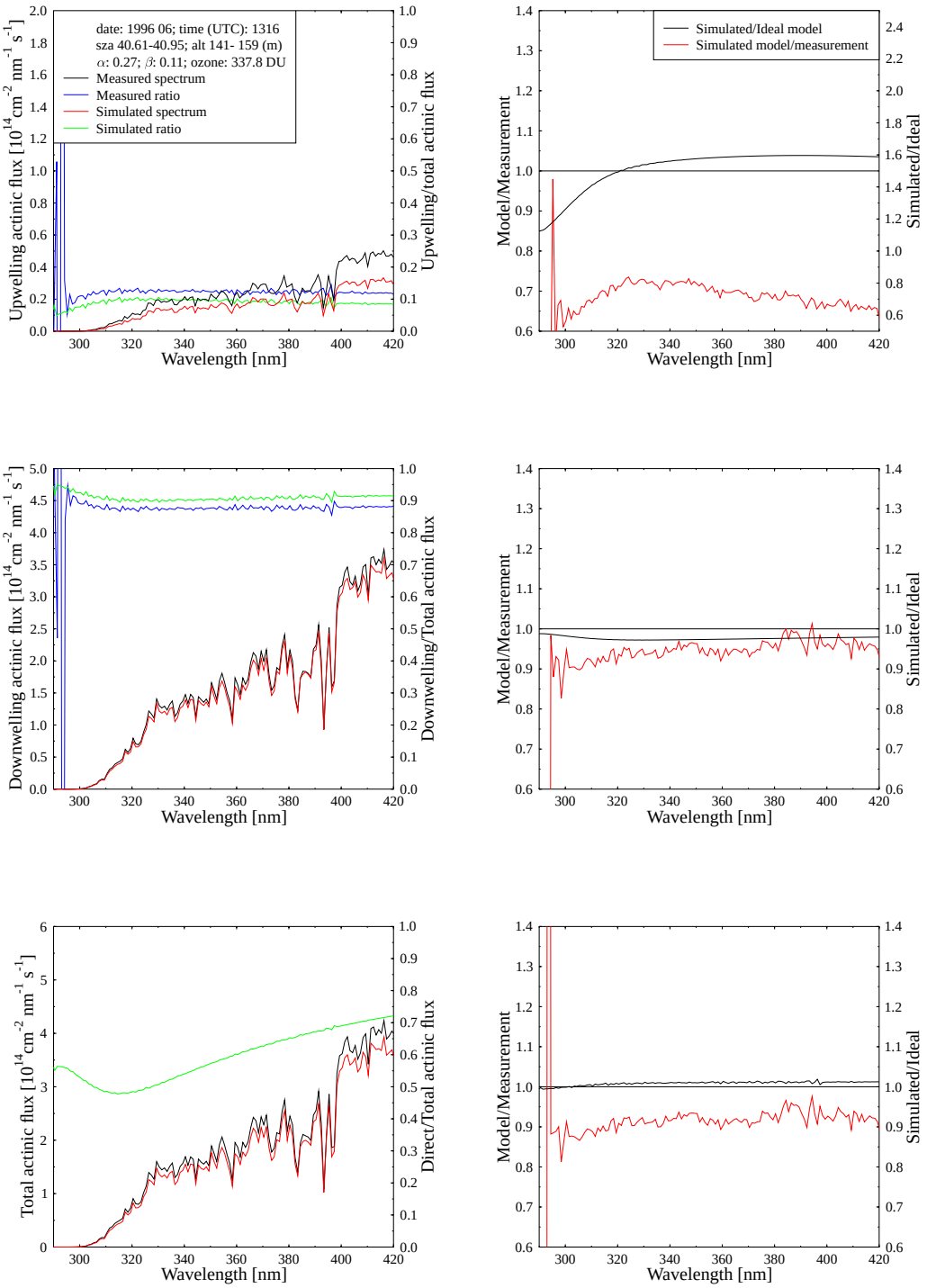

Figure 51: Same as Figure 10, except for 1316 UTC, 11 June 1996, and altitude 159 m.a.s.l.

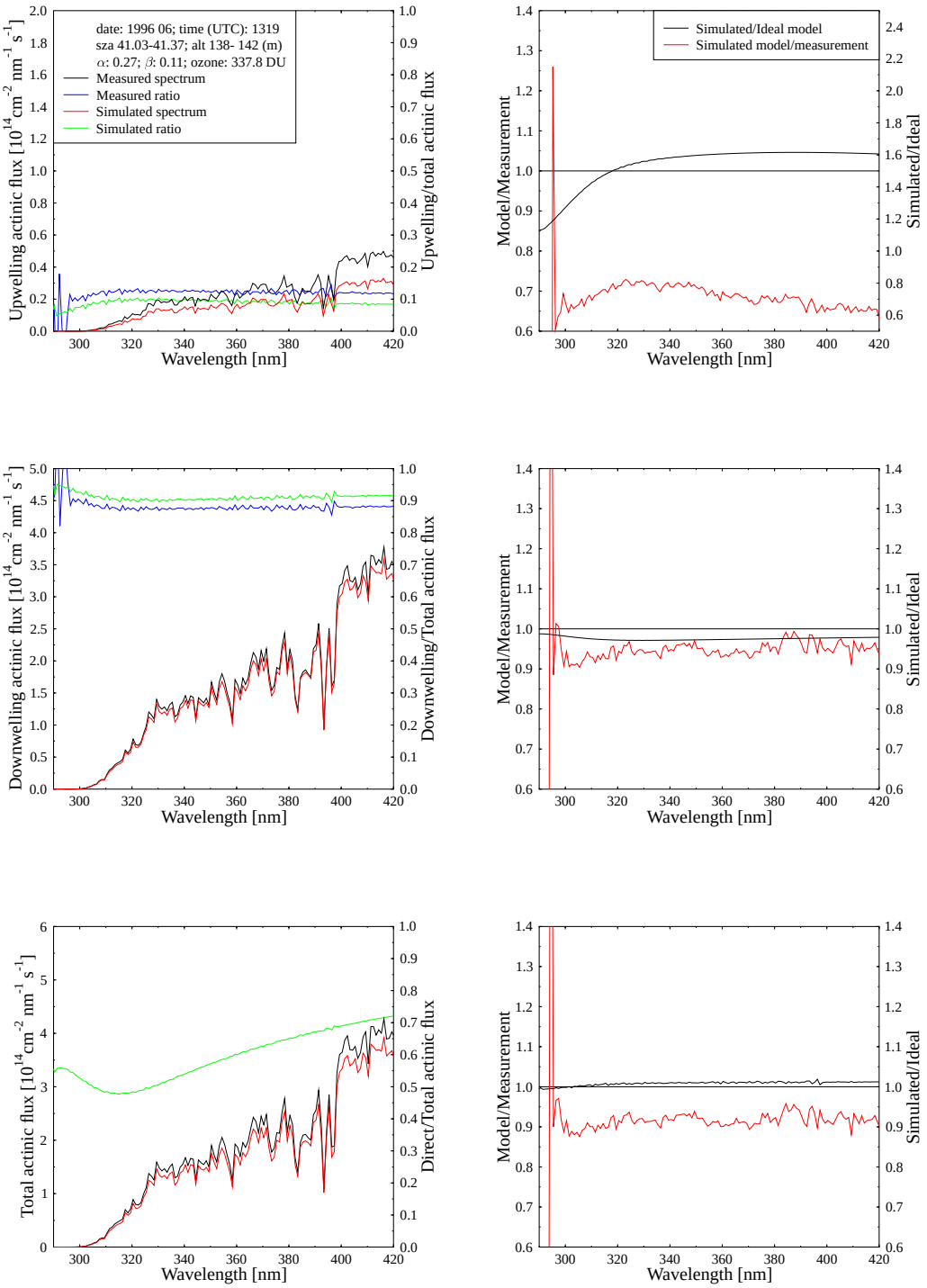

Figure 52: Same as Figure 10, except for 1319 UTC, 11 June 1996, and altitude 141 m.a.s.l.

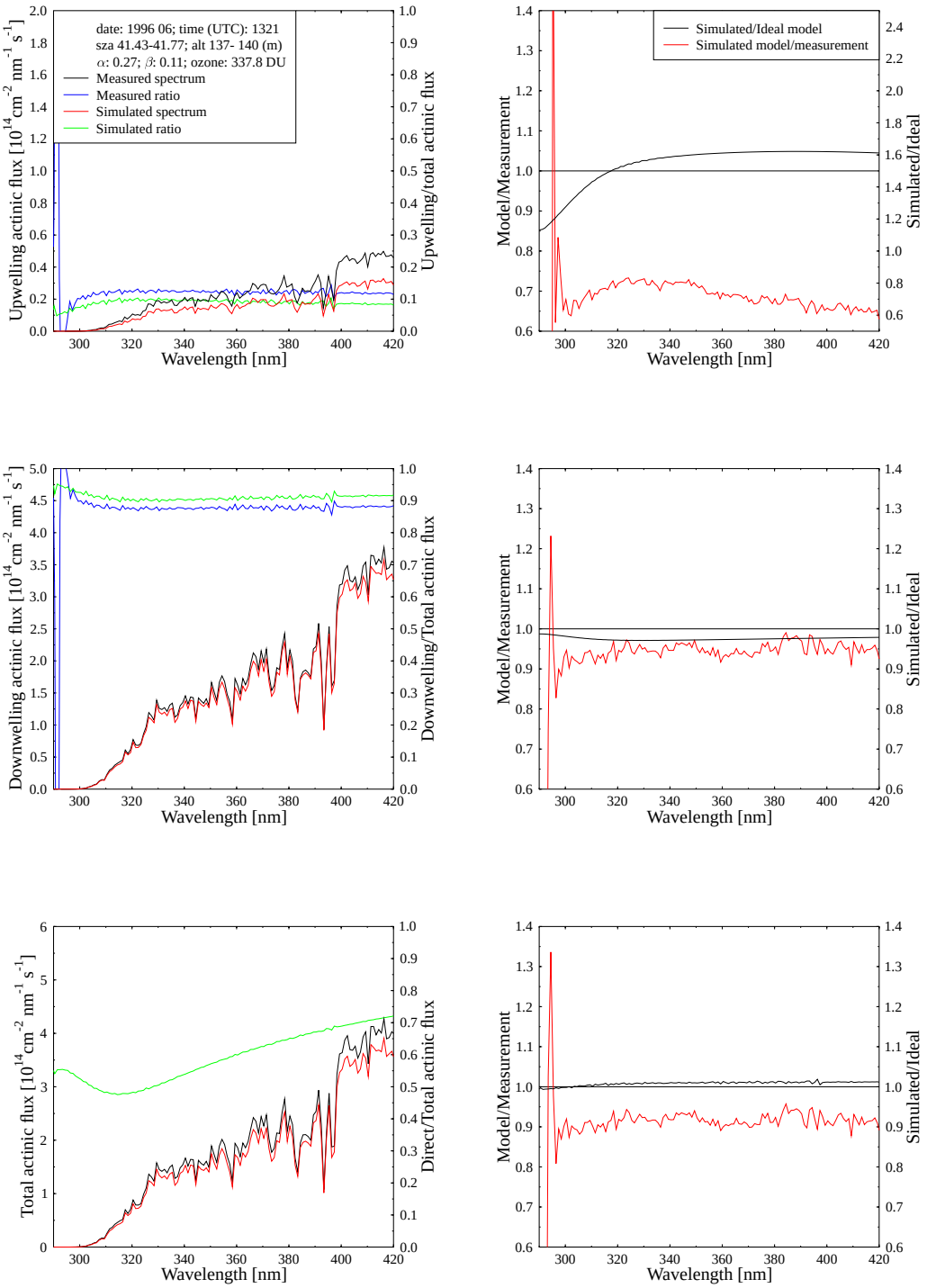

Figure 53: Same as Figure 10, except for 1321 UTC, 11 June 1996, and altitude 140 m.a.s.l.

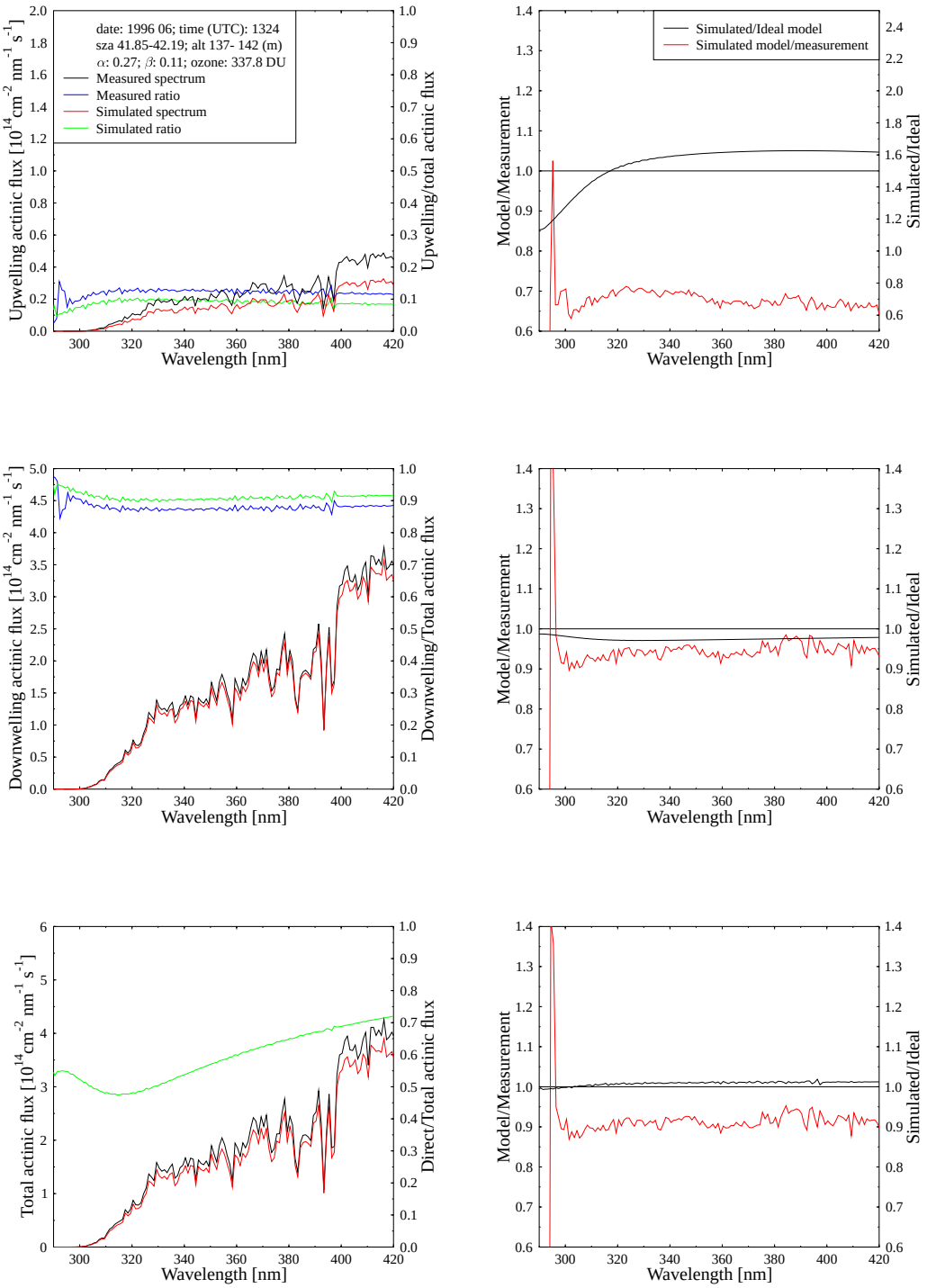

Figure 54: Same as Figure 10, except for 1324 UTC, 11 June 1996, and altitude 142 m.a.s.l.

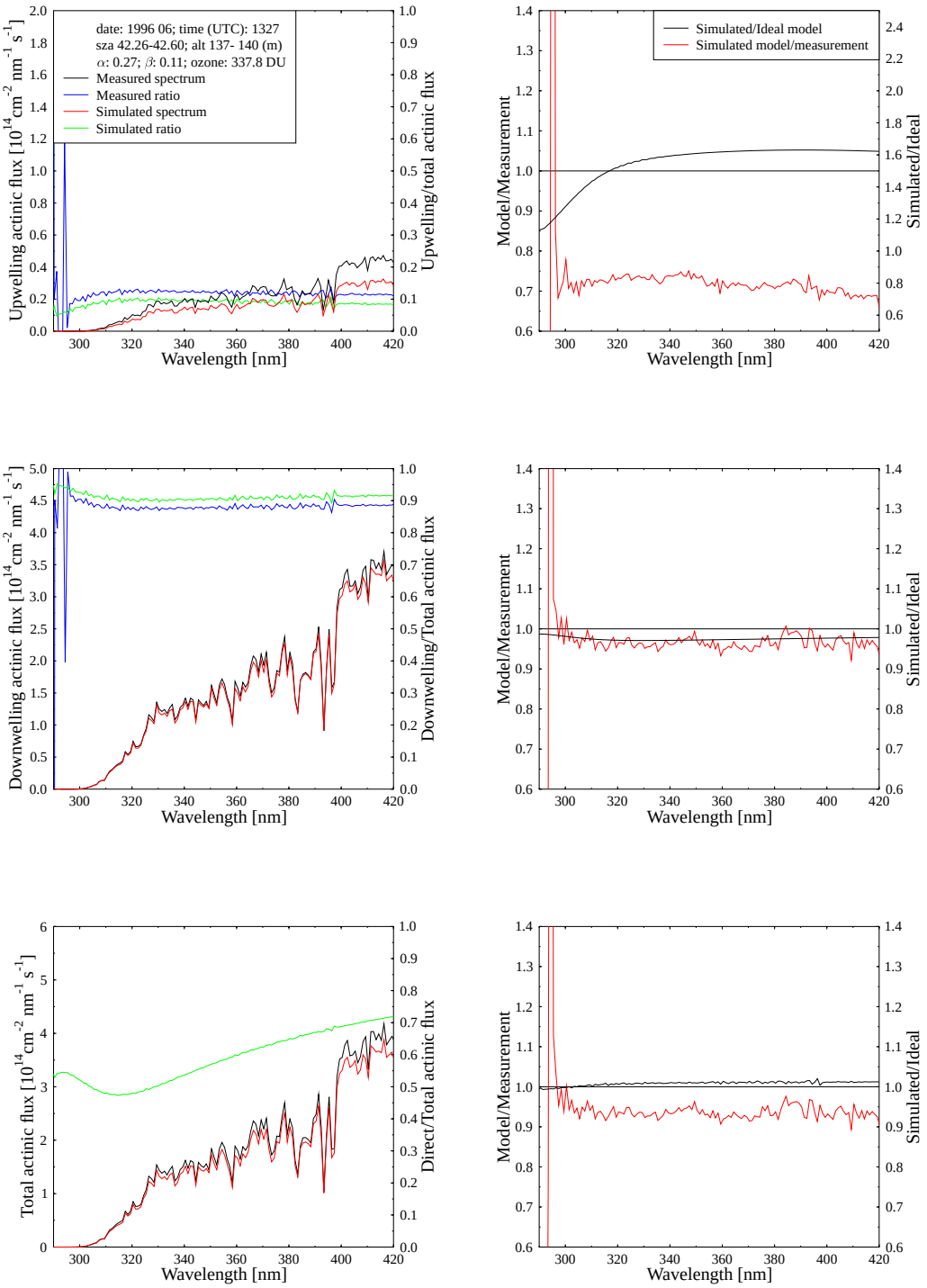

Figure 55: Same as Figure 10, except for 1327 UTC, 11 June 1996, and altitude 138 m.a.s.l.

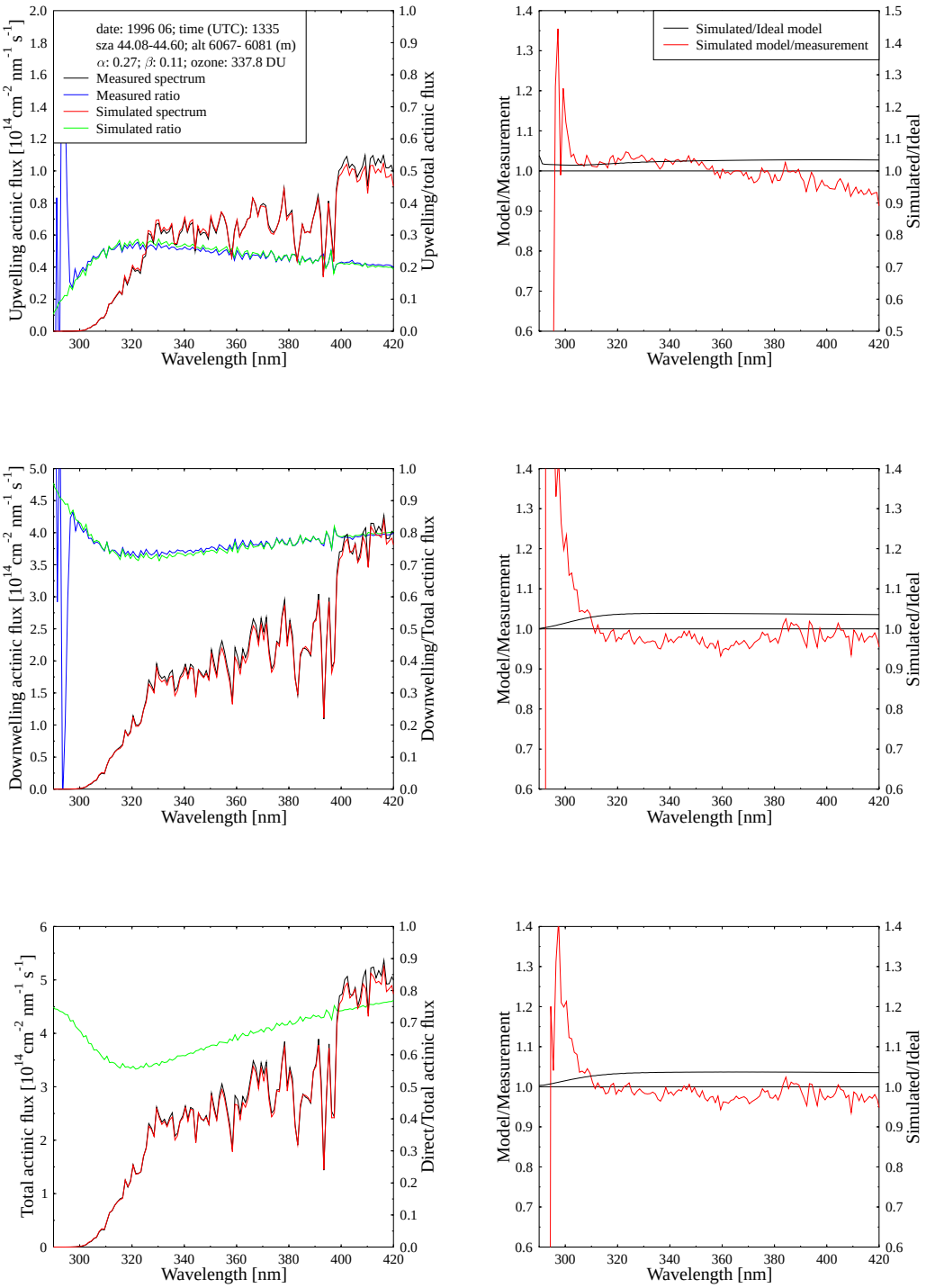

Figure 56: Same as Figure 10, except for 1335 UTC, 11 June 1996, and altitude 6077 m.a.s.l.

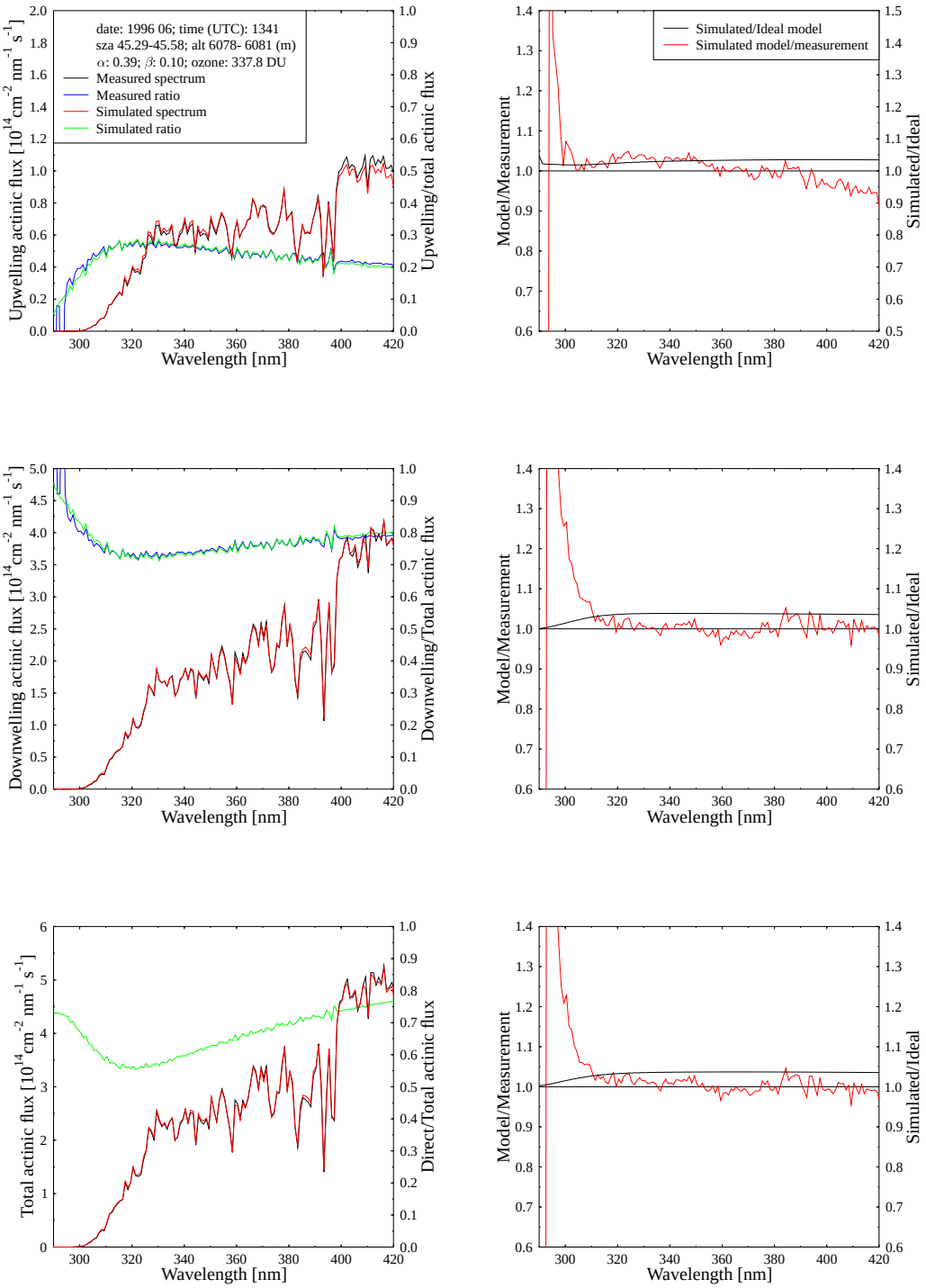

Figure 57: Same as Figure 10, except for 1341 UTC, 11 June 1996, and altitude 6080.82 m.a.s.l.

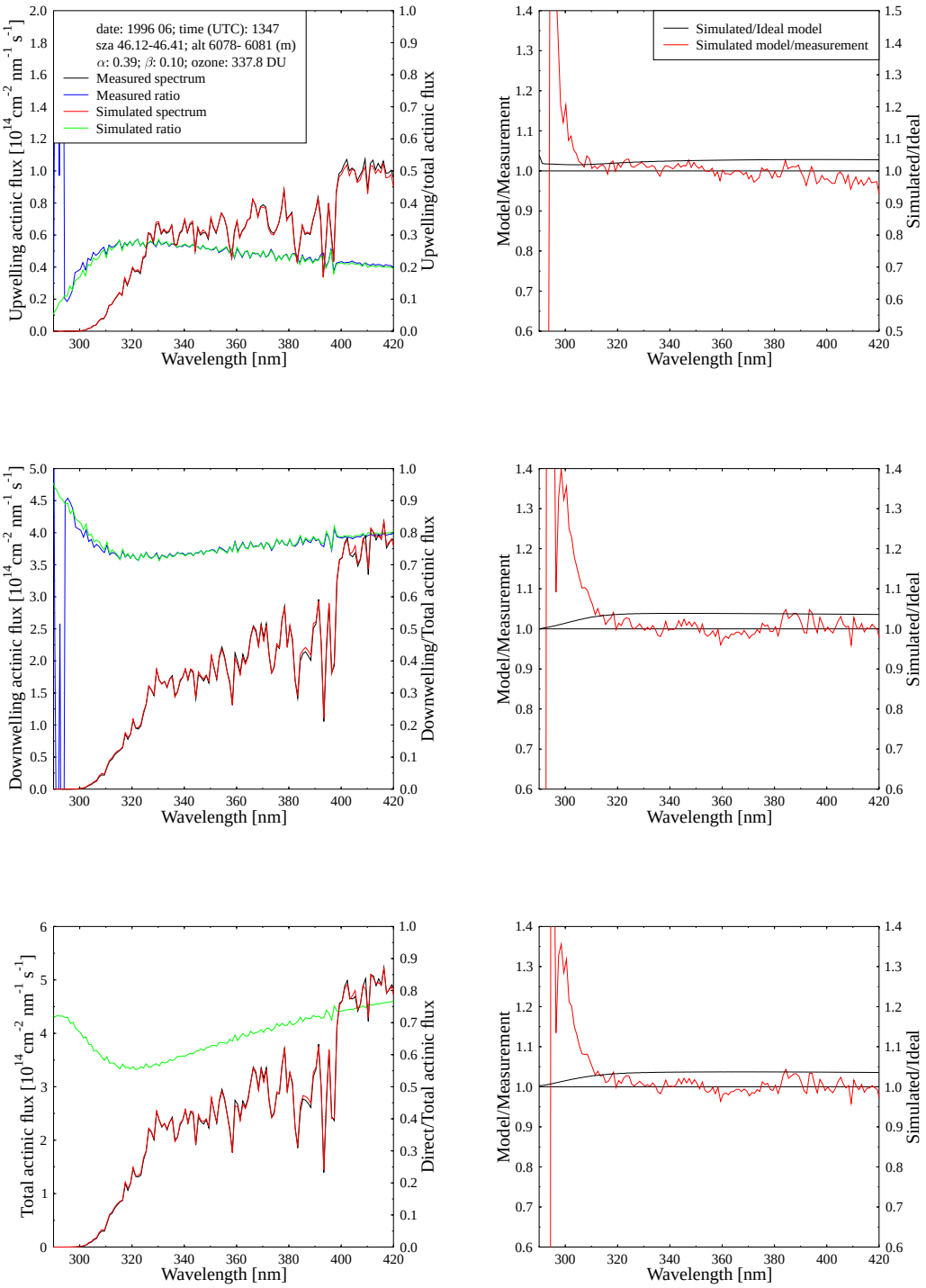

Figure 58: Same as Figure 10, except for 1347 UTC, 11 June 1996, and altitude 6079 m.a.s.l.

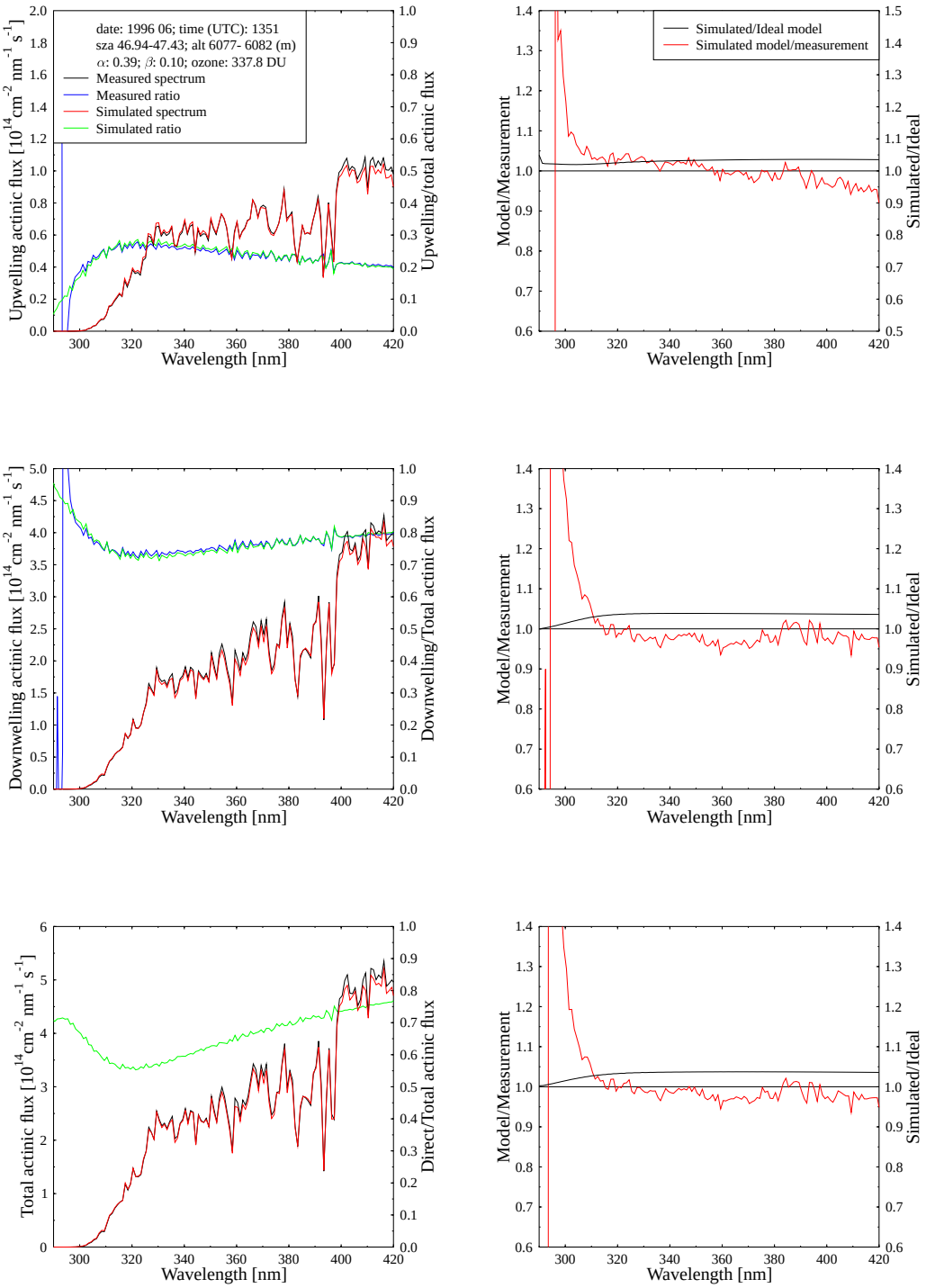

Figure 59: Same as Figure 10, except for 1351 UTC, 11 June 1996, and altitude 6077 m.a.s.l.

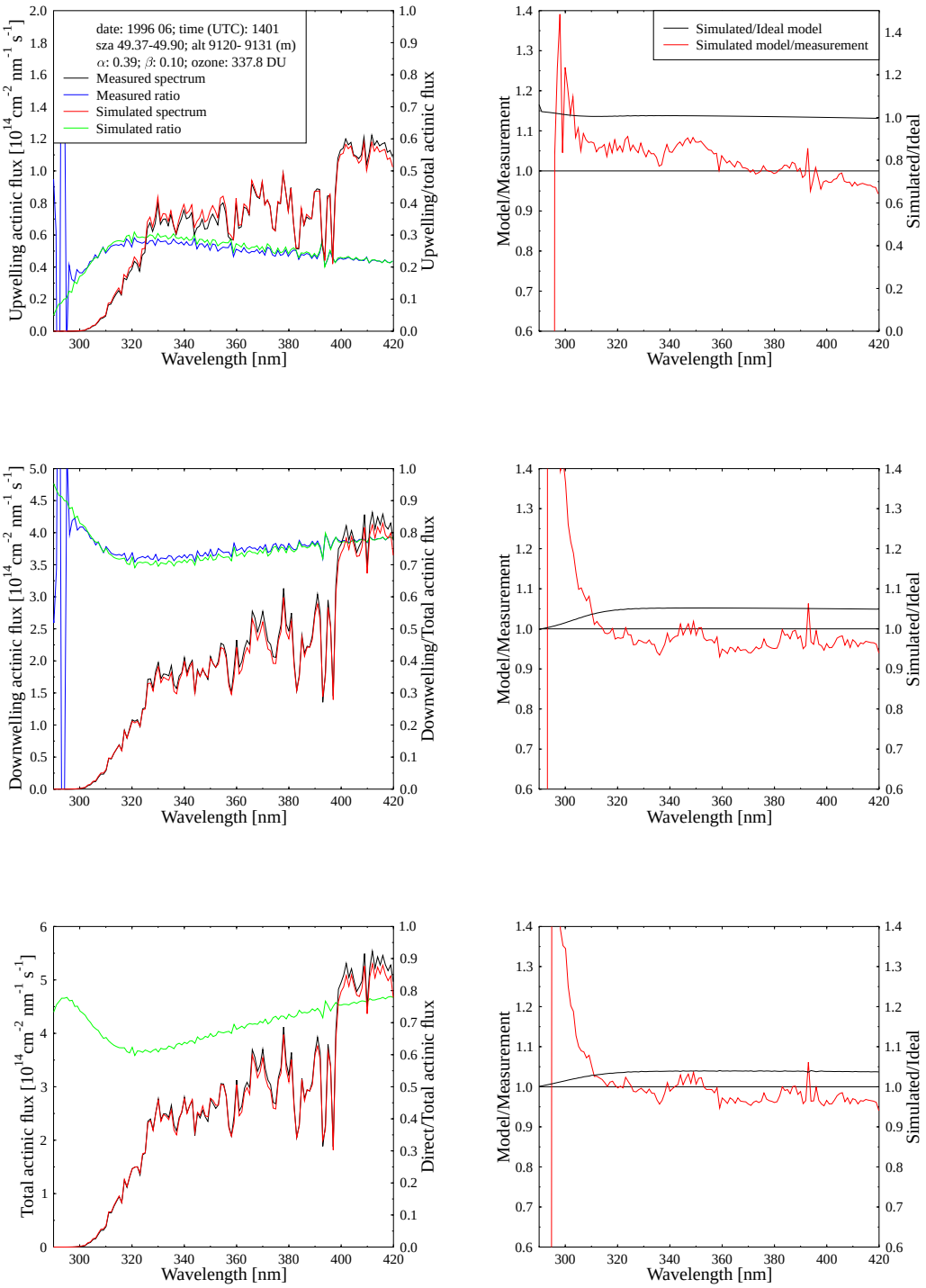

Figure 60: Same as Figure 10, except for 1401 UTC, 11 June 1996, and altitude 9120.21 m.a.s.l.

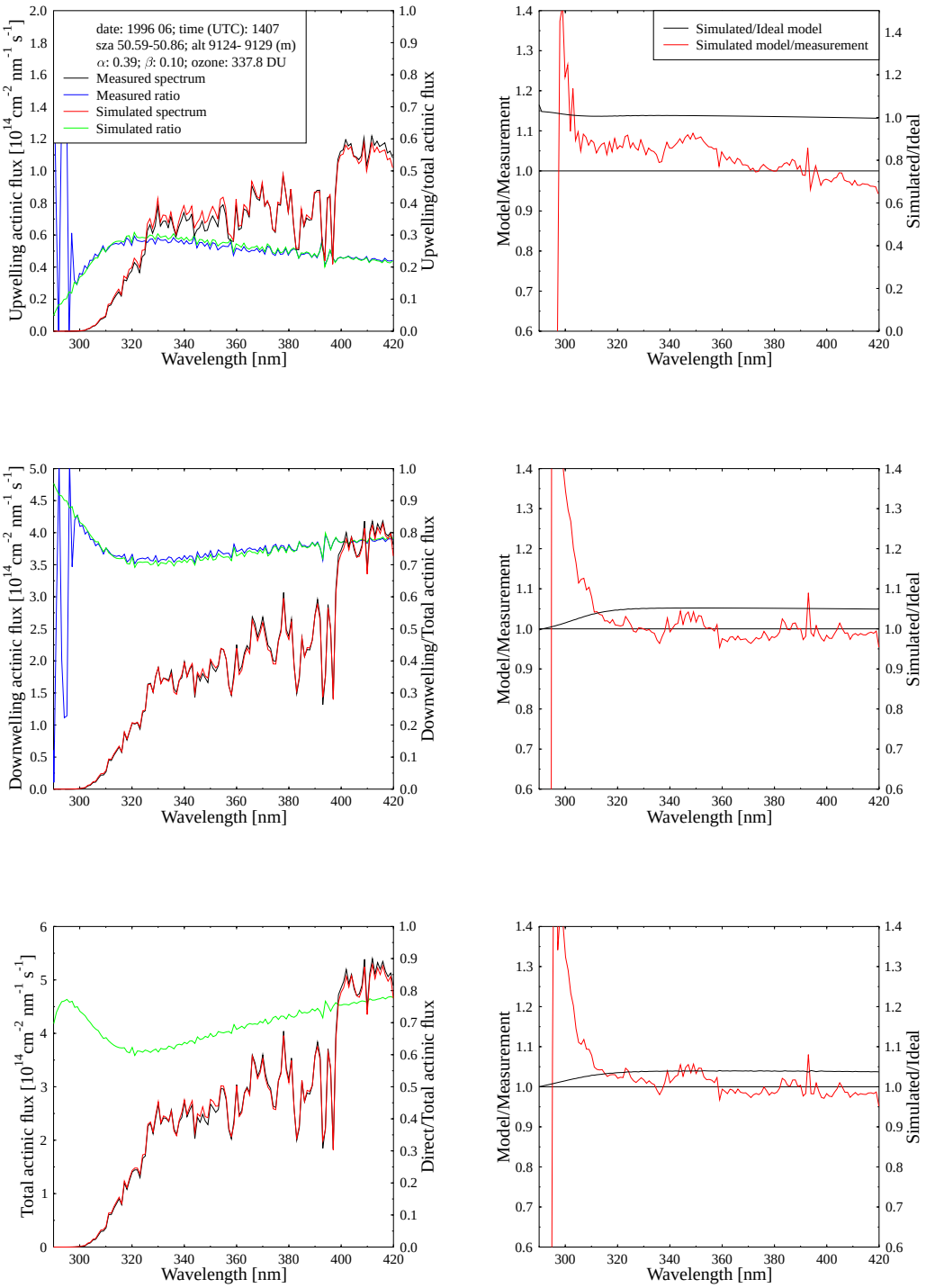

Figure 61: Same as Figure 10, except for 1407 UTC, 11 June 1996, and altitude 9124 m.a.s.l.

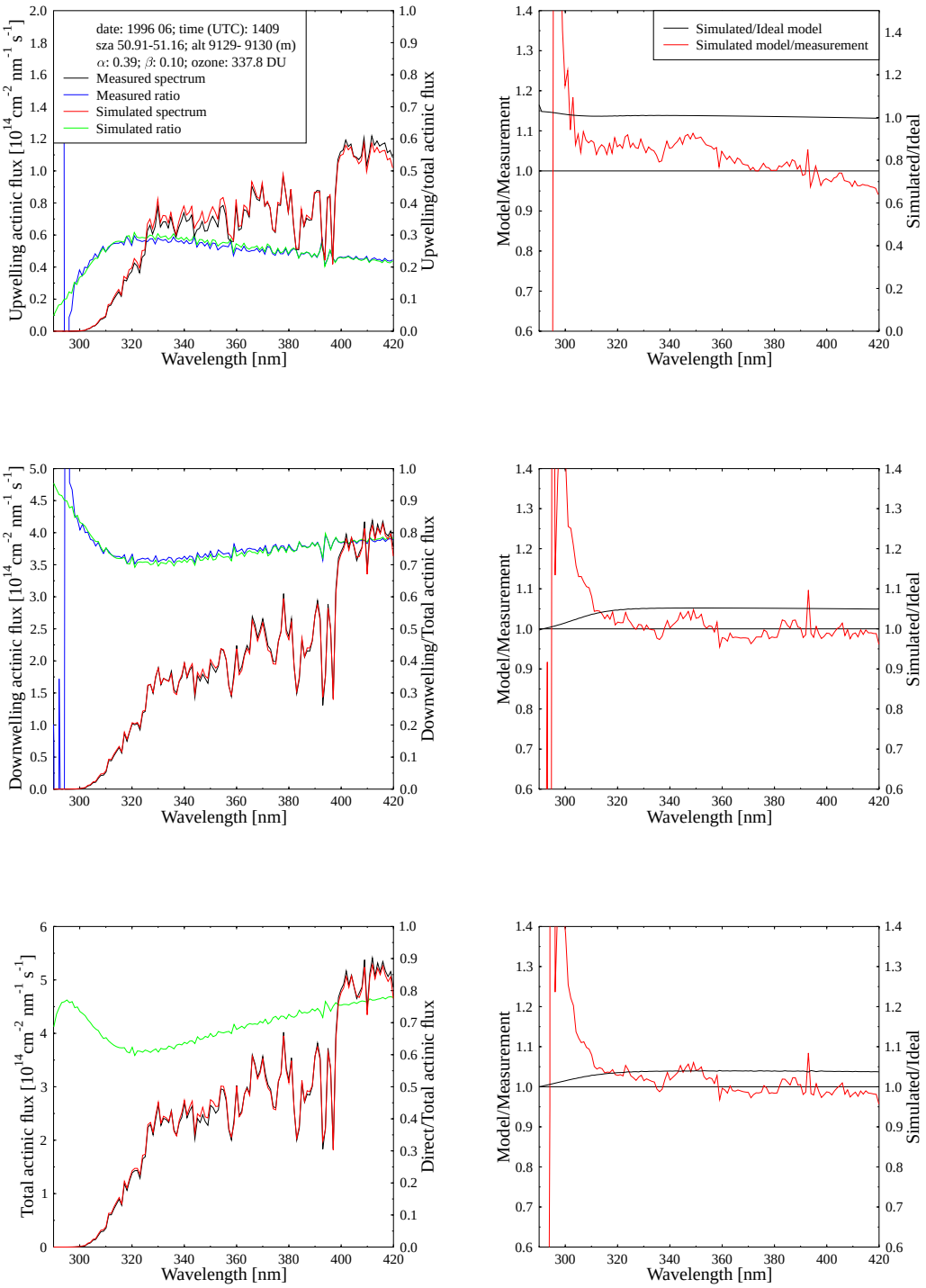

Figure 62: Same as Figure 10, except for 1409 UTC, 11 June 1996, and altitude 9130 m.a.s.l.

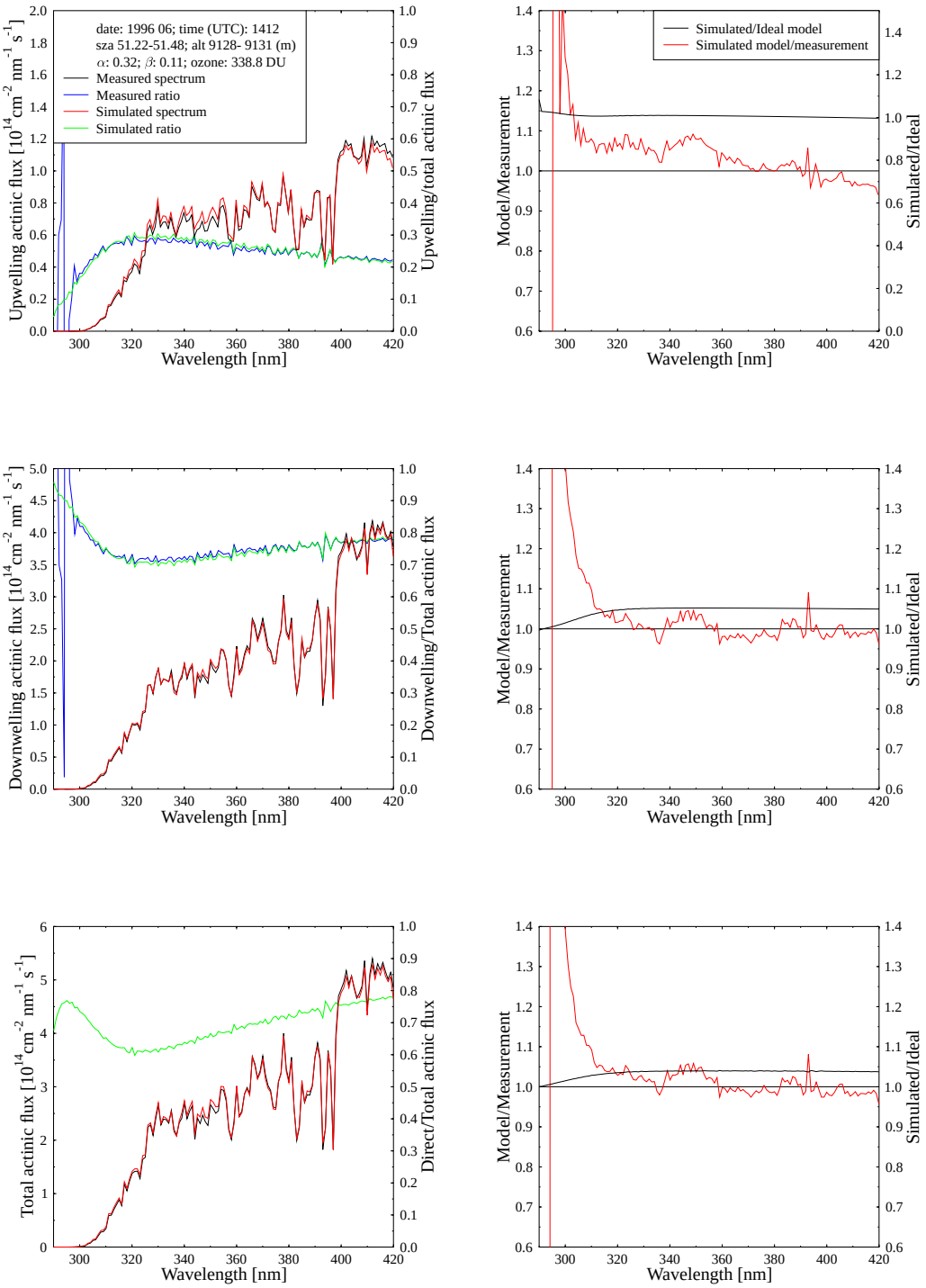

Figure 63: Same as Figure 10, except for 1412 UTC, 11 June 1996, and altitude 9130 m.a.s.l.

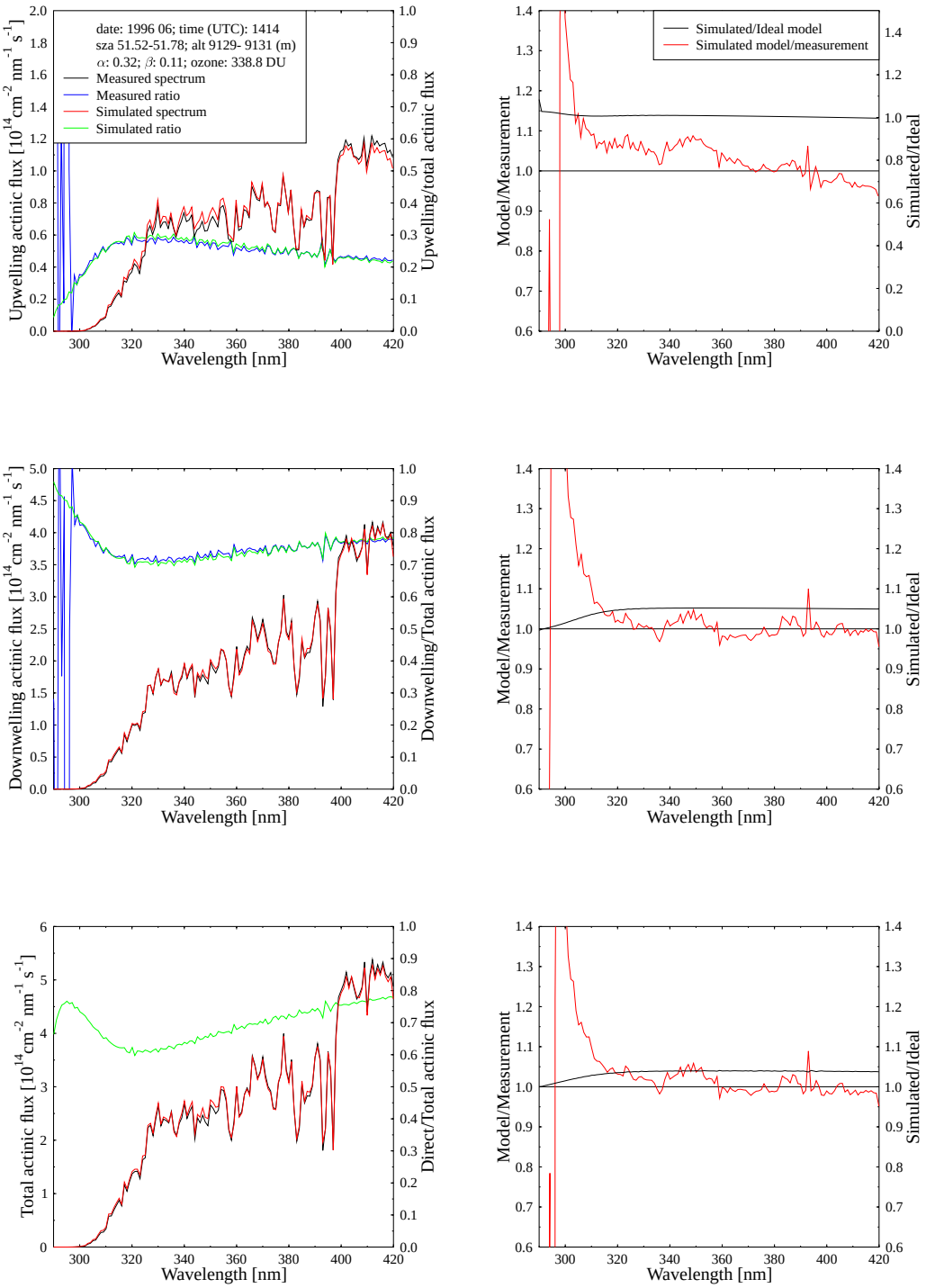

Figure 64: Same as Figure 10, except for 1414 UTC, 11 June 1996, and altitude 9129 m.a.s.l.

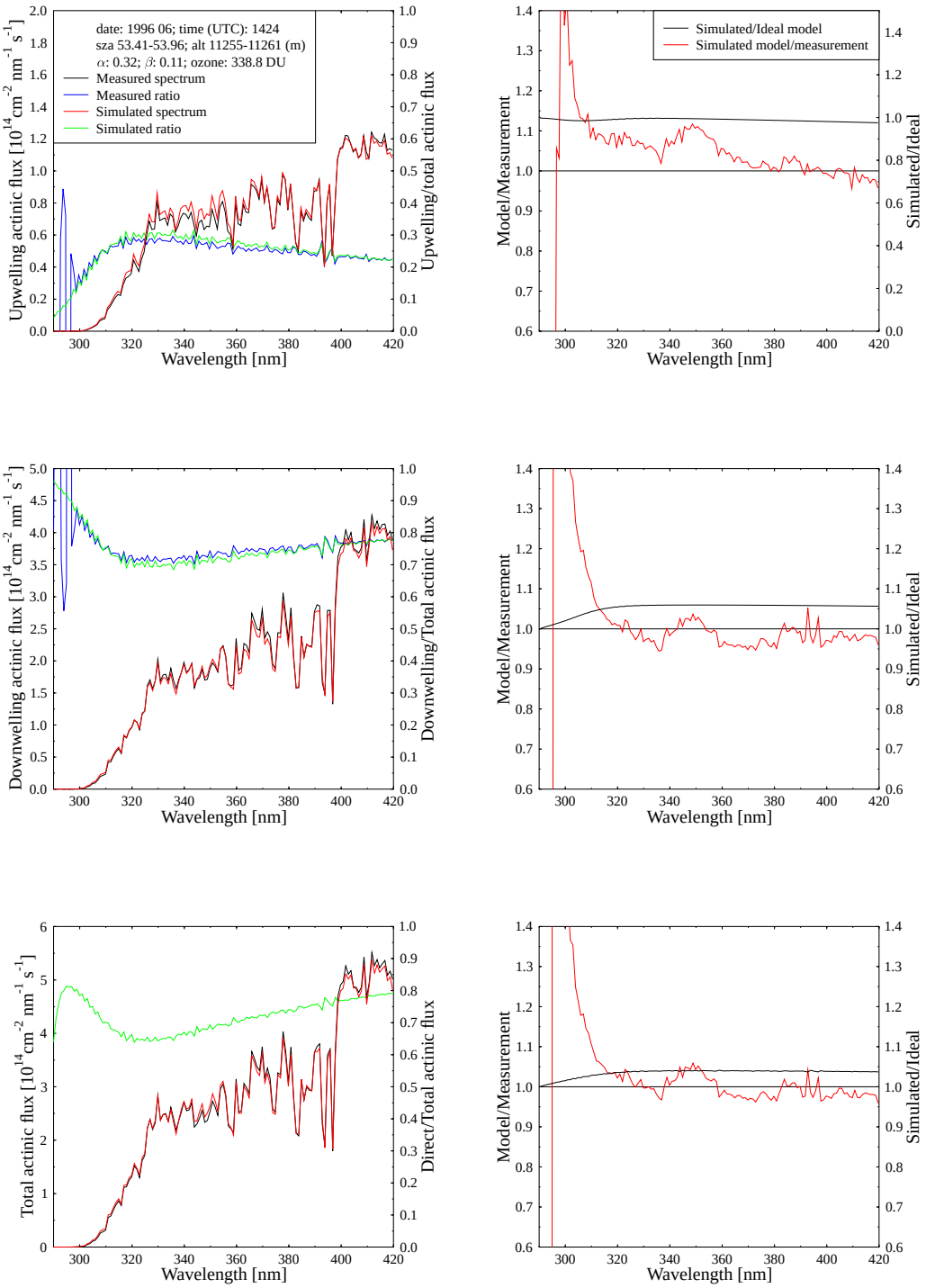

Figure 65: Same as Figure 10, except for 1424 UTC, 11 June 1996, and altitude 11258 m.a.s.l.

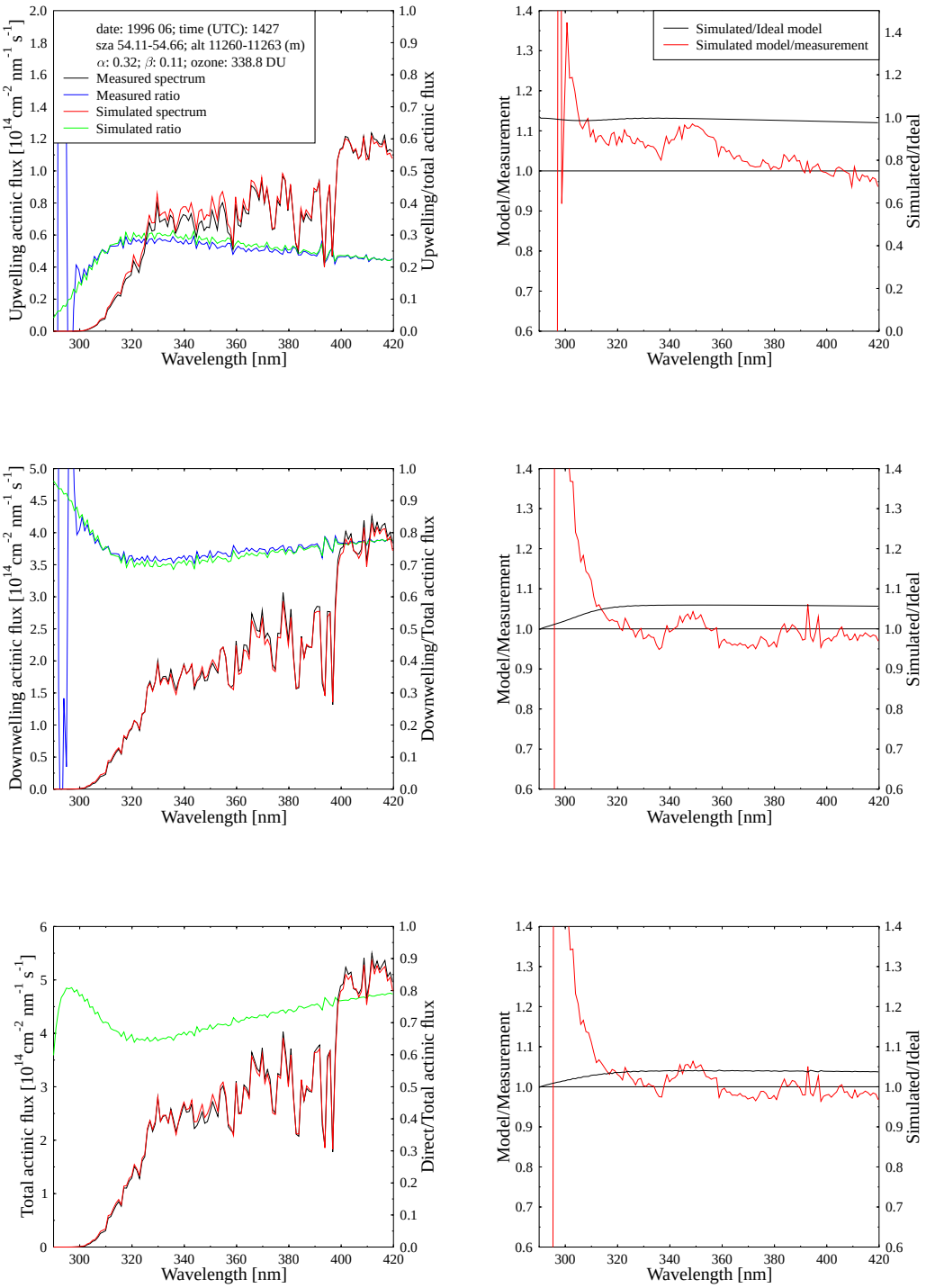

Figure 66: Same as Figure 10, except for 1427 UTC, 11 June 1996, and altitude 11262 m.a.s.l.

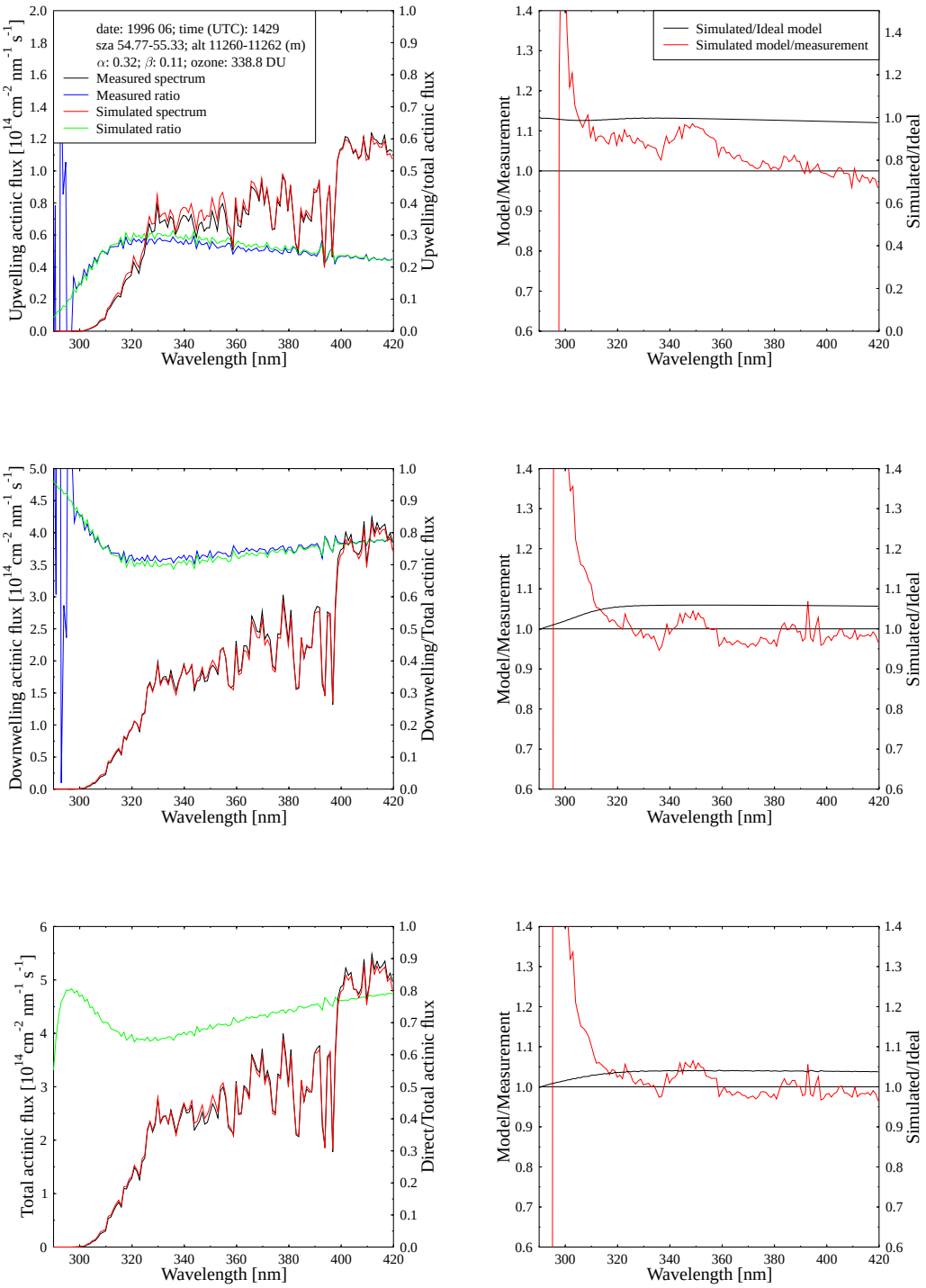

Figure 67: Same as Figure 10, except for 1429 UTC, 11 June 1996, and altitude 11260 m.a.s.l.

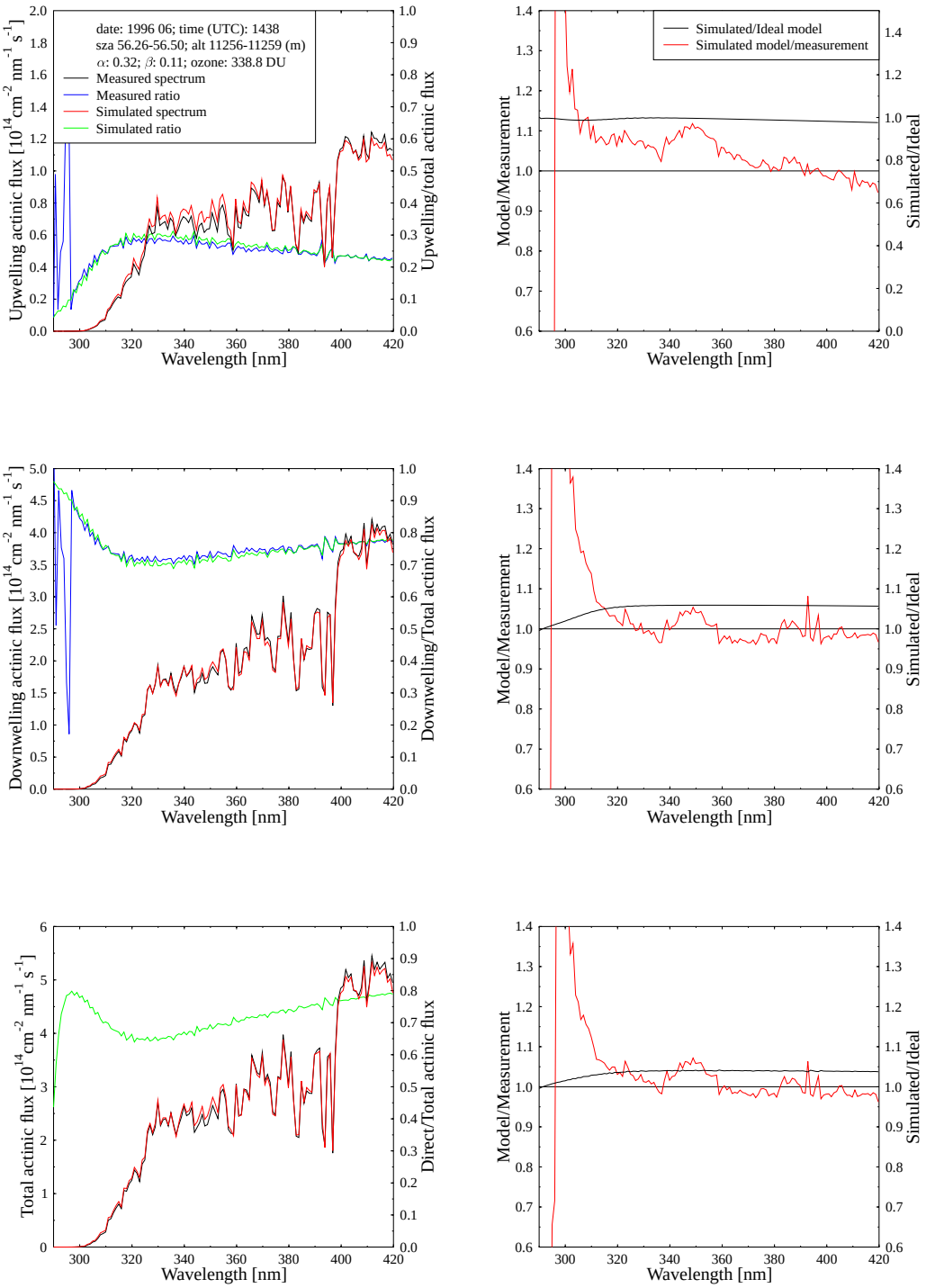

Figure 68: Same as Figure 10, except for 1438 UTC, 11 June 1996, and altitude 11259 m.a.s.l.

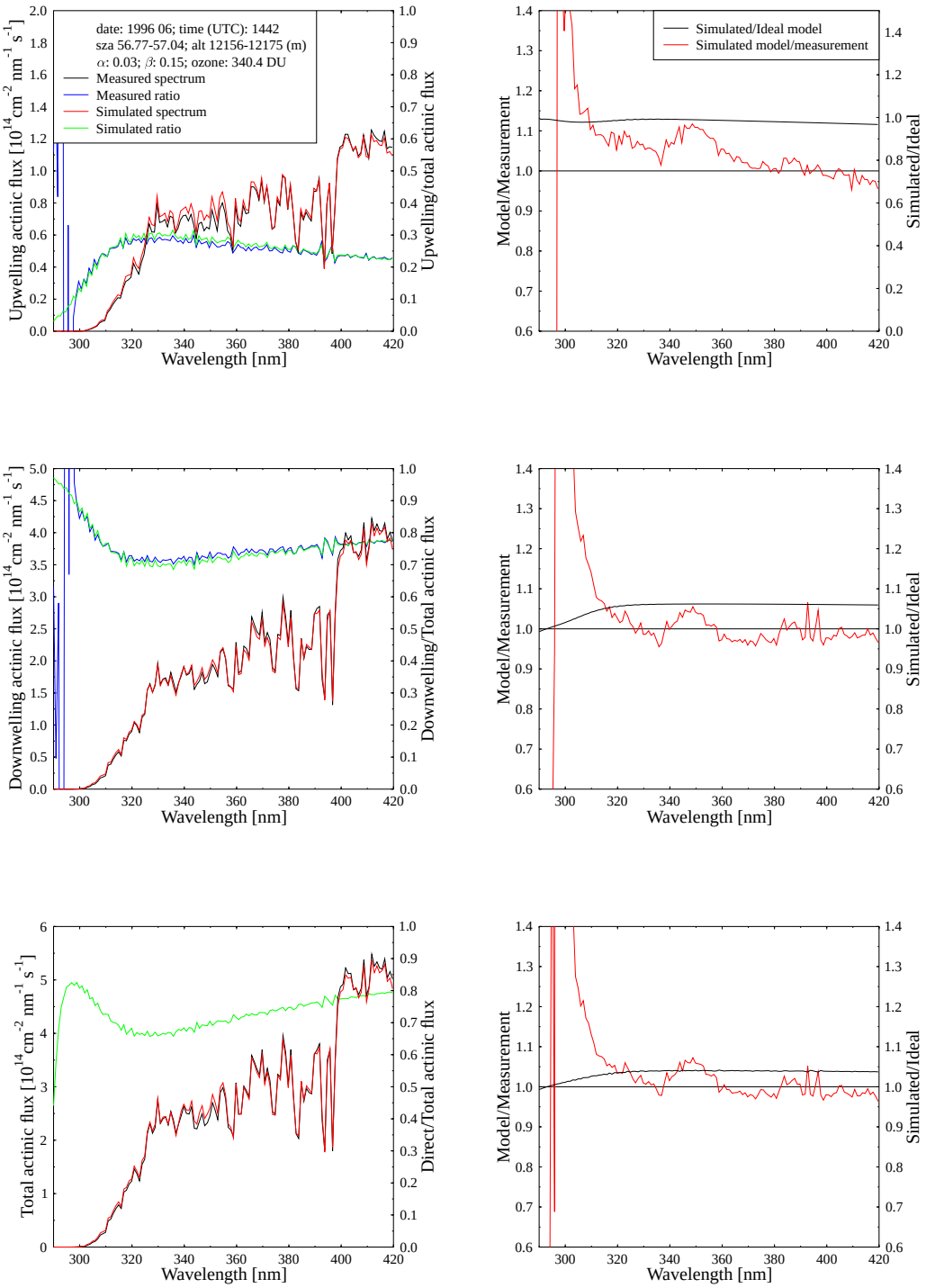

Figure 69: Same as Figure 10, except for 1442 UTC, 11 June 1996, and altitude 12156 m.a.s.l.

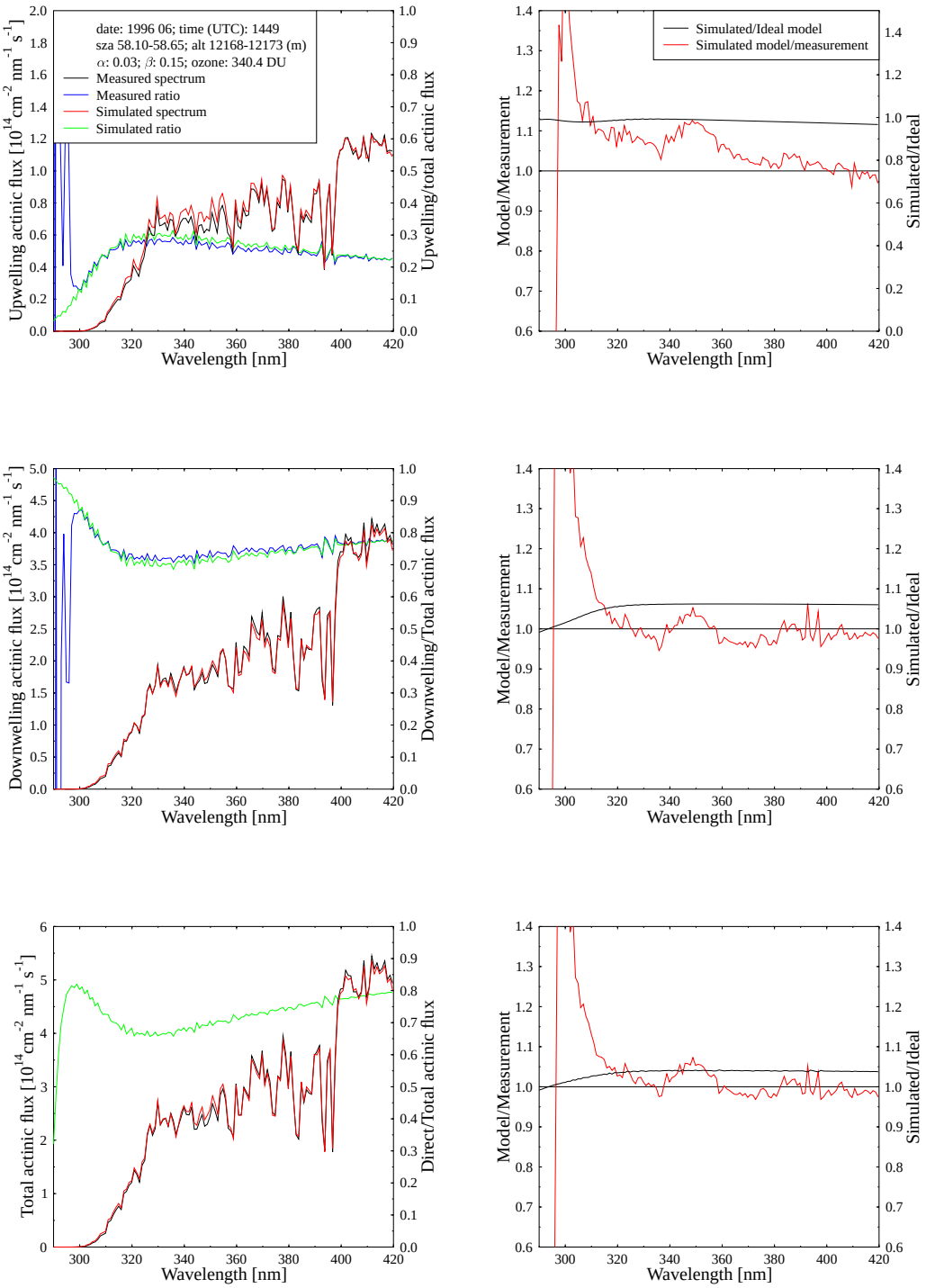

Figure 70: Same as Figure 10, except for 1449 UTC, 11 June 1996, and altitude 12171 m.a.s.l.

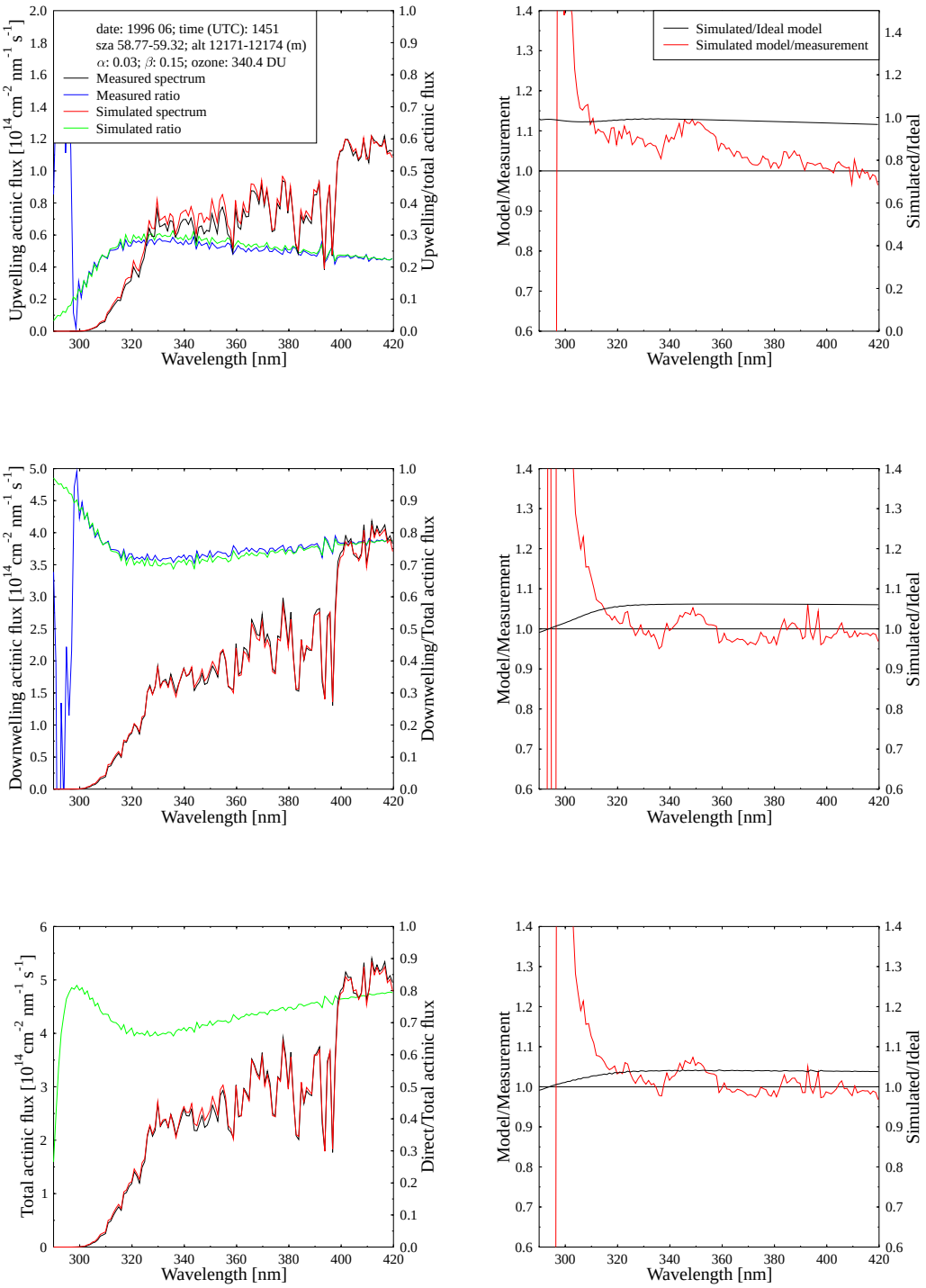

Figure 71: Same as Figure 10, except for 1451 UTC, 11 June 1996, and altitude 12173 m.a.s.l.

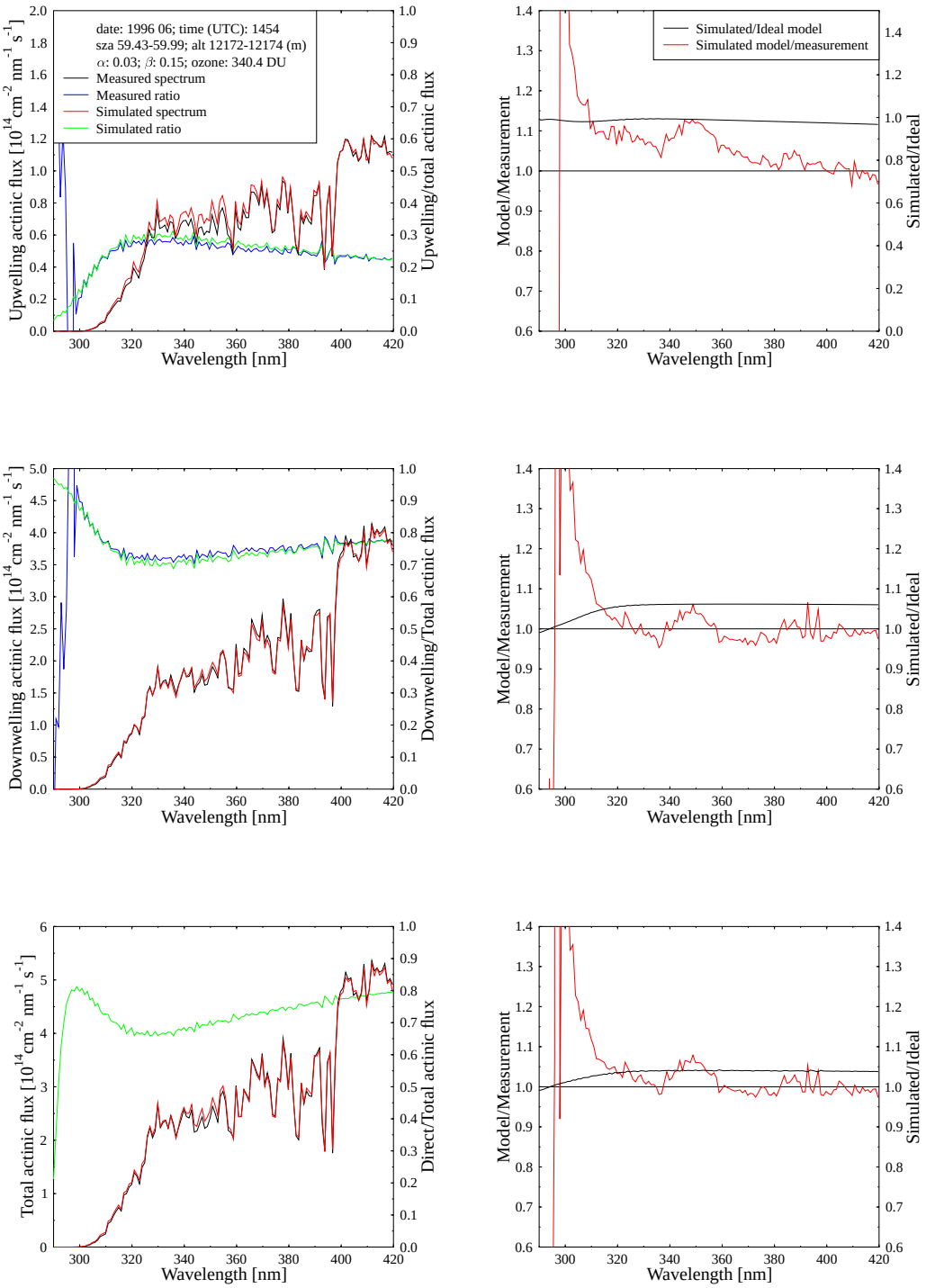

Figure 72: Same as Figure 10, except for 1454 UTC, 11 June 1996, and altitude 12173.01 m.a.s.l.

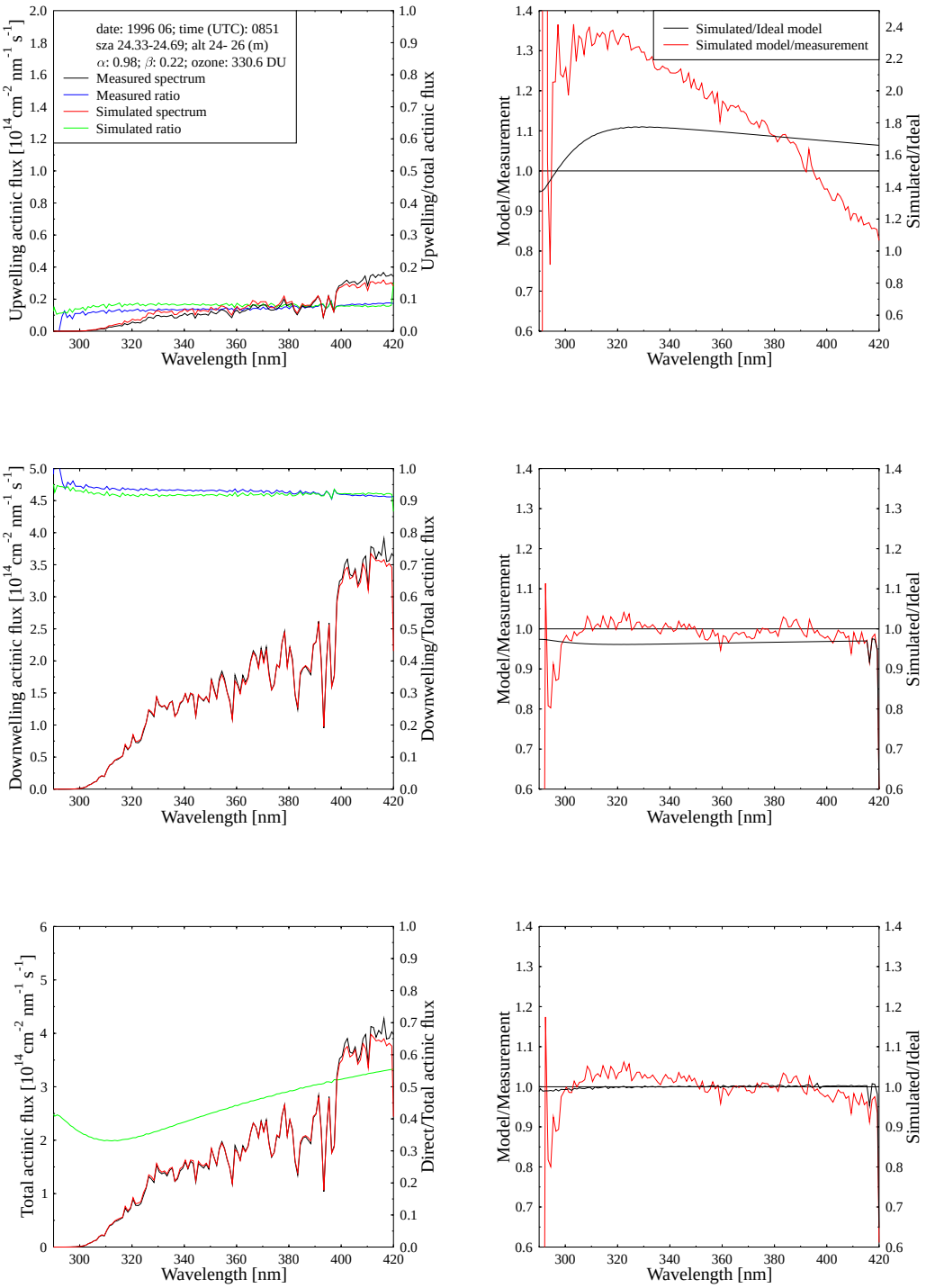

Figure 73: Same as Figure 10, except for 0851 UTC, 13 June 1996, and altitude 24.12 m.a.s.l.

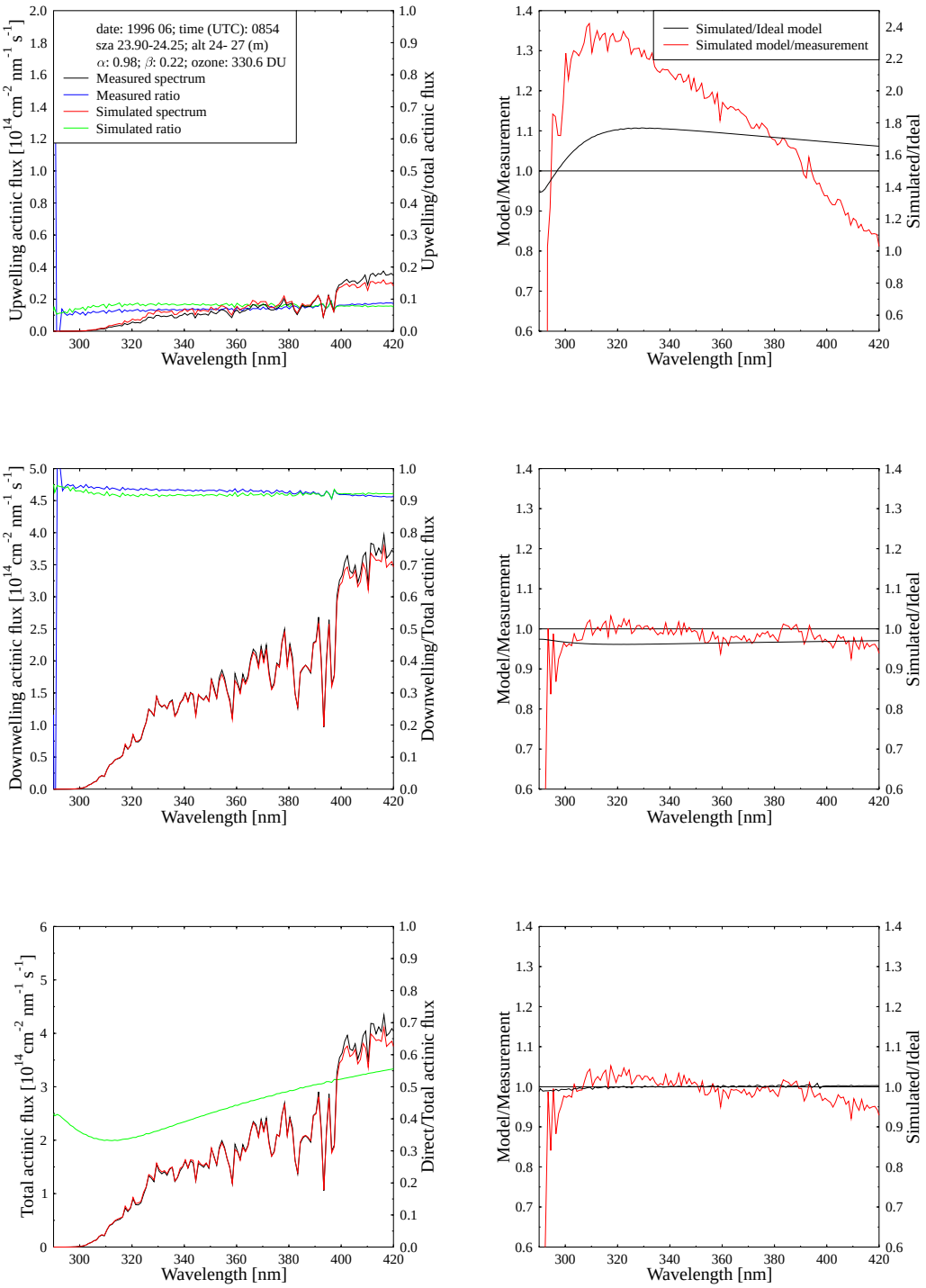

Figure 74: Same as Figure 10, except for 0854 UTC, 13 June 1996, and altitude 27.92 m.a.s.l.

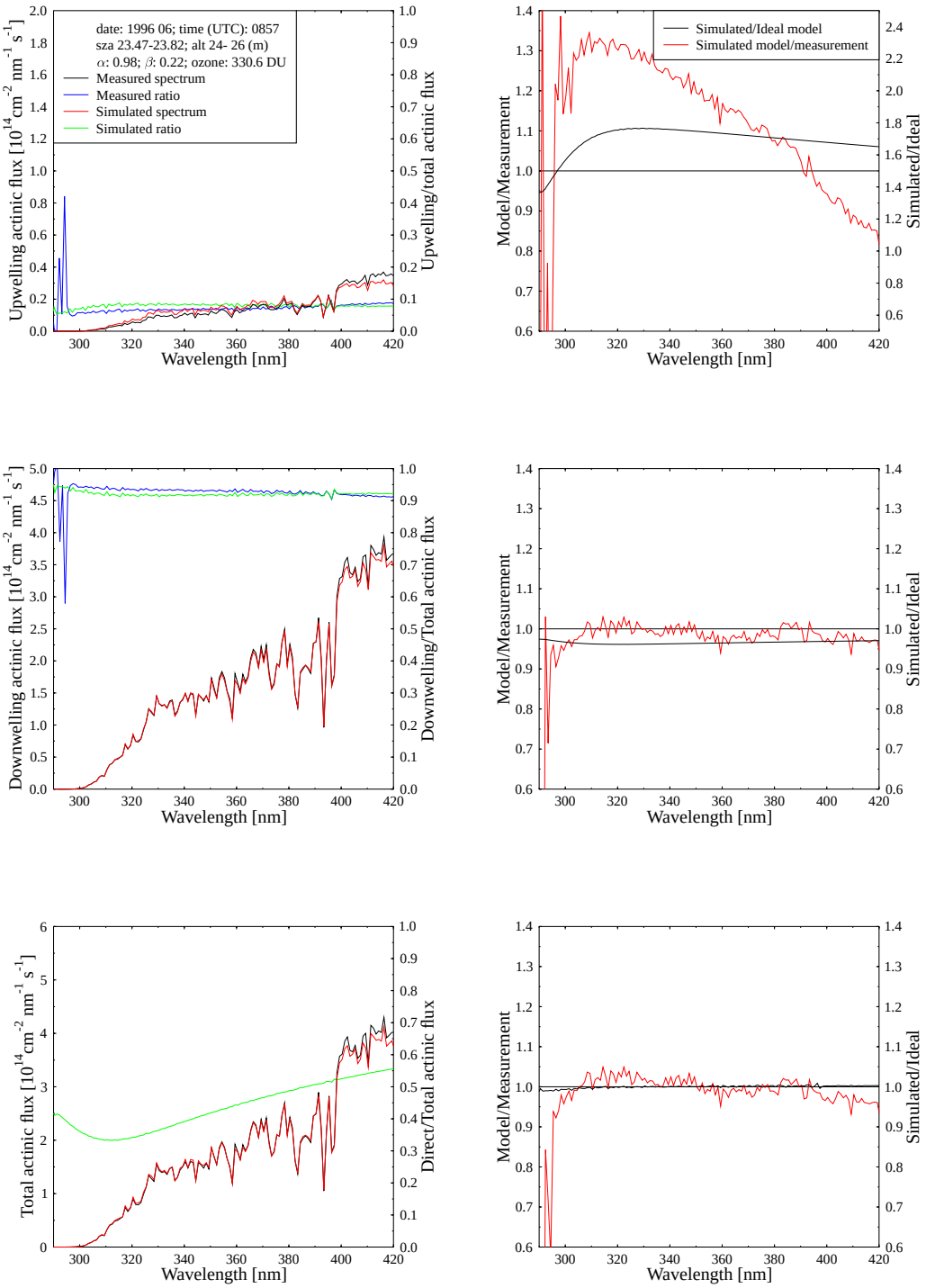

Figure 75: Same as Figure 10, except for 0857 UTC, 13 June 1996, and altitude 25.69 m.a.s.l.

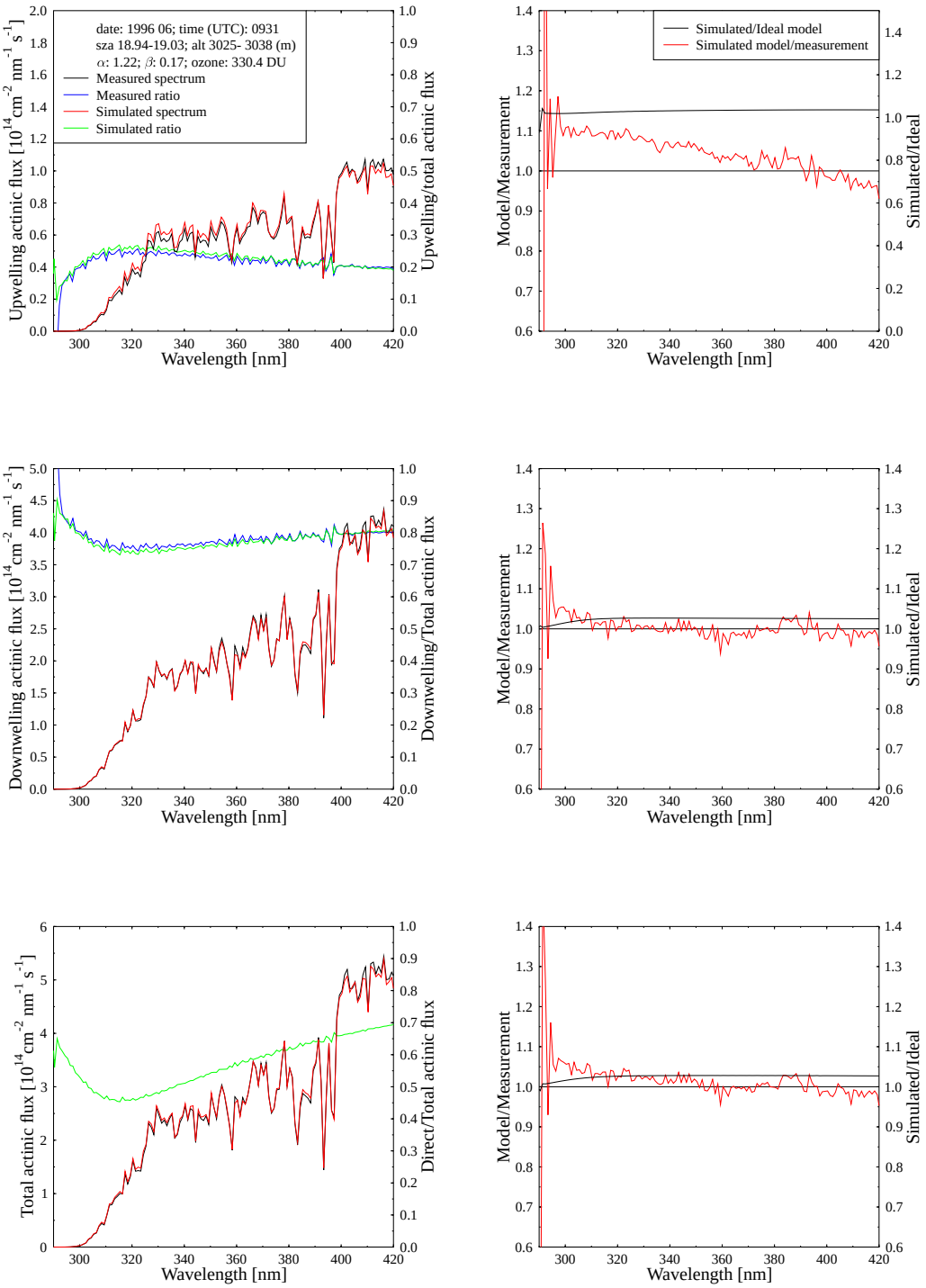

Figure 76: Same as Figure 10, except for 0931 UTC, 13 June 1996, and altitude 3029 m.a.s.l.

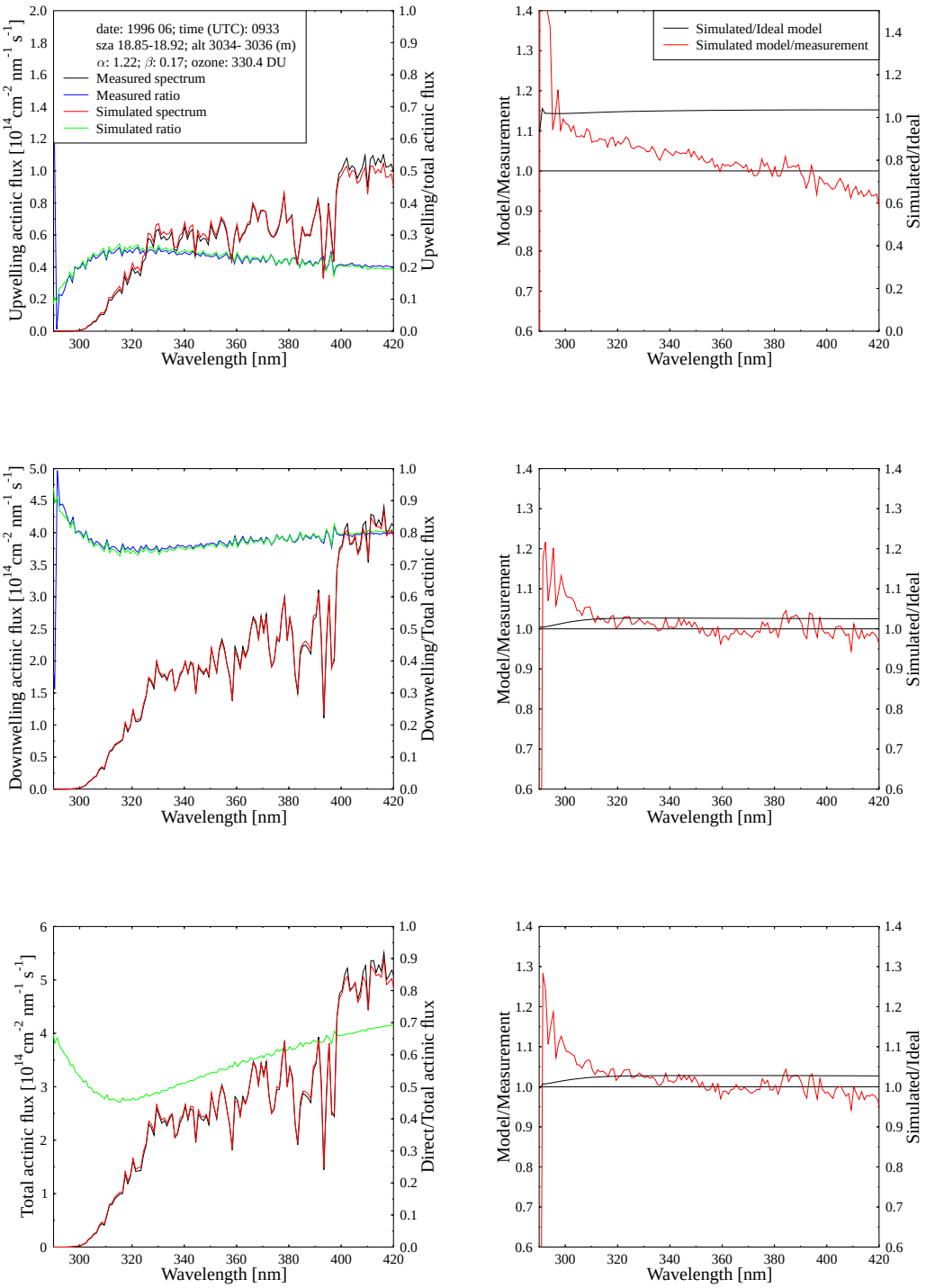

Figure 77: Same as Figure 10, except for 0933 UTC, 13 June 1996, and altitude 3036.52 m.a.s.l.

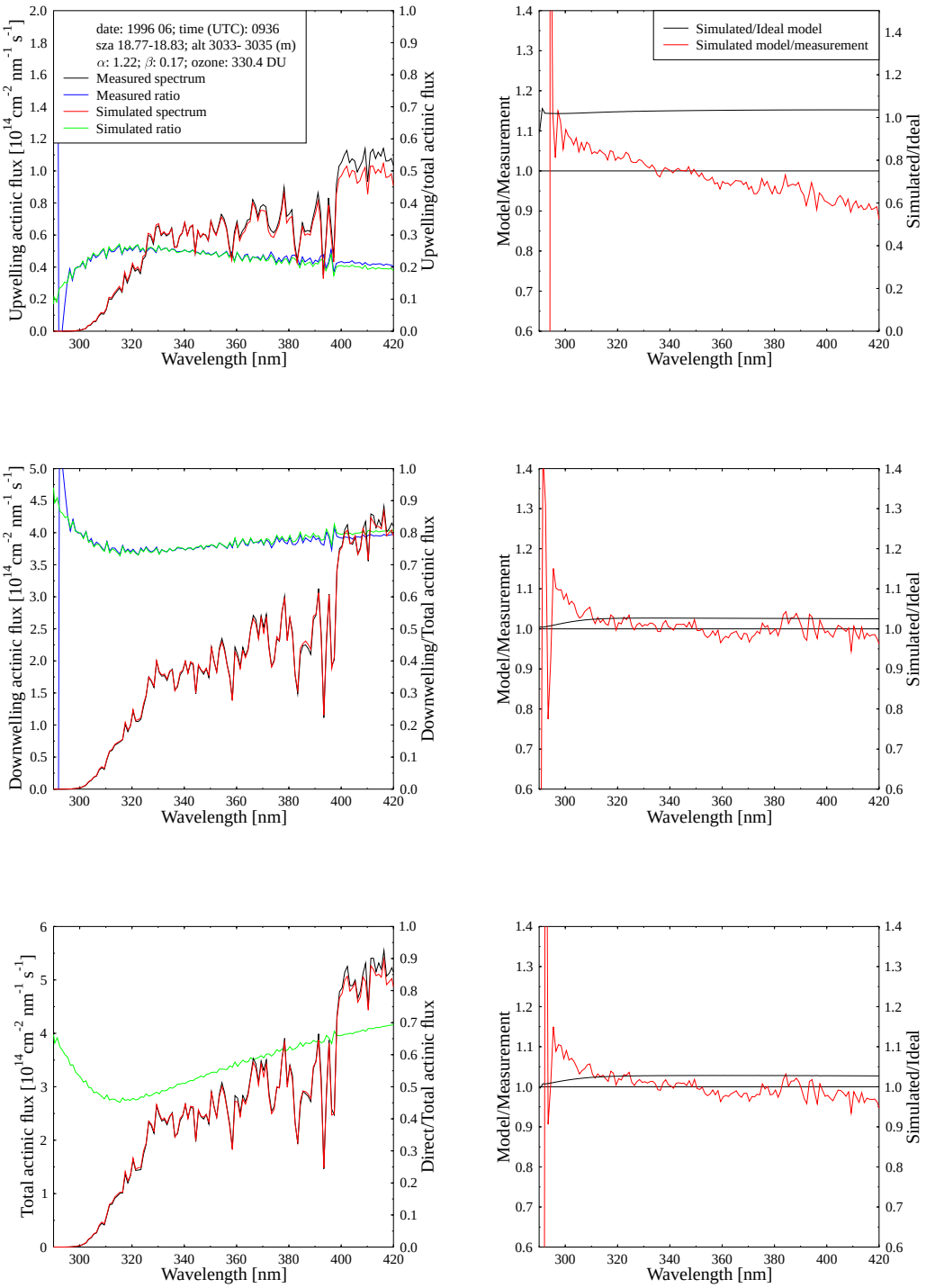

Figure 78: Same as Figure 10, except for 0936 UTC, 13 June 1996, and altitude 3035.2 m.a.s.l.

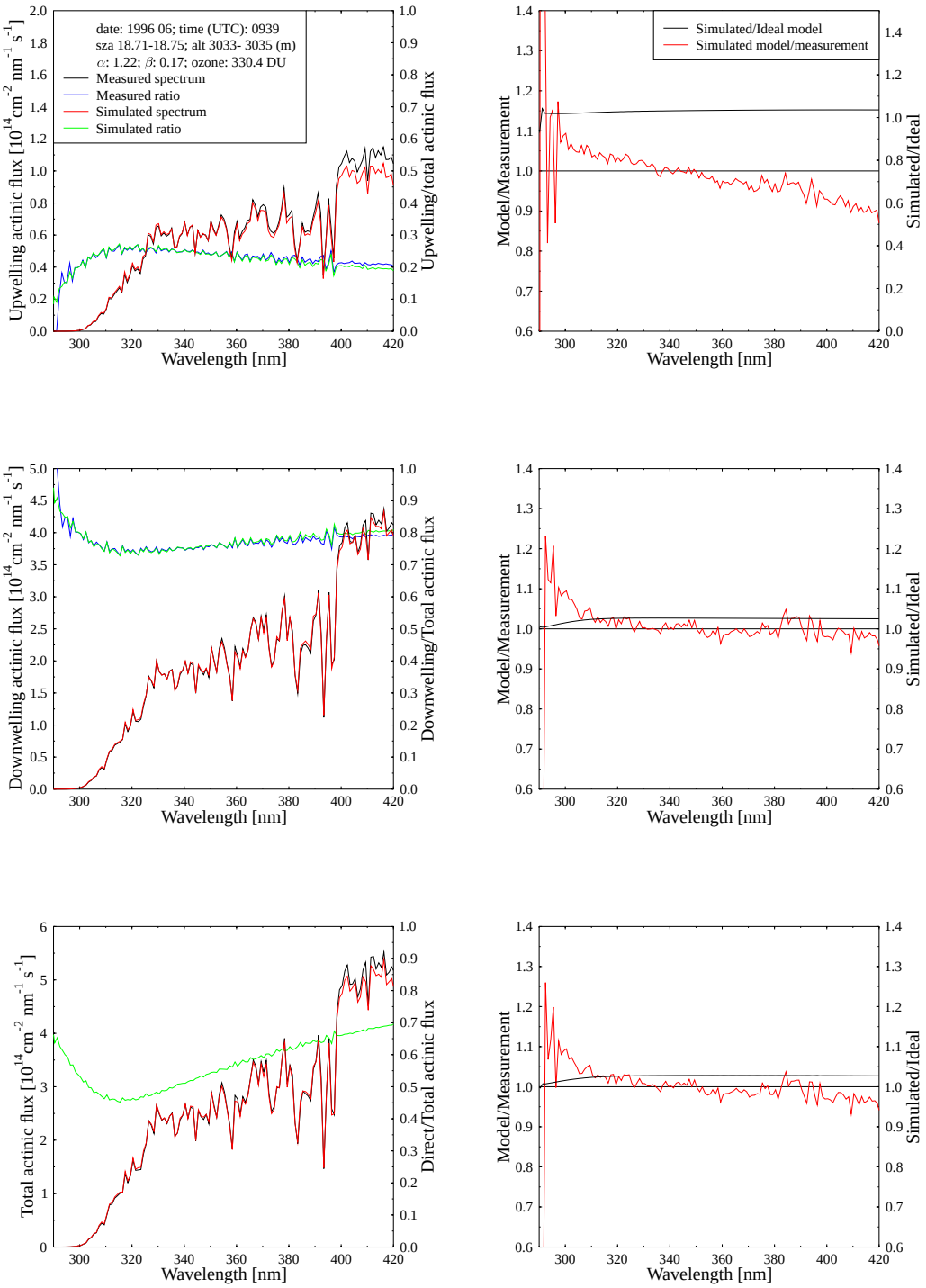

Figure 79: Same as Figure 10, except for 0939 UTC, 13 June 1996, and altitude 3034.58 m.a.s.l.

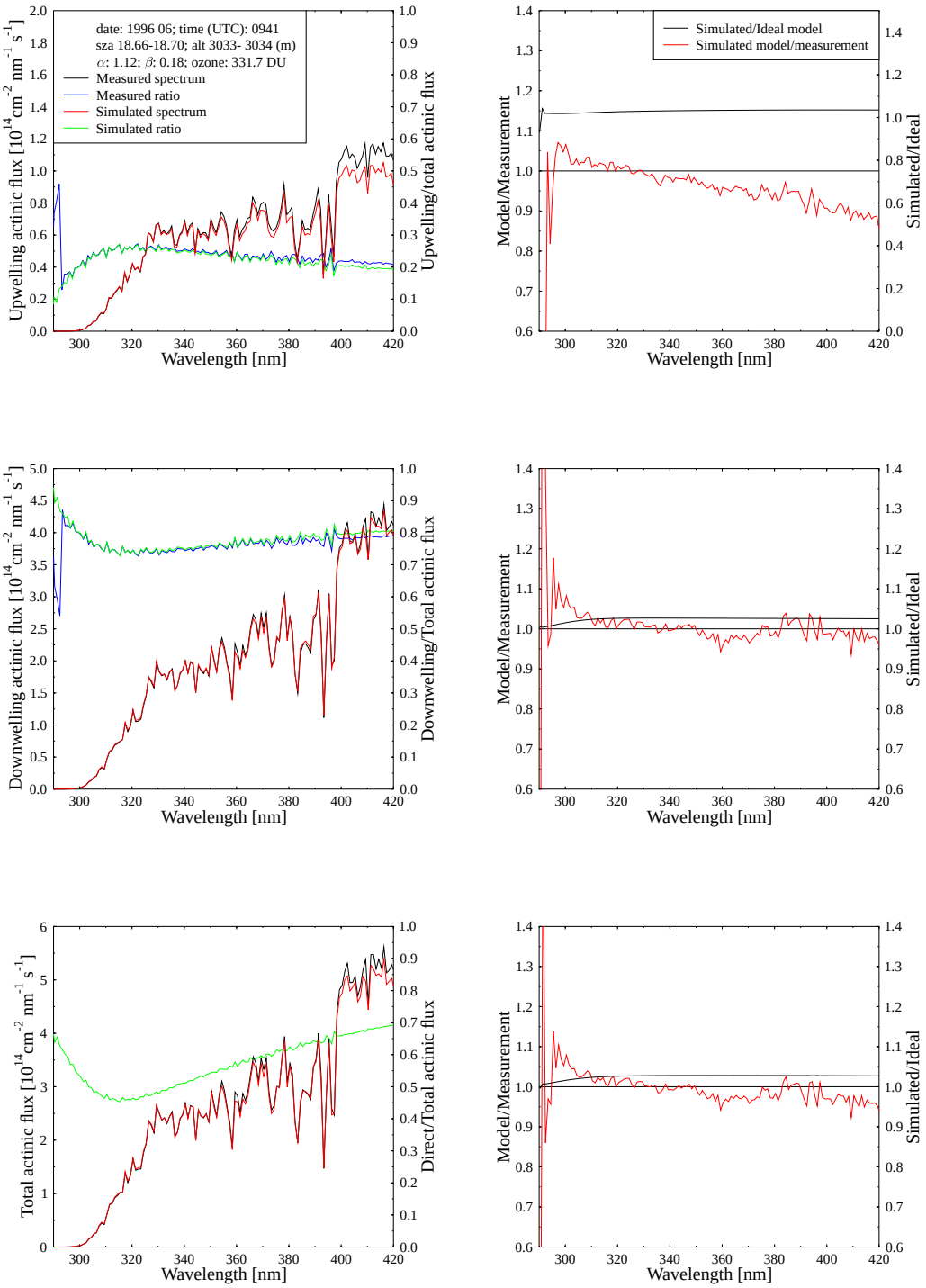

Figure 80: Same as Figure 10, except for 0941 UTC, 13 June 1996, and altitude 3034.6 m.a.s.l.

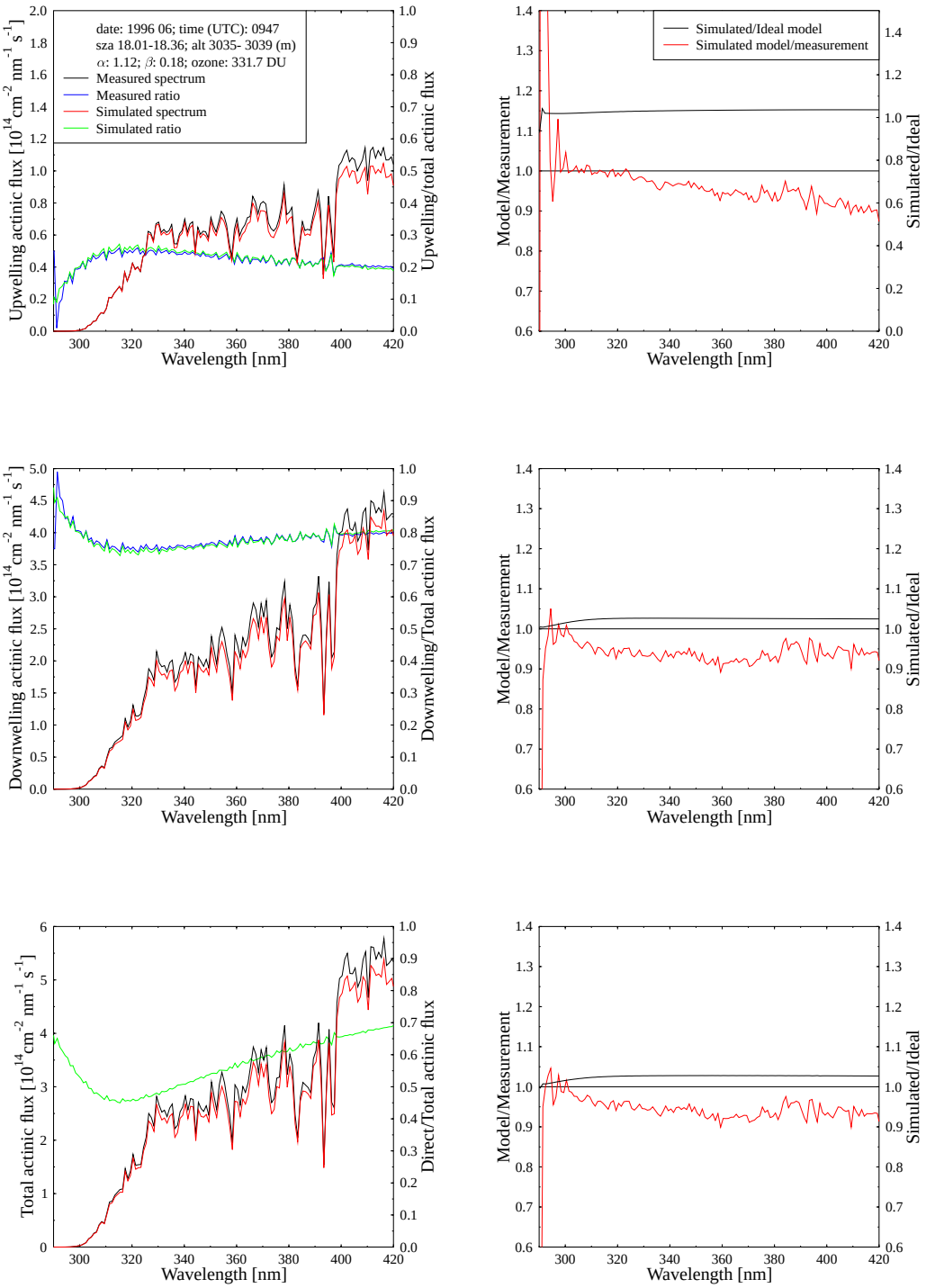

Figure 81: Same as Figure 10, except for 0947 UTC, 13 June 1996, and altitude 3039.54 m.a.s.l.

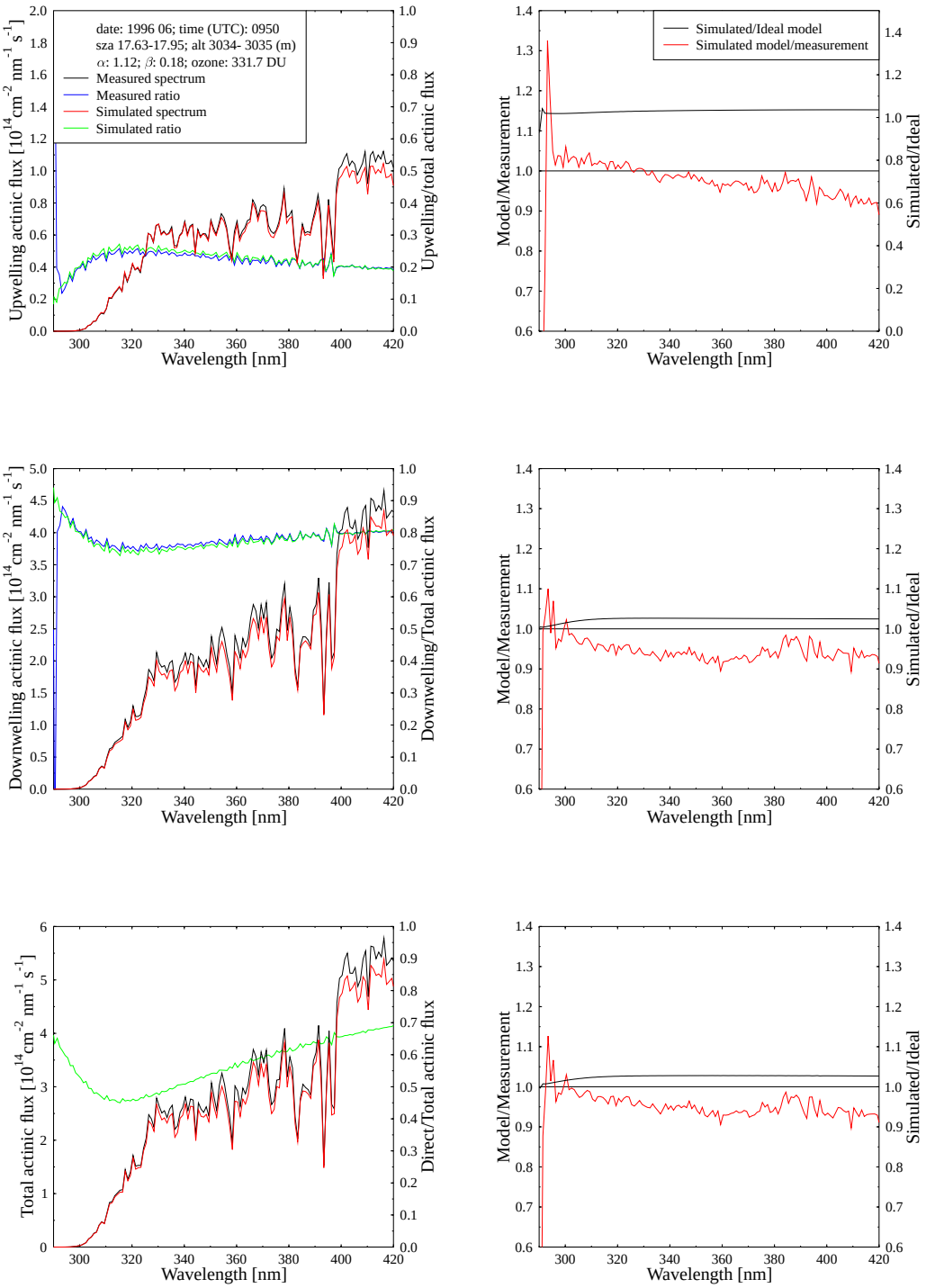

Figure 82: Same as Figure 10, except for 0950 UTC, 13 June 1996, and altitude 3035.63 m.a.s.l.

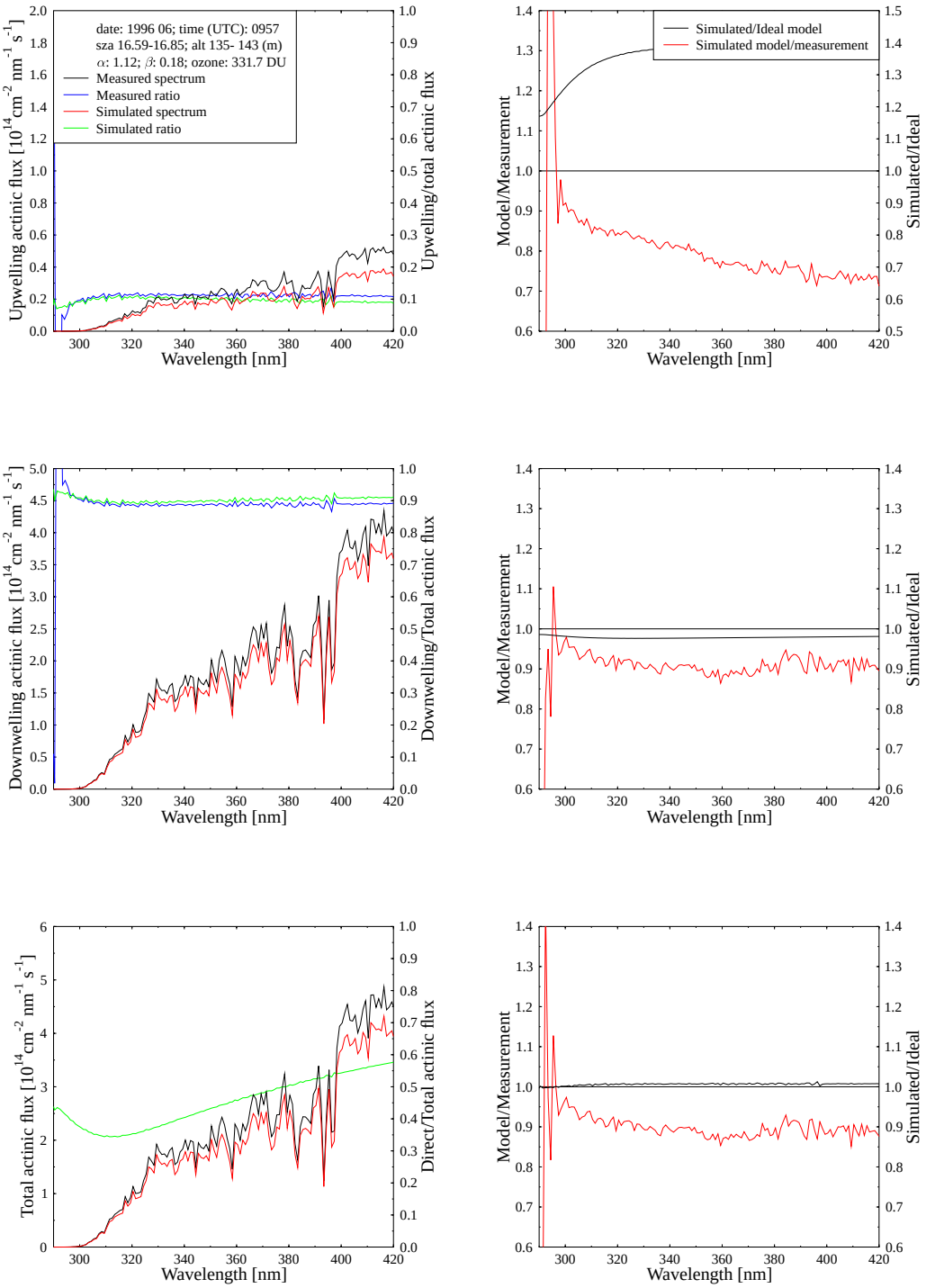

Figure 83: Same as Figure 10, except for 0957 UTC, 13 June 1996, and altitude 139.32 m.a.s.l.

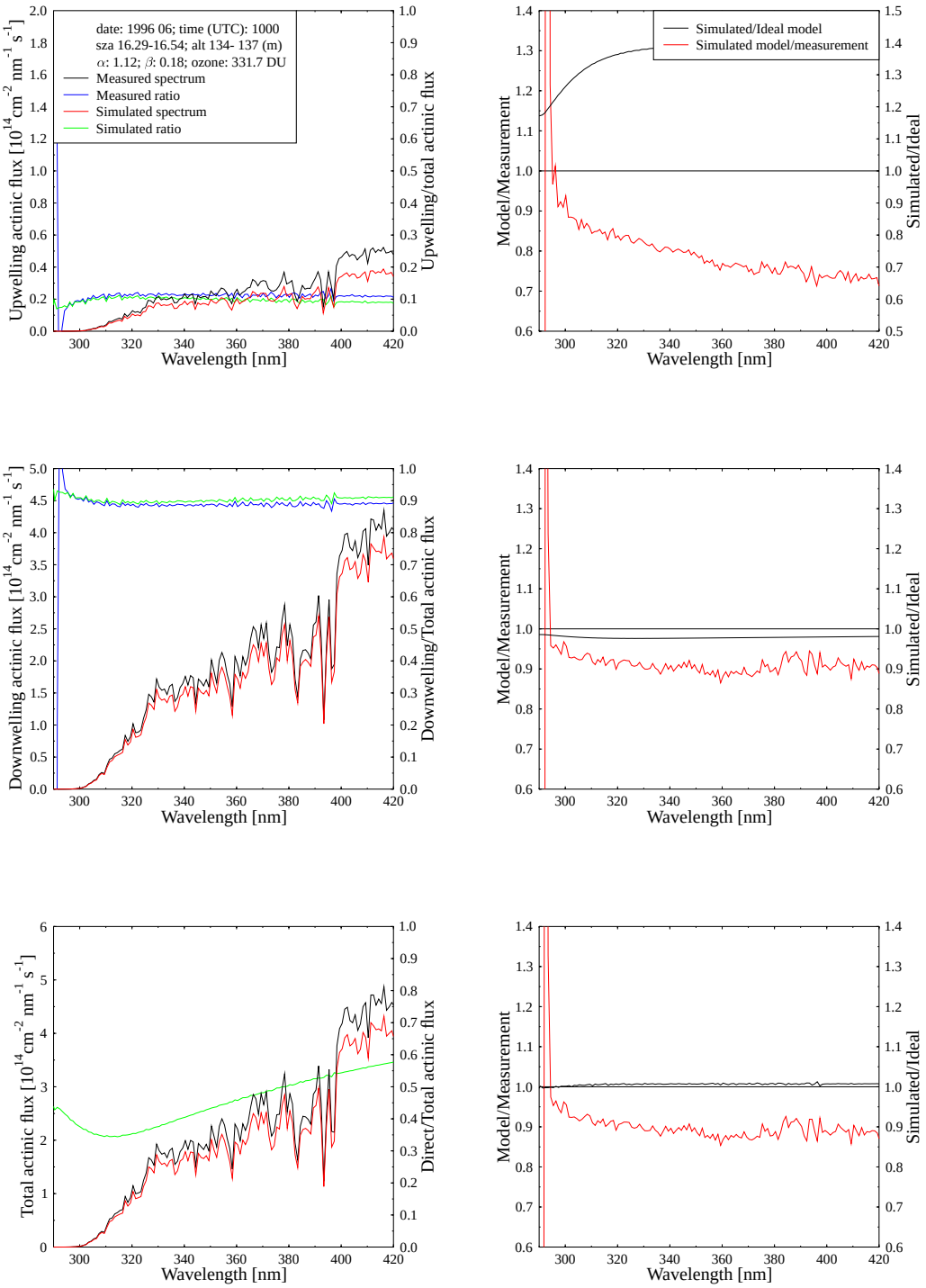

Figure 84: Same as Figure 10, except for 1000 UTC, 13 June 1996, and altitude 134.46 m.a.s.l.

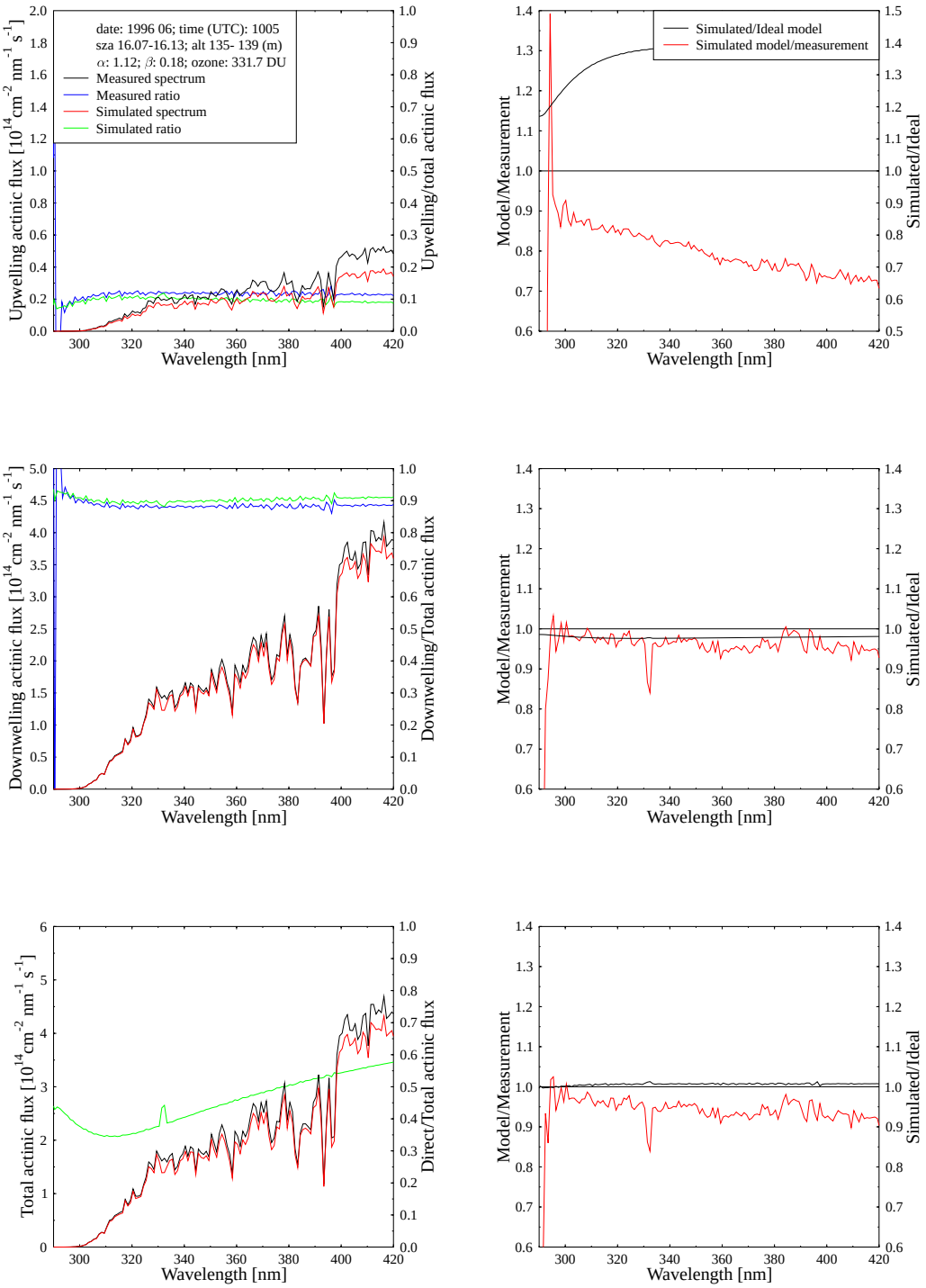

Figure 85: Same as Figure 10, except for 1005 UTC, 13 June 1996, and altitude 135.56 m.a.s.l.

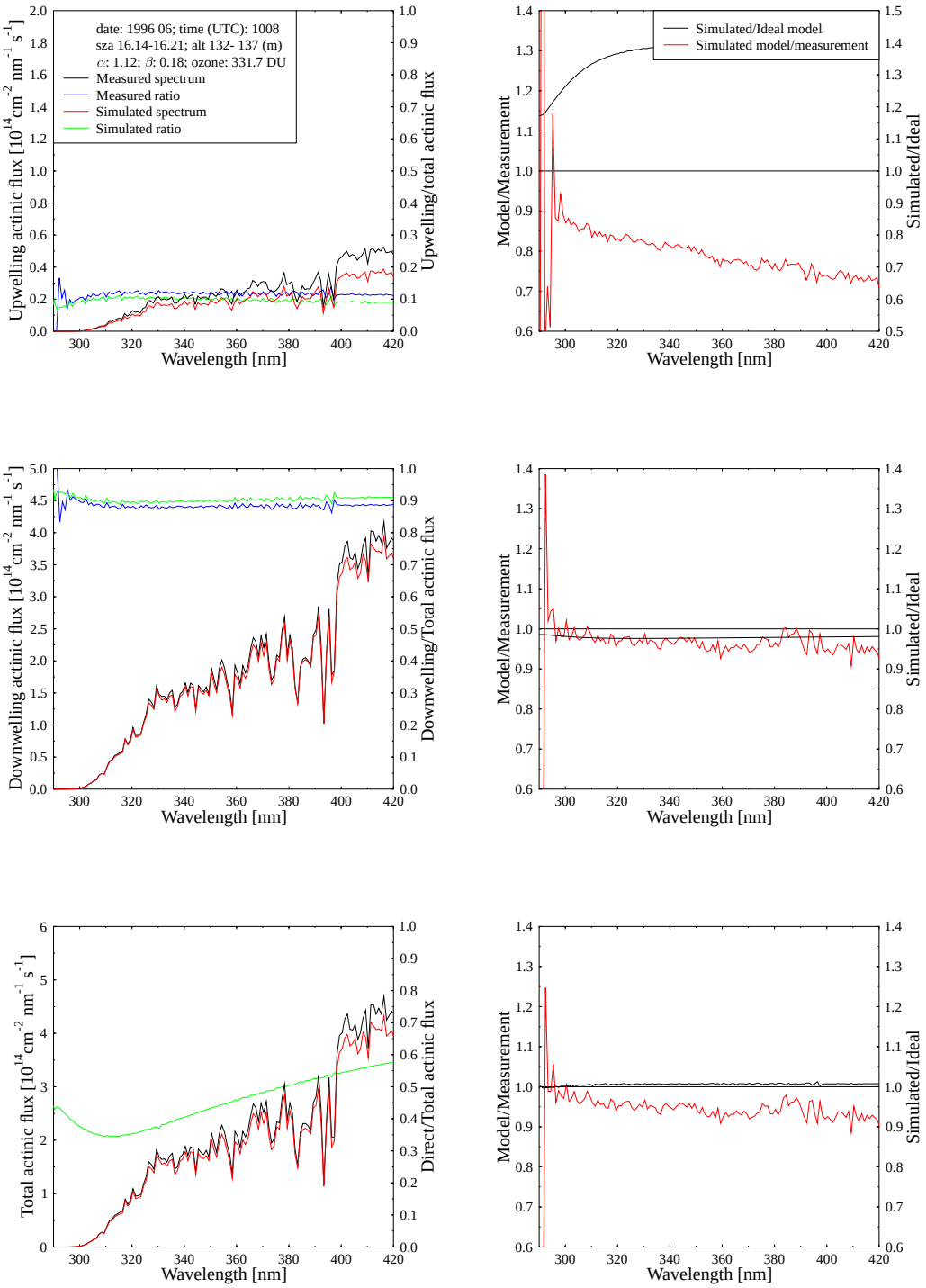

Figure 86: Same as Figure 10, except for 1008 UTC, 13 June 1996, and altitude 134.18 m.a.s.l.

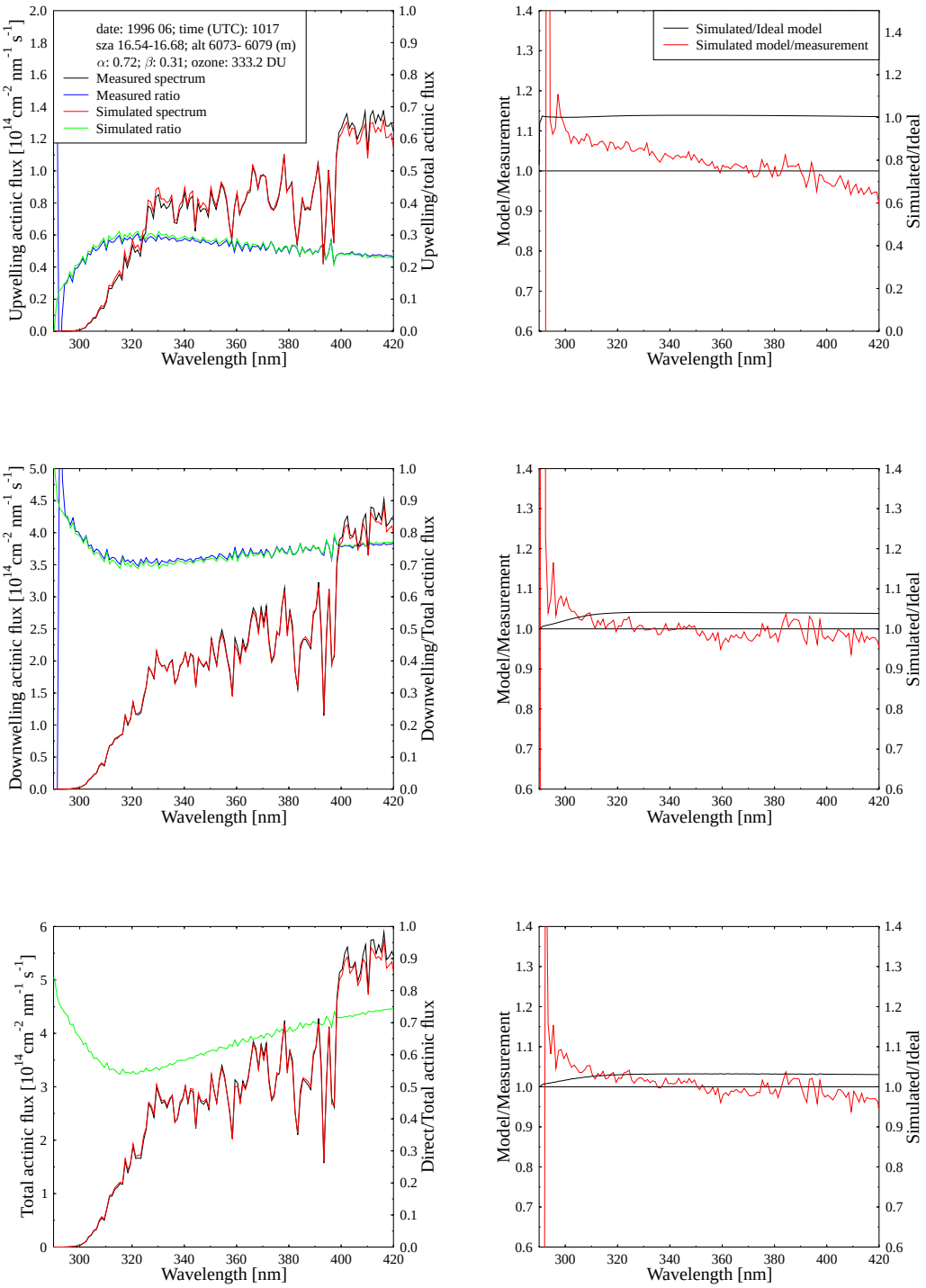

Figure 87: Same as Figure 10, except for 1017 UTC, 13 June 1996, and altitude 6073.94 m.a.s.l.

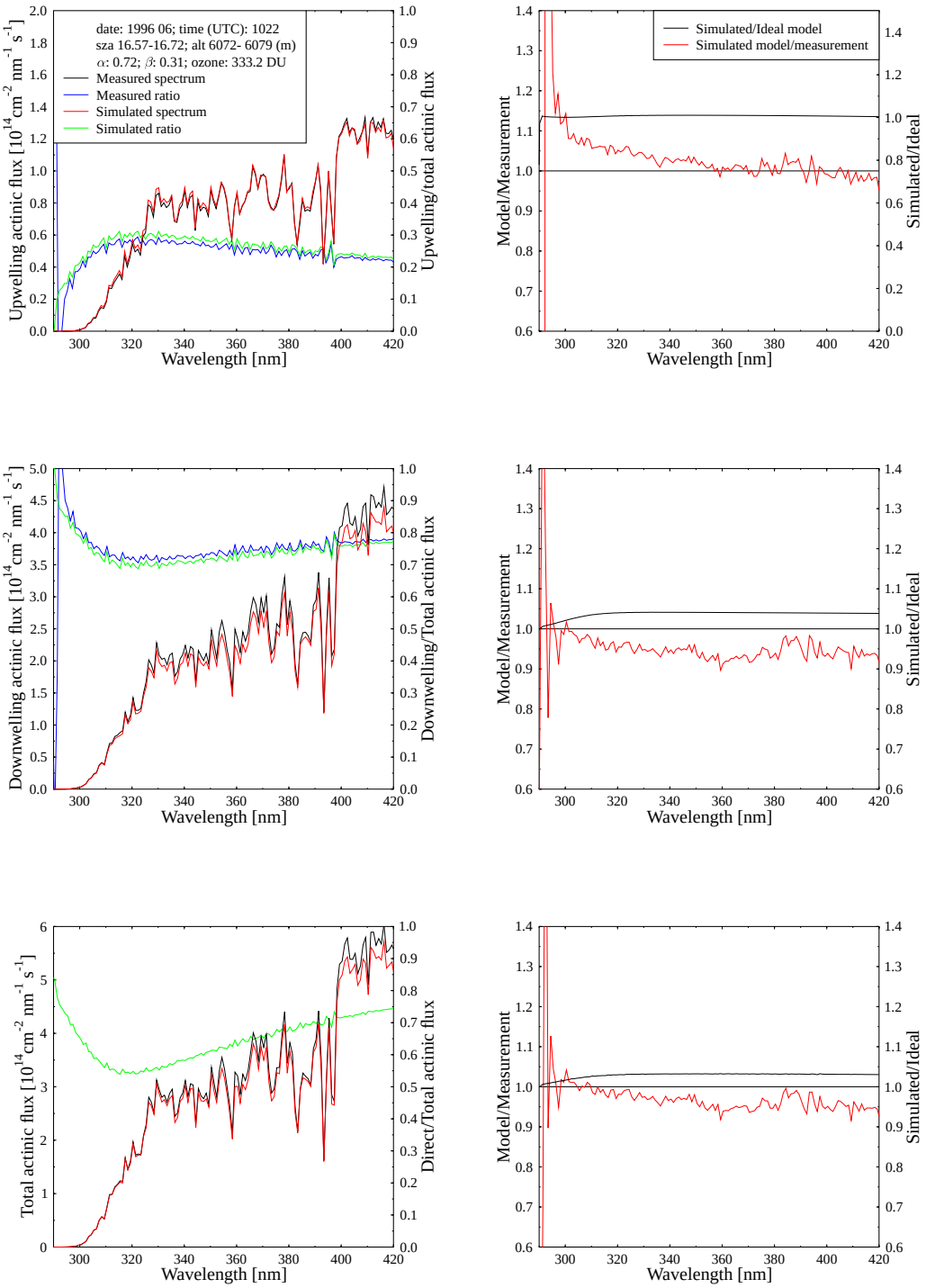

Figure 88: Same as Figure 10, except for 1022 UTC, 13 June 1996, and altitude 6072.7 m.a.s.l.

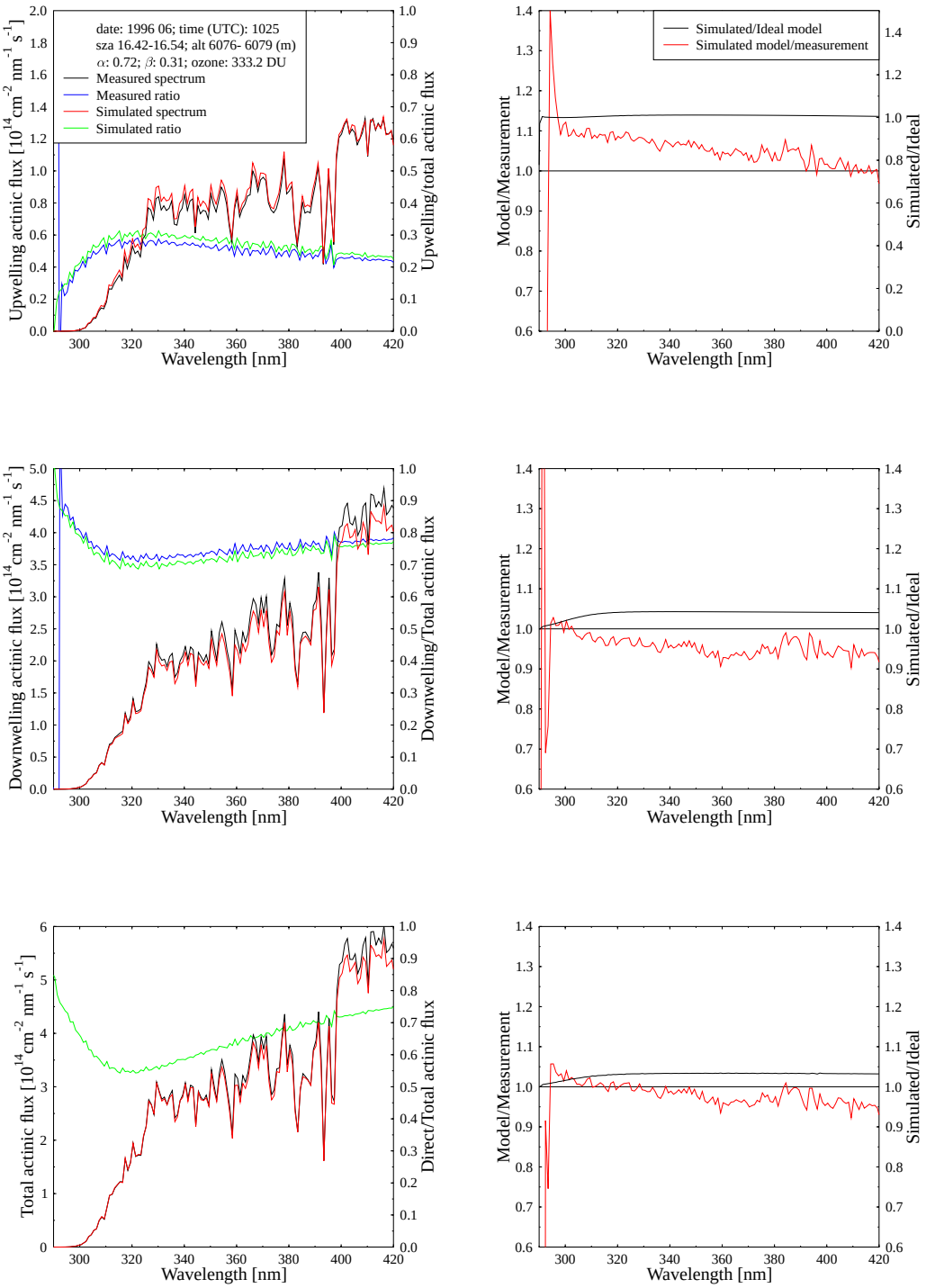

Figure 89: Same as Figure 10, except for 1025 UTC, 13 June 1996, and altitude 6077.54 m.a.s.l.

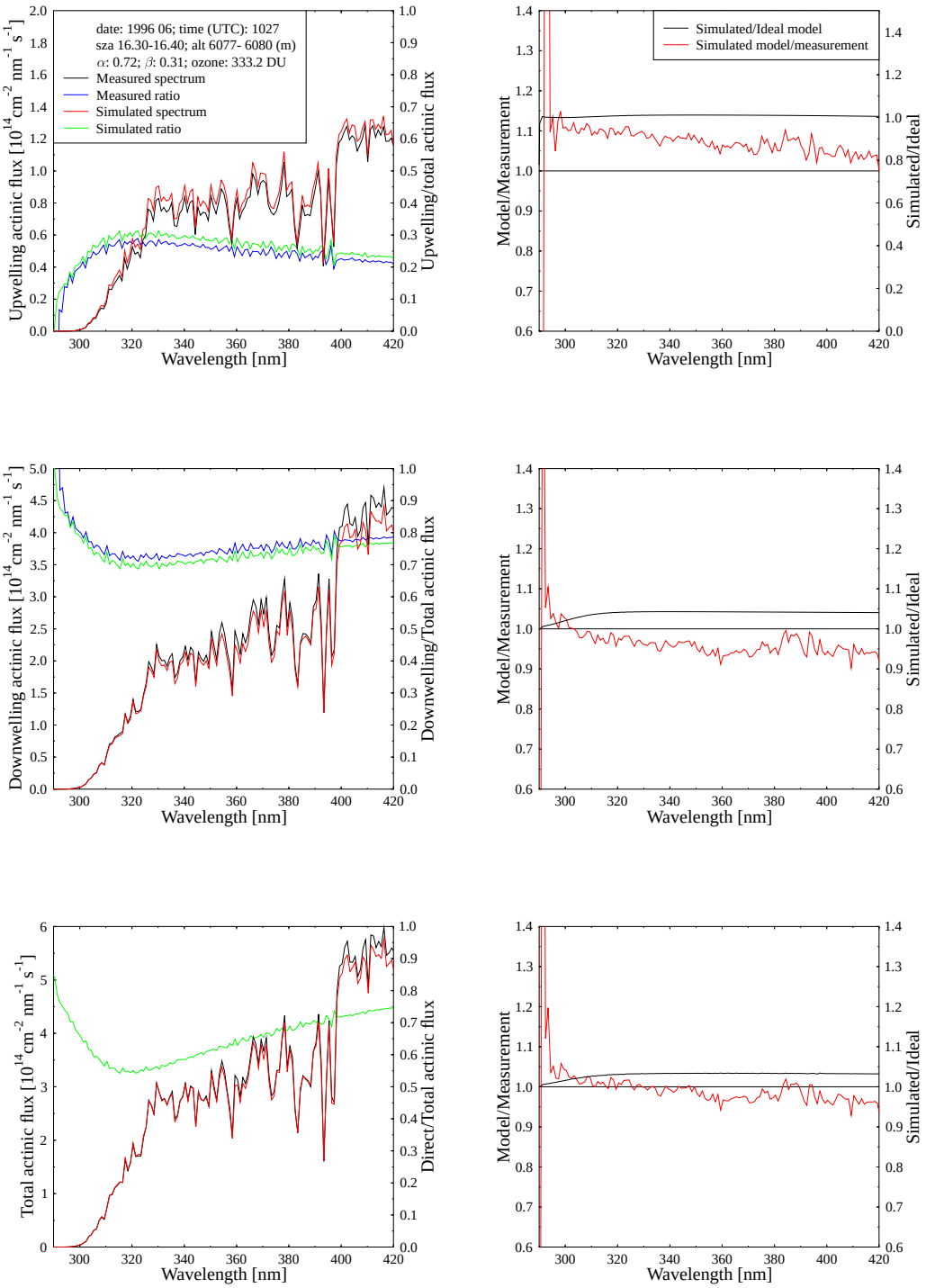

Figure 90: Same as Figure 10, except for 1027 UTC, 13 June 1996, and altitude 6078.32 m.a.s.l.

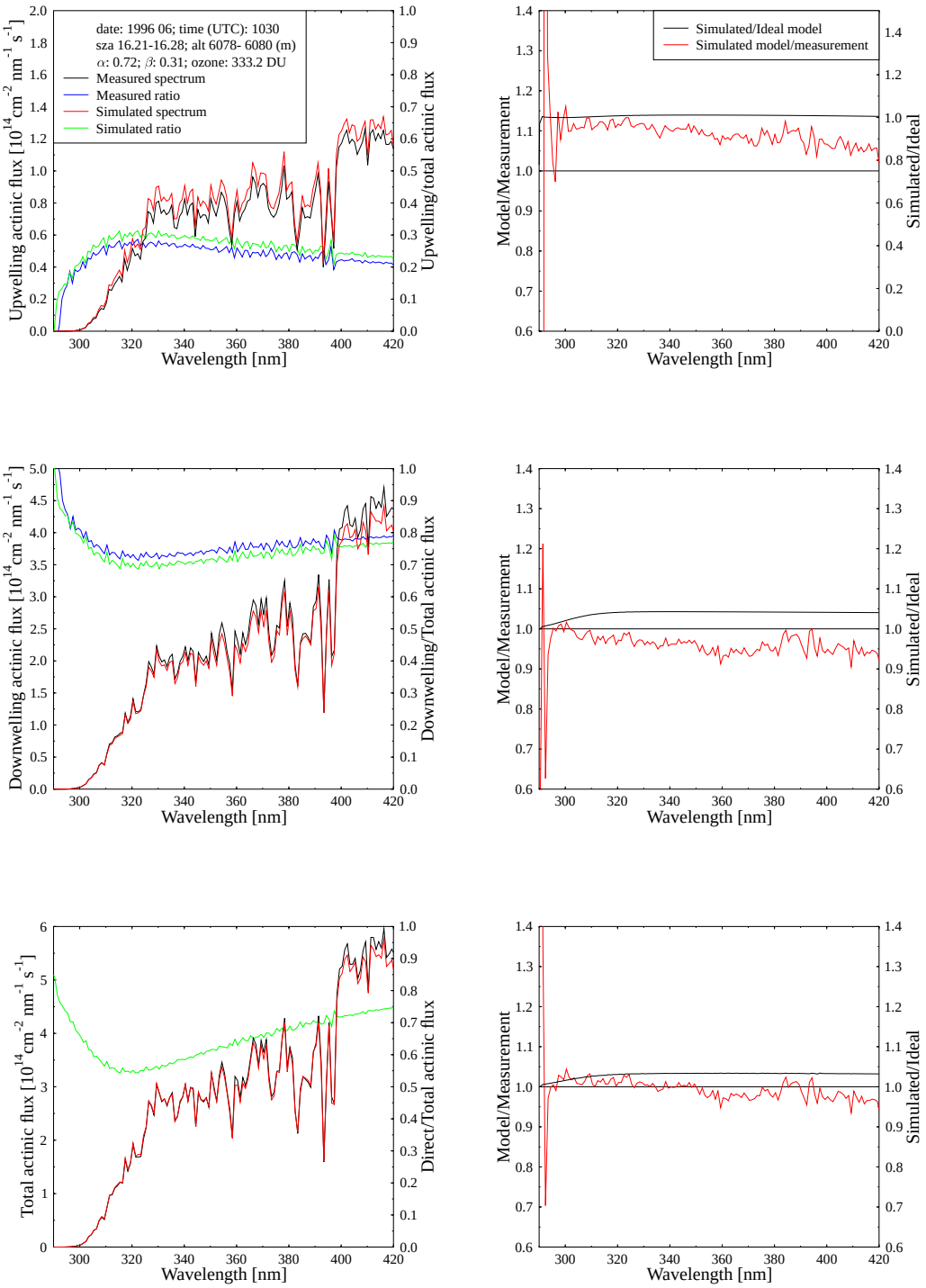

Figure 91: Same as Figure 10, except for 1030 UTC, 13 June 1996, and altitude 6078.78 m.a.s.l.

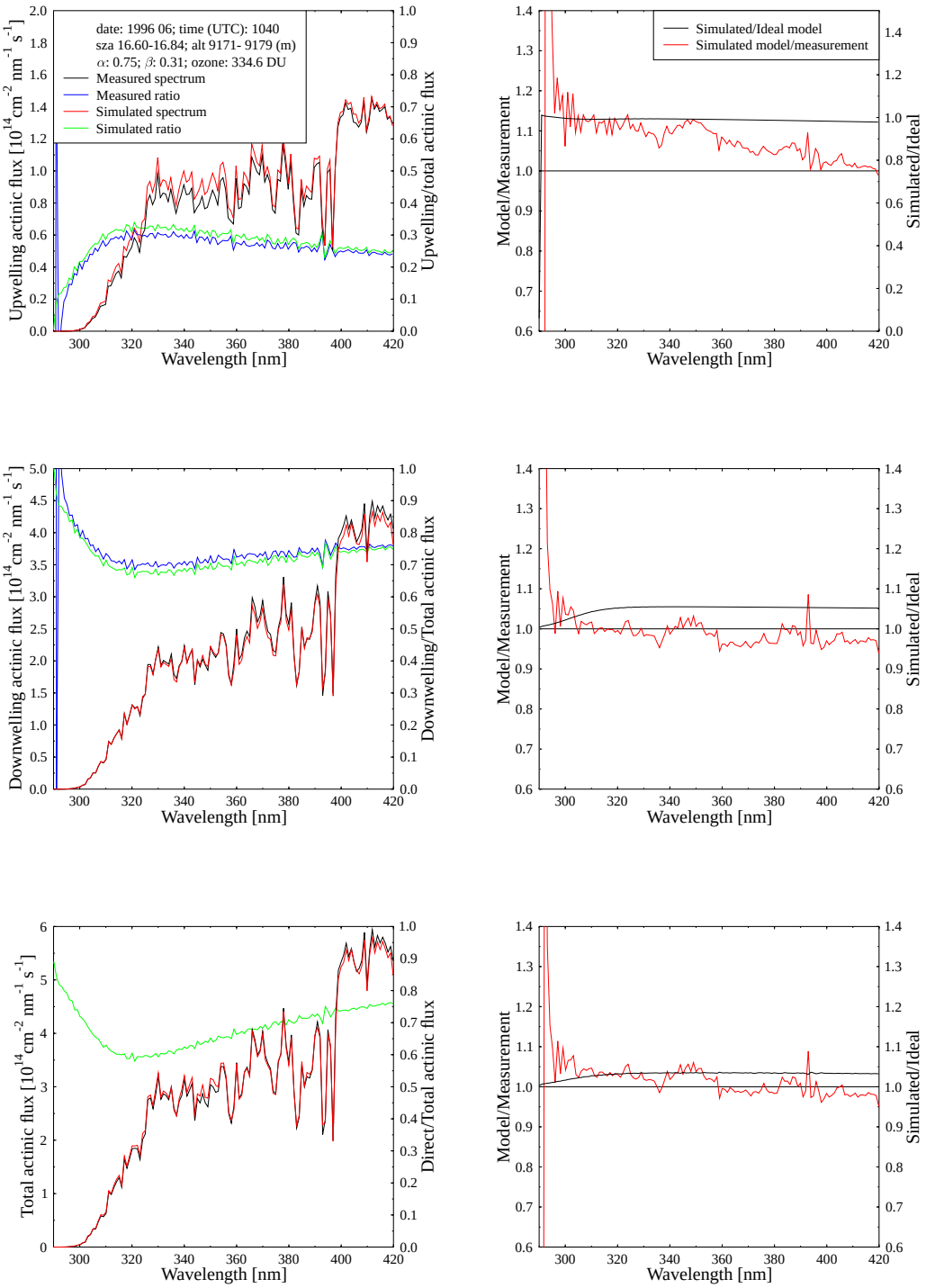

Figure 92: Same as Figure 10, except for 1040 UTC, 13 June 1996, and altitude 9171.24 m.a.s.l.

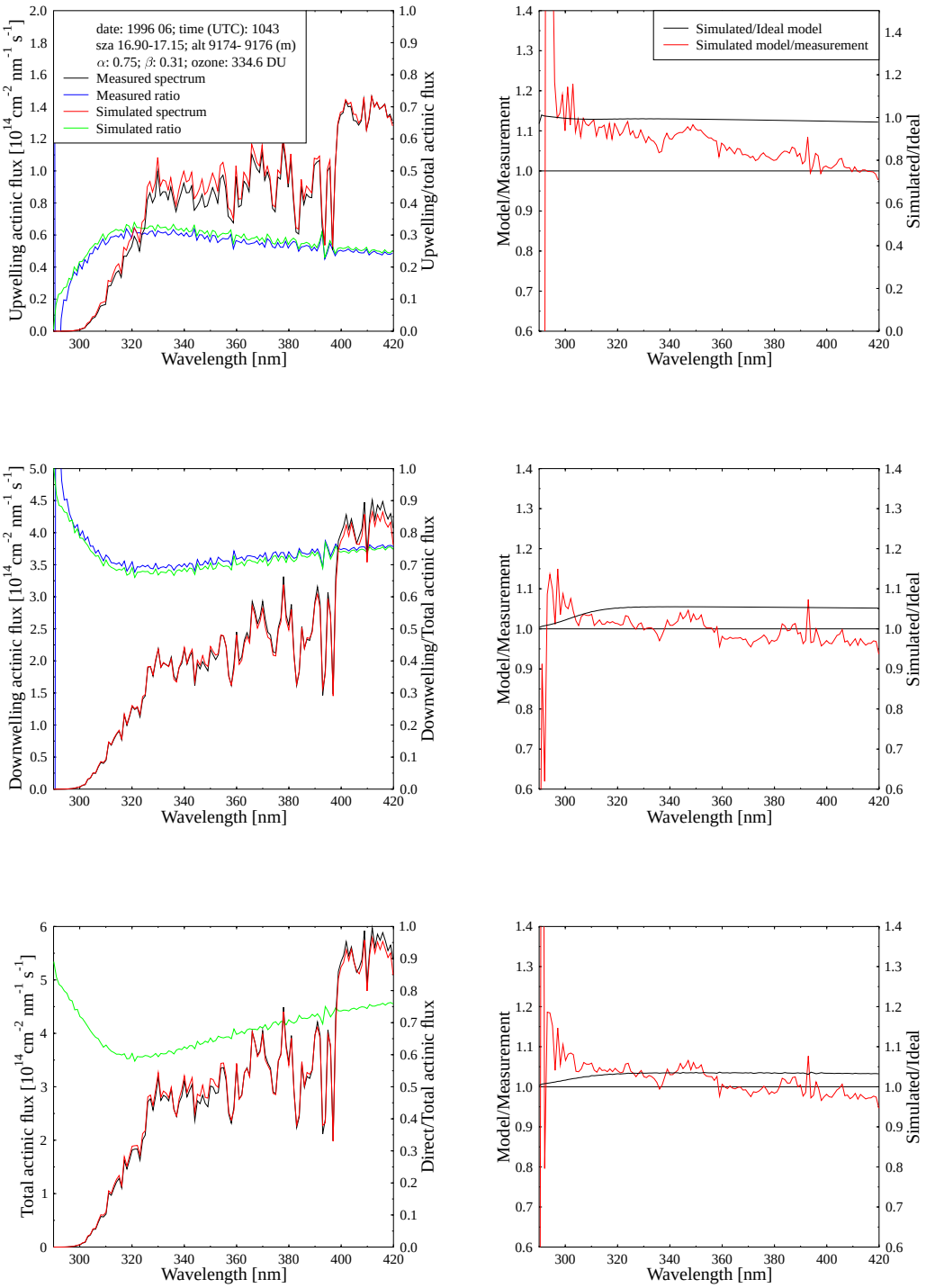

Figure 93: Same as Figure 10, except for 1043 UTC, 13 June 1996, and altitude 9175.16 m.a.s.l.

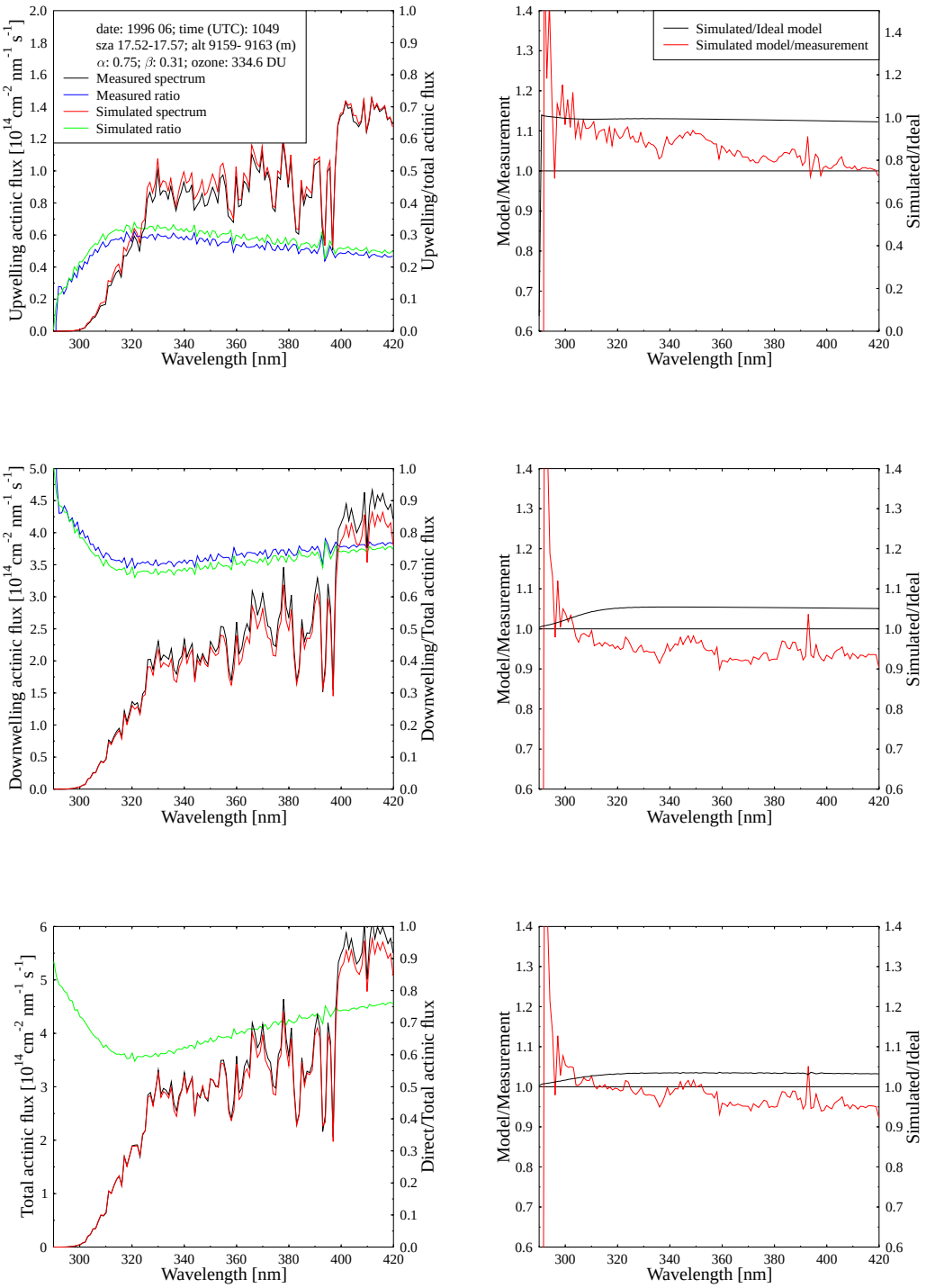

Figure 94: Same as Figure 10, except for 1049 UTC, 13 June 1996, and altitude 9159.29 m.a.s.l.

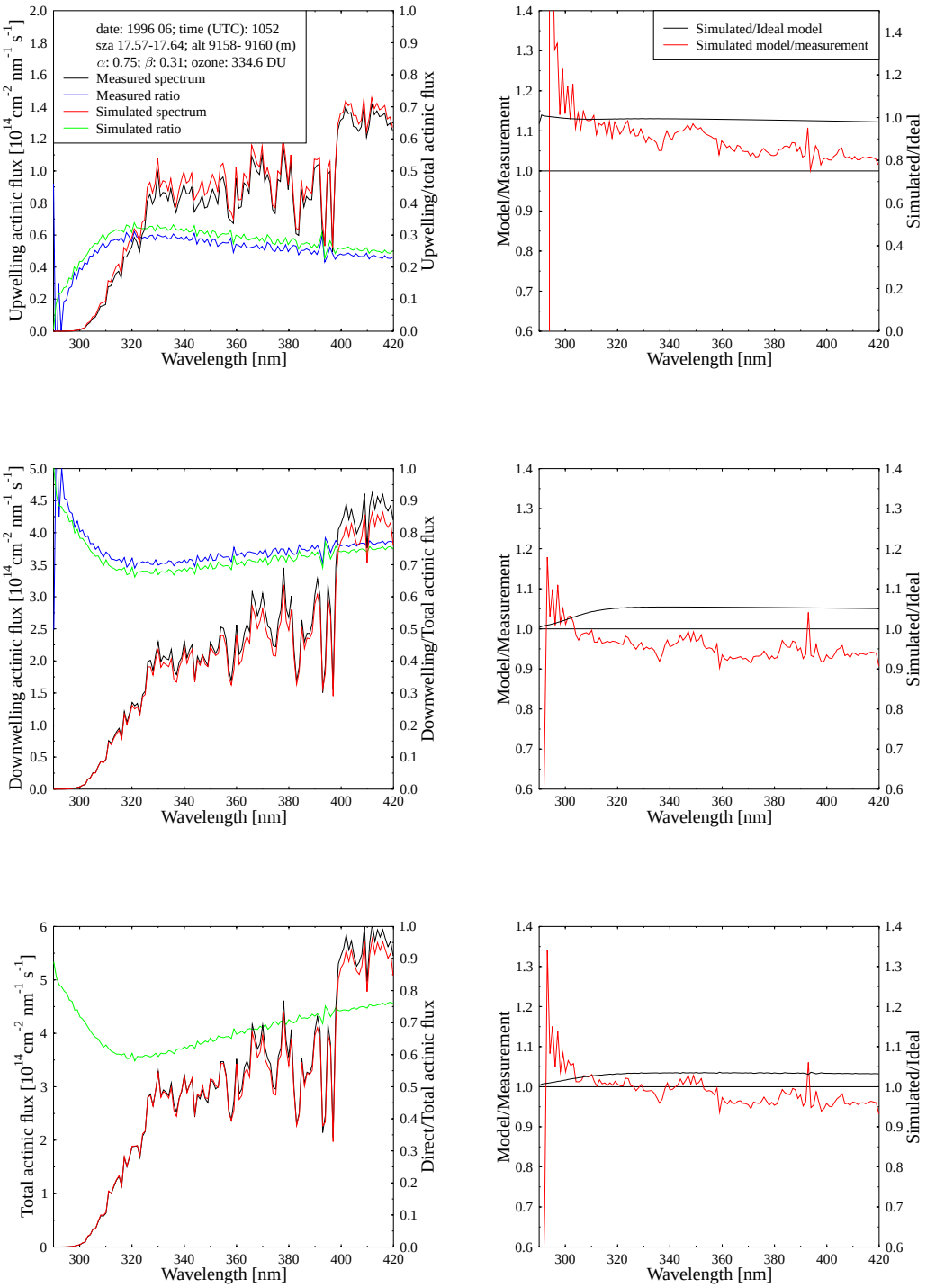

Figure 95: Same as Figure 10, except for 1052 UTC, 13 June 1996, and altitude 9160.24 m.a.s.l.

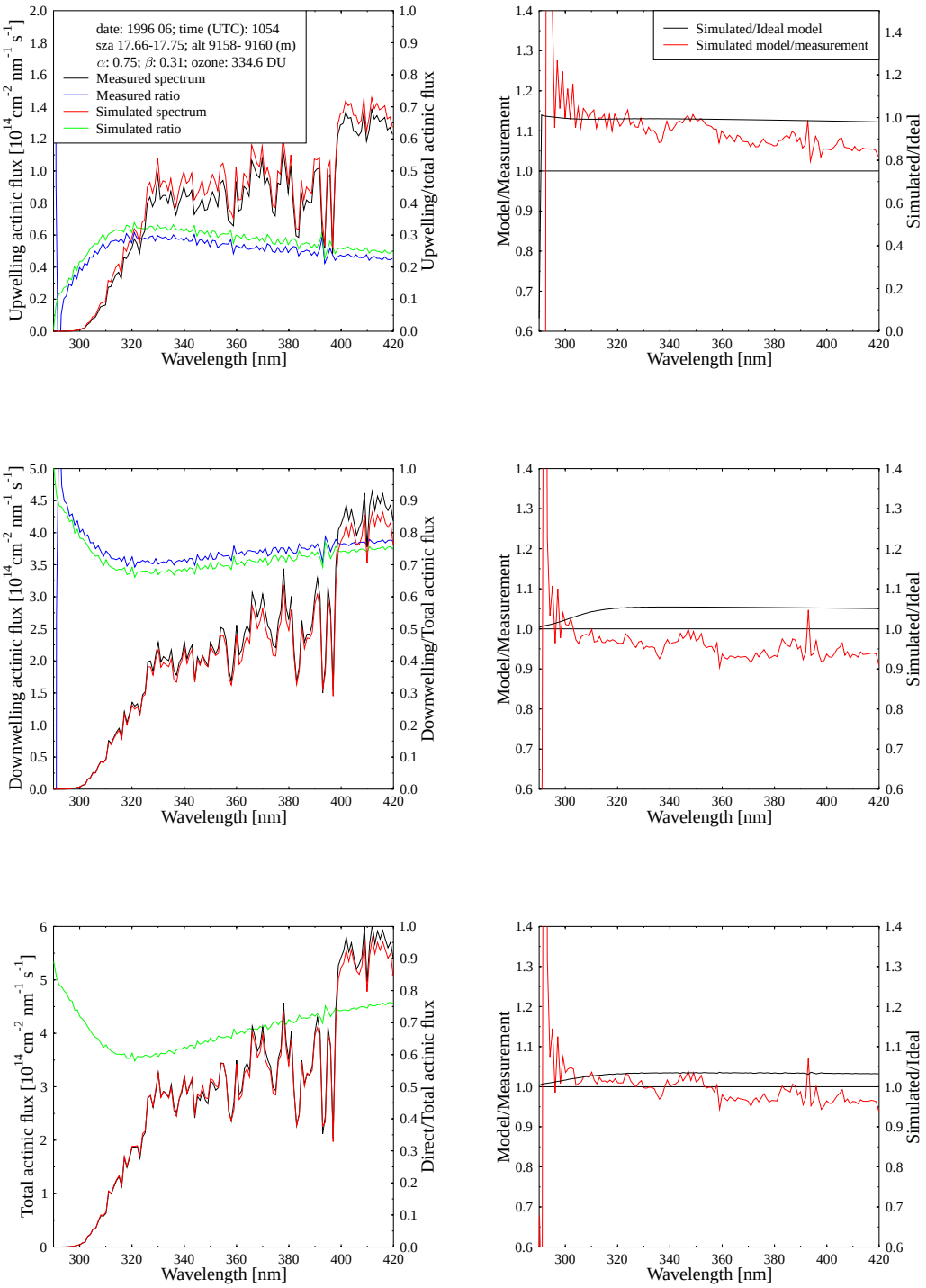

Figure 96: Same as Figure 10, except for 1054 UTC, 13 June 1996, and altitude 9160.18 m.a.s.l.

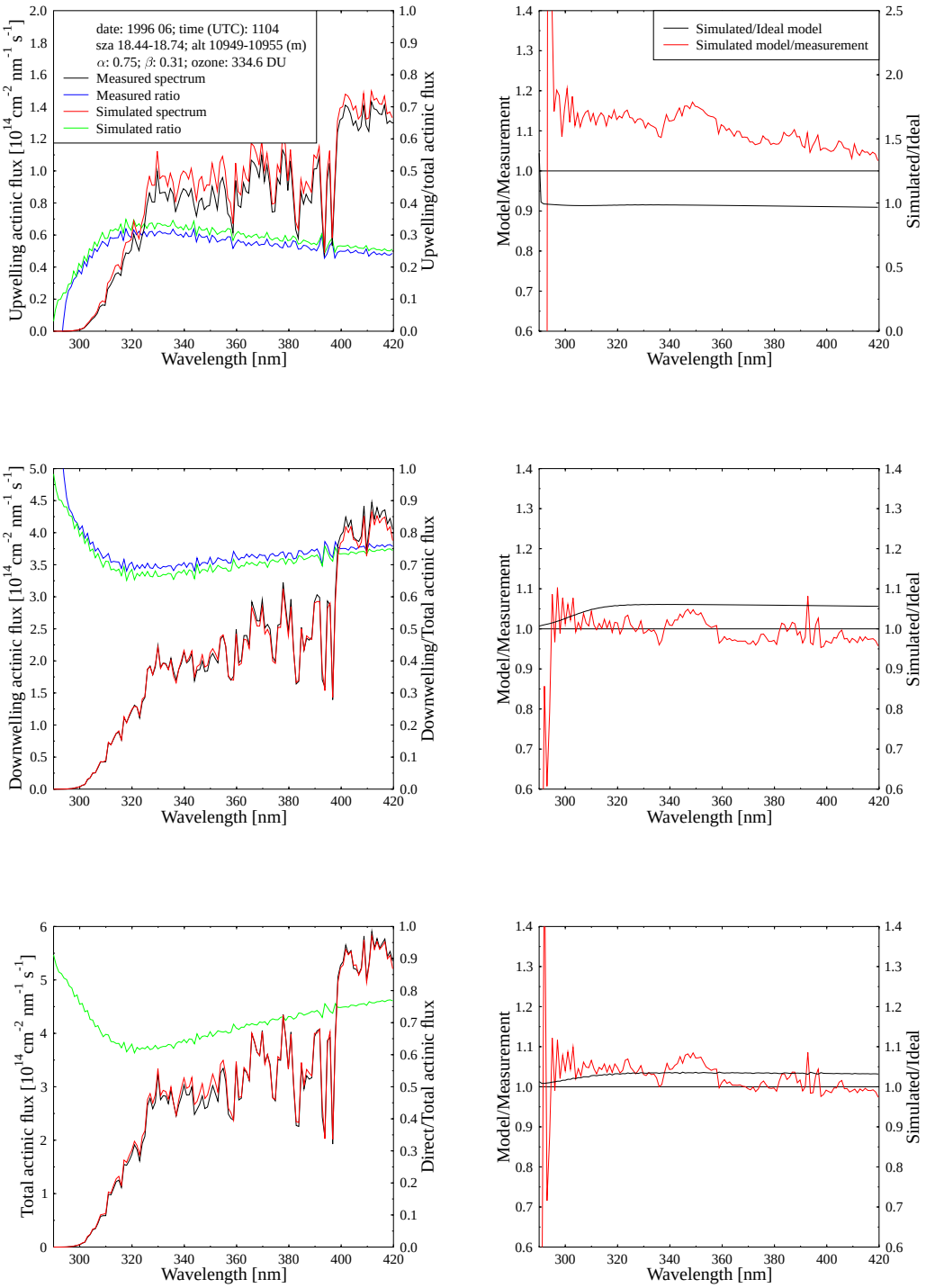

Figure 97: Same as Figure 10, except for 1104 UTC, 13 June 1996, and altitude 10949.24 m.a.s.l.

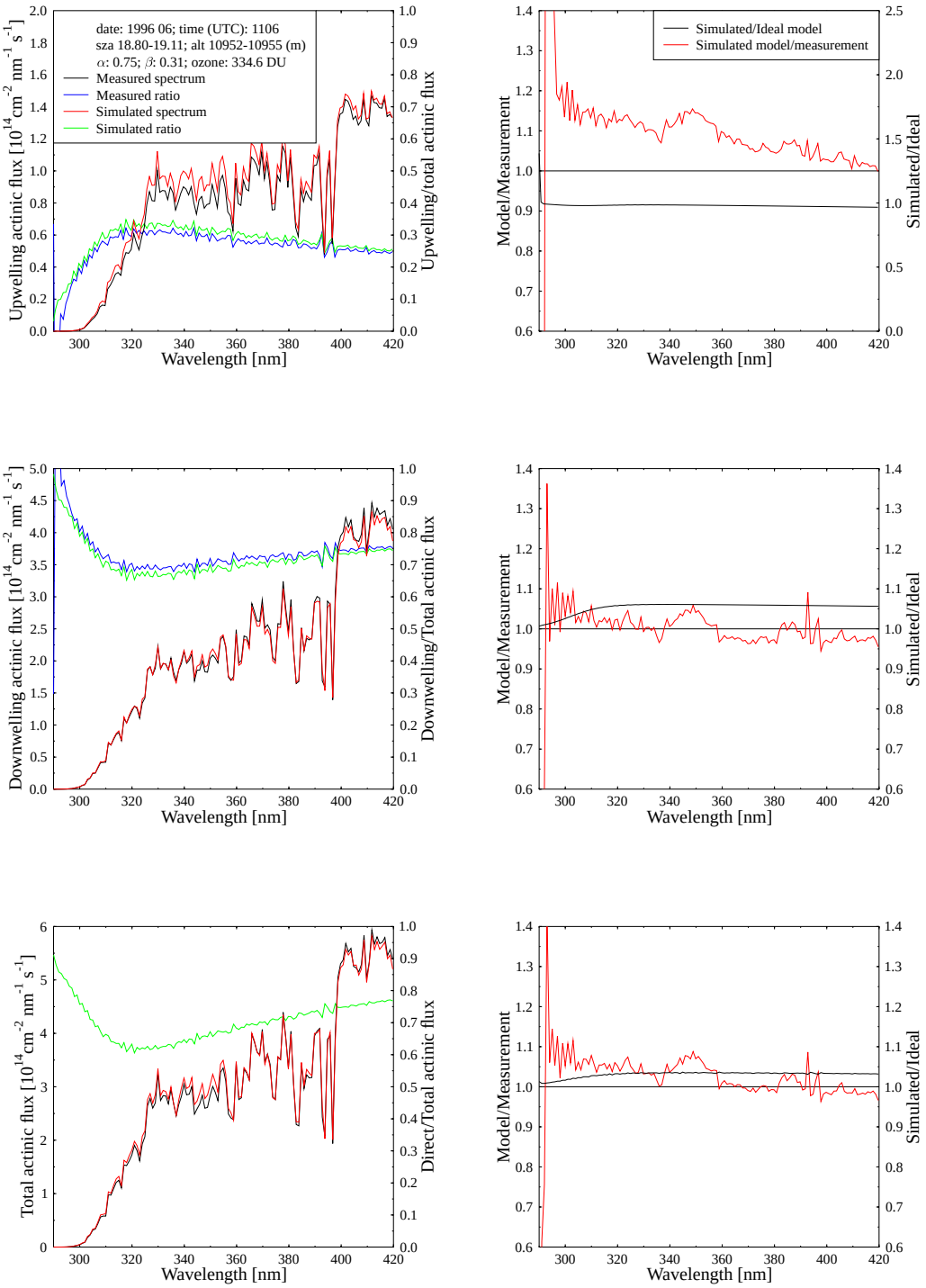

Figure 98: Same as Figure 10, except for 1106 UTC, 13 June 1996, and altitude 10954.36 m.a.s.l.

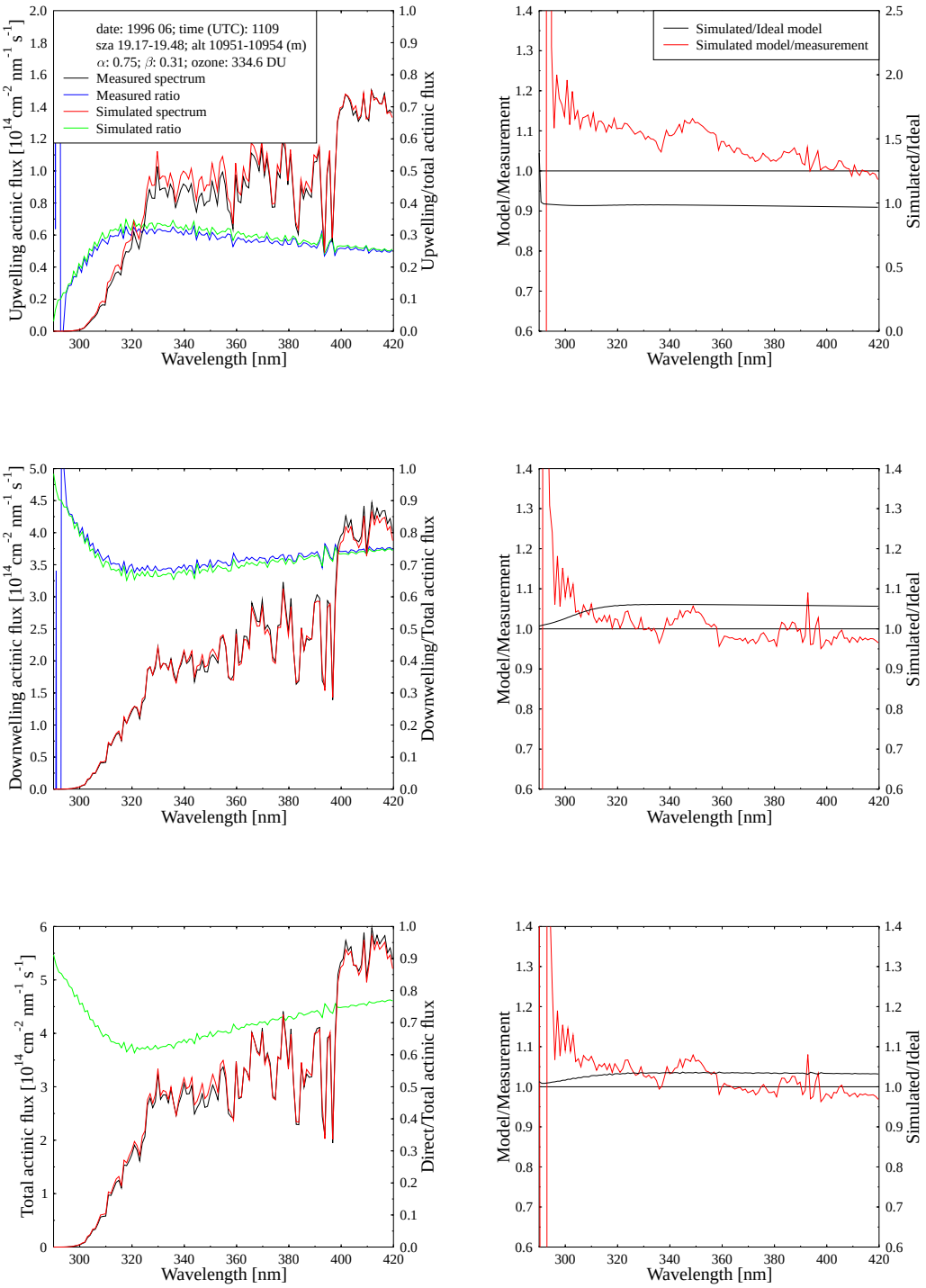

Figure 99: Same as Figure 10, except for 1109 UTC, 13 June 1996, and altitude 10953.16 m.a.s.l.

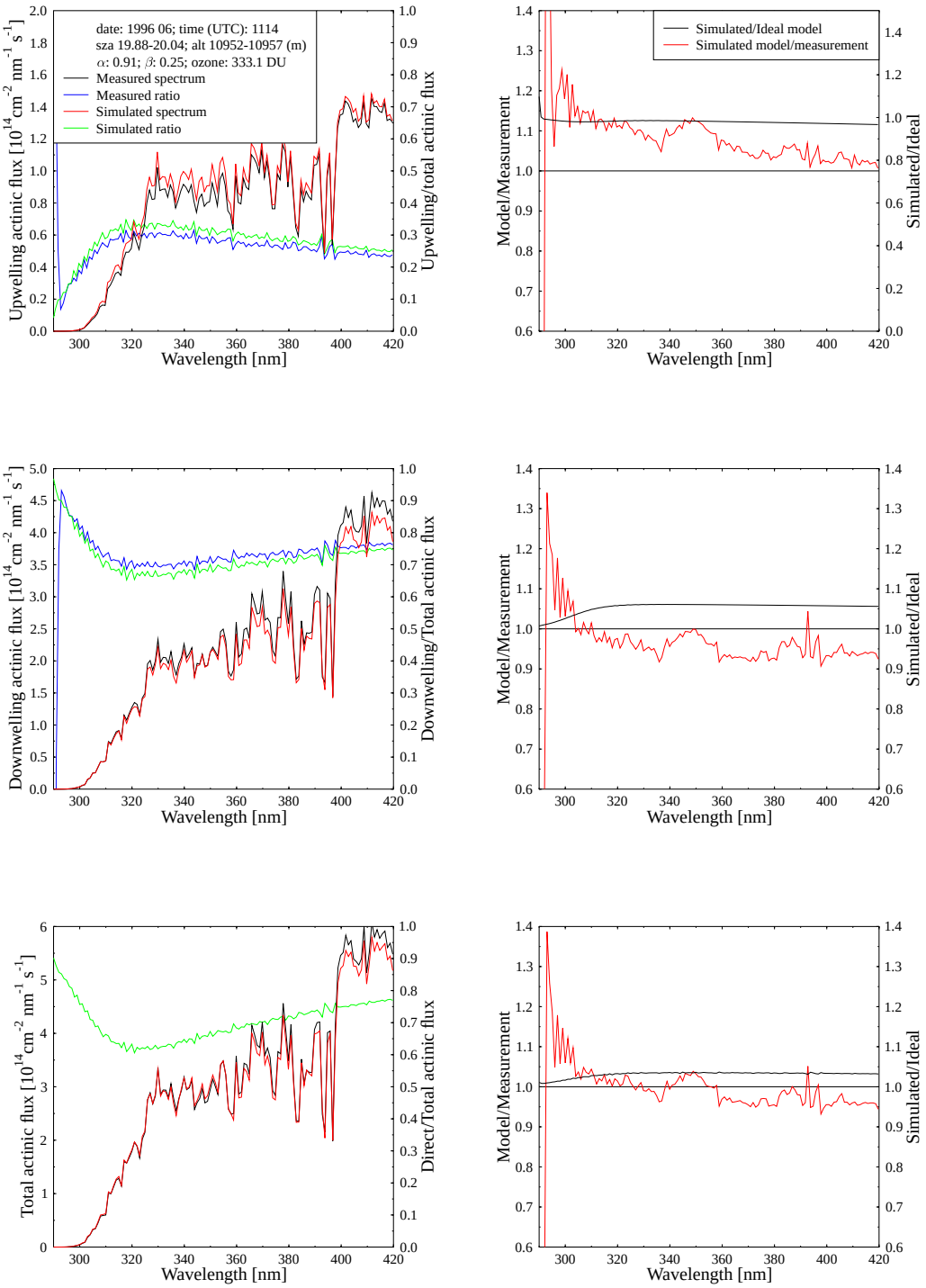

Figure 100: Same as Figure 10, except for 1114 UTC, 13 June 1996, and altitude 10957.12 m.a.s.l.

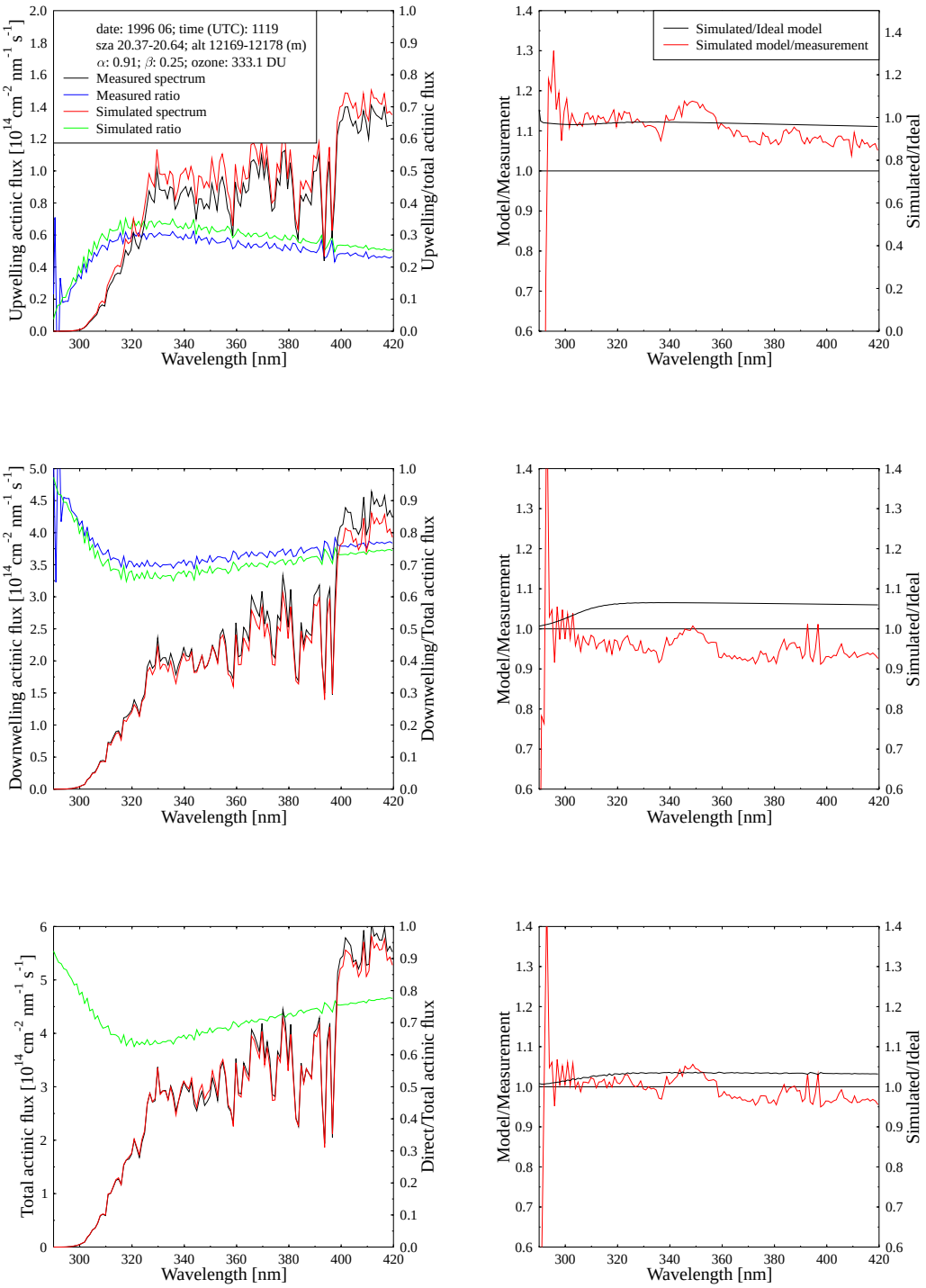

Figure 101: Same as Figure 10, except for 1119 UTC, 13 June 1996, and altitude 12169.76 m.a.s.l.

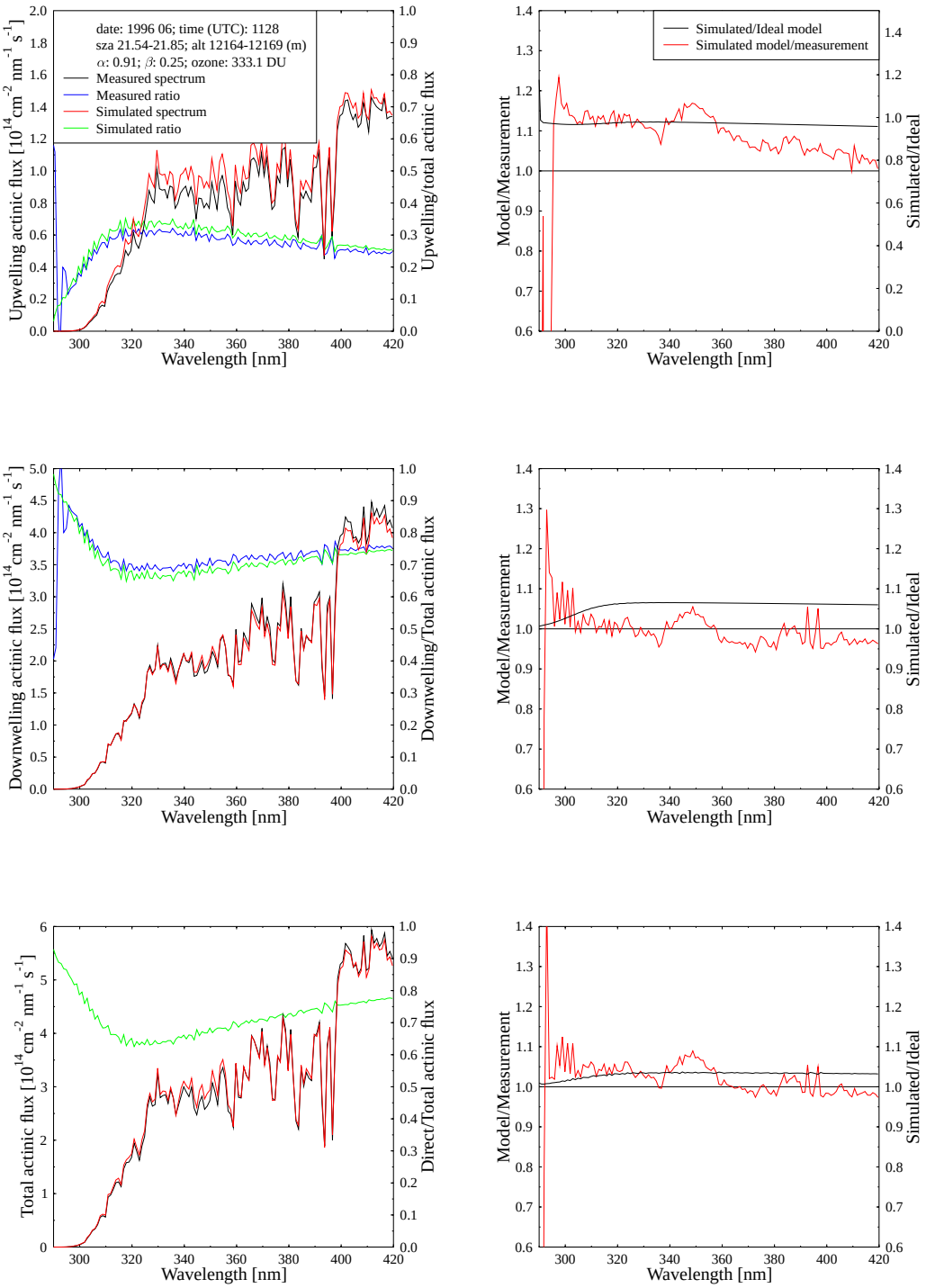

Figure 102: Same as Figure 10, except for 1128 UTC, 13 June 1996, and altitude 12165.98 m.a.s.l.

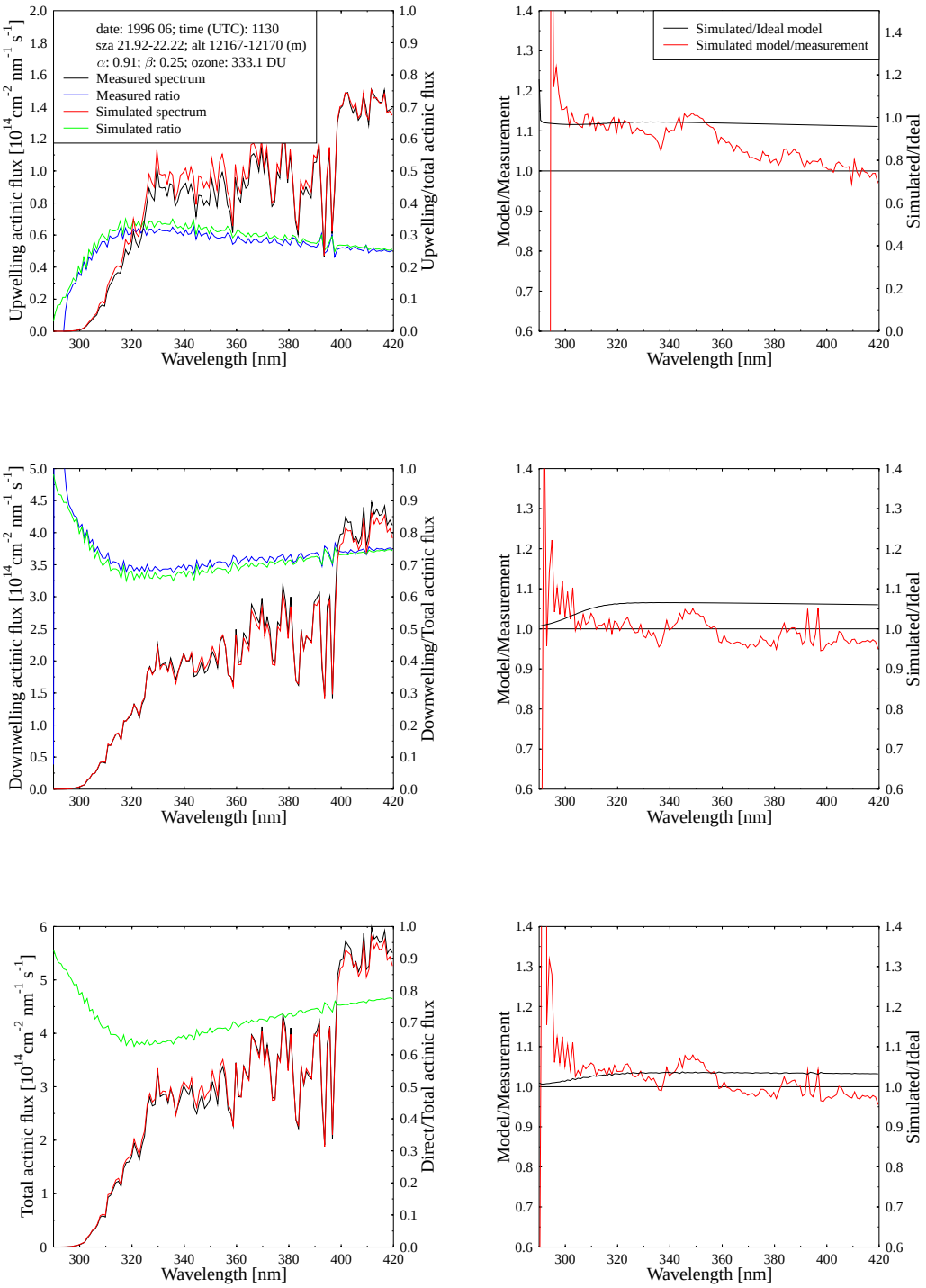

Figure 103: Same as Figure 10, except for 1130 UTC, 13 June 1996, and altitude 12170.76 m.a.s.l.

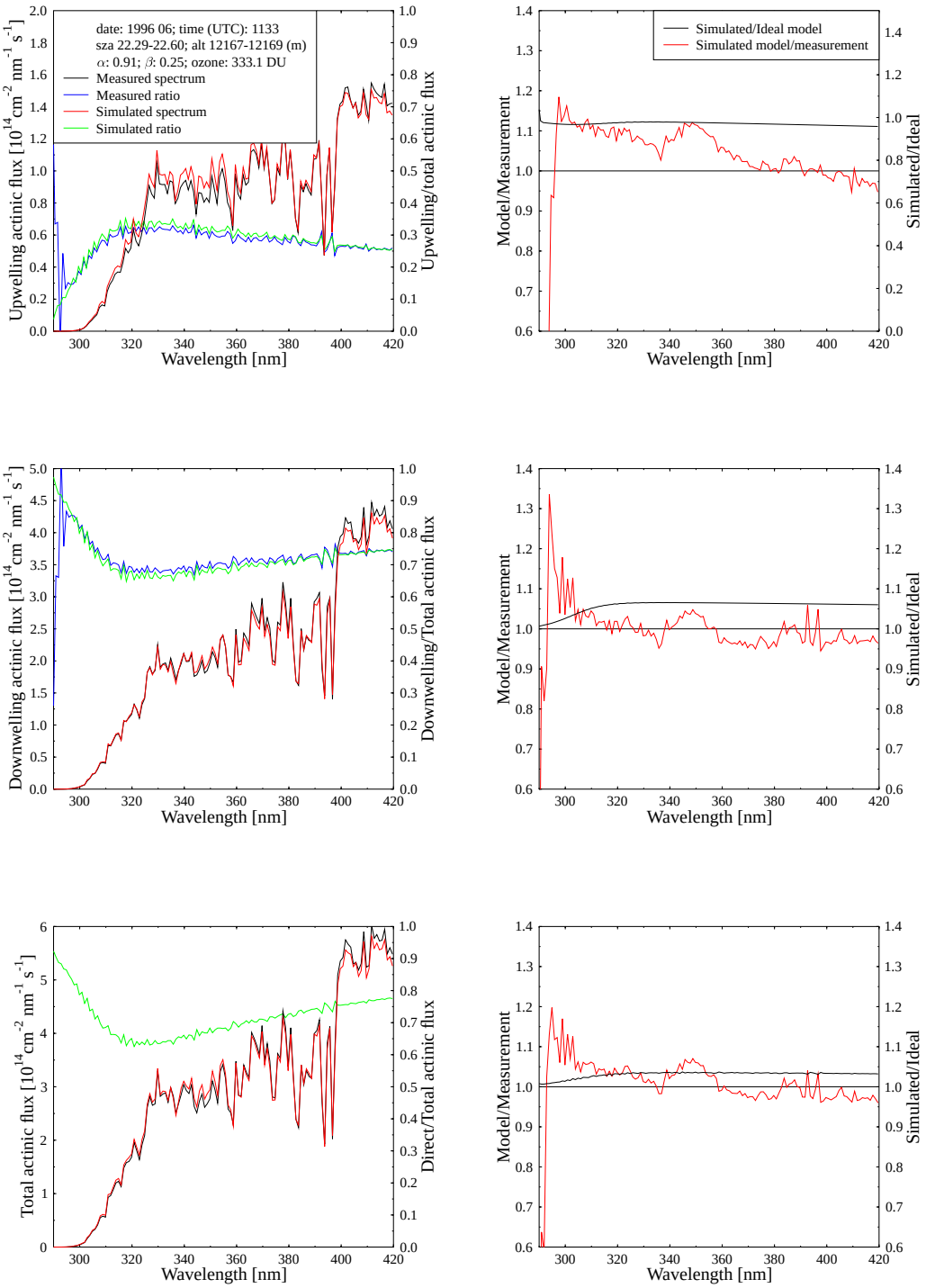

Figure 104: Same as Figure 10, except for 1133 UTC, 13 June 1996, and altitude 12167.26 m.a.s.l.

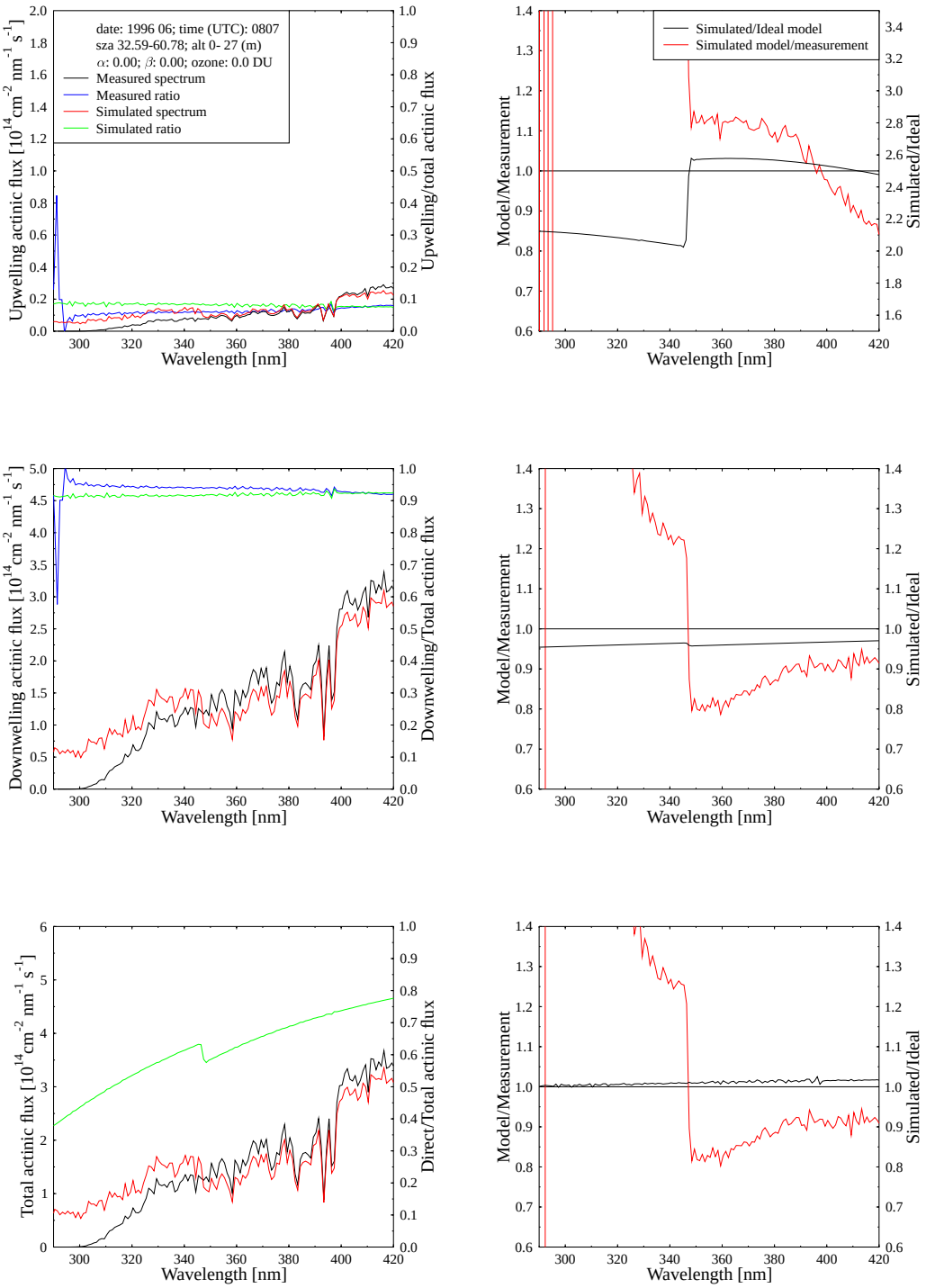

Figure 105: Same as Figure 10, except for 0807 UTC, 14 June 1996, and altitude 27 m.a.s.l.

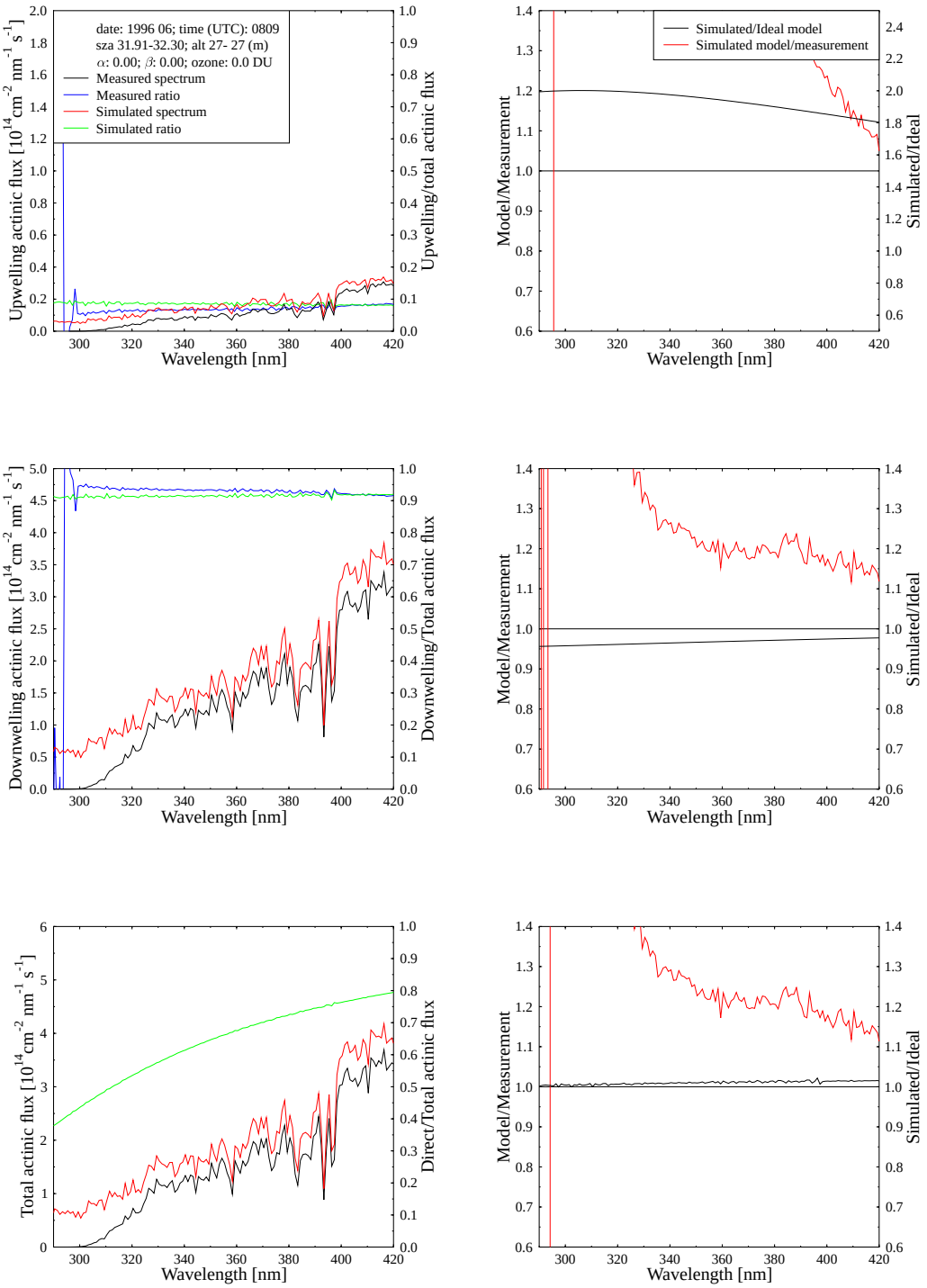

Figure 106: Same as Figure 10, except for 0809 UTC, 14 June 1996, and altitude 27 m.a.s.l.

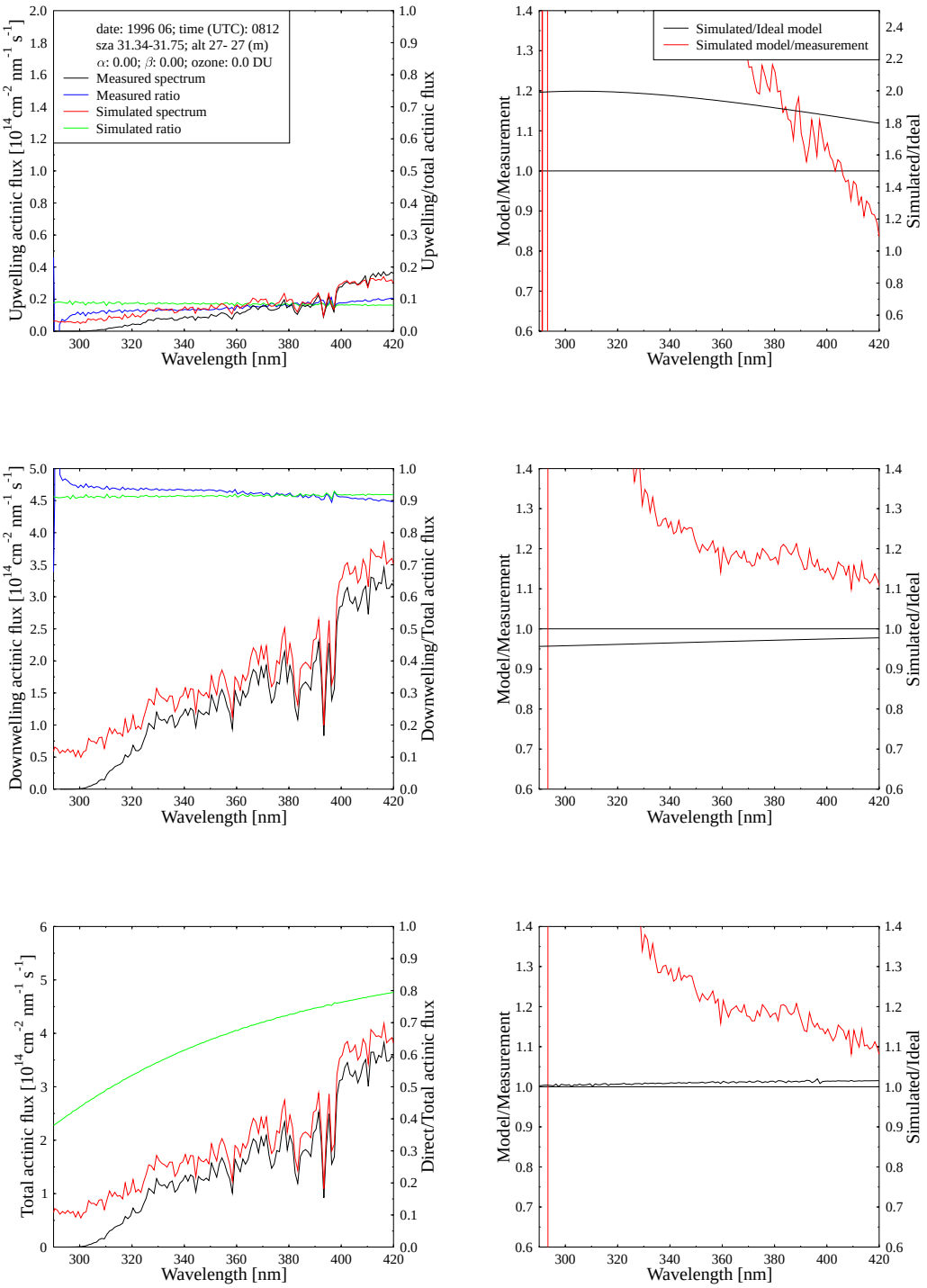

Figure 107: Same as Figure 10, except for 0812 UTC, 14 June 1996, and altitude 27 m.a.s.l.

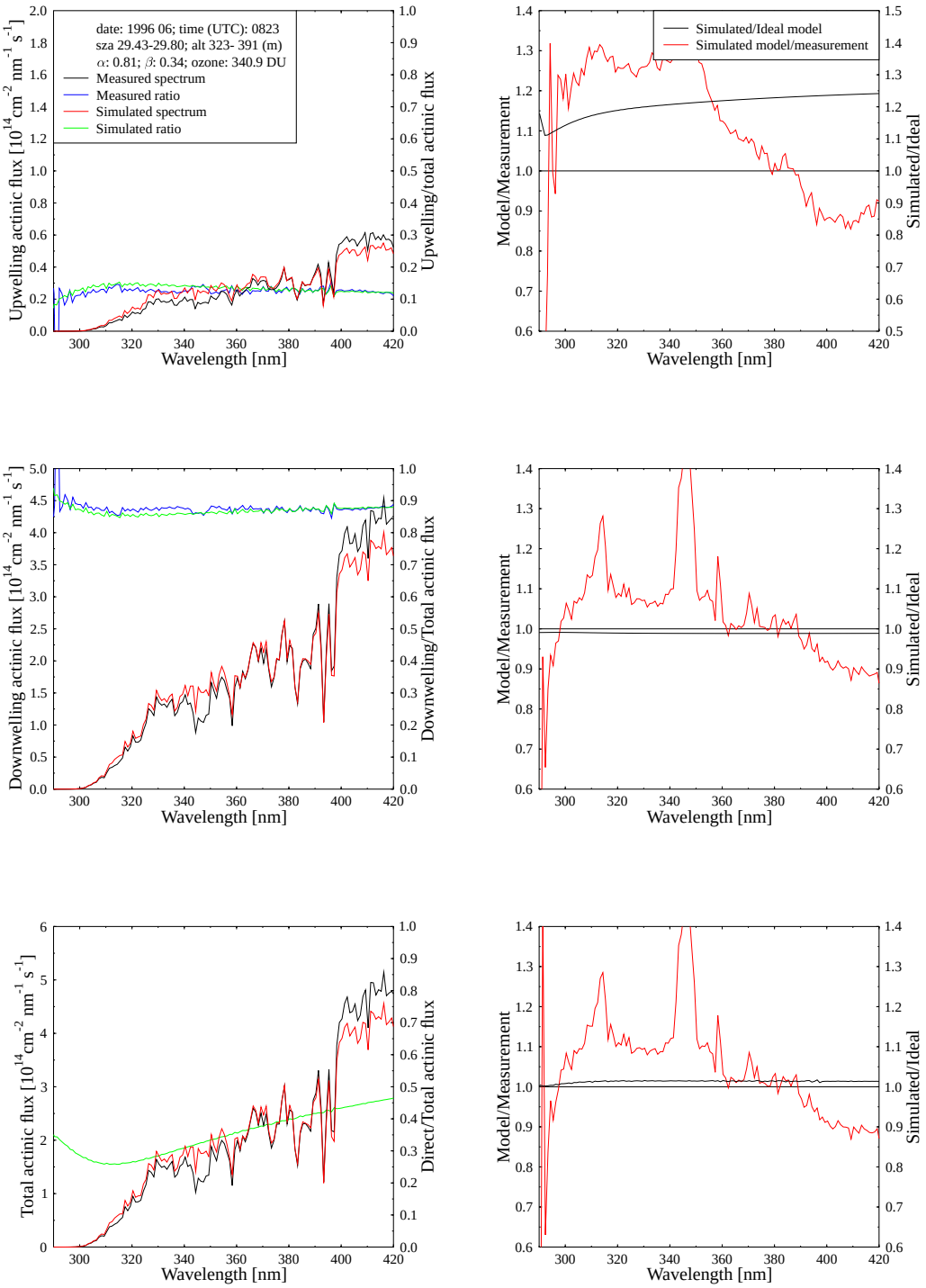

Figure 108: Same as Figure 10, except for 0823 UTC, 14 June 1996, and altitude 352 m.a.s.l.

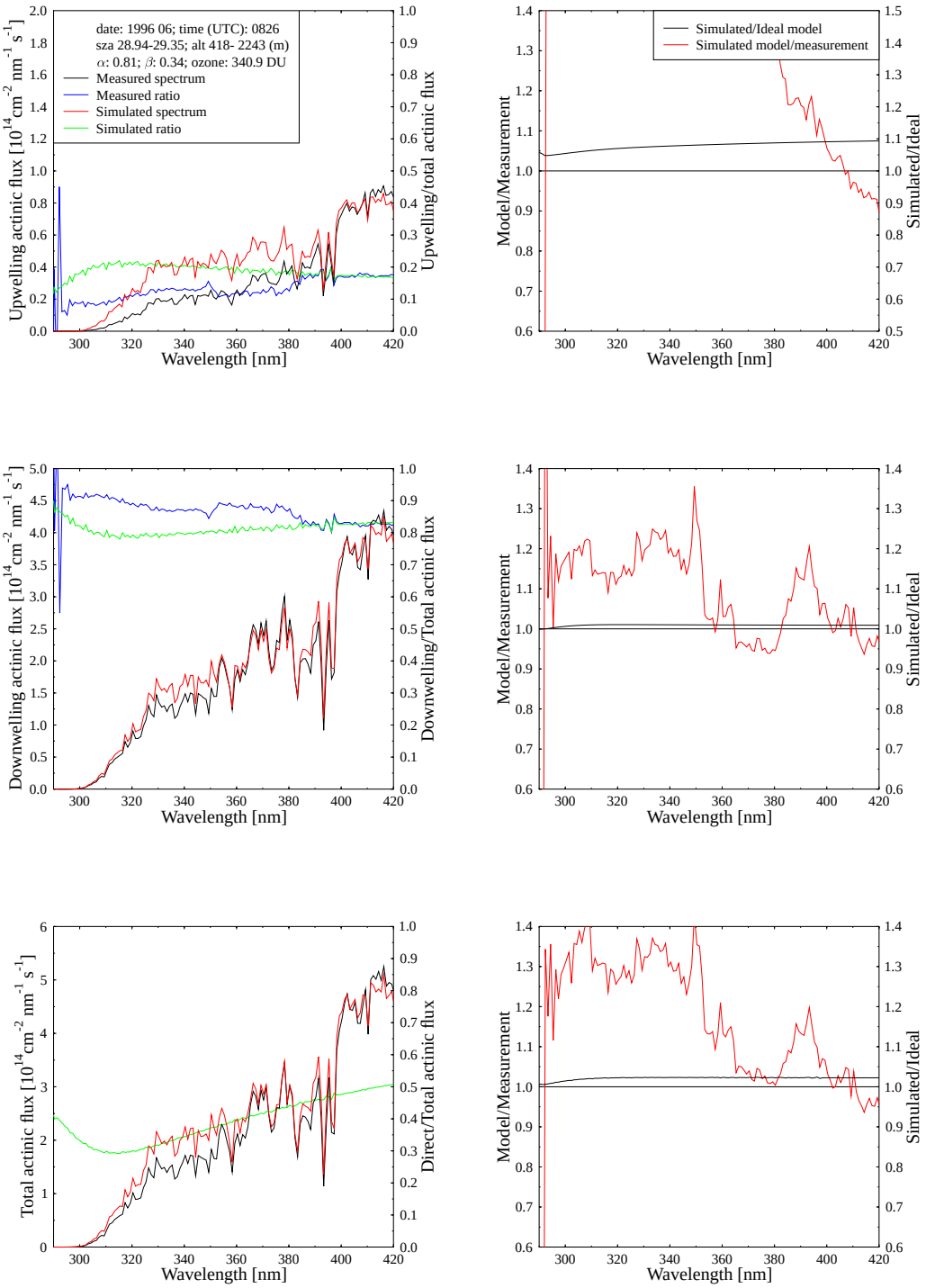

Figure 109: Same as Figure 10, except for 0826 UTC, 14 June 1996, and altitude 418 m.a.s.l.

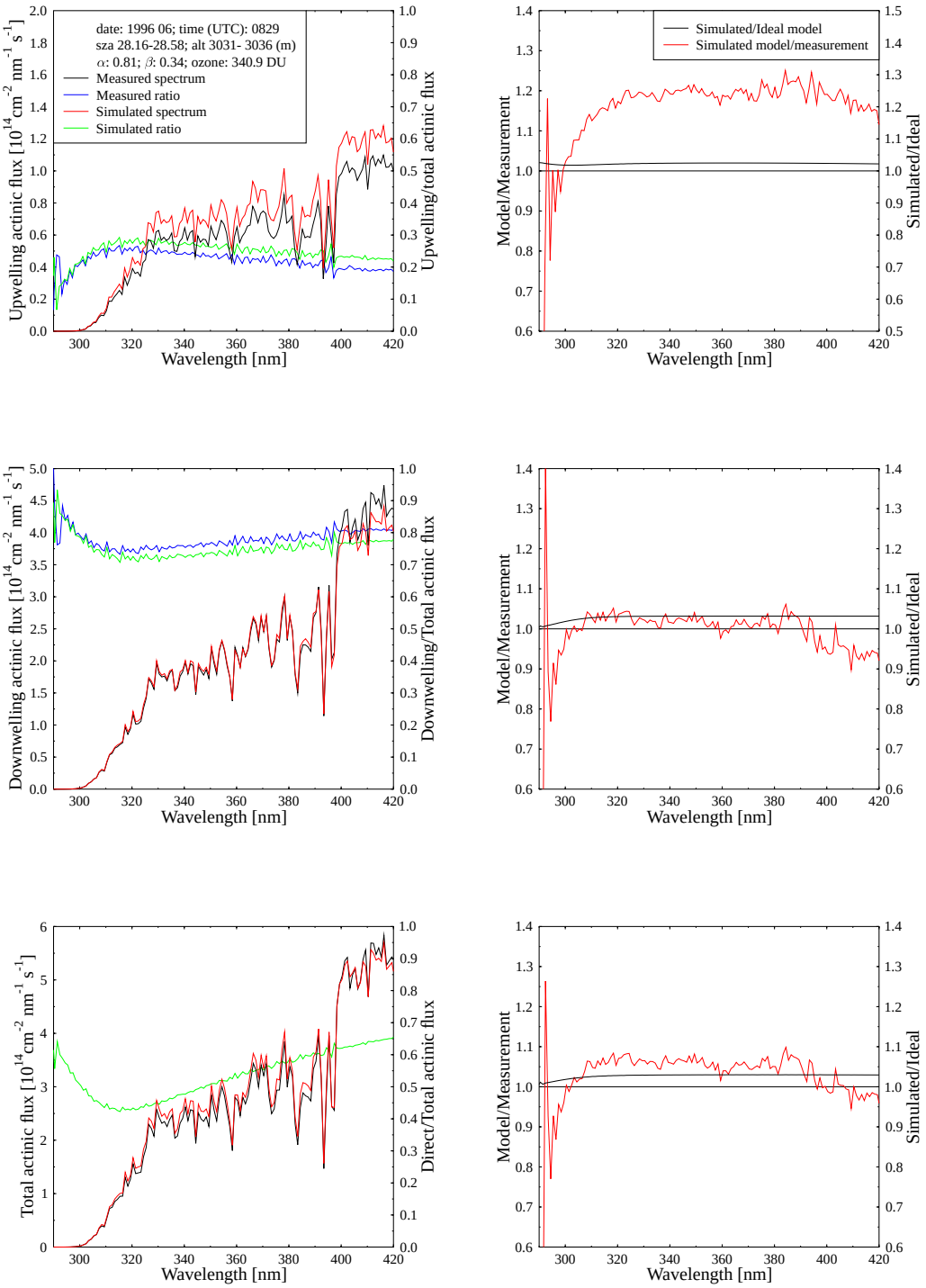

Figure 110: Same as Figure 10, except for 0829 UTC, 14 June 1996, and altitude 3031 m.a.s.l.

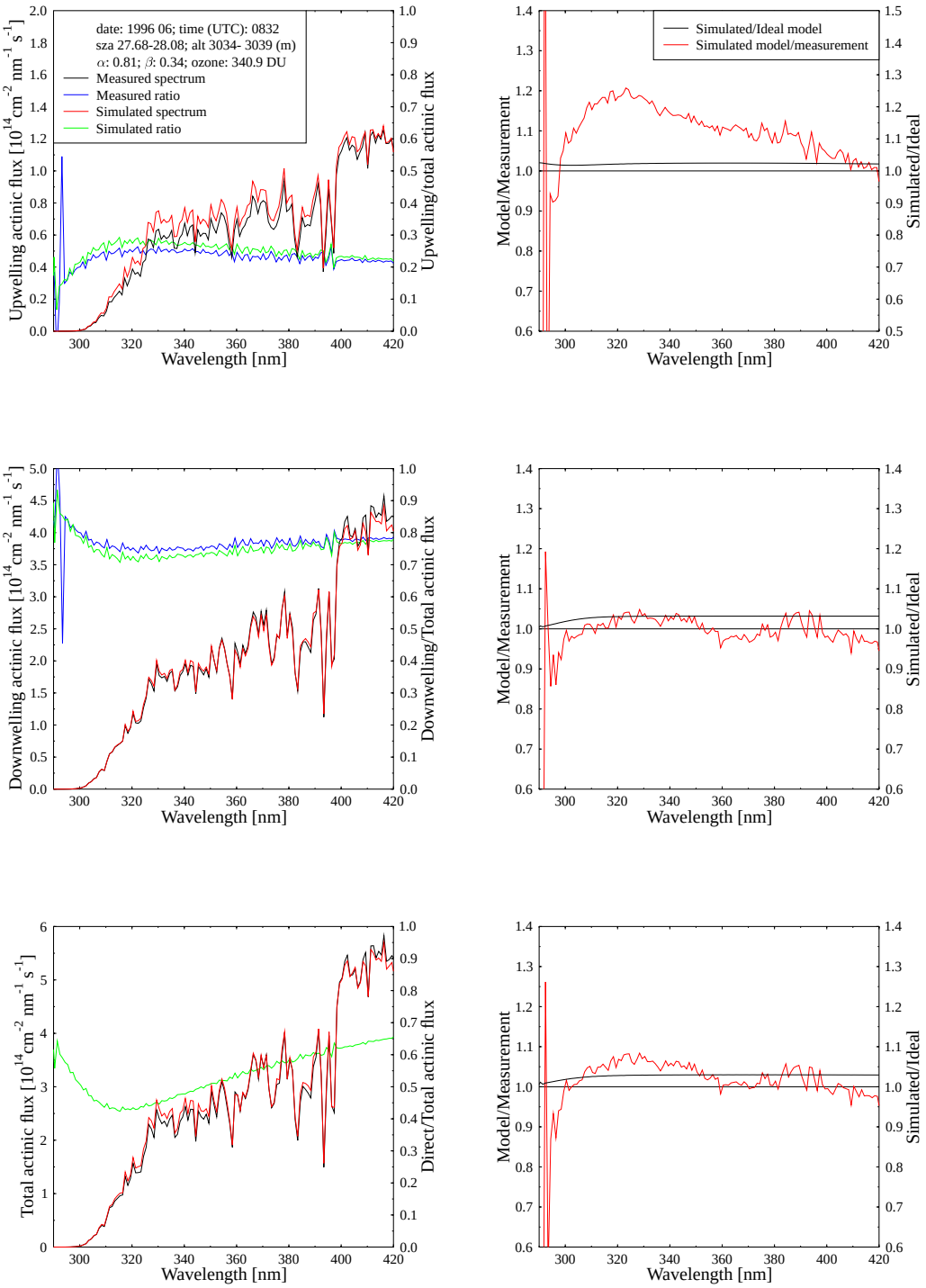

Figure 111: Same as Figure 10, except for 0832 UTC, 14 June 1996, and altitude 3037 m.a.s.l.

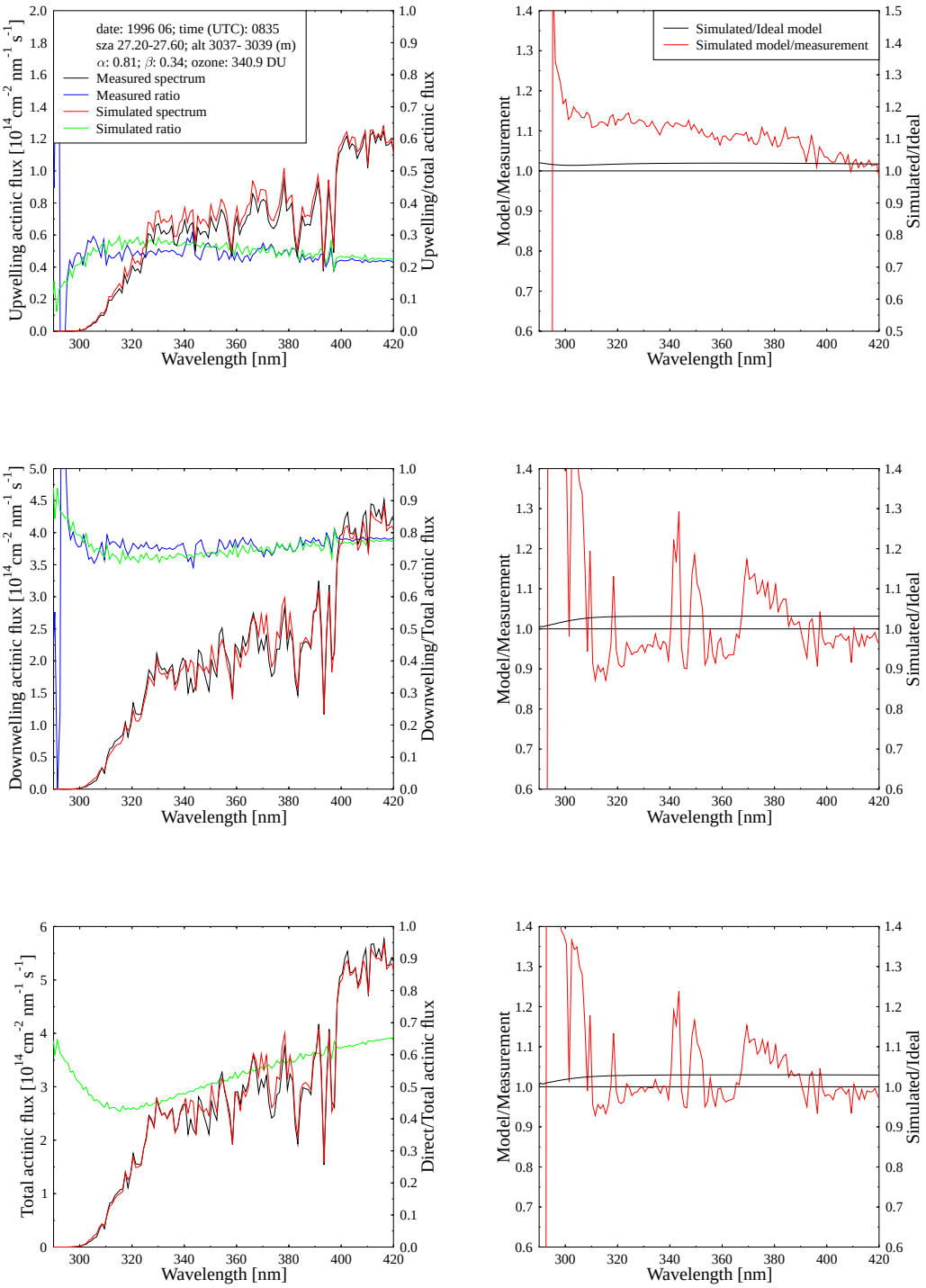

Figure 112: Same as Figure 10, except for 0835 UTC, 14 June 1996, and altitude 3037 m.a.s.l.

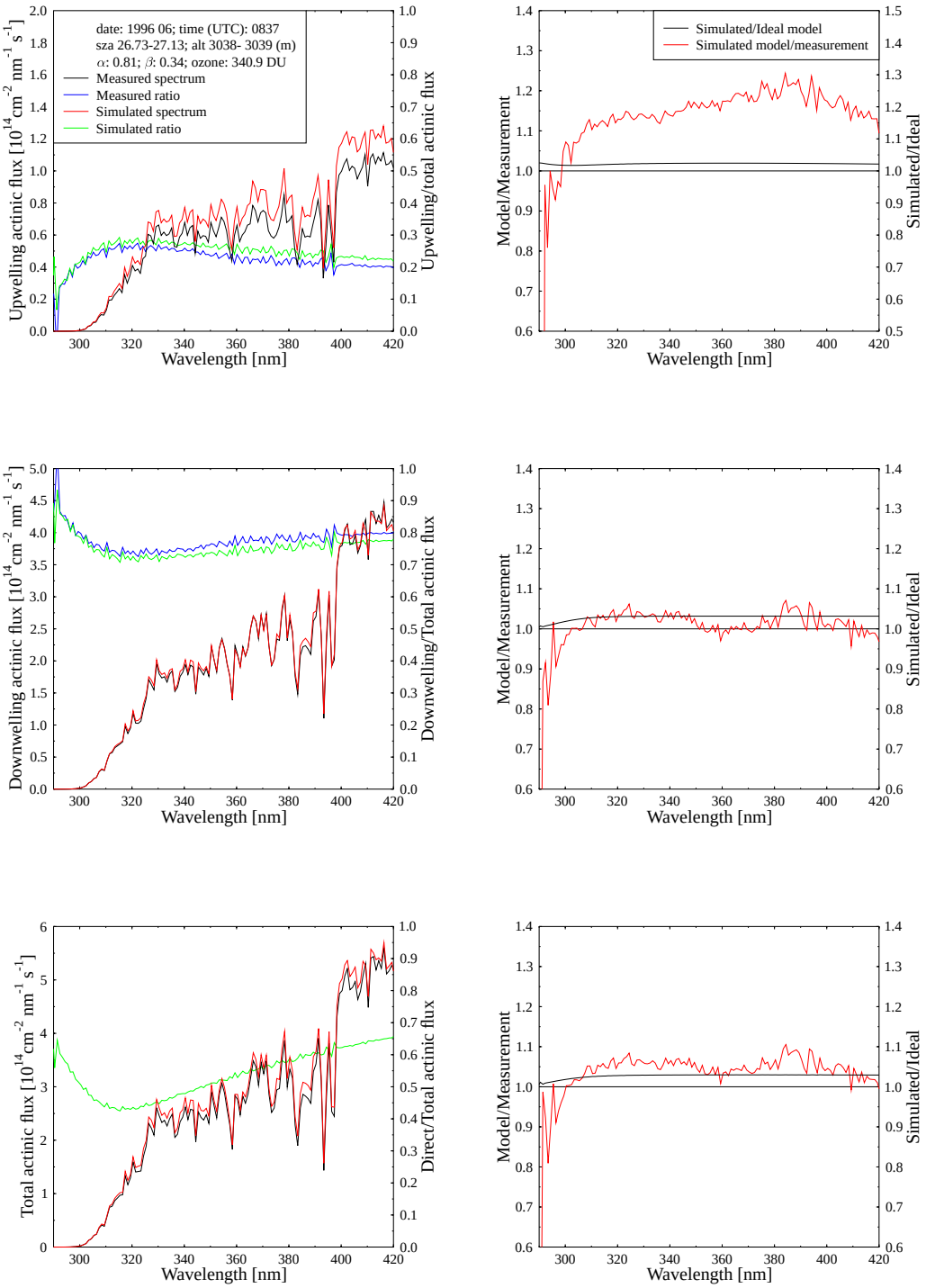

Figure 113: Same as Figure 10, except for 0837 UTC, 14 June 1996, and altitude 3038.99 m.a.s.l.

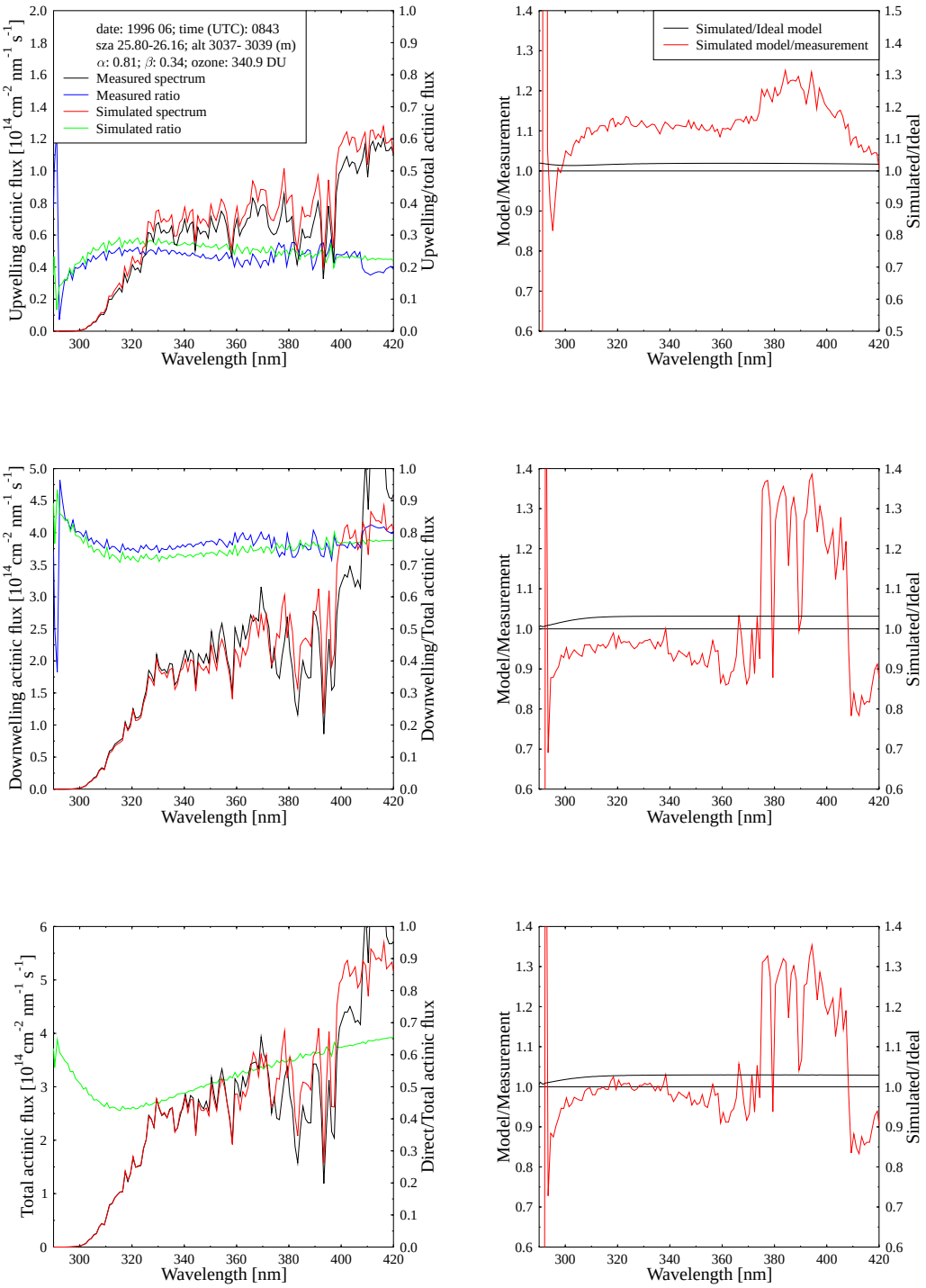

Figure 114: Same as Figure 10, except for 0843 UTC, 14 June 1996, and altitude 3038 m.a.s.l.

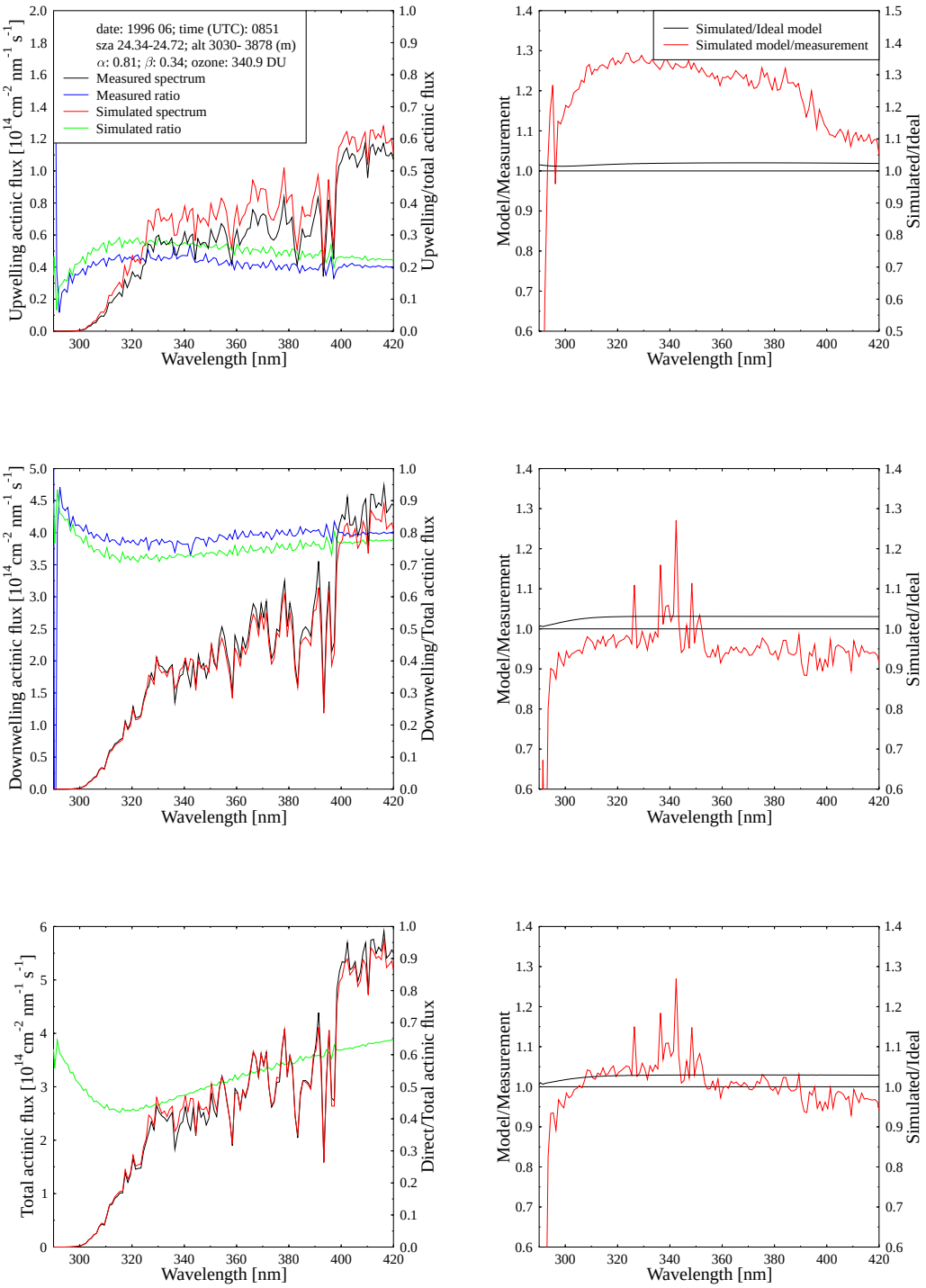

Figure 115: Same as Figure 10, except for 0851 UTC, 14 June 1996, and altitude 3033.79 m.a.s.l.

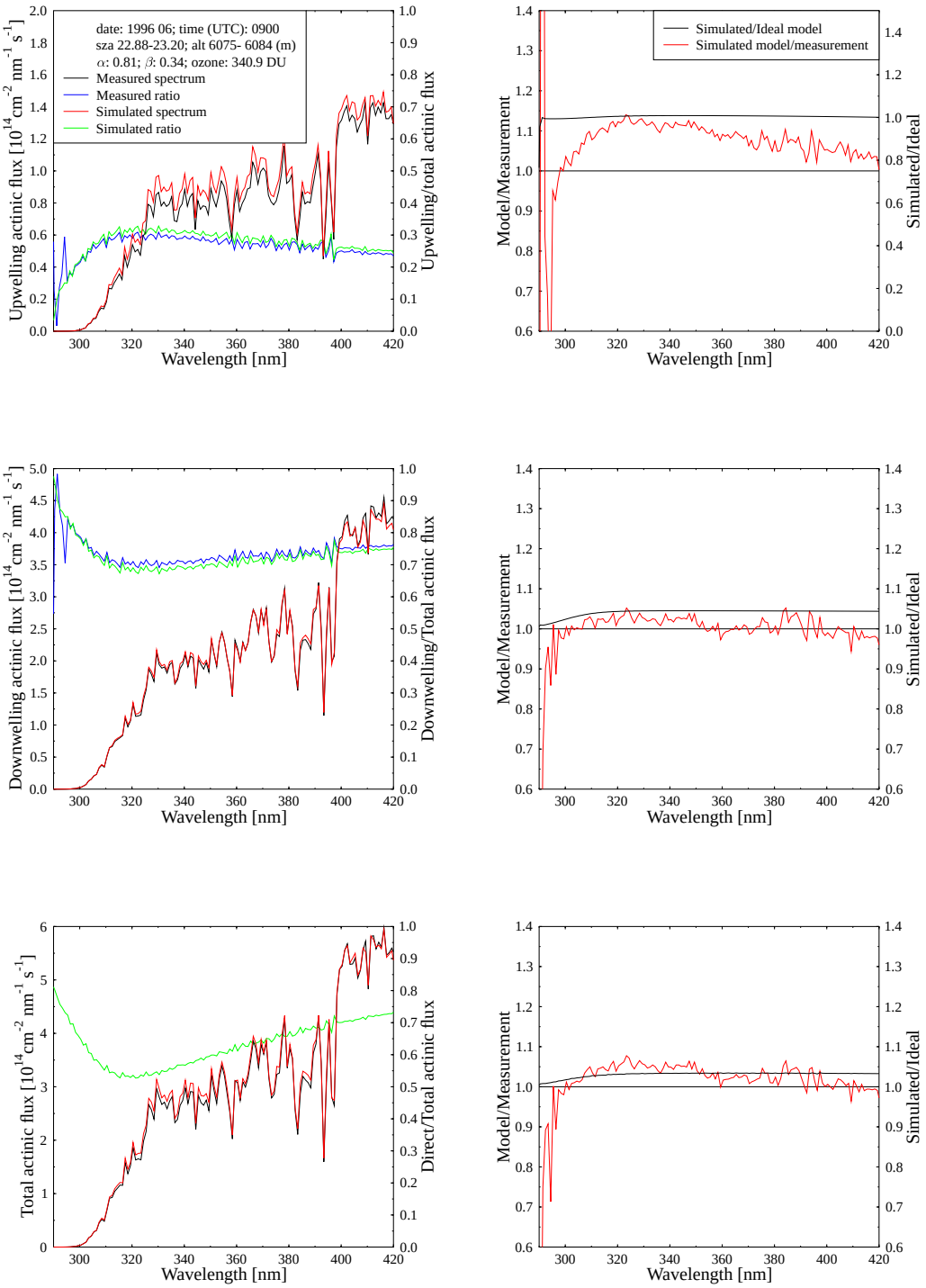

Figure 116: Same as Figure 10, except for 0900 UTC, 14 June 1996, and altitude 6075 m.a.s.l.

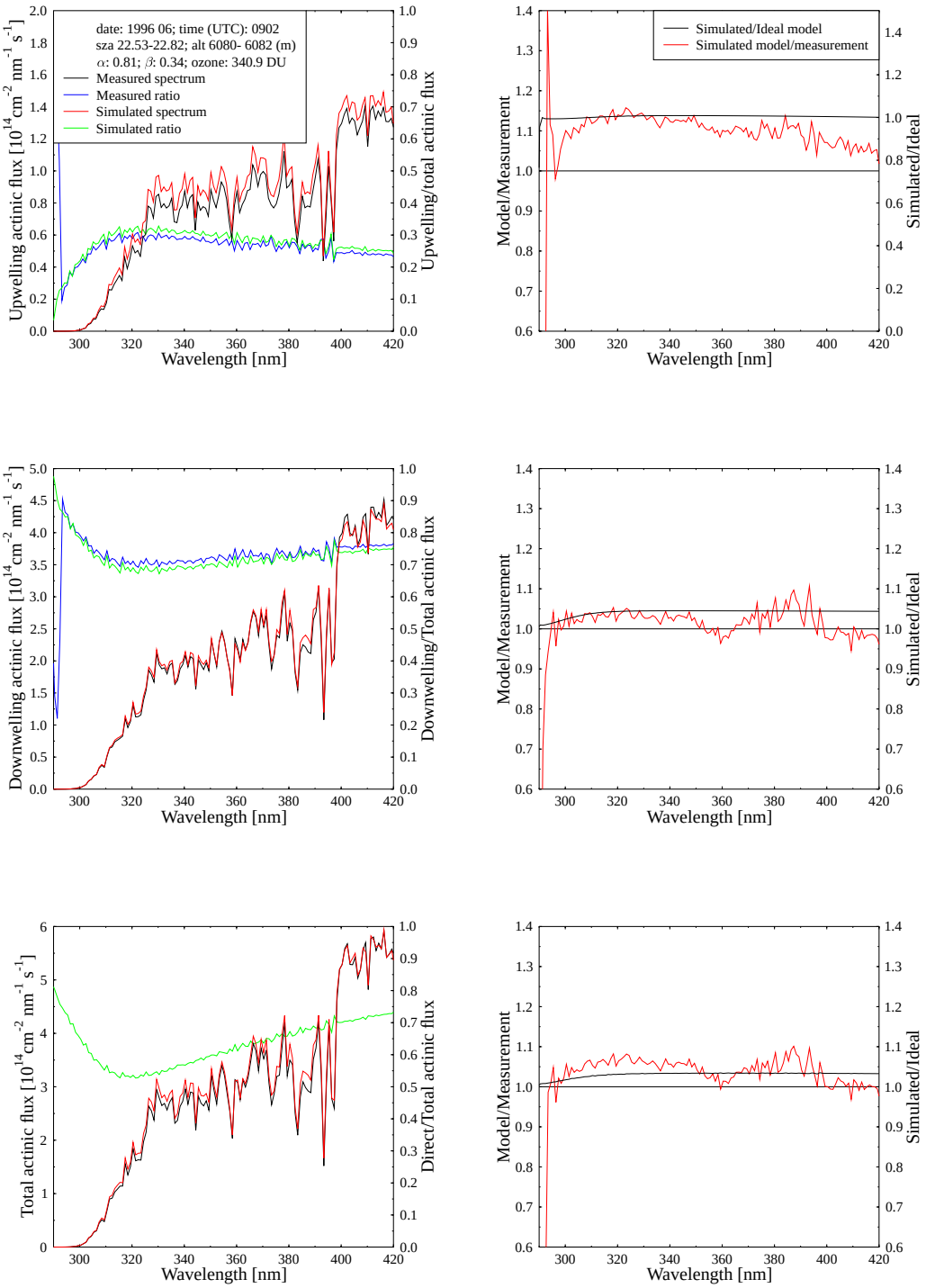

Figure 117: Same as Figure 10, except for 0902 UTC, 14 June 1996, and altitude 6081 m.a.s.l.

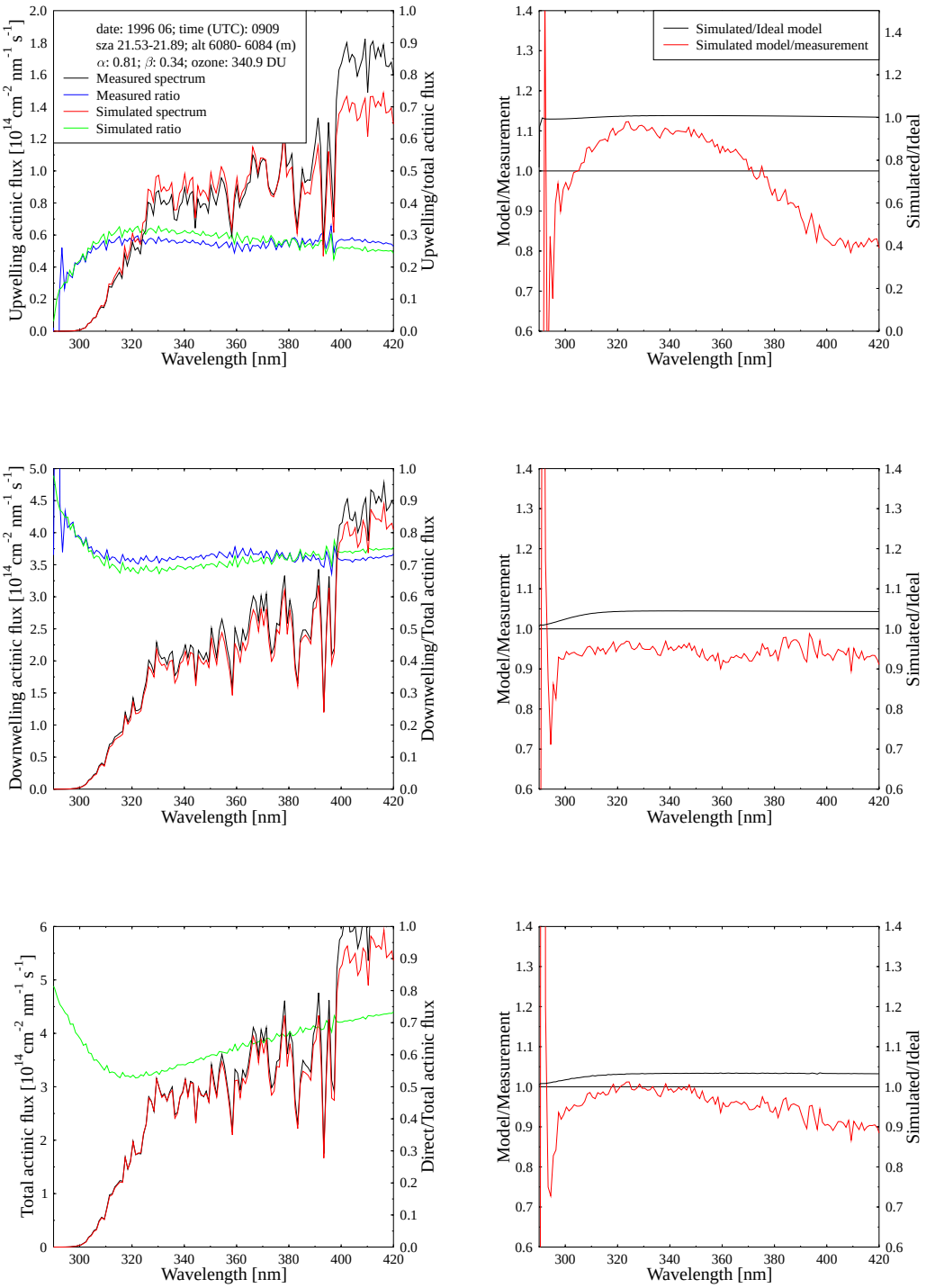

Figure 118: Same as Figure 10, except for 0909 UTC, 14 June 1996, and altitude 6083 m.a.s.l.

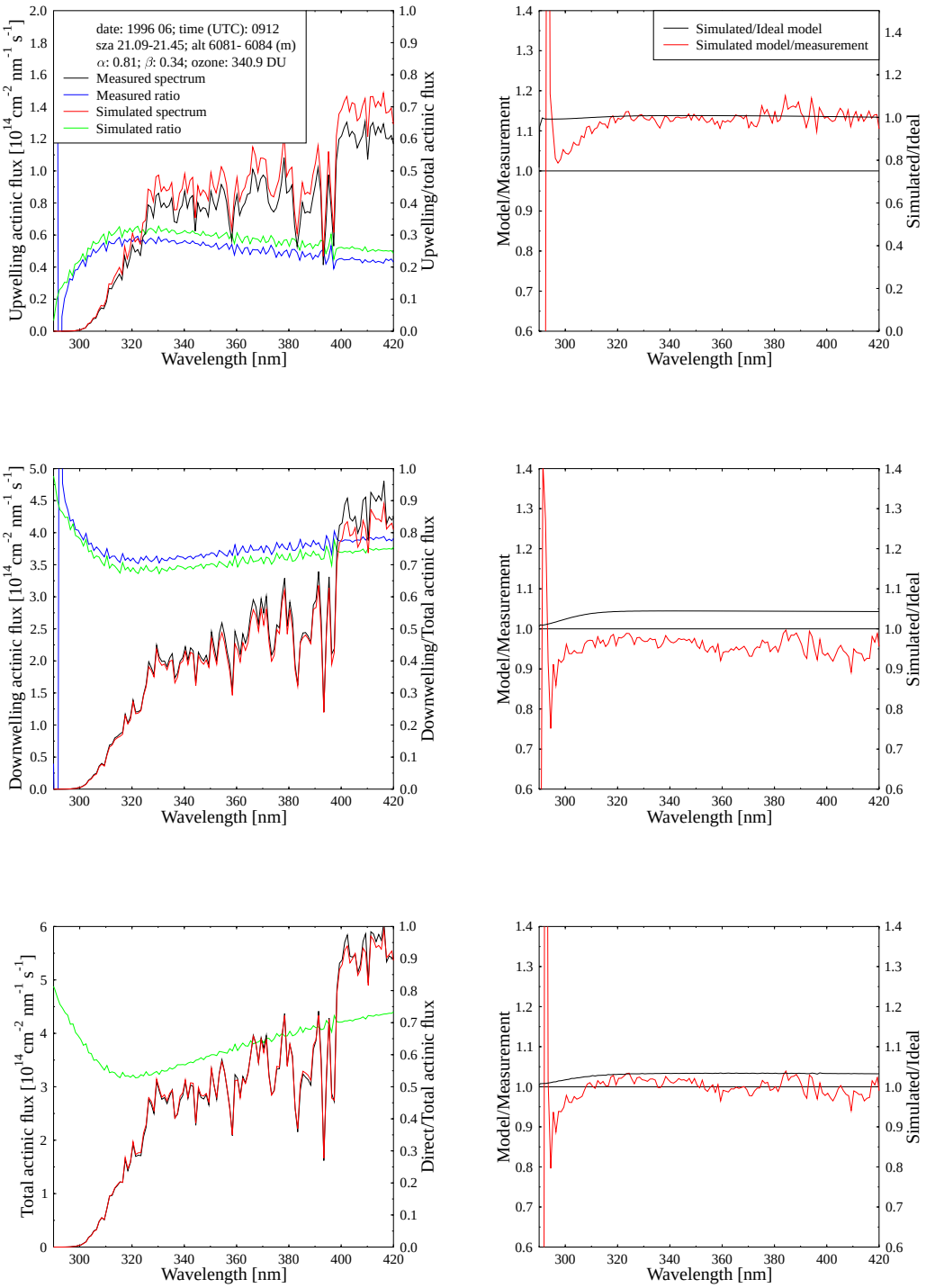

Figure 119: Same as Figure 10, except for 0912 UTC, 14 June 1996, and altitude 6083 m.a.s.l.

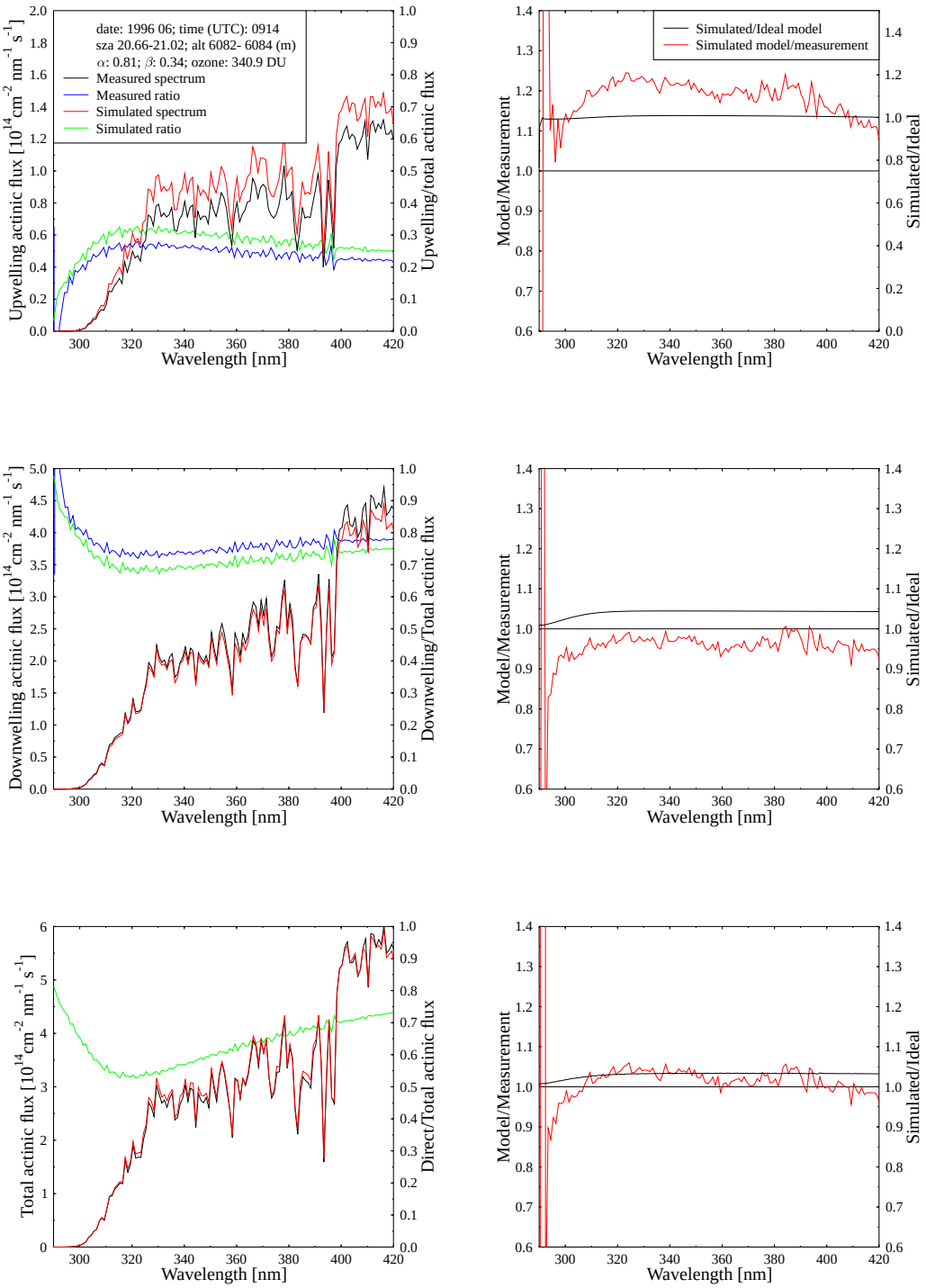

Figure 120: Same as Figure 10, except for 0914 UTC, 14 June 1996, and altitude 6082 m.a.s.l.

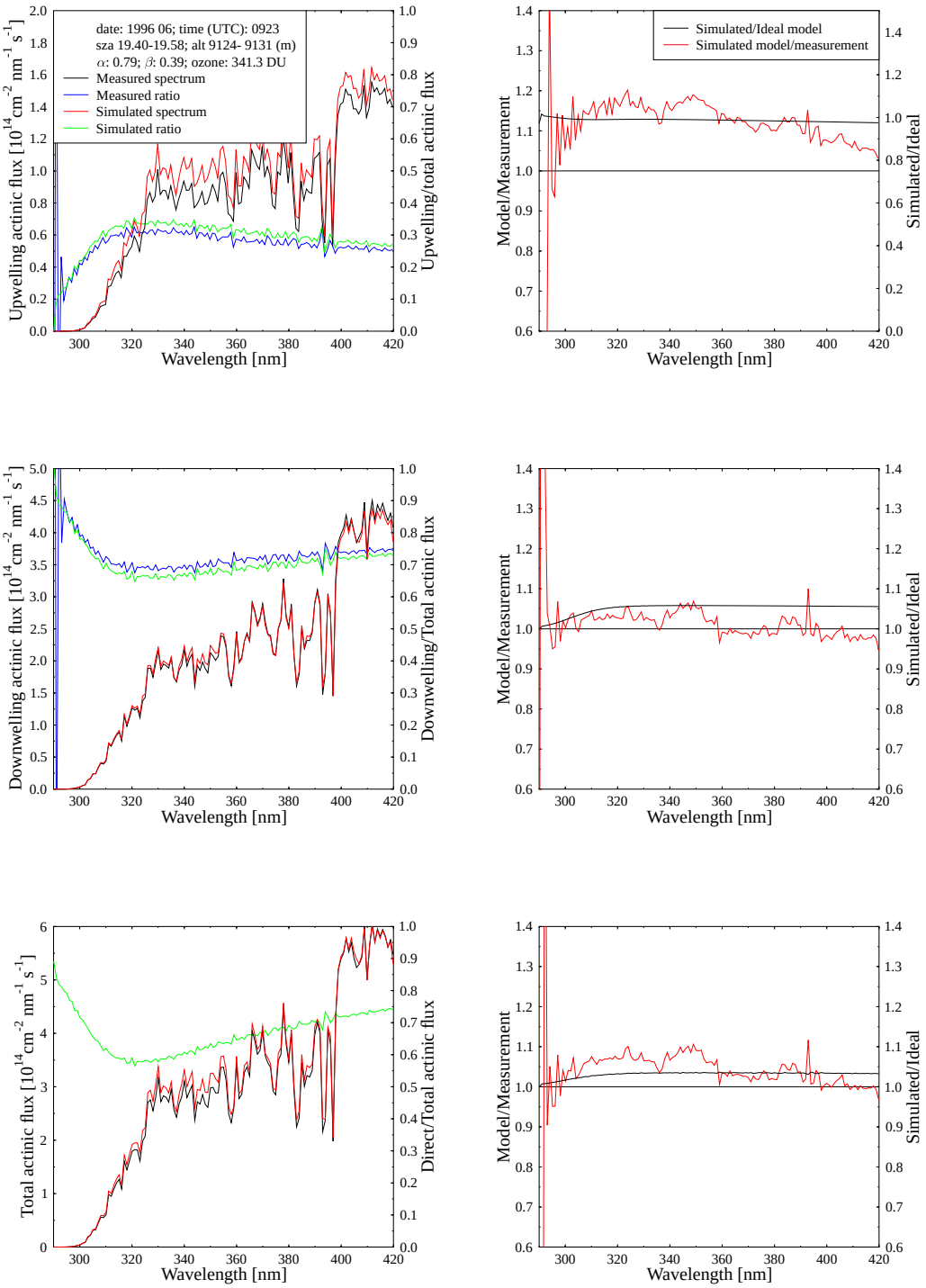

Figure 121: Same as Figure 10, except for 0923 UTC, 14 June 1996, and altitude 9124 m.a.s.l.

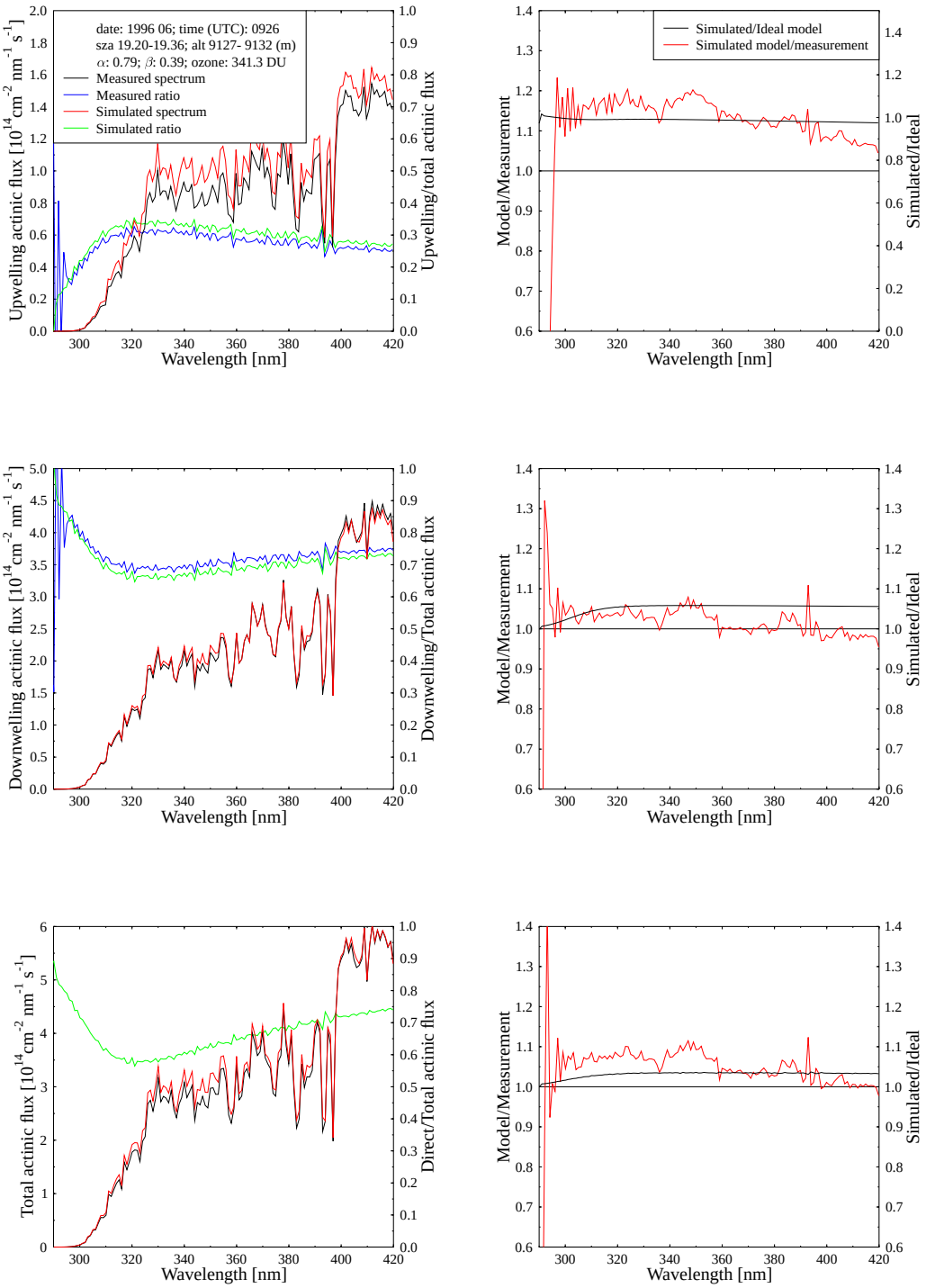

Figure 122: Same as Figure 10, except for 0926 UTC, 14 June 1996, and altitude 9127 m.a.s.l.

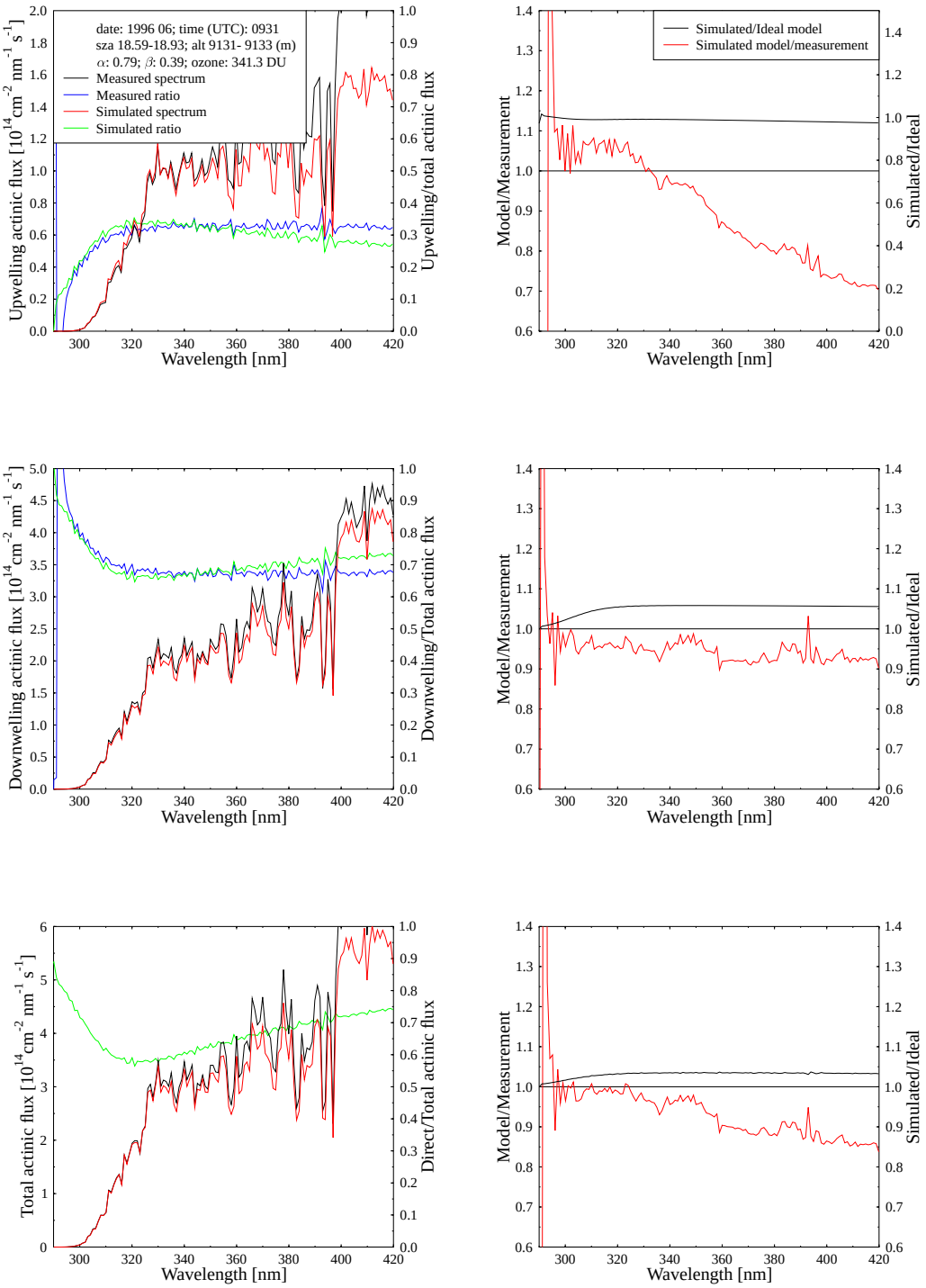

Figure 123: Same as Figure 10, except for 0931 UTC, 14 June 1996, and altitude 9132 m.a.s.l.

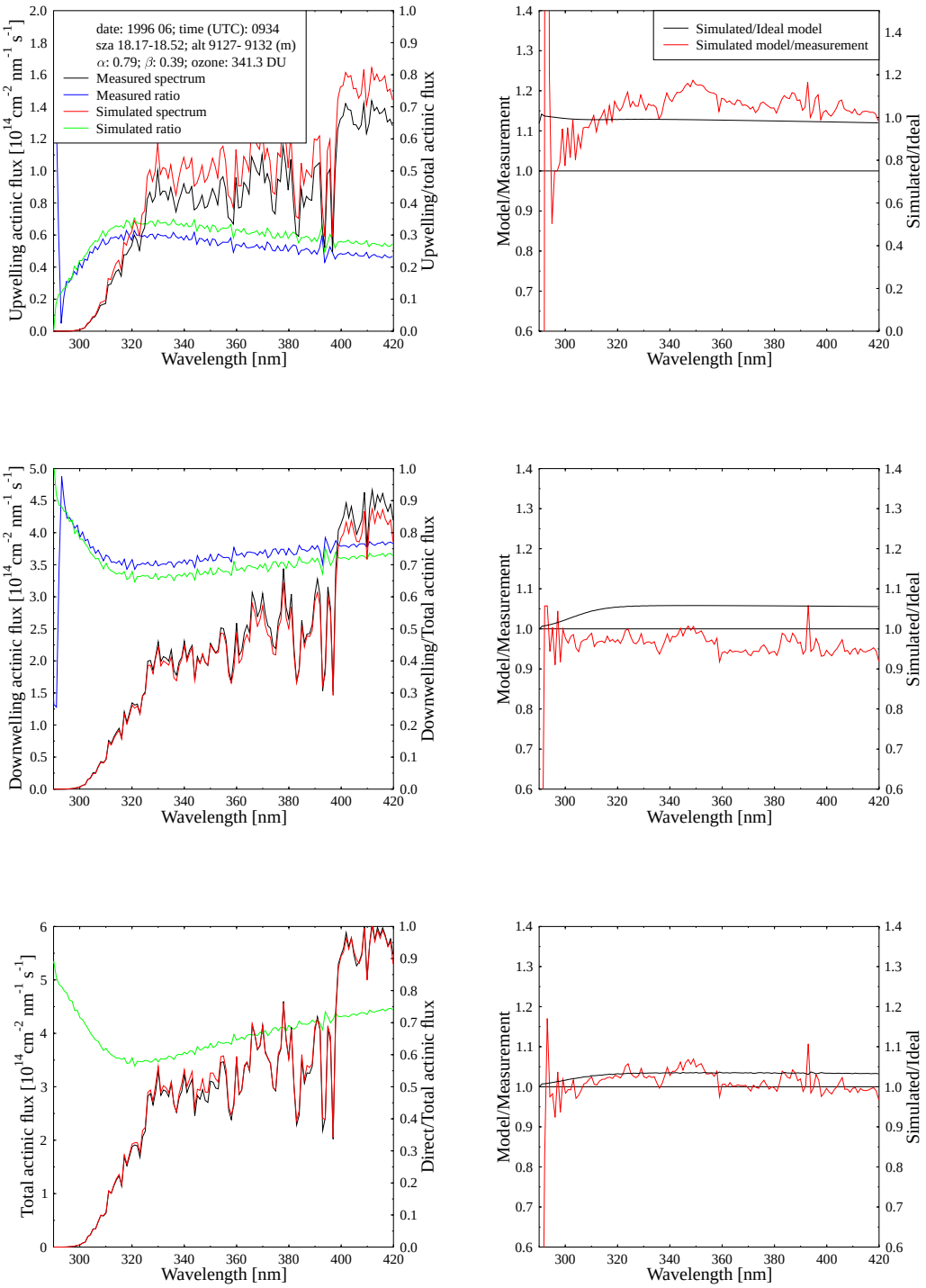

Figure 124: Same as Figure 10, except for 0934 UTC, 14 June 1996, and altitude 9132 m.a.s.l.

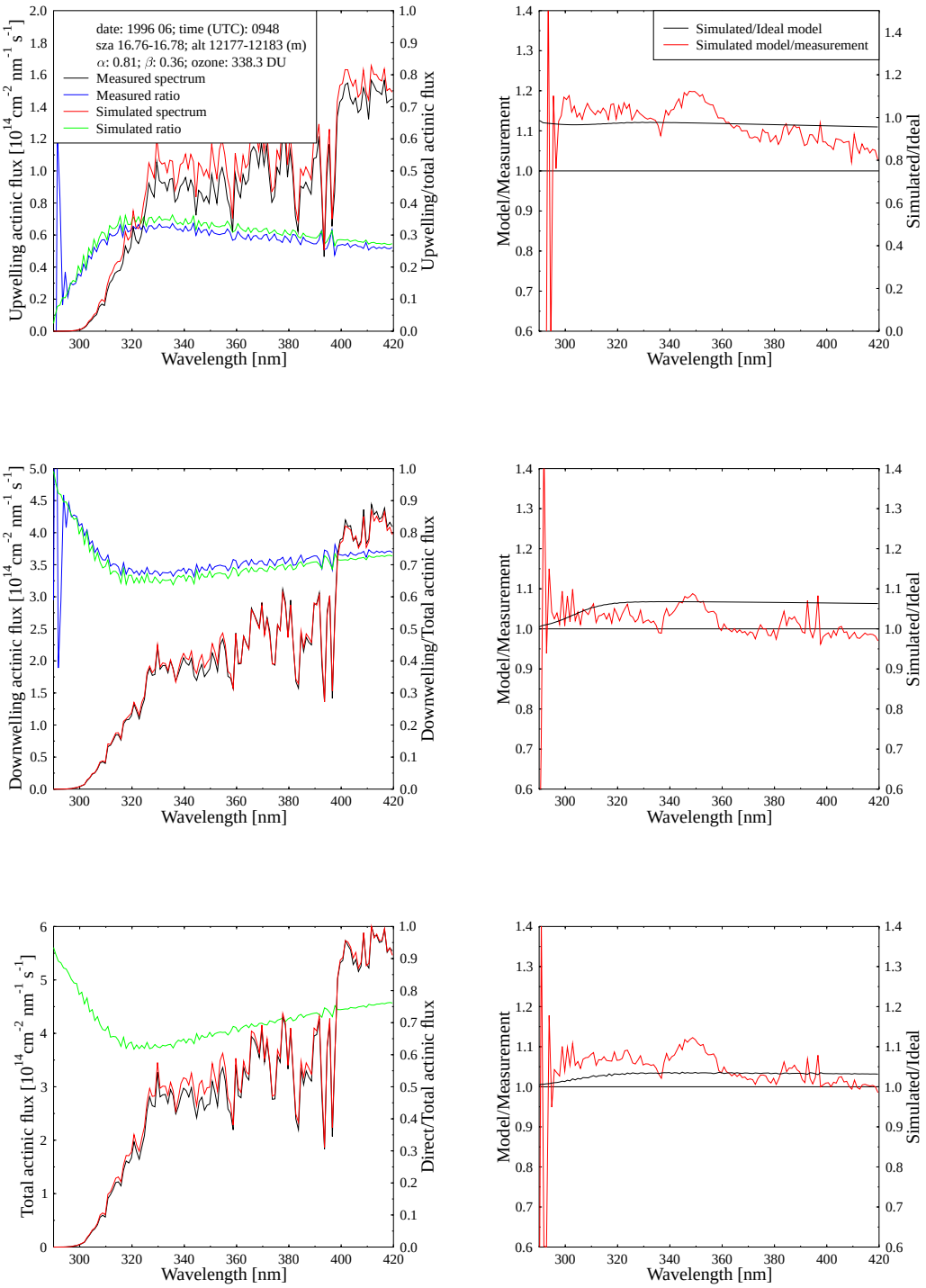

Figure 125: Same as Figure 10, except for 0948 UTC, 14 June 1996, and altitude 12183 m.a.s.l.

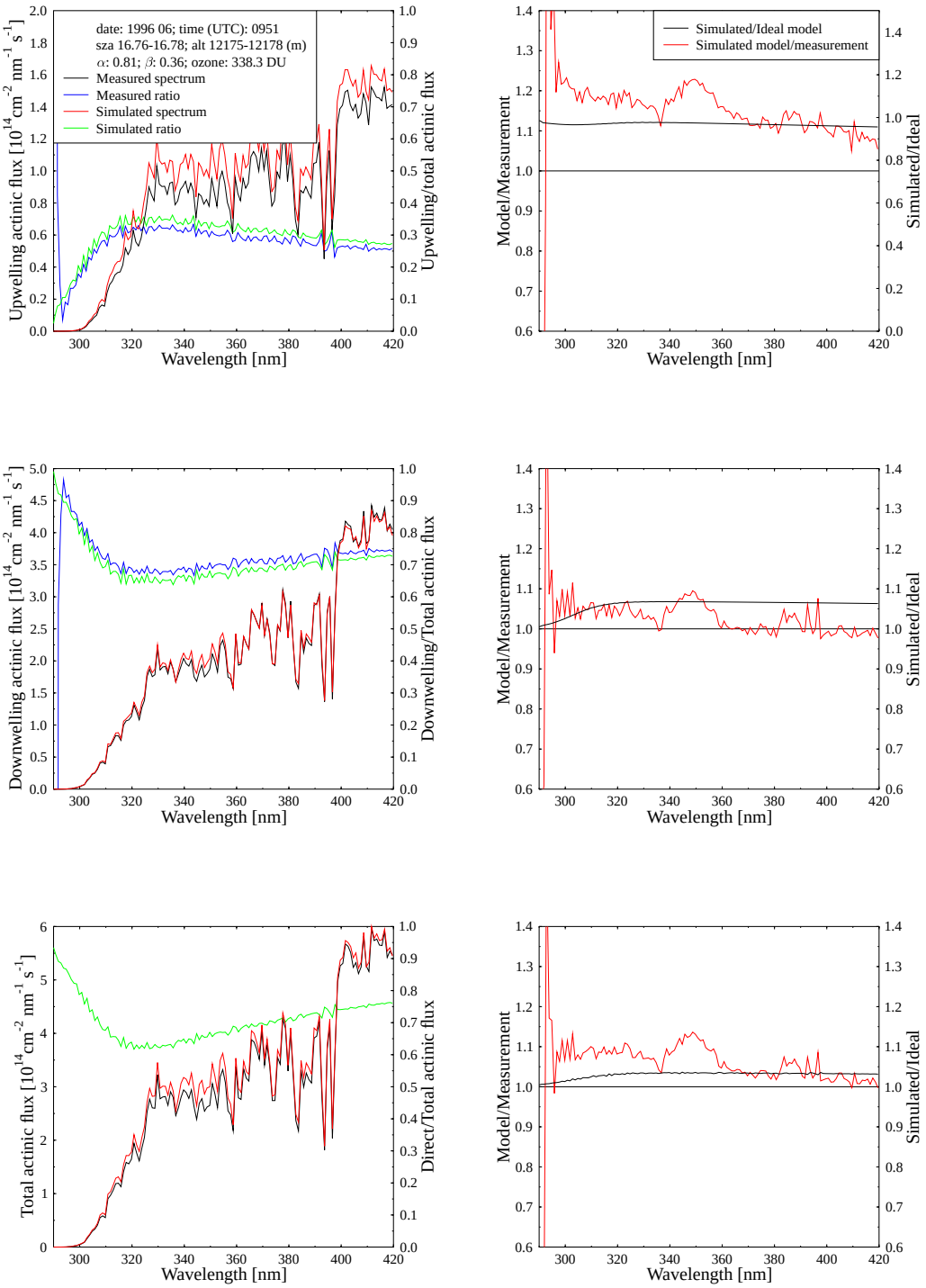

Figure 126: Same as Figure 10, except for 0951 UTC, 14 June 1996, and altitude 12178 m.a.s.l.

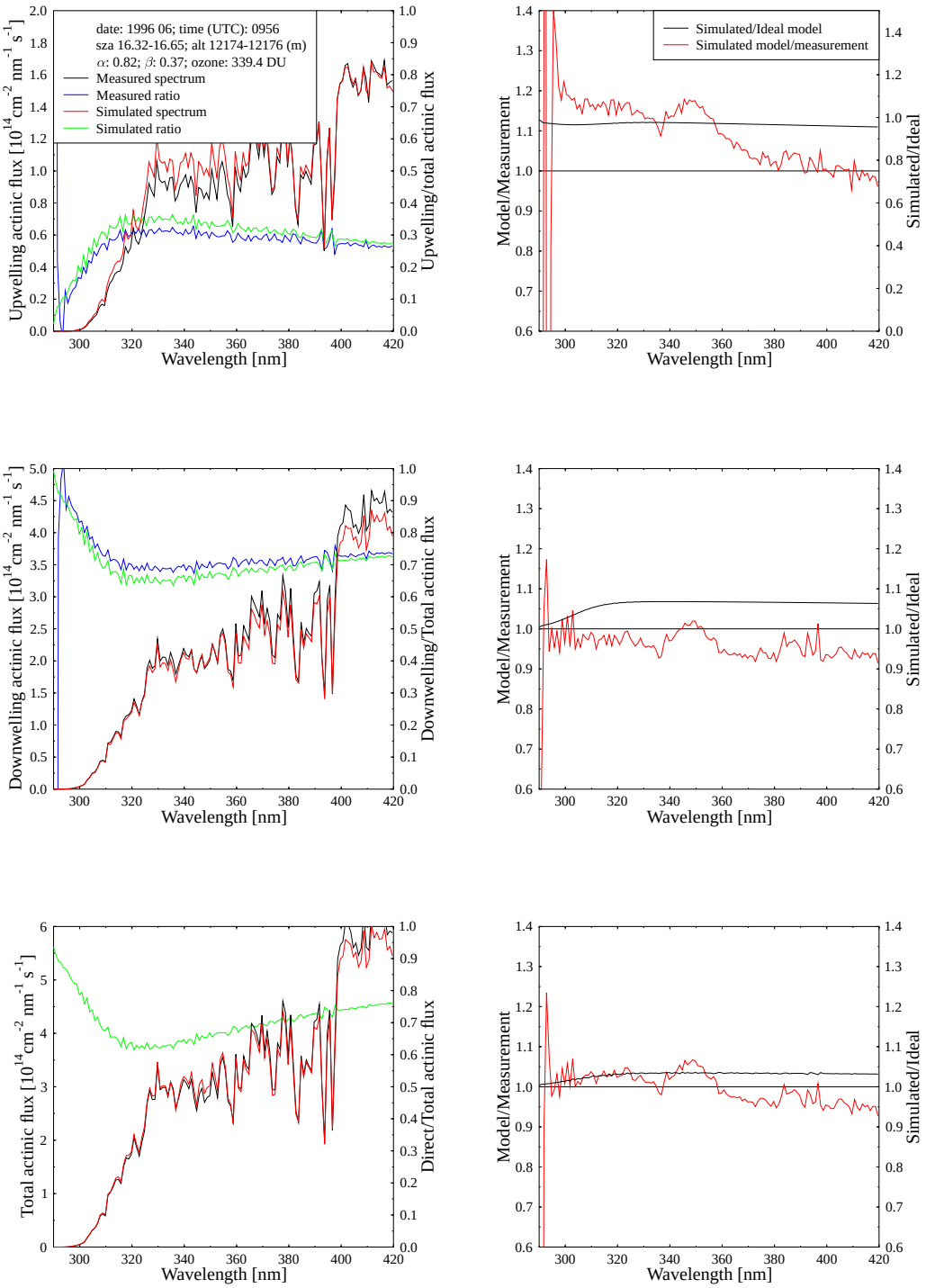

Figure 127: Same as Figure 10, except for 0956 UTC, 14 June 1996, and altitude 12174 m.a.s.l.

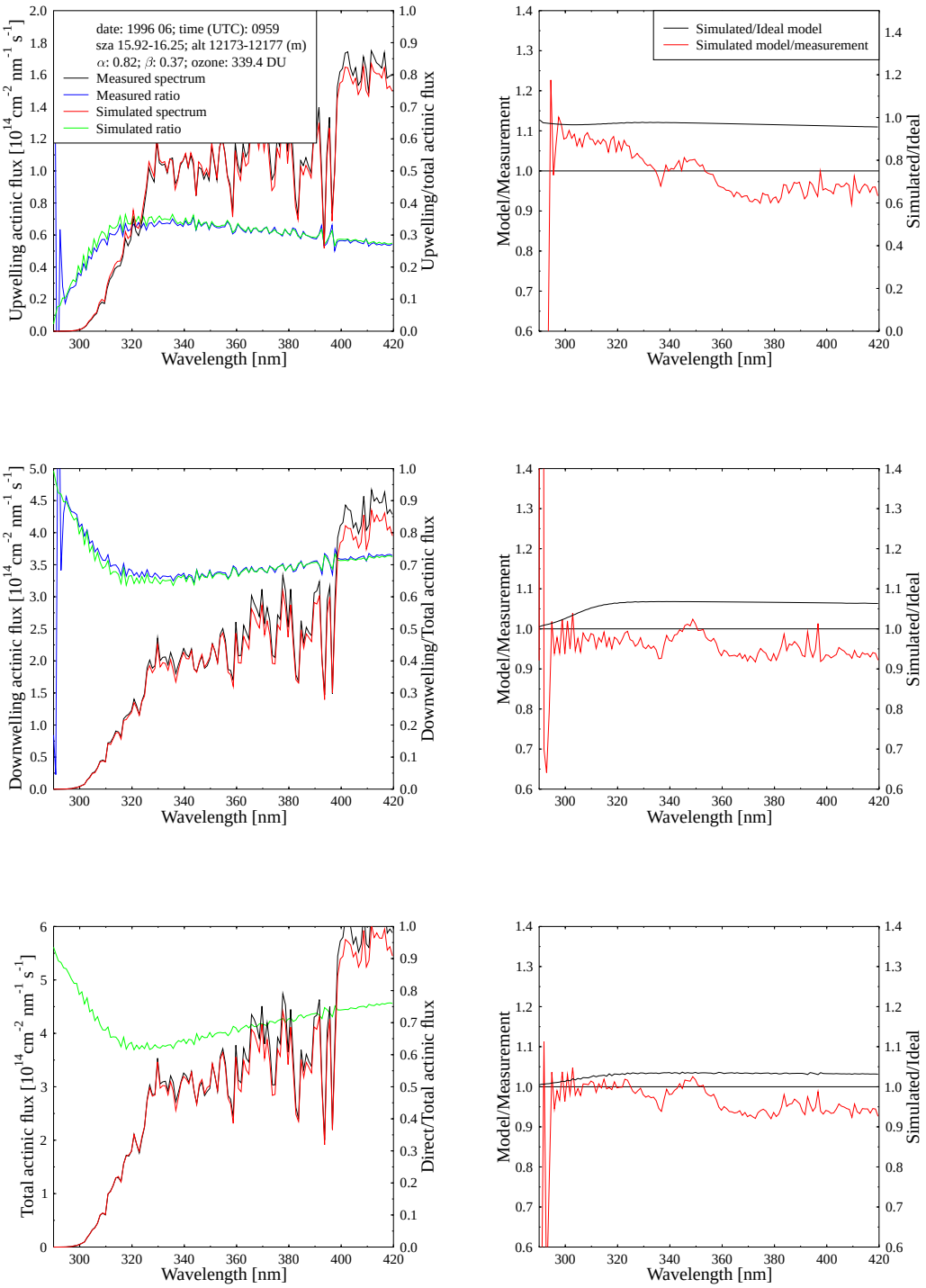

Figure 128: Same as Figure 10, except for 0959 UTC, 14 June 1996, and altitude 12175 m.a.s.l.